UNIVERSIDAD COMPLUTENSE DE MADRID
FACULTAD DE CIENCIAS FÍSICAS

TESIS DOCTORAL

Nanostructuring of soft matter for organic electronics

Nanoestructurado de materia condensada blanda con aplicaciones en electrónica orgánica

MEMORIA PARA OPTAR AL GRADO DE DOCTOR

PRESENTADA POR

Edgar Gutiérrez Fernández

Directores

Aurora Nogales Ruiz
Mari Cruz García Gutiérrez
Esther Rebollar González

Madrid

Nanostructuring of soft matter for organic electronics

Nanoestructurado de materia condensada blanda con aplicaciones en electrónica orgánica

Memoria presentada para optar al título de Doctor en Física por la Universidad Complutense de Madrid

Facultad de ciencias físicas

Presentada por

Edgar Gutiérrez Fernández

Directoras:

Aurora Nogales Ruiz (IEM-CSIC)

Mari Cruz García Gutiérrez (IEM-CSIC)

Esther Rebollar González (IQFR-CSIC)

Madrid, 2019

UNIVERSIDAD COMPLUTENSE MADRID

DECLARACIÓN DE AUTORÍA Y ORIGINALIDAD DE LA TESIS PRESENTADA PARA OBTENER EL TÍTULO DE DOCTOR

D./Dña. Edgar Gutiérrez Fernández,
estudiante en el Programa de Doctorado en Física,
de la Facultad de Ciencias Físicas de la Universidad Complutense de Madrid, como autor/a de la tesis presentada para la obtención del título de Doctor y titulada:

Nanostructuring of soft matter for organic electronics

Nanoestructurado de materia condensada blanda con aplicaciones en electrónica orgánica

y dirigida por: la Dra. Aurora Nogales Ruiz, la Dra. Mari Cruz García Gutiérrez y la Dra. Esther Rebollar González

DECLARO QUE:

La tesis es una obra original que no infringe los derechos de propiedad intelectual ni los derechos de propiedad industrial u otros, de acuerdo con el ordenamiento jurídico vigente, en particular, la Ley de Propiedad Intelectual (R.D. legislativo 1/1996, de 12 de abril, por el que se aprueba el texto refundido de la Ley de Propiedad Intelectual, modificado por la Ley 2/2019, de 1 de marzo, regularizando, aclarando y armonizando las disposiciones legales vigentes sobre la materia), en particular, las disposiciones referidas al derecho de cita.

Del mismo modo, asumo frente a la Universidad cualquier responsabilidad que pudiera derivarse de la autoría o falta de originalidad del contenido de la tesis presentada de conformidad con el ordenamiento jurídico vigente.

En Madrid, a 1 de julio de 2019

Fdo.: EDGAR GUTIÉRREZ FERNÁNDEZ

Esta DECLARACIÓN DE AUTORÍA Y ORIGINALIDAD debe ser insertada en la primera página de la tesis presentada para la obtención del título de Doctor.

A mis padres

Agradecimientos

Mis mayores agradecimientos son para todos los miembros de mi grupo de investigación, el grupo de materia blanda y polimérica (SoftMatPol), del Instituto de Estructura de la Materia. Considero que la suerte me acompaña si he acabado en este grupo trabajando con ellos. Ellos aceptaron un compromiso conmigo hace años y desde entonces no puedo más que agradecer el tiempo y la paciencia que dedicaron en mí.

En especial, a mis directoras de tesis: Aurora Nogales, Mari Cruz García y Esther Rebollar: tres personas y científicas de primera. Al resto del grupo SoftMatPol por su inestimable ayuda y colaboración durante estos años: Tiberio Ezquerra, Amelia Linares, José Carlos Canalda, y a mis antiguos compañeros que también ejercieron de profesores: Margarita Hernández, Jing Cui y Álvaro Rodríguez. A mis compañeros temporales de despacho: Iza, Ángel, Denisse, Andrés y Clara, a todos buena suerte. También a René, al cual podía encontrar a cualquier hora en el AFM para alguna buena conversación. Agradezco también la ayuda técnica, indispensable para el desarrollo de esta Tesis, de Carolina García, Moisés Martín y Douglas Vinson Laurents. Agradecimiento especial para nuestros colegas de la Universidad de Barcelona: Ismael Gabaldón, Aïda Varea, Anna Vilà y Albert Cirera. A los compañeros de noches en el sincrotrón: Michela Soccio, Marta Fernández, Laura Evangelio, Steven Gottlieb, Francesc Pérez, Jordi Fraxedas, Sara Marina y Jaime Martín. Obtener todos esos gigas de datos no sería posible sin la ayuda de los científicos de línea: Manuel Valvidares, Pierluigi Gargiani, Daniel Hermida, Marc Malfois y Heinz Amenitsch, con un agradecimiento especial para Eduardo Solano por su ilimitada disposición para solucionar problemas. A los compañeros de IMDEA Nanociencia: Jaime Hernández, Isabel Rodríguez, Alejandra y Manuel. A los compañeros y amigos del ICTP: Rubén, Rosa, Fran, Rebeca Hernández, Juan Rodríguez, Alberto Gallardo, Miguel Ángel López Manchado y Raquel Verdejo.

También quiero dar gracias a las primeras personas que me encontré cuando inicié mi camino científico en la Facultad de Física allá en 2011: Dani, Miguel, Emilio y Alex. Sin duda, su compañerismo y amistad ha sido crucial en muchos momentos.

Entre todas las personas que me han acompañado los últimos años, tengo mucho que agradecer a Julia, de no ser por ella yo no estaría aquí.

Por último, a mi familia, a mi hermano Eric, científico también, el cual tiene como naturales todas las cualidades que a mi cuestan; no tengo duda de que será el número uno en lo suyo. Y a mis padres Ángel y Pilar, mi suerte empezó con ellos, cada una de mis virtudes como humano tienen su origen ahí. Este trabajo es para vosotros.

Table of contents

Abstract

Organic, light, flexible materials with functional properties as electrical conductivity and ferroelectricity that can be used in electronic devices are likely to be a safe bet for the future. However, these materials present much lower efficiencies compared with their analog inorganic materials. Therefore, a lot of research is still to be done to put organic materials in the competitive market. Nanostructuring is one of the most important approaches to achieve this objective, due in part to the requirement of miniaturization of electronic devices and because of the possibility of tuning the properties of these materials by modifying their structure at the nanoscale. This Thesis is focused on the fabrication of nanostructures on soft matter, mainly polymeric materials, with semiconducting and/or ferroelectric properties. Three kinds of nanostructures were fabricated: nanolayers or thin films (Chapter 3), surface nanostructures generated by laser irradiation (Chapter 4) and by nanoimprint lithography (Chapter 5), and nanoparticles (Chapter 6). Every approach is applied to different functional materials and it has different motivations that include fundamental understanding of the system and possible applications in electronic devices such as organic solar cells, organic field-effect transistors, non-volatile memories and mechanical transductors.

Chapter 1 contains a descriptive introduction that includes the motivation of this Thesis, related to the potential of nanostructured systems with functional organic materials, including semiconducting and ferroelectric materials. Chapter 1 also contains an historical and contextual description of the materials used in this Thesis. Chapter 2 contains a description for every experimental technique applied, including deposition of samples, nanostructuring and characterization techniques, and also the experimental details used to prepare the samples investigated in this Thesis. Chapter 3 is dedicated to the study of functional thin film systems, both from the fundamental point of view and from their functional properties. Synergetic multilayer semiconducting/ferroelectric systems were prepared by sequential spin-coating. The samples were prepared by depositing a layer of the ferroelectric polymer poly(vinylidene fluoride-trifluoroethylene) (P(VDF-TrFE)) over a layer with variable thickness of the semiconducting polymer poly(3-hexylthiophene) (P3HT). The ferroelectric behavior of these systems was characterized by Piezoresponse Force Microscopy (PFM). In this chapter we also report a study of thin films of the conducting polymer poly(3,4-ethylenedioxythiophene):poly(styrene sulfonate) (PEDOT:PSS) fabricated by depositing the aqueous dispersion of PEDOT:PSS blended with high boiling point additives by spin-coating. The effect of these high boiling point additives on the inner structure of PEDOT:PSS either in the aqueous dispersion or in the corresponding thin films was studied by X-ray scattering. In addition, the morphology of the thin films was analyzed by Atomic Force Microscopy (AFM). In the last section of Chapter 3, a study on the

fabrication and analysis of PEDOT:PSS thin films deposited by inkjet printing is presented. The mechanical and electrical properties at the nanoscale of these films were characterized by Quantitative Nanomechanical Mapping (QNM) and conductive-AFM (C-AFM). The formation of Laser Induced Periodic Surface Structures (LIPSS) on several functional organic systems, together with the impact of laser irradiation on their inner structures and electrical properties are investigated and presented in Chapter 4. LIPSS on PEDOT:PSS were reported for the first time by irradiating with nanosecond laser pulses at 266 nm. On the other hand, the molecular orientation induced by laser irradiation on the semiconducting polymers P3HT and poly[N-9'-heptadecanyl-2,7-carbazole-alt-5,5-(4',7'-di-2-thienyl-2',1',3'-benzothiadiazole)] (PCDTBT) was analyzed by Near Edge X-ray Absorption Fine Structure (NEXAFS) in Total Electron Yield (TEY) mode. Furthermore, the formation of complex superficial structures, i.e. with more than one hierarchical degree, upon sequential laser irradiations was studied on P3HT thin films and also on bilayered systems of P3HT/P(VDF-TrFE). In addition, conducting nanowires of [6,6]-Phenyl-C_{71}-butyric acid methyl ester ($PC_{71}BM$) were fabricated through solution washing on samples of $PC_{71}BM$ previously irradiated at 532 nm. Chapter 5 contains a study on the fabrication of nanogratings of PEDOT:PSS by Nanoimprint Lithography (NIL), using different concentrations of glycerol, that acts as plasticizer agent of PEDOT:PSS. The strong effect of glycerol on the PEDOT:PSS structure was demonstrated in Chapter 3. The formation and the aspect ratio of the nanogratings were studied in detail by AFM as a function of the glycerol concentration used. Furthermore, the order of the gratings and the structural changes induced by NIL were addressed by X-ray scattering and Raman spectroscopy. In Chapter 6, the fabrication and characterization of functional polymer nanoparticles are reported. P3HT nanoparticles were fabricated by different solvent-exchange approaches. Structural differences between them were elucidated by optical and X-ray scattering experiments. Furthermore, nanoparticles of ferroelectric polymers poly(vinylidene fluoride) (PVDF) and P(VDF-TrFE) were prepared as well. The inner structure of PVDF and P(VDF-TrFE) nanoparticles was addressed by X-ray scattering and the ferroelectric behavior of P(VDF-TrFE) nanoparticles inferred by PFM.

In conclusion, during this Thesis the fabrication of nanostructured organic material systems with semiconducting and ferroelectric properties has been developed and studied, either towards the fundamental knowledge of the structure of the system or the potential use of their functional properties, since both fields are intimately related.

Resumen

Los materiales orgánicos que presentan propiedades funcionales como la conductividad eléctrica y la ferroelectricidad, además de sus propiedades de ligereza y flexibilidad, son una apuesta segura para el futuro debido a la posibilidad de emplearlos en dispositivos electrónicos. Sin embargo, comparados con materiales inorgánicos análogos, presentan eficiencias mucho menores. Es por ello que aún debe realizarse un esfuerzo de investigación y desarrollo considerable, con el objetivo de colocar a estos materiales orgánicos en un nivel competitivo en el mercado. La nanoestructuración es uno de los caminos más investigados para conseguir este objetivo, no solo por la demanda actual de miniaturización de dispositivos electrónicos sino también por la posibilidad de modificar las propiedades funcionales de estos materiales mediante la alteración de su nanoestructura. Esta Tesis está enfocada a la fabricación y al estudio de nanoestructuras de materia condensada blanda, principalmente polímeros, con propiedades semiconductoras y/o ferroeléctricas. Se han fabricado tres tipos de nanoestructuras: nanocapas o películas delgadas (Capítulo 3), nanoestructuras superficiales mediante irradiación con láser (Capítulo 4) y nanoestructuras mediante litografía de nanoimpresión (Capítulo 5), así como nanopartículas (Capítulo 6). En cada capítulo, el enfoque se centra en distintos materiales, motivado tanto por el conocimiento fundamental del sistema fabricado como por su posible aplicación en dispositivos electrónicos como las células solares orgánicas, transistores orgánicos de efecto campo, memorias no volátiles y transductores mecánicos.

El Capítulo 1 contiene una introducción descriptiva sobre la motivación de esta Tesis, basada en el potencial de los sistemas nanoestructurados de materiales orgánicos con propiedades funcionales, en particular, de los polímeros semiconductores y ferroeléctricos. Así mismo, el Capítulo 1 también contiene una descripción de los materiales usados en esta Tesis, desde un contexto histórico y bibliográfico. En el Capítulo 2 se detallan las técnicas experimentales empleadas durante la Tesis, desde la deposición de las muestras, las técnicas de nanoestructurado y las técnicas de caracterización de las muestras preparadas, así como las condiciones experimentales empleadas para la preparación de las mismas. En el Capítulo 3 se reporta el estudio de películas delgadas de materiales funcionales, tanto desde el punto de vista fundamental como desde una perspectiva más funcional. Se prepararon sistemas multicapa de polímero ferroeléctrico/semiconductor por *spin-coating* (recubrimiento por giro) secuencial, para estudiar sus sinergias. Las muestras estaban formadas por una capa del polímero ferroeléctrico poli(fluoruro de vinilideno-trifluoroetileno) (P(VDF-TrFE)) sobre otra capa de espesor variable del polímero semiconductor poli(3-hexiltiofeno) (P3HT). El comportamiento ferroeléctrico del sistema se ha caracterizado por microscopía de piezorespuesta (PFM). También se han fabricado películas delgadas del polímero conductor poli(3,4-etilendioxitiofeno):poli(estireno-sulfonato)

(PEDOT:PSS) por spin-coating a partir de dispersiones acuosas a las que se añadían aditivos de alto punto de ebullición. El efecto de estos aditivos sobre la estructura interna de PEDOT:PSS, tanto en la dispersión acuosa como en las correspondientes películas delgadas ha sido estudiado por dispersión de rayos-X. Por otro lado, la morfología de estas películas delgadas ha sido analizada por microscopía de fuerza atómica (AFM). Otra parte del Capítulo 3 está dedicada a la fabricación y al estudio de películas delgadas de PEDOT:PSS depositadas mediante impresión por inyección de tinta (*inkjet printing*). Las propiedades mecánicas y eléctricas de estas películas de PEDOT:PSS se han caracterizado a escala nanoscópica mediante análisis mecánico cuantitativo y AFM conductivo (C-AFM). En el Capítulo 4 se presenta un estudio sobre la formación de estructuras superficiales periódicas inducidas por láser (LIPSS) en varios sistemas funcionales orgánicos, así como el estudio del impacto que provoca la irradiación por láser sobre la estructura interna del sistema irradiado y sobre sus propiedades eléctricas. En este capítulo se reporta por primera vez la generación de LIPSS en PEDOT:PSS empleando para ello pulsos de nanosegundos a una longitud de onda de 266 nm. Por otro lado, la orientación molecular inducida por el tratamiento láser sobre los polímeros semiconductores P3HT y poli[N-9'-heptadecanil-2,7-carbazol-alt-5,5-(4',7'-di-2-tienil-2',1',3'-benzotiadiazol)] (PCDTBT) se ha investigado mediante absorción de rayos-X a energías cercanas al borde de absorción K del carbono (NEXAFS) en modo *Total Electron Yield* (TEY). En la siguiente sección del Capítulo 4 se presenta un estudio sobre la formación de estructuras superficiales complejas, es decir, con más de un orden de jerarquía, mediante irradiación láser secuencial sobre películas delgadas de P3HT, y también sobre sistemas multicapas de P3HT/P(VDF-TrFE). Asimismo, se han fabricado nanohilos conductores de [6,6]-Fenil-C_{71}-ácido butírico metil éster ($PC_{71}BM$) mediante lavado con un disolvente orgánico sobre películas delgadas de $PC_{71}BM$, que anteriormente habían sido irradiadas a 532 nm. En el Capítulo 5 se reporta la fabricación de nanoestructuras de PEDOT:PSS mediante litografía de nanoimpresión (NIL), usando diferentes concentraciones de glicerol, que actúa como agente plastificante del PEDOT:PSS. La influencia que tiene el glicerol sobre la estructura del PEDOT:PSS se ha demostrado en el Capítulo 3. La morfología de las estructuras se ha estudiado en detalle mediante AFM. Asimismo, el impacto del proceso de NIL sobre la estructura interna del PEDOT:PSS se ha analizado mediante dispersión de rayos-X, así como espectroscopía Raman. En el Capítulo 6 se presenta un estudio sobre la fabricación y caracterización de nanopartículas de varios polímeros funcionales. En la primera sección del capítulo se recogen los resultados obtenidos sobre la fabricación de nanopartículas de P3HT mediante dos métodos basados en el intercambio de un buen disolvente por otro líquido en el cual el polímero no se disuelve. Se han analizado las diferencias estructurales entre las nanopartículas preparadas por los dos métodos mediante técnicas de absorción y emisión de luz en el rango ultravioleta y visible y dispersión de rayos-X. A continuación, se presenta el estudio sobre la fabricación de nanopartículas de los polímeros ferroeléctricos poli(fluoruro de vinilideno)

(PVDF) y P(VDF-TrFE). La estructura interna de ambos sistemas se ha caracterizado por dispersión de rayos-X y el comportamiento ferroeléctrico de las nanopartículas de P(VDF-TrFE) se ha estudiado mediante PFM.

En conclusión, durante esta Tesis se ha profundizado en la fabricación de nanoestructuras de materiales orgánicos con propiedades semiconductoras y ferroeléctricas, desde el punto de vista del conocimiento fundamental y ante la perspectiva de las posibles aplicaciones que puedan aprovechar las propiedades funcionales de estos sistemas.

List of symbols and abbreviations

α	Exit angle in the vertical direction
$\boldsymbol{\alpha}$	Absorption coefficient
$\boldsymbol{\alpha^{-1}}$	Optical penetration depth
α_i	Incident angle
β	Full Width at Half Maximum in degrees
γ_s	Total surface free energy component of a solid
γ_l	Total surface free energy component of a liquid
γ_x^+	Electron-acceptor surface free energy component (x=s (solid), l (liquid))
γ_x^-	Electron-donor surface free energy component (x=s (solid), l (liquid))
γ_x^p	Polar surface free energy component (x=s (solid), l (liquid))
γ_x^d	Apolar surface free energy component (x=s (solid), l (liquid))
δ	Angle between electric field vector and transition dipole vector
ε	Dielectric constant
ε_0	Dielectric constant in vacuum
ε_{FE}	Dielectric constant in the ferroelectric layer
Θ	Angle between propagation vector of the laser and normal vector of the substrate
θ	Scattering angle
Λ	Period
λ	Wavelength
ν_s	Poisson ratio of the sample
ν_t	Poisson ratio of the tip
ξ	Correlation length
π	π-molecular orbital
ρ	Density
σ	σ-molecular orbital
σ_p	Polarization charge density
τ	Crystal mean size
τ_p	Pulse duration

φ	Contact angle (value)
χ	Azimuthal angle
ψ	Angle between tangents of two points within a polymer chain
ω	Exit angle in the horizontal direction
ω_{cyc}	Rotational speed
2θ	Scattering angle
3D	Three-dimensional
A, A_0, A_1, A_2	Constants
a	Persistence length
AC	Alternating current
AFM	Atomic Force Microscopy
BaO	Barium oxide
BHJ	Bulk Heterojunction
C	Heat capacity
c	Specific heat
C-AFM	Conductive-AFM
C_6H_5Cl	Chlorobenzene
CA	Contact Angle (Technique)
$CHCl_3$	Chloroform
D	Thermal diffusivity
d	Distance
d_{ts}	Distance between the tip and the sample
DC	Direct current
DLIP	Direct Laser Interference Patterning
DLS	Dynamic Light Scattering
DMA	N,N-Dimethylacetamide
DMSO	Dimethyl sulfoxide
DMT	Dejarguin-Muller Toporov
DSC	Differential Scanning Calorimetry
E	Energy
$\boldsymbol{E}$	Electric field

E_0	Built-in field
E_r	Reduced Young Modulus
E_s	Young Modulus of the sample
E_{tip}	Young Modulus of the tip
EG	Ethylene glycol
ESRF	European Synchrotron Radiation Facility
F	Fluence
$F_{adhesion}$	Adhesion force between the tip and the sample
F_{tip}	Force applied by the tip
fcc	Face-centered cubic
FFT	Fast Fourier Transform
G	Glycerol
g	Paracrystalline disorder parameter
GISAXS	Grazing-Incidence Small-Angle X-ray Scattering
GIWAXS	Grazing-Incidence Wide-Angle X-ray Scattering
H_2O_2	Hydrogen peroxide
H_2SO_4	Sulfuric acid
HOMO	Highest Occupied Molecular Orbital
I	Intensity
ICP	Intrinsic Conducting Polymer
I_H	Intensity of peak from TEY-NEXAFS spectrum taken at horizontal polarization
IP	In-plane
IPA	Isopropyl Alcohol
IPS	Intermediate Polymer Stamp
ITO	Indium Tin Oxide
I_V	Intensity of peak from TEY-NEXAFS spectrum taken at vertical polarization
J_0	Excitonic coupling
K	Shape factor
k	Scaling exponent
$\boldsymbol{k}$	Wavenumber vector

L	Screening length of the interchain interaction
LD	Linear dichroism
LinAc	Linear Accelerator
LIPSS	Laser Induced Periodic Surface Structures
LUMO	Lowest Unoccupied Molecular Orbital
m	High-q scaling exponent
MEK	Methyl Ethyl Ketone
M_n	Number Average Molecular Weight
M_o	Molecular weight
M_w	Weight Average Molecular Weight
N	Total number of molecules
n	Low-q scaling exponent
$\boldsymbol{n}$	Refractive index
n_I	Integer number
n_i	Number of molecules with molecular weight M_i
NEXAFS	Near Edge X-ray Absorption Fine Structure
NIL	Nanoimprint Lithography
NPs	Nanoparticles
$\boldsymbol{O}$	Transition dipole vector
OFET	Organic Field-Effect Transistor
OH	Hydroxyl group
OLED	Organic Light-Emitting Diode
OOP	Out-of-plane
OPVs	Organic Photovoltaics
OSC	Organic Solar Cell
P	Polarity
$\boldsymbol{P}$	Polarization vector
P(t)	Temporal shape of the laser pulse
P3HT	Poly(3-hexylthiophene-2,5-diyl)
PA	Polyacetylene
$PC_{61}BM$	Phenyl-C_{61}-butyric acid methyl ester

$PC_{71}BM$	Phenyl-C_{71}-butyric acid methyl ester
PCDTBT	Poly[N-9'-heptadecanyl-2,7-carbazole-alt-5,5-(4',7'-di-2-thienyl-2',1',3'-benzothiadiazole)]
PDI	Polydispersity Index
PDMS	Polydimethylsiloxane
PEDOT	Poly(3,4-ethylenedioxythiophene)
PFM	Piezoresponse Force Microscopy
PF-QNM	Peak-Force Quantitative Nanomechanical Mapping
PRI	Photo-induced Resist-free Imprinting
PS	Polystyrene
PSS	Polystyrene sulfonate
PSSH	Polystyrene sulfonic acid
PT	Polythiophene
PVDF	Polyvinylidene fluoride
P(VDF-TrFE)	Poly(vinylidene fluoride-trifluoro ethylene)
Q	Heat
q	Modulus of scattering vector
$\boldsymbol{q}$	Scattering vector
q_r	Radial component of scattering vector
$q_{x,y,z}$	x,y,z component of scattering vector
R	Radius of the tip end
RCP	Randomly Close Packed
R_g	Radius of gyration
RH	Relative humidity
Rpm	Revolutions per minute
R_q	Quadratic Roughness
RR	Regioregularity
s	Dimensionality
SAXS	Small-Angle X-ray Scattering
sdd	Sample-detector distance
SDS	Sodium dodecyl sulfate

SEM	Scanning Electron Microscope
STM	Scanning Tunneling Microscope
T	Temperature
$\boldsymbol{T}$	Trans
t	Time
t_f	Thickness of the ferroelectric layer
t_s	Thickness of the semiconducting layer
t_d	Thermal diffusion time
TEY	Total Electron Yield
T_g	Glass transition Temperature
THF	Tetrahydrofuran
TiO_2	Titanium dioxide
T_m	Melting Temperature
UV	Ultraviolet
V_c	Coercive voltage
VIS	Visible
WAXS	Wide-Angle X-ray Scattering
w_i	Weight fraction
wt. %	Weight relation in percentage
XANES	X-ray Absorption Near Edge Structure
x_0, y_0, z_0	Coordinates in pixels of the direct beam
x_p, y_p, z_p	Coordinates in pixels in the detector map
x_i	Degree of polymerization
z	Depth

Chapter 1. Introduction

Organic electronics and nanoscience have emerged into a promising research branch that it is yet to generate a technological revolution. Soft materials that could combine the lightness and flexibility of a plastic sheet with the electric properties of silicon are a reality since decades. Flexible organic electronics is based on semiconducting polymers and in polymers whose properties can be modified with an electric field. However, in the case of semiconducting polymers, low electric charge transport properties and irregular morphologies are part of the issues that soft materials must overcome in order to become a real adversary of silicon devices. Inorganic electronics still hold the market of electronic devices. On the other hand, due to their relative economic handling and production, and their extreme versatility, polymers are nowadays the most popular material in the earth and are used virtually in every aspect of daily life. In addition, scientific research on polymers is soaring due to the required development of biodegradable polymers that could substitute commodity plastics, composites with outstanding thermal and mechanical properties with great lightness, and special functional polymers as conducting polymers that could substitute rigid-inorganic conducting materials.

Many developments have been achieved since initial insoluble, unstable conducting polymers were synthesized. The milestone that began the era of conducting polymers is considered the publication by Chiang et al. in 1977[1], who reported high conductivity in polyacetylene (PA) doped with different halogens vapors. By varying the level of doping, reversible conductivity values were achieved over a range of eight orders of magnitude. For this discovery, Heeger, Shirakawa and McDiarmid received the Nobel Prize in Chemistry in 2000. This discovery was seen as a revolutionary step in the material technology, because it joined the possibility of achieving a material with metallic-electronic properties with the lightness, processability and functionalization properties of organic polymers that metals cannot meet[2].

The first and simpler conjugated polymers such as PA and polythiophene (PT) were insoluble and infusible, complicating their versatility on future applications. This drawback was solved, among other approaches, by adding flexible alkyl chains to the conjugated backbone thus enhancing the solubility. The second generation of semiconducting polymers started with the synthesis of the first soluble polymers with semiconducting behavior. Then, thin flexible layers with semiconducting behavior could be produced by only depositing the solution of semiconducting polymer on a flexible substrate. Thus, the concept of "printed electronics" was introduced. These layers were seen as potential candidates to the fabrication of a new generation of electronic devices with an organic functional component, such as organic solar cells (OSCs), organic light-

emitting diodes (OLEDs) and organic-field effect transistors (OFETs). Further improvements on synthesis led to the development of a series of conjugated polymers with more complex chemical structures, which present enhanced thermal stability and lower energy gap that remarkably improved the efficiencies of OSCs[2,3]. Conducting polymers, or "electronic plastics", are considered materials for the future. Although there have been exceptional advances in this area in the last decades, there are still many important steps to develop in order to enhance the presence of these materials in the global market.

Besides organic materials with conducting or semiconducting properties, the other functional materials studied in this Thesis are ferroelectric polymers. Ferroelectric materials are those whose electric dipoles can be polarized, i.e. oriented in the same direction under the application of an electric field and can retain that state when the electric field is zero. This polarized state can be switched under the application of an electric field with opposite direction. These systems with two bistable states that can be switched between them are called "flip-flop". This is the idea behind every memory device. In addition, ferroelectric materials suffer a mechanical stress when they are polarized. This effect is called piezoelectricity[4]. In a reciprocal way, ferroelectric materials suffer a mechanical deformation when an electric voltage is applied (inverse piezoelectricity). Therefore, ferroelectric polymers blend the bistable and piezoelectric nature of ferroelectric materials with the low-cost, flexibility, lightness and nanostructuring possibilities of polymers, allowing the fabrication of organic non-volatile memories or mechanical transductors.

Besides the synthetic approaches for new functional polymers with semiconducting or ferroelectric properties, recent developments on fabrication and characterization of nanostructures have become a fundamental partner for organic electronics[5]. The access to the nanoscale in soft materials allows us to understand the correlation between their nanostructure and the macroscopic properties that will be used in electronic devices. This understanding is essential to keep developing the field of organic electronics.

These mentioned organic functional materials with electrical properties, together with the possibility of manipulating its structure and the generation of nanostructures with controlled geometries, open the doors to innovative applications. The merging of these topics is the main motivation of this Thesis, as outlined in Figure 1.1. The devices built with either conducting or ferroelectric polymers are expected to be essential in the near future, towards the known concept of 'internet of things'[6]; in which wearable electronic devices as solar cells or mechanical transductors are ubiquitous concepts involved in a sustainable future of the society.

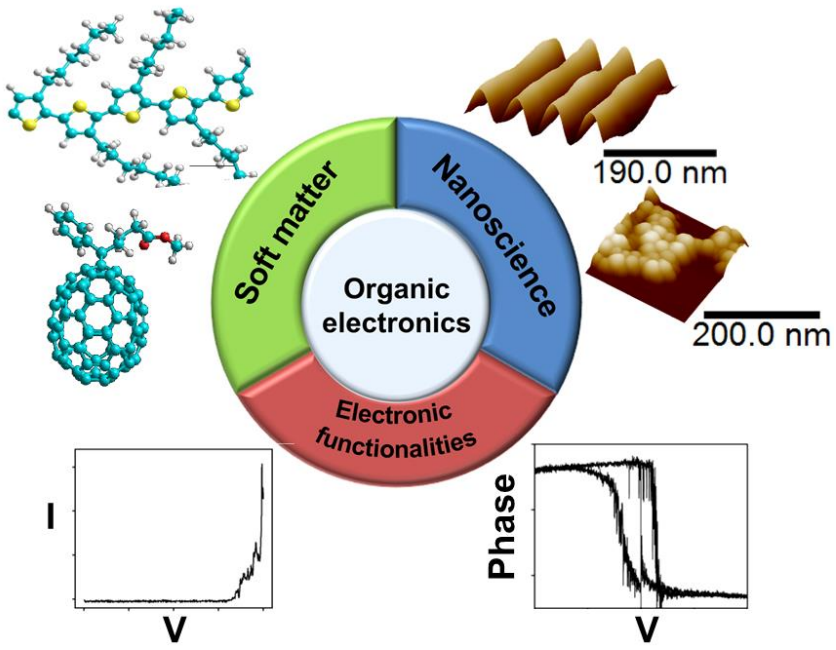

Figure 1.1 Scheme of main scientific branches developed in this Thesis.

1.1 Conjugated polymers

The most common polymers in the world are insulating. Saturated polymers are those whose carbon atoms have all their electrons occupying σ molecular orbitals. These orbitals stabilize the backbone[7] but inhibit charge transport. All the polymer commodities are saturated polymers and show electrical conductivity values under 10^{-10} S·cm^{-1} unless they are blended with conducting additives like graphene or carbon nanotubes[8]. All the intrinsically conducting polymers (ICPs) are conjugated polymers, i.e. present an alternating chemical structure of single and double carbon-carbon bonds, and their mechanisms of conductivity were not discovered until the second half of the XX century[9]. Figure 1.2 shows the most known families of conducting polymers.

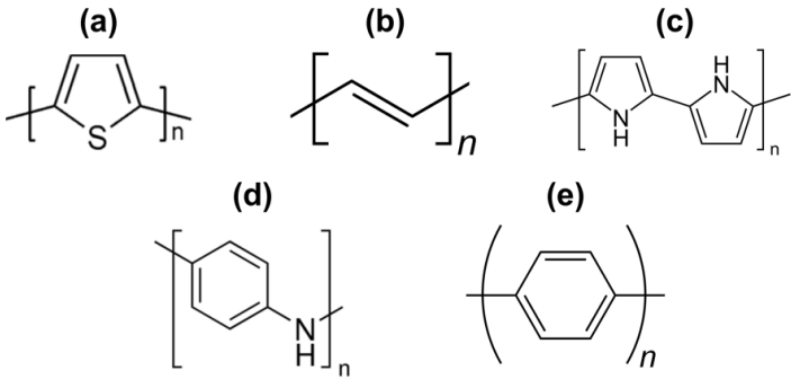

Figure 1.2 Common families of conjugated polymers: **(a)** polythiophene, **(b)** polyacetylene, **(c)** polypyrrole, **(d)** polyaniline and **(e)** poly(p-phenylene).

The main characteristic of conjugated polymers is the presence of delocalized π-electrons along the carbon backbone. From each carbon, three of the four valence electrons are in σ-bonding orbitals, whereas the fourth takes part in a delocalized p_z atomic orbital, that hybridizes with neighbouring p_z orbitals generating π molecular orbitals along the chains[9]. An energy barrier is formed between the highest occupied molecular orbital (HOMO) (π) and the lowest unoccupied molecular orbital (LUMO) (π*). This barrier is called the band gap energy of the semiconducting polymer. The electron at the π orbital must overcome this barrier to generate charge transport. Organic semiconductors present this energy gap between the HOMO and the LUMO, in analogy with the energy gap between valence and conduction bands in inorganic semiconductors[4].

This is a paradigmatic situation for all the conjugated polymers, which usually present semiconducting behavior. The extended conjugation along long polymeric chains yields a reduction of the band gap, and in many conjugated polymers this energy gap is in the visible or infrared range of the electromagnetic spectrum. This is what makes semiconducting polymer interesting for photovoltaics applications[10,11].

In order to enhance the charge carrier density and with that the conductivity, conjugated polymers are usually doped chemically or electrochemically[1,2,12]. Unlike the addition of impurity atoms in inorganic semiconductors, doping organic semiconductors means adding (reducing) or retiring (oxidizing) electrons from the material using a doping agent which also could act as a counter-ion. P-type doping means oxidizing the polymer by retiring electrons from the HOMO, leaving an excess of positive charges. In this case, positive charges (holes) are the main charge carrier. In the other case, n-type doping implies reducing the polymer by adding electrons. In n-type semiconductors, electrons are the main charge carrier.

When we talk about an ICP, we generally talk about a conjugated polymer, doped or not, whose main charge carriers are holes. The conductivity of these materials is highly dependent on the chemical structure[13,14] and the oxidation level[1]. The morphology at the nanoscale is also important because the conductivity of a polymer is highly anisotropic[3].

1.1.1 Optical properties of conjugated polymers

The electrical behavior of conjugated polymers is directly connected with their optical properties. This relation is widely known and studied in solid state physics. Saturated polymers are insulators and colorless because the energy gap to produce a free charge is considerably high: the lowest-energy electronic excitation is in the ultraviolet range[15]. On the other hand, conjugated polymers have a strong sensitivity to the visible light. The theory for optical features in conjugated polymers was mainly developed in the last two decades by Spano and coworkers[16–18] on the basis of the exciton-aggregation model proposed by Kasha and coworkers in the middle of the XX century[19].

An exciton is a quasiparticle formed by an electron and a hole. It is formed, for example, in semiconductors when the electron promotes from the valence to the conduction band. This bound state between the electron and the hole left at the valence band is an exciton.

Conjugated polymers are treated as strings of coupled absorption entities (chromophores) that present quite different optical properties than their corresponding single chromophores. In polymer aggregates, the exciton could travel through coupled chromophores in the same molecule and between chromophores of adjacent molecules[16]. In short, the physical framework consists in describing assemblies of conjugated polymers as a combination of J-type and H-type aggregates with different excitonic couplings that yield different absorption and emission features. In a J-aggregate, the chromophores are arranged in a head-to-tail fashion, leading to a negative excitonic coupling (J_0) (Figure 1.3.a). This is the physical situation where there is a strong interaction within the same chain. On the other hand, H-aggregates are associated with a strong interchain coupling. In this situation, chromophores are organized in a side-to-side fashion, with a positive excitonic coupling (Figure 1.3.b). Both types of aggregates contribute to the optical response of conjugated polymers, justifying the use of a generalized H-J system (Figure 1.3.c).

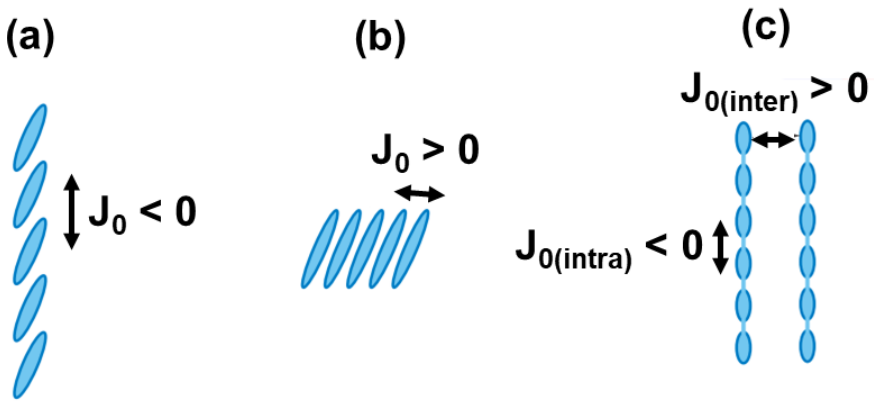

Figure 1.3 Scheme of molecular orientations within **(a)** a J-aggregate, **(b)** an H-aggregate, and **(c)** an HJ-aggregate. Modified figure from reference[17]. $J_{o(inter)}$ is the excitonic coupling between adjacent chains. $J_{o(intra)}$ is the excitonic coupling between consecutive repeat units.

Modifications on the inner structure of a conjugated polymer system induce a preferential J- or H-aggregate behavior, leading to changes in spectral signatures. For example, long and extended conjugated chains may present exciton coupling along the same chain (1D) rendering J-aggregate behavior, whereas many conjugated chains stacked along the π-π direction will couple the exciton between chains (2D), presenting H-aggregate features. Therefore, the competition between J- and H- aggregate behaviors is usually seen as a competition between predominant intra and interchain interactions. Analysis of absorption and emission spectra of conjugated polymers is a useful

approach for extracting information about physical features of the sample like the level of disorder and the planarization of the backbone.

Figure 1.4 presents the absorption spectra in the range of λ=300-700 nm of the conjugated polymer poly(3-hexylthiophene-2,5-diyl) (P3HT) in different states of aggregation. The spectrum from solution (black curve) presents a single absorption peak produced by intrachain states from chains in a coil conformation[20]. On the other hand, the spectrum of a thin film of P3HT (red curve) is red-shifted (towards higher λ) with clearly different peaks that arise from coupling between exciton and vibronic modes.

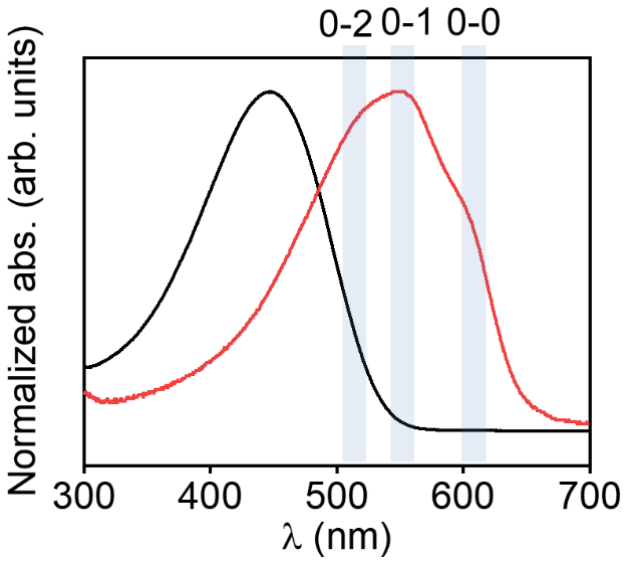

Figure 1.4 Absorption in the ultraviolet and visible range of a P3HT solution (black curve) and of a P3HT thin film (red curve). Labels show the quantum numbers associated with vibronic transitions.

The spectral features of conjugated polymers are indicators of their nano and microstructure. Specially, the intensity ratio between the 0-0 and 0-1 vibronic transition peaks from both absorption and emission spectra in the UV-VIS range is sensitive to the balance between intrachain and interchain excitonic coupling[16,17]. Thus, when the chain presents longer correlation, and intrachain coupling dominates, the 0-0 transition becomes more prominent.

1.2 Ferroelectric polymers

As it was said in the previous section, most of the commonly used polymers are electrically insulating. These materials do not have free electrons to transport charge since their electrons are strongly attached in the molecules. Even in conjugated polymers, as explained in the previous section, electrons need to overcome a relatively low energy barrier to transport charge, exhibiting semiconducting behavior. As a general rule, saturated polymers are dielectric, i.e. an external

electric field can displace the electrons in the material inducing a net polarization. When the electric field goes to zero, the dipoles cannot maintain this orientation and the net polarization is zero (Figure 1.5.a). On the other hand, ferroelectric polymers, due to their particular chemical structure, can maintain this preferential polarization when the external electric field is zero (Figure 1.5.b). This polarized state can be removed by applying an electric field in the opposite direction and a further increase of electric field in the opposite direction will cause complete reversal of orientation of all domains in the direction of the field. Therefore, the polarization of ferroelectric materials presents typical hysteresis loops as a function of the applied electric field (Figure 1.5.b). Above a certain temperature called transition temperature[4] or Curie temperature the ferroelectric material shows paraelectric behavior (Figure 1.5.c).

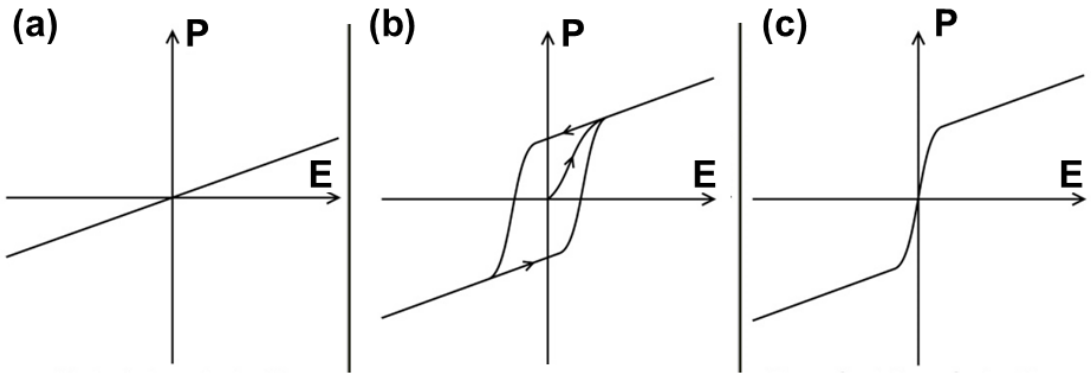

Figure 1.5 Polarization (*P*) as a function of electric field (*E*) for a **(a)** dielectric, **(b)** ferroelectric and **(c)** paraelectric.

1.3 General properties of polymers in the context of organic electronic functional materials

Functional polymers with applications in organic electronics can be described using the classical concepts for polymers in general. Yet, they are basically large molecules (macromolecules) built from the sequential covalent union of repeating small units through a process called polymerization, as defined by Hermann Staudinger[21] in the 1920s. The main concepts of polymer physics, developed between 1930 and 1960, like the work of Kuhn on ideal chain models and the work of Flory on chains in solutions[22] can be applied to functional polymers. And their dynamics can be described using the main principles of modern polymer physics introduced, like the reptation theory by de Gennes[21,23], in the 1980s.

The main parameter that characterizes a polymer is the number of repeating units of its chain: the degree of polymerization. The molecular weight of a particular sample of polymer is statistical

and is defined by the number average (M_n) (Equation 1.1) and the weight average (M_w) (Equation 1.2).

$$M_n = \frac{\sum_i n_i M_i}{\sum_i n_i} = \frac{\sum_i n_i x_i M_0}{N} \quad (\mathbf{1.1}) \quad ; \quad M_w = \frac{\sum_i n_i {M_i}^2}{\sum_i n_i M_i} = \frac{\sum_i w_i M_i}{\sum_i w_i} \quad (\mathbf{1.2})$$

N is the total number of molecules, n_i the number of molecules with molecular weight M_i, which is the product of its particular degree of polymerization x_i with the molecular weight of the monomer M_0. The number average is the mean value of the number-of-molecules distribution whereas the weight average averages the weight fractions w_i. M_w is always larger (or equal) than M_n. Its relation is called the polydispersity index (PDI) (Equation 1.3).

$$PDI = \frac{M_w}{M_n} \quad (\mathbf{1.3})$$

The same chain can present a huge number of conformations that depends on its molecular weight. Another feature that influences the molecular characteristics of a polymer is its regioregularity, that describes the way the substituent groups are ordered around the main chain. Regiorandom polymers present a random distribution of their substituents groups (Figure 1.6.a) with respect to the main chain, whereas regioregular polymers present a periodic configuration along the chain (Figure 1.6.b).

Figure 1.6 Scheme of different configurations of Poly(3-hexylthiophene-2,5-diyl) (P3HT): **(a)** regiorandom and **(b)** regioregular. Adapted figure from reference[24].

The composition of the chain can be homogeneous or formed by two or more different monomers giving rise to a copolymer.

Polymers can be amorphous or semicrystalline, attending to their interchain structural arrangement. Amorphous polymers do not present any translational and rotational order between chains in the solid state. Semicrystalline polymers, however, have nano or microscopic domains

in which the chains are arranged in a periodic three-dimensional structure: a crystal. A polymeric crystal consists of stacked chains in the same conformation[15], parallel to each other, in a way that form a unit cell of atoms covalently bonded in the direction of the chain and linked by Van der Waals bonds between chains. Due to kinetic reasons, a polymer cannot achieve a 100% crystallized state. Therefore, they are named semicrystalline, with localized crystalline and amorphous domains. Figure 1.7 shows the usual structural motifs at different scales found in a semicrystalline polymer.

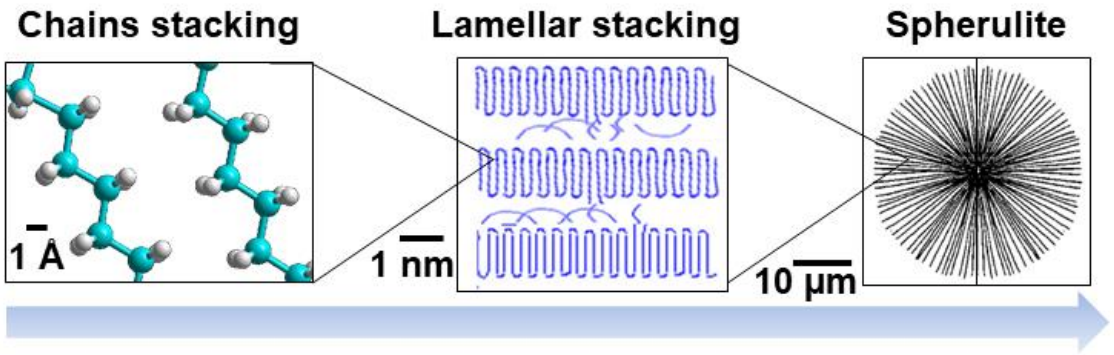

Figure 1.7 Structural motifs at different scales in a semicrystalline polymer from atomic scale **(left)** to mesoscopic **(center)** and microscopic scale **(right)**, the latter image modified from reference[25].

Polymer chains in an amorphous domain are disordered, without translational order and with a certain level of mobility, which is determined by the glass transition temperature (T_g). Above the T_g, the chains have long-range segmental motion; the non-covalent bonds between chains cannot retain them so they can wiggle around, changing their conformations easily; the material is soft and flexible, i.e. deformable[26]. Below the T_g it becomes a 'glassy' material and is considered a kinetically frozen state. The chains have enough mobility to vibrate but not enough for long range displacements, thus chains are frozen in their conformations. Therefore, in the glassy state, the polymers are generally brittle and rigid. T_g is an important parameter for every polymer application.

On the other hand, the temperature relevant for crystalline domains is the one of their melting (T_m), at which the polymer loses the translational order and becomes an isotropic liquid. There is also a special kind of phase that could be present in polymers called the 'liquid crystalline phase' in which features from solid and liquid are combined, for example, translational order but rotational disorder[27].

When a polymer is cooled down from its melt, it may crystallize at temperatures between the T_m and T_g. Crystallization, though, can also be achieved at room temperature or relatively low temperatures from a diluted solution. In this Thesis, the majority of the semicrystalline polymeric

systems investigated are crystallized from solutions. Crystallization of polymers depends on many factors: the chemical structure of the chain must have a certain degree of flexibility and symmetry of its atoms, the molecular weight is also important, together with the experimental conditions such as temperature and the concentration of the solution regarding the crystallization from solution.

In the case of semicrystalline polymers, whose structure is formed by crystalline and amorphous domains, the macroscopic properties could be very dependent on the inner structure and a deeper understanding of how this structure is formed and its dependence on temperature or structural modifications is required to develop future applications.

1.4 Functional materials investigated in this Thesis

1.4.1 P3HT

Poly(3-hexylthiophene-2,5-diyl) (P3HT) (Figure 1.8.a) is one of the most studied conjugated polymers due to its simple chemical structure, ease of synthesis and high level of self-assembly that make it a touchstone for the study of relations between optoelectronic properties and polymeric dynamics and structure. Unlike PT, P3HT is soluble in several organic solvents due to the attached alkyl chains on the thiophene rings. Thin films of regioregular P3HT deposited from a chloroform solution present high degree of crystallinity and orientation. P3HT commonly crystallizes in a monoclinic lattice[28], with the molecules planarized and stacked in the perpendicular direction of the thiophene rings due to interaction between π molecular orbitals of adjacent molecules, forming lamellas stacked in the direction perpendicular to the substrate plane (Figure 1.8.b).

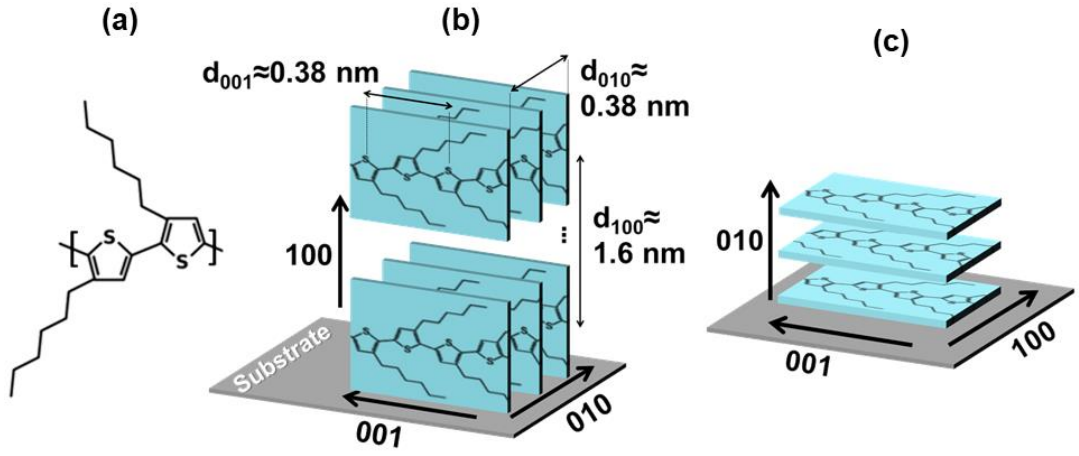

Figure 1.8 (a) Chemical structure of P3HT. Scheme of different crystalline orientations of P3HT thin films: **(b)** "edge-on", and **(c)** "face-on". Miller indexes (hkl) from crystallographic planes and their corresponding interplanar distances d_{hkl} are labelled.

This orientation is called "edge-on" (Figure 1.8.b) and it is reported to be the most thermodynamically favored state[29]. "Face-on" orientation (Figure 1.8.c) consists of molecules lying in the substrate plane. Therefore, the lamellar stacking direction is on the substrate plane and the π-π stacking direction is perpendicular to this plane. These crystalline orientations can be identified by means of X-rays diffraction, technique described in detail in section 2.3.5. It has been demonstrated that different preferential orientations of the crystals could be achieved by varying the thickness of the film[30], the substrate[31], the deposition method[32], by nanostructuring[33] or by laser irradiation[34]. Since all conjugated polymers present a certain degree of π-π stacking, "edge-on" and "face-on" are commonly used terms to describe orientations for conjugated polymers that present some degree of crystallinity.

P3HT is semicrystalline at room temperature[35–38]; it is hard to determine a single T_g because of convolution of stiff backbone-torsion transition (twist-glass transition[39]) with flexible side chain melting[35]. Above this latter value, the molten side chains and the still solid main chains can yield the structure to a called layered mesophase[40]. T_g of P3HT has been placed experimentally and theoretically to occur between -60ºC and 50ºC[38,41–43], being 12ºC a usually reported value[44,45]. The melting point is around 230ºC[46], though it is reported that P3HT undergoes to a liquid crystalline nematic phase before total melting into an isotropic state[38,47]. P3HT chains can crystallize into three polymorphs: I, I', and II; all of which have been reported experimentally[48–50].

P3HT has an energy gap between the HOMO and the LUMO of E≈2 eV. It is the archetypical electronic donor component in OSCs[51–54] (Figure 1.9.a). In OSCs, the energy of the absorbed solar photons is used to promote electrons from the HOMO to the LUMO and then transferred to the acceptor component –usually a fullerene derivative molecule[55]- through the interface between both components. P3HT is also widely applied as semiconducting material in OFETs[56–58] (Figure 1.9.b). As it was mentioned in section 1.1, the main difference between conductivity in polymers and, for example, metals or conducting oxides, is that polymer conductivity depends always on charge transport through insulating spaces between molecules. Therefore, the conductivity of P3HT and other conjugated polymers, is highly anisotropic[59,60]. The highest value of hole mobility is in the backbone direction within the same molecule (through intrachain electronic delocalization). A medium value of hole mobility is found in the π-π stacking direction. Along the lamellar stacking the hole mobility is orders of magnitude lower because the charge carriers have to pass through the σ-bonded carbons of the alkyl side chains, which act as insulating regions. The control of P3HT morphology, and extrapolated to all conjugated polymers, is crucial to the final performance of devices, because a higher conductivity along the thickness of thin films would be convenient in OSCs (Figure 1.9.a) whereas OFETs could require a higher lateral charge transport (Figure 1.9.b).

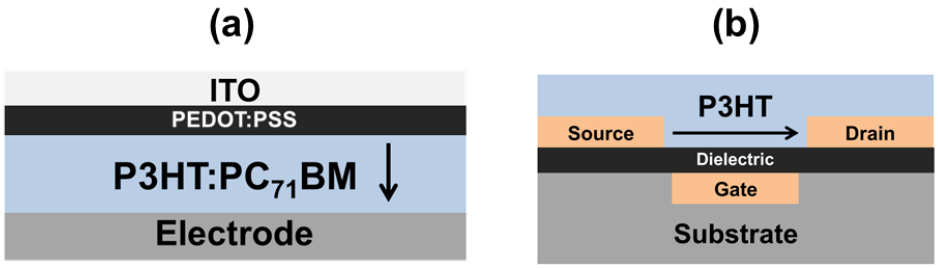

Figure 1.9 (a) Scheme of an organic solar cell, with a photosensitive layer of P3HT blended with the fullerene derivative [6,6]-Phenyl-C_{71}-butyric acid methyl ester ($PC_{71}BM$), a hole-selective layer of conducting polymer poly(3,4-ethylenedioxythiophene)-poly(styrenesulfonate) (PEDOT:PSS) and a transparent electrode made of indium-tin oxide (ITO). **(b)** Scheme of an organic field-effect transistor, with a layer of P3HT as a semiconducting path for electrons between source and drain electrodes. The arrows indicate the path of electrons in OPVs and electrons or holes in OFETs, depending on the polarization of the gate electrode.

1.4.2 PCDTBT

Poly[N-9′-heptadecanyl-2,7-carbazole-alt-5,5-(4′,7′-di-2-thienyl-2′,1′,3′-benzothiadiazole)] (PCDTBT) (Figure 1.10) belongs to the family of donor-acceptor electronic polymers, i.e. with electronic donor groups in its chemical structure as well as electronic acceptor groups, that yield a low energy gap between HOMO and LUMO (≈1.8 eV). PCDTBT was designed originally for potential applications in OSCs[61,62], and it is reported to achieve high performances in these kind of devices[63,64].

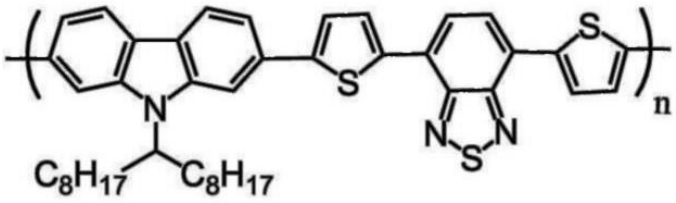

Figure 1.10 Chemical structure of PCDTBT**.**

PCDTBT is a mainly amorphous polymer with a stiff main chain[65]. Its glass transition temperature is located around 130ºC[61].

1.4.3 $PC_{71}BM$

[6,6]-Phenyl-C_{71}-butyric acid methyl ester ($PC_{71}BM$) is a fullerene-derivative of the C_{70} molecule. $PC_{71}BM$ plays an important role in organic photovoltaics as acceptor-electronic component in the active layer. It is an n-type semiconductor. Unlike the spherical buckminsterfullerene C_{60}[66], C_{70}

is made of 70 carbon atoms bonded into 25 hexagons and 12 pentagons, forming a prolate spheroid (Figure 1.11). The substituent adds stability and solubility to the molecule, which is a quite important requirement for $PC_{71}BM$ processing in general and for preparation of blends. In particular, for blends with electronic-donor polymers like P3HT in the same organic solvent, such as chloroform or chlorobenzene.

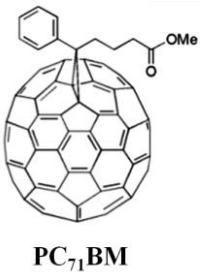

Figure 1.11 Chemical structure of $PC_{71}BM$.

$PC_{71}BM$ has stronger absorption in the visible range than $PC_{61}BM$[67], which was initially the common option as electronic acceptor in the active layer of polymeric solar cells[52]. Therefore, $PC_{71}BM$ has been used as acceptor in many of the most efficient organic photovoltaic cells[68,69].

1.4.4 PEDOT:PSS

Among the conjugated polymers, poly(3,4-ethylenedioxythiophene)-poly(styrenesulfonate) (PEDOT:PSS) occupies a special position because it presents some properties that are usually complicated for other conjugated polymers: "solubility" in water, high conductivity values, high transparency in the visible region when processed as thin films and good ambient stability. PEDOT:PSS is formed by two polymers: the stable conjugated poly(3,4-ethylenedioxythiophene) (PEDOT) (Figure 1.12, left), which, like P3HT, belongs to the group of polythiophenes and is insoluble in water or any organic solvent, and polystyrene sulfonate (PSS) (Figure 1.12, right) which is water-soluble and also acts as charge-balancing counter ion during PEDOT:PSS polymerization.

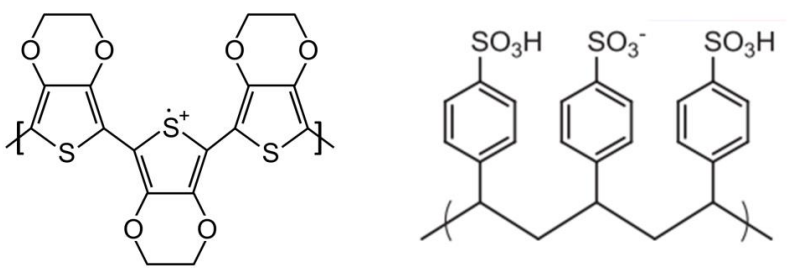

Figure 1.12 Chemical structure of PEDOT **(left)** and PSS **(right)**.

PEDOT:PSS is supplied as an aqueous dispersion, which promotes the formation of micelles; the hydrophobic polycationic PEDOT segments tend to form dispersed grains surrounded by the polyanionic PSS chains, which constitute the hydrophilic shell, forming PEDOT:PSS micelles or "grains" of around 80 nm of diameter (Figure 1.13). This is the general model used to describe the PEDOT:PSS system[9].

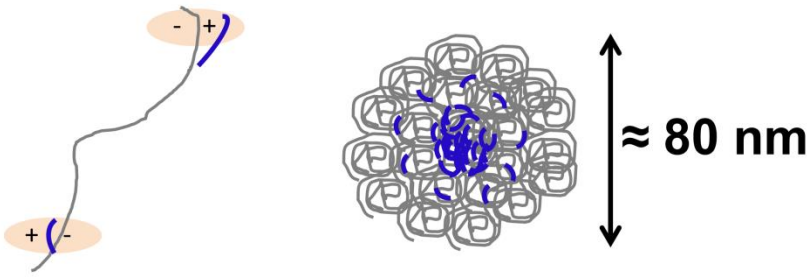

Figure 1.13 Scheme of the arrangement between PEDOT oligomers (blue segments) and PSS high-molecular weight chains (grey lines) at a single chain level **(left)**, and at a single micelle level **(right)**.

The discovery of PEDOT was a result of the search for an optimal conjugated polymer in terms of conductivity and stability, due to the lack of air stability of first synthetic conductive polymers[9,13,70]. Poly(alkylenedioxythiophene)s showed good conductivity levels against temperature, especially PEDOT[9,71]. However, it was insoluble and infusible. The PSS solved this problem. Polystyrene sulfonic acid (PSSH) was a widely used polyelectrolyte that could form durable and transparent films. PEDOT is insoluble in all solvents. To make it processable, it has to be polymerized in the PSS water-solution, in the presence of an oxidative agent[12]. The result is a dark blue, almost opaque black slightly viscous water-dispersion. PEDOT:PSS is fabricated with different PEDOT-to-PSS ratios depending on the future application because the ratio influences critical properties as the wettability, conductivity and work function.

PEDOT:PSS has not any glass transition due to the strong ionic interactions between PEDOT and PSS and does not show melting behavior before degradation[72].

Many applications have been accomplished with this material. In OSCs (Figure 1.9.a), PEDOT:PSS is prominent as hole-extracting layer, enhances the work function (minimum thermodynamic work needed to extract an electron from the material surface) in comparison with the usual transparent electrode ITO, and improves the contact between electrode and polymer in the active layer[73]. It is also used in perovskite solar cells[74], OLEDs[75] and OFETs[76]. Different oxidation levels lead to changes in the visible absorption spectra of PEDOT:PSS, making it suitable for electrochromic windows[77]. Besides its high conductivity, PEDOT:PSS is also a pseudocapacitive material, which makes it an interesting candidate for supercapacitor applications[78]. Controlled stimuli of PEDOT:PSS films to water ambient opens also the possibility

of fabricating humidity sensors[79]. Furthermore, the water-component offers potential applications in biology and medicine[80–82].

PEDOT:PSS can form conducting thin supported films which are transparent if the thickness is low enough[83–85], as well as free-standing thin films by using different deposition procedures including solution cast[86], spin-coating[87,88], electro-spinning[89] or inkjet printing[90–92], among others. For all these techniques of deposition, the final properties may strongly depend on film uniformity[91,93]. In particular, the thickness uniformity of PEDOT:PSS deposited by inkjet on ITO-coated glass substrates has been reported to have a strong impact on photovoltaic performance[94,95]. Surface roughness has also been shown to affect significantly the electrical properties of PEDOT:PSS deposited by inkjet on glass substrates[93].

Some of the potential applications for PEDOT:PSS require much higher values of conductivity than the one provided by the as-received PEDOT:PSS. There is a wide branch of research towards the enhancement of PEDOT:PSS conductivity by the addition of polar liquids with a high boiling point. The high boiling point (above 100ºC) ensures that the additive is present during the evaporation of solvent step when the sample is prepared, for example, by spin-coating or inkjet printing. If there are additive residues in the sample, they are commonly removed by heat treatment. The interaction between PEDOT, PSS and high boiling point additives as ethylene glycol[96] or glycerol and their consequences on the morphology and electrical properties of the final sample are not clearly understood. The effect of the additive, commonly known as 'secondary doping', has been explained in terms of solubility of PSS and PSSH with the additive[97,98], conformational changes[99] and crystallinity enhancement of PEDOT oligomers[92]. All these effects have been correlated with a phase segregation between segments of PEDOT and PSS, initially strongly attached by electrostatic forces, as schematized by Mengistie et al. when poly(ethylene glycol) is added in the aqueous dispersion of PEDOT:PSS[100] (Figure 1.14).

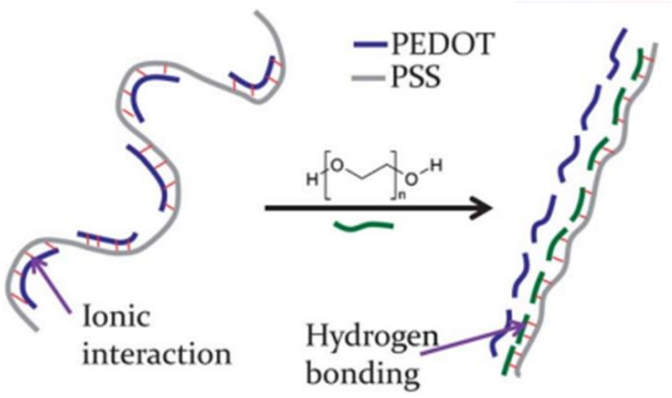

Figure 1.14 Scheme of the impact of poly(ethylene glycol) on the chain structure of PEDOT:PSS. Figure adapted from reference[100].

1.4.5 PVDF and P(VDF-TrFE)

Poly(vinylidene fluoride) (PVDF) is the most known ferroelectric polymer[101]. Its backbone is composed by alternating CH_2 and CF_2 groups (Figure 1.15.a) giving rise to a strong electric dipole perpendicular to the backbone caused by the partially negatively charged zones near the fluorine atoms and the positively charged zones at the hydrogen regions. PVDF can crystallize in several phases: named as α, β, γ and δ. β and γ phases are ferroelectric, all trans (***T***) and ***TTT***-gauche, respectively[102–104]. δ phase, which is a less common polar version of α, is also reported as ferroelectric[105].

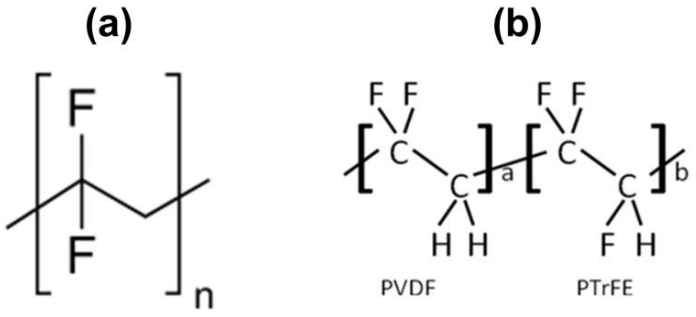

Figure 1.15 Chemical structure of **(a)** PVDF and **(b)** P(VDF-TrFE).

Random copolymer poly(vinylidene fluoride-tetrafluoroethylene) (P(VDF-TrFE)) (Figure 1.15.b) presents spontaneous ferroelectric β phase when crystallized from solution[106]. PVDF and P(VDF-TrFE) have been reported to be used as memory devices[107–109], piezoelectric transductors[110,111] or non-volatile memory thin film transistors[112]. In addition, the good compatibility of these polymers with biological systems makes them of interest to tissue engineering applications[113].

1.5 Nanostructured polymers

Nowadays the interest in polymer science and nanotechnology is notably increasing. Miniaturization of electronic devices demands straightforward and effective methods to fabricate nanostructured materials. On the other side, soft matter introduces the characteristic components of conventional polymers such as good mechanical properties, environmental stability and the possibility of fabricating samples at room temperature.

One important part of nanotechnology is centered on the fabrication of nanocomposites with a polymer matrix and nanofillers[114]. Nanofillers could improve mechanical properties of the polymer, influence on the crystallization and change the glass transition temperature. Block-copolymer self-assembly is also an interesting approach to generate nanostructure patterns[115].

Many diverse applications of interest are found for nanoconfined polymers like CO_2 capture through polystyrene/polyurethane nanofibers[116], energy harvesting through triboelectric transductors of PVDF nanowires[117], liquid crystal alignment by photolithography[118] or photocatalysis with nanostructured conducting polymers[119].

The confinement of polymers establishes spatial constraints on the molecules, whose crystalline and mesoscopic arrangements are defined by nanometric and microscopic distances (Figure 1.7 and Figure 1.8). The properties that polymers show at the macroscale are influenced by their nanostructure. It is reported that nanoconfinement of amorphous polymers could change their glass transition temperature[120,121]. However, the influence of confined geometries on the glass transition temperature of amorphous polymers is not fully understood[122]. Nanoconfinement in cylindrical spaces affects the crystallization, orientation and phase of P3HT[123]. Due to its strong anisotropy (see section 1.1), the conductivity of conjugated polymers is highly sensitive to the chain orientation, thus confinement of conjugated polymers at this range is crucial on their electrical behavior. Nanostructured polymers are also of interest from the fundamental point of view as they reveal insights on the intrinsic relationship between the nanostructure of the material and its macroscopic properties[47,124].

1.5.1 Nanostructuring organic functional materials

In this Thesis, three kind of nanostructured systems have been investigated depending on the dimensions of confinement: confinement in one dimension (thin films), in two dimensions (superficial nanogratings) and in three dimensions (nanoparticles).

One of the most valued characteristic of polymers is the possibility of fabricating thin layers with thickness below 100 nm, at ambient conditions, with all the functionalities of the polymer of interest. In fact, the requirement for miniaturization in nowadays devices and the need of low voltage operation for portable electronic devices implies that the polymer layers included should be thin enough but maintaining their functionality intact. There is also interest on the fabrication of electronic devices that combine two or more functional properties of polymers, like ferroelectricity and semiconducting behavior. In all-polymer memory devices[107,108], two polymers with different functionalities are combined. On one side, the two state 'on-off' requirement and non-volatile information storage is provided by the ferroelectric polymer. On the other side, the probe of the state is performed by reading the response to an electrical signal through a semiconducting polymer. This pair ferroelectric/semiconducting polymer has also been used in a variety of geometries as basis of different devices such as capacitors[109], field-effect transistors[125] or diodes[126].

Nanostructured surfaces have found a potential application frame in photovoltaics. Although OSCs continue improving their efficiencies through last years[127,128], they are still far from the standard efficiency of inorganic materials[129] and many more efforts are needed to become polymeric solar cells competitive. Approaches to deal with this problem are centered on synthesizing high efficiency polymers with low band gap energy[130] or modifying the architecture of the device. Regarding the last option, nanostructuring the polymeric layers that form the solar cell is a successful reported approach[131] since the superficial nanostructures enhance the active area of the layer and they act as a light-trap[132,133]. Since the standard photovoltaic device consists of a series of stacked layers, the interfaces between layers are of crucial importance to the final efficiency, as long as the initial exciton induced by the photon encounters an interface between donor and acceptor components, an interface with a buffer layer and finally with the electrode to produce effective electric current. Therefore, many efforts have been made to nanostructure polymers for the active layer of the OSCs[33,134–136], as well as polymers for the hole-extracting layer, usually PEDOT:PSS[137–141]. Motivated by photovoltaic applications, several different geometries of nanostructuring have been accomplished as nanogratings[134,142] (Figure 1.16.a), nanobowls[143,144] (Figure 1.16.b) and nanopyramids[145] (Figure 1.16.c)

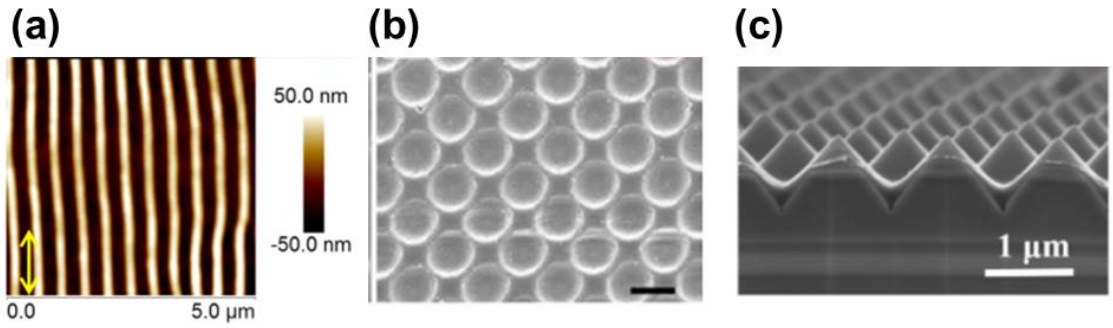

Figure 1.16 Different geometries of nanopatterned organic semiconductors. **(a)** Nanogratings of P3HT obtained by laser-irradiation. Adapted picture from reference[134]. **(b)** Nanobowls of P3HT/$PC_{61}BM$ obtained by deposition over an imprinted substrate. Adapted picture from reference[144]. Scale bar is 1 µm length. **(c)** Nanopyramids of PEDOT:PSS obtained by deposition over a patterned silicon substrate. Adapted picture from reference[145].

It is important that the fabrication methods would be reproducible, quick and effective. Avoiding the necessity of stringent environmental conditions like those implied in using clean rooms, high vacuum or complex mask fabrication is one of the driving forces to develop more straightforward alternatives to produce these kinds of structures. Nanostructuring by laser of semiconducting polymers has been recently accomplished rendering to functional surfaces of selective electrical conductivity[134] and with photovoltaic properties[136] without using templates or under tricky ambient conditions.

A lot of efforts are also being done to fabricate complex functional surfaces with more than one degree of hierarchical structures. Examples of complex structures possessing specific functions and properties may be found in nature[146]. For instance, the control of wettability by the presence of hierarchical surface structures ranging from micro to nanoscale may provide self-cleaning properties as the lotus leaf does in nature[147]. Hierarchical structures play also a role in the excellent adhesion of the gecko feet[148], and the presence of anisotropic micro and nanostructures affects the friction as it happens in the snake's skin[149]. Mimicking of these natural nanostructures is being accomplished through the combination of different laser techniques such as direct laser writing and Direct Laser Interference Patterning (DLIP)[150,151] that may induce the formation of more complex structures[152], as well as laser micropatterning followed by Laser-Induced Periodic Surface Structures (LIPSS) formation[153] or LIPSS simultaneously with diffraction patterns[154].

Polymeric nanoparticles[155] have found important applications over a huge variety of research branches: molecular imaging[156], drug delivery[157–159], adhesives[160] and nanolithography[161]. Regarding organic electronics, functional nanoparticles of semiconducting polymers[157,162] have reached a position of interest due to the processing benefits of using conjugated polymers dispersed in water or to the possibility of generating nanostructures with controlled morphology before the deposition and implementation in the device.

Nanoparticles of P3HT are being extensively investigated motivated by controlling the domain size and the separation in the active layer of bulk heterojunction OSCs, and also the enhancement of the interfacial surface between acceptor and donor domains. OSCs with nanoparticles of donor P3HT and acceptor $PC_{61}BM$ have been fabricated[163], showing comparable efficiencies to standard bulk heterojunction cells. The size of the nanoparticles can be controlled by changing the solvent[164], tuning polymer concentration[165] or additive concentration, usually a surfactant[166]. This possibility opens the potential application of nanoparticles in OSCs where the performance is highly dependent on the size of the polymer domains in the active layer.

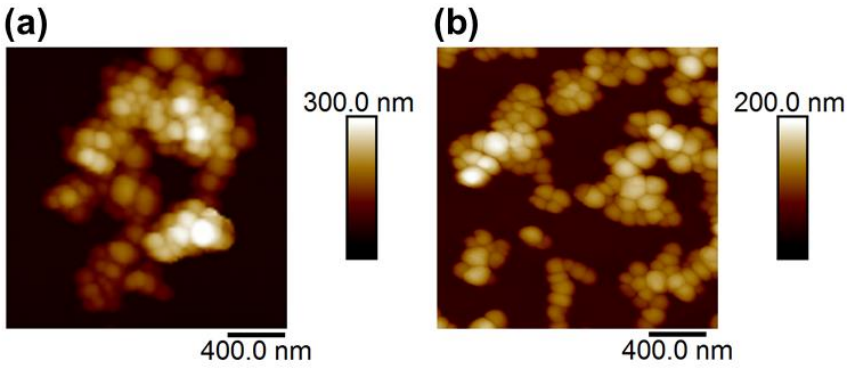

Figure 1.17 Nanoparticles of **(a)** a semiconducting polymer (P3HT), and **(b)** a ferroelectric polymer (P(VDF-TrFE)).

On the other hand, functional nanoparticles of ferroelectric polymers are interesting for ferroelectric nanodevices as non-volatile memories[167], piezoelectric actuators[168] or mechanical nanotransductors[110]. Interestingly, inclusion of P(VDF-TrFE) nanoparticles have been shown to enhance OSCs performance[169]. Figure 1.17 shows atomic force microscopy images of nanoparticles from two different functional polymers prepared during the research reported in this Thesis.

1.6 Thesis outline

The Thesis is divided in seven chapters. In Chapter 1, an introduction about polymeric materials is presented, with a detailed description of two kinds of functional polymers (semiconducting and ferroelectric) that are investigated in this Thesis, followed by some trending researches focused on nanostructuring these functional polymers. Chapter 2 contains descriptions of all the experimental techniques used along this Thesis including sample deposition, nanostructuring and characterization techniques. Every section is supported with an outline of the corresponding technique and the motivations from technological and physical perspectives. Also in Chapter 2 are listed all the characteristics of the materials and the experimental conditions used to fabricate the samples that have been studied. Chapter 3 deals with the nanostructured materials in the form of thin films. Chapter 4 reports the work focused on nanostructuring thin films of different materials by nanosecond pulsed laser irradiation and subsequent characterization. In Chapter 5, the study on the fabrication of nanogratings of PEDOT:PSS by Nanoimprint Lithography is presented, together with the characterization of their morphology and inner structure. Chapter 6 deals with confinement of P3HT and ferroelectric polymers in the form of nanoparticles. The final chapter is a summary with the main ideas developed in this Thesis and our conclusions for every system studied.

1.7 References

(1) Shirakawa, H.; Macdiarmid, A. G.; Chiang, C. K.; Fincher Jr., C. R.; Park, Y. W.; Heeger, A. J.; Louis, E. J.; Gau, S. C. Electical Conductivity in Doped Polyacetylene. *Phys. Rev. Lett.* **1977**, *39* (17), 1098–1101. https://doi.org/10.1103/PhysRevLett.39.1098.

(2) Heeger, A. J. Semiconducting and Metallic Polymers: The Fourth Generation of Polymeric Materials. *Curr. Appl. Phys.* **2001**, *1* (4–5), 247–267. https://doi.org/10.1016/S1567-1739(01)00053-0.

(3) Heeger, A. J. Semiconducting Polymers: The Third Generation. *Chem. Soc. Rev.* **2010**, *39* (7), 2354–2371. https://doi.org/10.1039/b914956m.

(4) Kittel, C.; McEuen, P.; McEuen, P. *Introduction to Solid State Physics*; Wiley New York, 1976; Vol. 8.

(5) Klauk, H. *Organic Electronics: Materials, Manufacturing, and Applications*; John Wiley & Sons, 2006.

(6) Zhan, Y.; Mei, Y.; Zheng, L. Materials Capability and Device Performance in Flexible Electronics for the Internet of Things. *J. Mater. Chem. C* **2014**, *2* (7), 1220–1232. https://doi.org/10.1039/c3tc31765j.

(7) Skotheim, T. A.; Reynolds, J. *Handbook of Conducting Polymers, 2 Volume Set*; CRC press, 2007.

(8) Paszkiewicz, S.; Szymczyk, A.; Sui, X. M.; Wagner, H. D.; Linares, A.; Cirera, A.; Varea, A.; Ezquerra, T. A.; Rosłaniec, Z. Electrical Conductivity and Transparency of Polymer Hybrid Nanocomposites Based on Poly(Trimethylene Terephthalate) Containing Single Walled Carbon Nanotubes and Expanded Graphite. *J. Appl. Polym. Sci.* **2017**, *134* (1), 1–9. https://doi.org/10.1002/app.44370.

(9) Elshchner, A.; Kirchmeyer, S.; Lovenich, W.; Merker, U.; Reuter, K. *PEDOT. Principles And Applications Of An Intrinsically Conductive Polymer*; Boca Raton, 2011.

(10) Yu, G.; Gao, J.; Hummelen, J. C.; Wudl, F.; Heeger, A. J. Polymer Photovoltaic Cells: Enhanced Efficiencies via a Network of Internal Donor-Acceptor Heterojunctions. *Science.* **1995**, *270* (5243), 1789–1791. https://doi.org/10.1126/science.270.5243.1789.

(11) Coakley, K. M.; McGehee, M. D. Conjugated Polymer Photovoltaic Cells. *Chem. Mater.* **2004**, *16* (23), 4533–4542. https://doi.org/10.1021/cm049654n.

(12) Groenendaal, L.; Jonas, F.; Freitag, D.; Pielartzik, H.; Reynolds, J. R. Poly (3, 4-ethylenedioxythiophene) and Its Derivatives: Past, Present, and Future. *Adv. Mater.* **2000**, *12* (7), 481–494.https://doi.org/10.1002/(SICI)1521-4095(200004)12:7<481::AID-ADMA481>3.0.CO;2-C

(13) Roncali, J. Conjugated Poly(Thiophenes): Synthesis, Functionalization, and Applications. *Chem. Rev.* **1992**, *92* (4), 711–738. https://doi.org/10.1021/cr00012a009.

(14) Ezquerra, T. A.; Rühe, J.; Wegner, G. Hopping Conduction in 3,4-Cycloalkylpolypyrrole Perchlorates: A Model Study of Conductivity in Polymers: *Chem. Phys. Lett.* **1988**, *144* (2), 194–198. https://doi.org/10.1016/0009-2614(88)87116-1.

(15) Strobl, G. *The Physics of Polymers (Vol. 2).* Springer, 1997.

(16) Yamagata, H.; Spano, F. C. Interplay between Intrachain and Interchain Interactions in Semiconducting Polymer Assemblies: The HJ-Aggregate Model. *J. Chem. Phys.* **2012**, *136* (18), 184901. https://doi.org/10.1063/1.4705272.

(17) Spano, F. C.; Silva, C. H- and J-Aggregate Behavior in Polymeric Semiconductors. *Annu. Rev. Phys. Chem.* **2014**, *65* (1), 477–500. https://doi.org/10.1146/annurev-physchem-040513-103639.

(18) Spano, F. C. The Spectral Signatures of Frenkel Polarons in H- and J-Aggregates: Accounts of Chemical Research. *Acc. Chem. Res.* **2009**, *43* (3), 429–439. https://doi.org/10.1021/ar900233v.

(19) Kasha, M.; Rawls, H. R.; Ashraf El-Bayoumi, M. The Exciton Model in Molecular Spectroscopy. *Pure Appl. Chem.* **2008**, *11* (3–4), 371–392. https://doi.org/10.1351/pac196511030371.

(20) Rahimi, K.; Botiz, I.; Agumba, J. O.; Motamen, S.; Stingelin, N.; Reiter, G. Light Absorption of Poly(3-Hexylthiophene) Single Crystals. *RSC Adv.* **2014**, *4* (22), 11121–11123. https://doi.org/10.1039/c3ra47064d.

(21) Rubinstein, M.; Colby, R. H. *Polymer Physics*; Oxford university press New York, 2003; Vol. 23.

(22) Flory, P. J.; Volkenstein, M. Statistical Mechanics of Chain Molecules. Wiley Online Library 1969.

(23) De Gennes, P. G. Reptation of a Polymer Chain in the Presence of Fixed Obstacles. *J. Chem. Phys.* **1971**, *55* (2), 572–579. https://doi.org/10.1063/1.1675789.

(24) Klauk, H. Organic Thin-Film Transistors. *Chem. Soc. Rev.* **2010**, *39* (7), 2643–2666.

(25) https://www.doitpoms.ac.uk/tlplib/polymers/spherulites.php.

(26) Instituto de Ciencia y Tecnología de Polímeros (ICTP-CSIC), *Ciencia y Tecnología de Materiales Poliméricos*; 2004; Vol. I.

(27) Wendorff, J. H. Scattering in Liquid Crystalline Polymer Systems. In *Liquid Crystalline Order in Polymers*; Elsevier, 2012; pp 1–41. https://doi.org/10.1016/b978-0-12-108650-3.50007-0.

(28) Brinkmann, M.; Rannou, P. Effect of Molecular Weight on the Structure and Morphology of Oriented Thin Films of Regioregular Poly(3-Hexylthiophene) Grown by Directional Epitaxial Solidification. *Adv. Funct. Mater.* **2007**, *17* (1), 101–108. https://doi.org/10.1002/adfm.200600673.

(29) Sirringhaus, H.; Brown, P. J.; Friend, R. H.; Nielsen, M. M.; Bechgaard, K.; Langeveld-Voss, B. M. W.; Spiering, a. J. H.; Janssen, R. a. J.; Meijer, E. W.; Herwig, P.; et al. Two-Dimensional Charge Transport in Self-Organized, High-Mobility Conjugated Polymers. *Nature* **1999**, *401* (6754), 685–688. https://doi.org/10.1038/44359.

(30) Joshi, S.; Joshi, S.; Grigorian, S.; Grigorian, S.; Pietsch, U.; Pietsch, U.; Pingel, P.; Pingel, P.; Zen, A.; Zen, A.; et al. Thickness Dependence of the Crystalline Structure and Hole Mobility in Thin Films of Low Molecular Weight Poly(3-Hexylthiophene). *Macromolecules* **2008**, *41* (18), 6800–6808. https://doi.org/10.1021/ma702802x.

(31) Boulanger, N.; Yu, V.; Hilke, M.; Toney, M. F.; Barbero, D. R. In Situ Probing of the Crystallization Kinetics of Rr-P3HT on Single Layer Graphene as a Function of Temperature. *Phys. Chem. Chem. Phys.* **2017**, *19* (12), 8496–8503. https://doi.org/10.1039/c6cp08589j.

(32) Yang, H.; Lefevre, S. W.; Ryu, C. Y.; Bao, Z. Solubility-Driven Thin Film Structures of Regioregular Poly(3-Hexyl Thiophene) Using Volatile Solvents. *Appl. Phys. Lett.* **2007**, *90* (17), 1–4. https://doi.org/10.1063/1.2734387.

(33) Mukti, A.; Krutarth, T.; Wenchuang, (Walter) Hu. Nano-Confinement Induced Chain Alignment in Ordered P3HT Nanostructures Defined by Nanoimprint Lithography. *ACS Nano* **2009**, *3* (10), 3085–3090. https://doi.org/10.1021/nn900831m.

(34) Feng, L.; Zheng, F.; Bi, P.-Q.; Yang, X.-Y.; Niu, M.-S.; Wang, F.; Hao, X.-T. Laser-Induced Crystallization and Conformation Control of Poly(3-Hexylthiophene) for Improving the Performance of Organic Solar Cells. *Org. Electron.* **2017**, *49*, 157–164. https://doi.org/10.1016/j.orgel.2017.06.053.

(35) Wu, Z.; Petzold, A.; Henze, T.; Thurn-Albrecht, T.; Lohwasser, R. H.; Sommer, M.; Thelakkat, M. Temperature and Molecular Weight Dependent Hierarchical Equilibrium Structures in Semiconducting Poly(3-Hexylthiophene). *Macromolecules* **2010**, *43* (10), 4646–4653. https://doi.org/10.1021/ma902566h.

(36) Liu, J.; Arif, M.; Zou, J.; Khondaker, S. I.; Zhai, L. Controlling Poly(3-Hexylthiophene) Crystal Dimension: Nanowhiskers and Nanoribbons. *Macromolecules* **2009**, *42* (24), 9390–9393. https://doi.org/10.1021/ma901955c.

(37) Brinkmann, M.; Wittmann, J. C. Orientation of Regioregular Poly(3-Hexylthiophene) by Directional Solidification: A Simple Method to Reveal the Semicrystalline Structure of a Conjugated Polymer. *Adv. Mater.* **2006**, *18* (7), 860–863. https://doi.org/10.1002/adma.200501838.

(38) Thurn-Albrecht, T.; Thomann, R.; Heinzel, T.; Hugger, S. Semicrystalline Morphology in Thin Films of Poly(3-Hexylthiophene). *Colloid Polym. Sci.* **2004**, *282* (8), 932–938. https://doi.org/10.1007/s00396-004-1100-9.

(39) Yazawa, K.; Inoue, Y.; Yamamoto, T.; Asakawa, N. Twist Glass Transition in Regioregulated Poly(3-Alkylthiophene). *Phys. Rev. B - Condens. Matter Mater. Phys.* **2006**, *74* (9), 1–12. https://doi.org/10.1103/PhysRevB.74.094204.

(40) Prosa, T. J.; Winokur, M. J.; Moulton, J.; Smith, P.; Heeger, A. J. X-Ray Structural Studies of Poly(3-Alkylthiophenes): An Example of an Inverse Comb. *Macromolecules* **1992**, *25* (17), 4364–4372. https://doi.org/10.1021/ma00043a019.

(41) Xie, R.; Lee, Y.; Aplan, M. P.; Caggiano, N. J.; Müller, C.; Colby, R. H.; Gomez, E. D. Glass Transition Temperature of Conjugated Polymers by Oscillatory Shear Rheometry. *Macromolecules* **2017**, *50* (13), 5146–5154. https://doi.org/10.1021/acs.macromol.7b00712.

(42) Martín, J.; Stingelin, N.; Cangialosi, D. Direct Calorimetric Observation of the Rigid Amorphous Fraction in a Semiconducting Polymer. *J. Phys. Chem. Lett.* **2018**, *9* (5), 990–995. https://doi.org/10.1021/acs.jpclett.7b03110.

(43) Bhatta, R. S.; Yimer, Y. Y.; Perry, D. S.; Tsige, M. Improved Force Field for Molecular Modeling of Poly(3-Hexylthiophene). *J. Phys. Chem. B* **2013**, *117* (34), 10035–10045. https://doi.org/10.1021/jp404629a.

(44) Zhao, Y.; Yuan, G.; Roche, P.; Leclerc, M. A Calorimetric Study of the Phase Transitions in Poly(3-Hexylthiophene). *Polymer (Guildf).* **1995**, *36* (11), 2211–2214. https://doi.org/10.1016/0032-3861(95)95298-F.

(45) Zhao, J.; Swinnen, A.; Van Assche, G.; Manca, J.; Vanderzande, D.; Van Mele, B. Phase Diagram of P3HT/PCBM Blends and Its Implication for the Stability of Morphology. *J. Phys. Chem. B* **2009**, *113* (6), 1587–1591. https://doi.org/10.1021/jp804151a.

(46) Balko, J.; Rinscheid, A.; Wurm, A.; Schick, C.; Lohwasser, R. H.; Thelakkat, M.; Thurn-Albrecht, T. Crystallinity of Poly(3-Hexylthiophene) in Thin Films Determined by Fast Scanning Calorimetry. *J. Polym. Sci. Part B Polym. Phys.* **2016**, *54* (18), 1791–1801. https://doi.org/10.1002/polb.24092.

(47) Martín, J.; Nogales, A.; Martín-González, M. The Smectic-Isotropic Transition of P3HT Determines the Formation of Nanowires or Nanotubes into Porous Templates. *Macromolecules* **2013**, *46* (4), 1477–1483. https://doi.org/10.1021/ma302516e.

(48) Brinkmann, M. Structure and Morphology Control in Thin Films of Regioregular Poly(3-Hexylthiophene). *J. Polym. Sci. Part B Polym. Phys.* **2011**, *49* (17), 1218–1233. https://doi.org/10.1002/polb.22310.

(49) Yuan, Y.; Zhang, J.; Sun, J.; Hu, J.; Zhang, T.; Duan, Y. Polymorphism and Structural Transition around 54°C in Regioregular Poly(3-Hexylthiophene) with High Crystallinity as Revealed by Infrared Spectroscopy. *Macromolecules* **2011**, *44* (23), 9341–9350. https://doi.org/10.1021/ma2017106.

(50) Ludwigs, S. *P3HT Revisited – From Molecular Scale to Solar Cell Devices*; 2014; Vol. 265. https://doi.org/10.1007/978-3-662-45145-8.

(51) Dang, M. T.; Hirsch, L.; Wantz, G. P3HT:PCBM, Best Seller in Polymer Photovoltaic Research. *Adv. Mater.* **2011**, *23* (31), 3597–3602. https://doi.org/10.1002/adma.201100792.

(52) Li, G.; Zhu, R.; Yang, Y. Polymer Solar Cells. *Nat. Photonics* **2012**, *6* (3), 153–161. https://doi.org/10.1038/nphoton.2012.11.

(53) Campoy-Quiles, M.; Ferenczi, T.; Agostinelli, T.; Etchegoin, P. G.; Kim, Y.; Anthopoulos, T. D.; Stavrinou, P. N.; Bradley, D. D. C.; Nelson, J. Morphology Evolution via Self-Organization and Lateral and Vertical Diffusion in Polymer:Fullerene Solar Cell Blends. *Nat. Mater.* **2008**, *7* (2), 158–164. https://doi.org/10.1038/nmat2102.

(54) Marrocchi, A.; Lanari, D.; Facchetti, A.; Vaccaro, L. Poly(3-Hexylthiophene): Synthetic Methodologies and Properties in Bulk Heterojunction Solar Cells. *Energy Environ. Sci.* **2012**, *5* (9), 8457–8474. https://doi.org/10.1039/c2ee22129b.

(55) Zhang, F.; Zhuo, Z.; Zhang, J.; Wang, X.; Xu, X.; Wang, Z.; Xin, Y.; Wang, J.; Wang, J.; Tang, W.; et al. Influence of PC60BM or PC70BM as Electron Acceptor on the Performance of Polymer Solar Cells. *Sol. Energy Mater. Sol. Cells* **2012**, *97*, 71–77. https://doi.org/10.1016/j.solmat.2011.09.006.

(56) Bao, Z.; Dodabalapur, A.; Lovinger, A. J. Soluble and Processable Regioregular Poly (3-hexylthiophene) for Thin Film Field-effect Transistor Applications with High Mobility. *Appl. Phys. Lett.* **1996**, *69* (26), 4108–4110. https://doi.org/10.1063/1.117834.

(57) Kim, D. H.; Park, Y. D.; Jang, Y.; Yang, H.; Kim, Y. H.; Han, J. I.; Moon, D. G.; Park, S.; Chang, T.; Chang, C.; et al. Enhancement of Field-Effect Mobility Due to Surface-Mediated Molecular Ordering in Regioregular Polythiophene Thin Film Transistors. *Adv. Funct. Mater.* **2005**, *15* (1), 77–82. https://doi.org/10.1002/adfm.200400054.

(58) Gburek, B.; Wagner, V. Influence of the Semiconductor Thickness on the Charge Carrier Mobility in P3HT Organic Field-Effect Transistors in Top-Gate Architecture on Flexible Substrates. *Org. Electron. physics, Mater. Appl.* **2010**, *11* (5), 814–819. https://doi.org/10.1016/j.orgel.2010.01.023.

(59) Lee, M. J.; Gupta, D.; Zhao, N.; Heeney, M.; Mcculloch, I.; Sirringhaus, H. Anisotropy of Charge Transport in a Uniaxially Aligned and Chain-Extended, High-Mobility, Conjugated Polymer Semiconductor. *Adv. Funct. Mater.* **2011**, *21* (5), 932–940. https://doi.org/10.1002/adfm.201001781.

(60) O'Connor, B.; Kline, R. J.; Conrad, B. R.; Richter, L. J.; Gundlach, D.; Toney, M. F.; DeLongchamp, D. M. Anisotropic Structure and Charge Transport in Highly Strain-Aligned Regioregular Poly(3-Hexylthiophene). *Adv. Funct. Mater.* **2011**, *21* (19), 3697–3705. https://doi.org/10.1002/adfm.201100904.

(61) Blouin, N.; Michaud, A.; Leclerc, M. A Low-Bandgap Poly(2,7-Carbazole) Derivative for Use in High-Performance Solar Cells. *Adv. Mater.* **2007**, *19* (17), 2295–2300. https://doi.org/10.1002/adma.200602496.

(62) Beiley, Z. M.; Hoke, E. T.; Noriega, R.; Dacuña, J.; Burkhard, G. F.; Bartelt, J. A.; Salleo, A.; Toney, M. F.; McGehee, M. D. Morphology-Dependent Trap Formation in High Performance Polymer Bulk Heterojunction Solar Cells. *Adv. Energy Mater.* **2011**, *1* (5), 954–962. https://doi.org/10.1002/aenm.201100204.

(63) Moon, J. S.; Jo, J.; Heeger, A. J. Nanomorphology of PCDTBT:PC70BM Bulk Heterojunction Solar Cells. *Adv. Energy Mater.* **2012**, *2* (3), 304–308. https://doi.org/10.1002/aenm.201100667.

(64) Beaupré, S.; Leclerc, M. PCDTBT: En Route for Low Cost Plastic Solar Cells. *J. Mater. Chem. A* **2013**, *1* (37), 11097–11105. https://doi.org/10.1039/c3ta12420g.

(65) Staniec, P. A.; Parnell, A. J.; Dunbar, A. D. F.; Yi, H.; Pearson, A. J.; Wang, T.; Hopkinson, P. E.; Kinane, C.; Dalgliesh, R. M.; Donald, A. M.; et al. The Nanoscale Morphology of a PCDTBT:PCBM Photovoltaic Blend. *Adv. Energy Mater.* **2011**, *1* (4), 499–504. https://doi.org/10.1002/aenm.201100144.

(66) Kroto, H. W.; Heath, J. R.; O'Brien, S. C.; Curl, R. F.; Smalley, R. E. C60: Buckminsterfullerene. *Nature* **1985**, *318* (6042), 162-163. https://doi.org/10.1038/318162a0.

(67) Hou, J.; Guo, X. Active Layer Materials for Organic Solar Cells BT - Organic Solar Cells: Materials and Device Physics. *Organic Solar Cells*; Springer, **2013**; pp 17–42. https://doi.org/10.1007/978-1-4471-4823-4_2.

(68) Chen, C. C.; Chang, W. H.; Yoshimura, K.; Ohya, K.; You, J.; Gao, J.; Hong, Z.; Yang, Y. An Efficient Triple-Junction Polymer Solar Cell Having a Power Conversion Efficiency Exceeding 11%. *Adv. Mater.* **2014**, *26* (32), 5670–5677. https://doi.org/10.1002/adma.201402072.

(69) Holliday, S.; Li, Y.; Luscombe, C. K. Recent Advances in High Performance Donor-Acceptor Polymers for Organic Photovoltaics. *Prog. Polym. Sci.* **2017**, *70*, 34–51. https://doi.org/10.1016/j.progpolymsci.2017.03.003.

(70) Mccullough, B. R. D.; McCullough, R. D. The Chemistry of Conducting Polythiophenes. *Adv. Mater.* **1998**, *10* (2), 93–116. https://doi.org/10.1002/(SICI)1521-4095(199801)10:2<93::AID-ADMA93>3.0.CO;2-F.

(71) Gerhard, H.; Friedrich, J. Poly(Alkylenedioxythiophene)s - New, Very Stable Conducting Polymers. *Adv. Mater.* **1992**, *4* (2), 116–118. https://doi.org/10.1002/adma.19920040213.

(72) Zhou, J.; Anjum, D. H.; Chen, L.; Xu, X.; Ventura, I. A.; Jiang, L.; Lubineau, G. The Temperature-Dependent Microstructure of PEDOT/PSS Films: Insights from Morphological, Mechanical and Electrical Analyses. *J. Mater. Chem. C* **2014**, *2* (46), 9903–9910. https://doi.org/10.1039/C4TC01593B.

(73) Lipomi, D. J.; Tee, B. C. K.; Vosgueritchian, M.; Bao, Z. Stretchable Organic Solar Cells. *Adv. Mater.* **2011**, *23* (15), 1771–1775. https://doi.org/10.1002/adma.201004426.

(74) Hu, L.; Li, M.; Yang, K.; Xiong, Z.; Yang, B.; Wang, M.; Tang, X.; Zang, Z.; Liu, X.; Li, B.; et al. PEDOT:PSS Monolayers to Enhance the Hole Extraction and Stability of Perovskite Solar Cells. *J. Mater. Chem. A* **2018**, *6* (34), 16583–16589. https://doi.org/10.1039/c8ta05234d.

(75) Benor, A.; Takizawa, S. ya; Pérez-Bolívar, C.; Anzenbacher, P. Efficiency Improvement of Fluorescent OLEDs by Tuning the Working Function of PEDOT:PSS Using UV-Ozone Exposure. *Org. Electron. physics, Mater. Appl.* **2010**, *11* (5), 938–945. https://doi.org/10.1016/j.orgel.2010.02.014.

(76) Hong, K.; Yang, S. Y.; Yang, C.; Kim, S. H.; Choi, D.; Park, C. E. Reducing the Contact Resistance in Organic Thin-Film Transistors by Introducing a PEDOT:PSS Hole-Injection Layer. *Org. Electron. physics, Mater. Appl.* **2008**, *9* (5), 864–868. https://doi.org/10.1016/j.orgel.2008.06.008.

(77) Heuer, H. W.; Wehrmann, R.; Kirchmeyer, S. Electrochromic Window Based on Conducting Poly(3,4-Ethylenedioxythiophene)- Poly(Styrene Sulfonate). *Adv. Funct. Mater.* **2002**, *12* (2), 89–94. https://doi.org/10.1002/1616-3028(20020201)12:2<89::AID-ADFM89>3.0.CO;2-1.

(78) Antiohos, D.; Folkes, G.; Sherrell, P.; Ashraf, S.; Wallace, G. G.; Aitchison, P.; Harris, A. T.; Chen, J.; Minett, A. I. Compositional Effects of PEDOT-PSS/Single Walled Carbon Nanotube Films on Supercapacitor Device Performance. *J. Mater. Chem.* **2011**, *21* (40), 15987–15994. https://doi.org/10.1039/c1jm12986d.

(79) Kang, T. G.; Park, J. K.; Yun, G. H.; Choi, H. H.; Lee, H. J.; Yook, J. G. A Real-Time Humidity Sensor Based on a Microwave Oscillator with Conducting Polymer PEDOT:PSS Film. *Sensors Actuators, B Chem.* **2019**, *282* (1), 145–151. https://doi.org/10.1016/j.snb.2018.09.080.

(80) Blau, A.; Murr, A.; Wolff, S.; Sernagor, E.; Medini, P.; Iurilli, G.; Ziegler, C.; Benfenati, F. Flexible, All-Polymer Microelectrode Arrays for the Capture of Cardiac and Neuronal Signals. *Biomaterials* **2011**, *32* (7), 1778–1786. https://doi.org/10.1016/j.biomaterials.2010.11.014.

(81) Cellot, G.; Lagonegro, P.; Tarabella, G.; Scaini, D.; Fabbri, F.; Iannotta, S.; Prato, M.; Salviati, G.; Ballerini, L. PEDOT:PSS Interfaces Support the Development of Neuronal Synaptic Networks with Reduced Neuroglia Response in Vitro. *Front. Neurosci.* **2016**, *9* , 1–11. https://doi.org/10.3389/fnins.2015.00521.

(82) Gkoupidenis, P.; Schaefer, N.; Garlan, B.; Malliaras, G. G. Neuromorphic Functions in PEDOT:PSS Organic Electrochemical Transistors. *Adv. Mater.* **2015**, *27* (44), 7176–7180. https://doi.org/10.1002/adma.201503674.

(83) Vosgueritchian, M.; Lipomi, D. J.; Bao, Z. Highly Conductive and Transparent PEDOT:PSS Films with a Fluorosurfactant for Stretchable and Flexible Transparent Electrodes. *Adv. Funct. Mater.* **2012**, *22* (2), 421–428. https://doi.org/10.1002/adfm.201101775.

(84) Xia, Y.; Sun, K.; Ouyang, J. Highly Conductive Poly(3,4-Ethylenedioxythiophene):Poly(Styrene Sulfonate) Films Treated with an Amphiphilic Fluoro Compound as the Transparent Electrode of Polymer Solar Cells. *Energy Environ. Sci.* **2012**, *5* (1), 5325–5332. https://doi.org/10.1039/c1ee02475b.

(85) Tait, J. G.; Worfolk, B. J.; Maloney, S. A.; Hauger, T. C.; Elias, A. L.; Buriak, J. M.; Harris, K. D. Spray Coated High-Conductivity PEDOT:PSS Transparent Electrodes for Stretchable and Mechanically-Robust Organic Solar Cells. *Sol. Energy Mater. Sol. Cells* **2013**, *110*, 98–106. https://doi.org/10.1016/j.solmat.2012.09.005.

(86) Lang, U.; Naujoks, N.; Dual, J. Mechanical Characterization of PEDOT:PSS Thin Films. *Synth. Met.* **2009**, *159* (5–6), 473–479. https://doi.org/10.1016/j.synthmet.2008.11.005.

(87) Greco, F.; Zucca, A.; Taccola, S.; Menciassi, A.; Fujie, T.; Haniuda, H.; Takeoka, S.; Dario, P.; Mattoli, V. Ultra-Thin Conductive Free-Standing PEDOT/PSS Nanofilms. *Soft Matter* **2011**, *7* (22), 10642. https://doi.org/10.1039/c1sm06174g.

(88) Lang, U.; Muller, E.; Naujoks, N.; Dual, J. Microscopical Investigations of PEDOT:PSS Thin Films. *Adv. Funct. Mater.* **2009**, *19* (8), 1215–1220. https://doi.org/10.1002/adfm.200801258.

(89) Zhao, W.; Yalcin, B.; Cakmak, M. Dynamic Assembly of Electrically Conductive PEDOT:PSS Nanofibers in Electrospinning Process Studied by High Speed Video. *Synth. Met.* **2015**, *203*, 107–116. https://doi.org/10.1016/j.synthmet.2015.02.018.

(90) Mannerbro, R.; Ranlöf, M.; Robinson, N.; Forchheimer, R. Inkjet Printed Electrochemical Organic Electronics. *Synth. Met.* **2008**, *158* (13), 556–560. https://doi.org/10.1016/j.synthmet.2008.03.030.

(91) Natori, A. Y.; Canestraro, C. D.; Roman, L. S.; Ceschin, A. M. Modification of the Sheet Resistance of Ink Jet Printed Polymer Conducting Films by Changing the Plastic Substrate. *Mater. Sci. Eng. B Solid-State Mater. Adv. Technol.* **2005**, *122* (3), 231–235. https://doi.org/10.1016/j.mseb.2004.11.026.

(92) Palumbiny, C. M.; Liu, F.; Russell, T. P.; Hexemer, A.; Wang, C.; Müller-Buschbaum, P. The Crystallization of PEDOT:PSS Polymeric Electrodes Probed in Situ during Printing. *Adv. Mater.* **2015**, *27* (22), 3391–3397. https://doi.org/10.1002/adma.201500315.

(93) Wilson, P.; Lekakou, C.; Watts, J. F. A Comparative Assessment of Surface Microstructure and Electrical Conductivity Dependence on Co-Solvent Addition in Spin Coated and Inkjet Printed Poly(3,4-Ethylenedioxythiophene):Polystyrene Sulphonate (PEDOT:PSS). *Org. Electron. physics, Mater. Appl.* **2012**, *13* (3), 409–418. https://doi.org/10.1016/j.orgel.2011.11.011.

(94) Eom, S. H.; Senthilarasu, S.; Uthirakumar, P.; Yoon, S. C.; Lim, J.; Lee, C.; Lim, H. S.; Lee, J.; Lee, S. H. Polymer Solar Cells Based on Inkjet-Printed PEDOT:PSS Layer. *Org. Electron. physics, Mater. Appl.* **2009**, *10* (3), 536–542. https://doi.org/10.1016/j.orgel.2009.01.015.

(95) Eom, S. H.; Park, H.; Mujawar, S. H.; Yoon, S. C.; Kim, S. S.; Na, S. I.; Kang, S. J.; Khim, D.; Kim, D. Y.; Lee, S. H. High Efficiency Polymer Solar Cells via Sequential Inkjet-Printing of PEDOT:PSS and P3HT:PCBM Inks with Additives. *Org. Electron. physics, Mater. Appl.* **2010**, *11* (9), 1516–1522. https://doi.org/10.1016/j.orgel.2010.06.007.

(96) Yan, H.; Jo, T.; Okuzaki, H. Highly Conductive and Transparent Poly(3,4-Ethylenedioxythiophene)/Poly(4-Styrenesulfonate) (PEDOT/PSS) Thin Films. *Polym. J.* **2009**, *41* (12), 1028–1029. https://doi.org/10.1295/polymj.PJ2009143.

(97) Jönsson, S. K. M.; Birgerson, J.; Crispin, X.; Greczynski, G.; Osikowicz, W.; Denier van der Gon, A. W.; Salaneck, W. R.; Fahlman, M. The Effects of Solvents on the Morphology and Sheet Resistance in Poly(3,4-Ethylenedioxythiophene)-Polystyrenesulfonic Acid (PEDOT-PSS) Films. *Synth. Met.* **2003**, *139* (1), 1–10. https://doi.org/10.1016/S0379-6779(02)01259-6.

(98) Xia, Y.; Ouyang, J. PEDOT:PSS Films with Significantly Enhanced Conductivities Induced by Preferential Solvation with Cosolvents and Their Application in Polymer Photovoltaic Cells. *J. Mater. Chem.* **2011**, *21* (13), 4927–4936. https://doi.org/10.1039/c0jm04177g.

(99) Ouyang, J.; Xu, Q.; Chu, C. W.; Yang, Y.; Li, G.; Shinar, J. On the Mechanism of Conductivity Enhancement in Poly(3,4- Ethylenedioxythiophene):Poly(Styrene Sulfonate) Film through Solvent Treatment. *Polymer (Guildf).* **2004**, *45* (25), 8443–8450. https://doi.org/10.1016/j.polymer.2004.10.001.

(100) Alemu Mengistie, D.; Wang, P. C.; Chu, C. W. Effect of Molecular Weight of Additives on the Conductivity of PEDOT:PSS and Efficiency for ITO-Free Organic Solar Cells. *J. Mater. Chem. A* **2013**, *1* (34), 9907–9915. https://doi.org/10.1039/c3ta11726j.

(101) Sessler, G. M. Piezoelectricity in Polyvinylidenefluoride. *J. Acoust. Soc. Am.* **2005**, *70* (6), 1596–1608. https://doi.org/10.1121/1.387225.

(102) Ruan, L.; Yao, X.; Chang, Y.; Zhou, L.; Qin, G.; Zhang, X. Properties and Applications of the β Phase Poly(Vinylidene Fluoride). *Polymers (Basel).* **2018**, *10* (3), 1–27. https://doi.org/10.3390/polym10030228.

(103) Sencadas, V.; Gregorio, R.; Lanceros-Mendez, S. α to β Phase Transformation and Microestructural Changes of PVDF Films Induced by Uniaxial Stretch. *J. Macromol. Sci. Part B* **2009**, *48* (3), 514–525. https://doi.org/10.1080/00222340902837527.

(104) Martins, P.; Lopes, A. C.; Lanceros-Mendez, S. Electroactive Phases of Poly(Vinylidene Fluoride): Determination, Processing and Applications. *Prog. Polym. Sci.* **2014**, *39* (4), 683–706. https://doi.org/10.1016/j.progpolymsci.2013.07.006.

(105) Li, M.; Wondergem, H. J.; Spijkman, M. J.; Asadi, K.; Katsouras, I.; Blom, P. W. M.; De Leeuw, D. M. Revisiting the δ-Phase of Poly(Vinylidene Fluoride) for Solution-Processed Ferroelectric Thin Films. *Nat. Mater.* **2013**, *12* (5), 433–438. https://doi.org/10.1038/nmat3577.

(106) Calleja, F. J. B.; Arche, A. G.; Ezquerra, T. A.; Santa Cruz, C.; Batallan, F.; Frick, B.; Cabarcos, E. L. Structure and Properties of Ferroelectric Copolymers of Poly (Vinylidene Fluoride). *Structure in Polymers with Special Properties*; Springer, **1993**; pp 1–48.

(107) Asadi, K.; Leeuw, D. M. D. E.; Boer, B. D. E.; Blom, P. W. M. Organic Non-Volatile Memories from Ferroelectric Phase-Separated Blends. *Nature Materials*. **2008**, *7* (7), 547–550. https://doi.org/10.1038/nmat2207.

(108) Naber, R. C. G.; Asadi, K.; Blom, P. W. M.; De Leeuw, D. M.; De Boer, B. Organic Nonvolatile Memory Devices Based on Ferroelectricity. *Adv. Mater.* **2010**, *22* (9), 933–945. https://doi.org/10.1002/adma.200900759.

(109) Naber, R. C. G.; Blom, P. W. M.; Marsman, A. W.; De Leeuw, D. M. Low Voltage Switching of a Spin Cast Ferroelectric Polymer. *Appl. Phys. Lett.* **2004**, *85* (11), 2032–2034. https://doi.org/10.1063/1.1788885.

(110) Chang, C.; Tran, V. H.; Wang, J.; Fuh, Y. K.; Lin, L. Direct-Write Piezoelectric Polymeric Nanogenerator with High Energy Conversion Efficiency. *Nano Lett.* **2010**, *10* (2), 726–731. https://doi.org/10.1021/nl9040719.

(111) Granstrom, J.; Feenstra, J.; Sodano, H. A.; Farinholt, K. Energy Harvesting from a Backpack Instrumented with Piezoelectric Shoulder Straps. *Smart Mater. Struct.* **2007**, *16* (5), 1810–1820. https://doi.org/10.1088/0964-1726/16/5/036.

(112) Lee, K. H.; Lee, G.; Lee, K.; Oh, M. S.; Im, S.; Yoon, S. M. High-Mobility Nonvolatile Memory Thin-Film Transistors with a Ferroelectric Polymer Interfacing ZnO and Pentacene Channels. *Adv. Mater.* **2009**, *21* (42), 4287–4291. https://doi.org/10.1002/adma.200900398.

(113) Ribeiro, C.; Sencadas, V.; Correia, D. M.; Lanceros-Méndez, S. Piezoelectric Polymers as Biomaterials for Tissue Engineering Applications. *Colloids Surfaces B Biointerfaces* **2015**, *136*, 46–55. https://doi.org/10.1016/j.colsurfb.2015.08.043.

(114) Paul, D. R.; Robeson, L. M. Polymer Nanotechnology: Nanocomposites. *Polymer (Guildf).* **2008**, *49* (15), 3187–3204. https://doi.org/10.1016/j.polymer.2008.04.017.

(115) Gunkel, I. Directing Block Copolymer Self-Assembly on Patterned Substrates. *Small* **2018**, *14* (46), 1–8. https://doi.org/10.1002/smll.201802872.

(116) Zainab, G.; Babar, A. A.; Iqbal, N.; Wang, X.; Yu, J.; Ding, B. Amine-Impregnated Porous Nanofiber Membranes for CO 2 Capture. *Compos. Commun.* **2018**, *10*, 45–51. https://doi.org/10.1016/j.coco.2018.06.005.

(117) Jing, Q.; Kar-Narayan, S. Nanostructured Polymer-Based Piezoelectric and Triboelectric Materials and Devices for Energy Harvesting Applications. *J. Phys. D. Appl. Phys.* **2018**, *51* (30), 303001. https://doi.org/10.1088/1361-6463/aac827.

(118) Lee, J. H.; Jeong, H. C.; Won, J.; Oh, B. Y.; Kim, D. H.; Lee, D. W.; Liu, Y.; Seo, D. S. Nano Pattern Transfer on Acrylic Polymers with UV Irradiation for Liquid Crystal Alignment. *Polymer (Guildf).* **2019**, *161*, 1–7. https://doi.org/10.1016/j.polymer.2018.12.002.

(119) Ghosh, S.; Kouamé, N. A.; Ramos, L.; Remita, S.; Dazzi, A.; Deniset-Besseau, A.; Beaunier, P.; Goubard, F.; Aubert, P. H.; Remita, H. Conducting Polymer Nanostructures for Photocatalysis under Visible Light. *Nat. Mater.* **2015**, *14* (5), 505–511. https://doi.org/10.1038/nmat4220.

(120) Martínez-Tong, D. E.; Cui, J.; Soccio, M.; García, C.; Ezquerra, T. A.; Nogales, A. Does the Glass Transition of Polymers Change upon 3D Confinement? *Macromol. Chem. Phys.* **2014**, *215* (17), 1620–1624. https://doi.org/10.1002/macp.201400244.

(121) Martínez-Tong, D. E.; Soccio, M.; Sanz, A.; García, C.; Ezquerra, T. A.; Nogales, A. Chain Arrangement and Glass Transition Temperature Variations in Polymer Nanoparticles under 3D-Confinement. *Macromolecules* **2013**, *46* (11), 4698–4705. https://doi.org/10.1021/ma400379a.

(122) Priestley, R. D.; Cangialosi, D.; Napolitano, S. On the Equivalence between the Thermodynamic and Dynamic Measurements of the Glass Transition in Confined Polymers. *J. Non. Cryst. Solids* **2015**, *407*, 288–295. https://doi.org/10.1016/j.jnoncrysol.2014.09.048.

(123) Martín, J.; Campoy-Quiles, M.; Nogales, A.; Garriga, M.; Alonso, M. I.; Goñi, A. R.; Martín-González, M. Poly(3-Hexylthiophene) Nanowires in Porous Alumina: Internal Structure under Confinement. *Soft Matter* **2014**, *10* (18), 3335. https://doi.org/10.1039/c3sm52378k.

(124) García-Gutiérrez, M. C.; Linares, A.; Martín-Fabiani, I.; Hernández, J. J.; Soccio, M.; Rueda, D. R.; Ezquerra, T. A.; Reynolds, M. Understanding Crystallization Features of P(VDF-TrFE) Copolymers under Confinement to Optimize Ferroelectricity in Nanostructures. *Nanoscale* **2013**, *5* (13), 6006–6012. https://doi.org/10.1039/c3nr00516j.

(125) Cai, R.; Jonas, A. M. Local Maps of the Polarization and Depolarization in Organic Ferroelectric Field-Effect Transistors. *Sci. Rep.* **2016**, *6*, 1–10. https://doi.org/10.1038/srep22116.

(126) Ghittorelli, M.; Lenz, T.; Sharifi Dehsari, H.; Zhao, D.; Asadi, K.; Blom, P. W. M.; Kovács-Vajna, Z. M.; De Leeuw, D. M.; Torricelli, F. Quantum Tunnelling and Charge Accumulation in Organic Ferroelectric Memory Diodes. *Nat. Commun.* **2017**, *8*, 2–9. https://doi.org/10.1038/ncomms15841.

(127) Zhao, W.; Li, S.; Yao, H.; Zhang, S.; Zhang, Y.; Yang, B.; Hou, J. Molecular Optimization Enables over 13% Efficiency in Organic Solar Cells. *J. Am. Chem. Soc.* **2017**, *139* (21), 7148–7151. https://doi.org/10.1021/jacs.7b02677.

(128) Yao, H.; Cui, Y.; Qian, D.; Ponseca, C. S.; Honarfar, A.; Xu, Y.; Xin, J.; Chen, Z.; Hong, L.; Gao, B.; et al. 14.7% Efficiency Organic Photovoltaic Cells Enabled by Active Materials with a Large Electrostatic Potential Difference. *J. Am. Chem. Soc.* **2019**, *141* (19), 7743-7750. https://doi.org/10.1021/jacs.8b12937.

(129) Green, M. A.; Yoshihiro, H.; D., D. E.; H., L. D.; Jochen, H.-E.; W.Y., H.-B. A. Solar Cell Efficiency Tables (Version 52). *Prog. Photovoltaics Res. Appl.* **2018**, *26* (7), 427–436. https://doi.org/10.1002/pip.3040.

(130) Yao, H.; Ye, L.; Zhang, H.; Li, S.; Zhang, S.; Hou, J. Molecular Design of Benzodithiophene-Based Organic Photovoltaic Materials. *Chem. Rev.* **2016**, *116* (12), 7397–7457. https://doi.org/10.1021/acs.chemrev.6b00176.

(131) He, X.; Gao, F.; Tu, G.; Hasko, D. G.; Hüttner, S.; Greenham, N. C.; Steiner, U.; Friend, R. H.; Huck, W. T. S. Formation of Well-Ordered Heterojunctions in Polymer:PCBM Photovoltaic Devices. *Adv. Funct. Mater.* **2011**, *21* (1), 139–146. https://doi.org/10.1002/adfm.201000573.

(132) Tang, Z.; Tress, W.; Inganäs, O. Light Trapping in Thin Film Organic Solar Cells. *Mater. Today* **2014**, *17* (8), 389–396. https://doi.org/10.1016/j.mattod.2014.05.008.

(133) Bi, Y.-G.; Feng, J.; Ji, J.-H.; Yi, F.-S.; Li, Y.-F.; Liu, Y.-F.; Zhang, X.-L.; Sun, H.-B. Nanostructures Induced Light Harvesting Enhancement in Organic Photovoltaics. *Nanophotonics* **2017**, *7* (2), 371-391. https://doi.org/10.1515/nanoph-2017-0060.

(134) Rodríguez-Rodríguez, Á.; Rebollar, E.; Soccio, M.; Ezquerra, T. A.; Rueda, D. R.; Garcia-Ramos, J. V.; Castillejo, M.; Garcia-Gutierrez, M. C. Laser-Induced Periodic Surface Structures on Conjugated Polymers: Poly(3-Hexylthiophene). *Macromolecules* **2015**, *48* (12), 4024–4031. https://doi.org/10.1021/acs.macromol.5b00804.

(135) Na, S. I.; Kim, S. S.; Jo, J.; Oh, S. H.; Kim, J.; Kim, D. Y. Efficient Polymer Solar Cells with Surface Relief Gratings Fabricated by Simple Soft Lithography. *Adv. Funct. Mater.* **2008**, *18* (24), 3956–3963. https://doi.org/10.1002/adfm.200800683.

(136) Cui, J.; Rodríguez-Rodríguez, Á.; Hernández, M.; García-Gutiérrez, M.-C.; Nogales, A.; Castillejo, M.; Moseguí González, D.; Müller-Buschbaum, P.; Ezquerra, T. A.; Rebollar, E. Laser-Induced Periodic Surface Structures on P3HT and on Its Photovoltaic Blend with PC $_{71}$ BM. *ACS Appl. Mater. Interfaces* **2016**, *8* (46), 31894–31901. https://doi.org/10.1021/acsami.6b09053.

(137) Petti, L.; Rippa, M.; Capasso, R.; Nenna, G.; De Girolamo Del Mauro, A.; Pandolfi, G.; Maglione, M. G.; Minarini, C. Fabrication of Novel Two-Dimensional Nanopatterned Conductive PEDOT:PSS Films for Organic Optoelectronic Applications. *ACS Appl. Mater. Interfaces* **2013**, *5* (11), 4777–4782. https://doi.org/10.1021/am401451r.

(138) ElMahmoudy, M.; Charrier, A. M.; Malliaras, G. G.; Sanaur, S. Facile Nanopatterning of PEDOT:PSS Thin Films. *Adv. Mater. Technol.* **2018**, *3* (5), 1–8. https://doi.org/10.1002/admt.201700344.

(139) Schaefer, M.; Holtkamp, J.; Gillner, A. Ablation of PEDOT/PSS with Excimer Lasers for Micro Structuring of Organic Electronic Devices. *Synth. Met.* **2011**, *161* (11–12), 1051–1057. https://doi.org/10.1016/j.synthmet.2011.03.014.

(140) McDonald, J. P.; Hendricks, J. L.; Mistry, V. R.; Martin, D. C.; Yalisove, S. M. Femtosecond Pulsed Laser Patterning of Poly(3,4-Ethylene Dioxythiophene)-Poly(Styrenesulfonate) Thin Films on Gold/Palladium Substrates. *J. Appl. Phys.* **2007**, *102* (1), 013107. https://doi.org/10.1063/1.2752137.

(141) Lasagni, A. F.; Hendricks, J. L.; Shaw, C. M.; Yuan, D.; Martin, D. C.; Das, S. Direct Laser Interference Patterning of Poly(3,4-Ethylene Dioxythiophene)-Poly(Styrene Sulfonate) (PEDOT-PSS) Thin Films. *Appl. Surf. Sci.* **2009**, *255* (22), 9186–9192. https://doi.org/10.1016/j.apsusc.2009.06.130.

(142) Meier, R.; Birkenstock, C.; Palumbiny, C. M.; Müller-Buschbaum, P. Efficiency-Improved Organic Solar Cells Based on Plasticizer Assisted Soft Embossed PEDOT:PSS Layers. *Phys. Chem. Chem. Phys.* **2012**, *14* (43), 15088–15098. https://doi.org/10.1039/c2cp42918g.

(143) Wei, H. Y.; Huang, J. H.; Hsu, C. Y.; Chang, F. C.; Ho, K. C.; Chu, C. W. Organic Solar Cells Featuring Nanobowl Structures. *Energy Environ. Sci.* **2013**, *6* (4), 1192–1198. https://doi.org/10.1039/c3ee24128a.

(144) Qiu, Y.; Leung, S. F.; Zhang, Q.; Mu, C.; Hua, B.; Yan, H.; Yang, S.; Fan, Z. Nanobowl Optical Concentrator for Efficient Light Trapping and High-Performance Organic Photovoltaics. *Sci. Bull.* **2015**, *60* (1), 109–115. https://doi.org/10.1007/s11434-014-0693-8.

(145) Wang, X.; Liu, Z.; Yang, Z.; He, J.; Yang, X.; Yu, T.; Gao, P.; Ye, J. Heterojunction Hybrid Solar Cells by Formation of Conformal Contacts between PEDOT:PSS and Periodic Silicon Nanopyramid Arrays. *Small* **2018**, *14* (15), 1–7. https://doi.org/10.1002/smll.201704493.

(146) Bar-Cohen, Y. *Biomimetics: Biologically Inspired Technologies*; CRC Press, 2005.

(147) Barthlott, W.; Mail, M.; Bhushan, B.; Koch, K. Plant Surfaces: Structures and Functions for Biomimetic Innovations. *Nano-Micro Lett.* **2017**, *9* (2), 23. https://doi.org/10.1007/s40820-016-0125-1.

(148) Autumn, K.; Liang, Y. A.; Hsieh, S. T.; Zesch, W.; Chan, W. P.; Kenny, T. W.; Fearing, R.; Full, R. J. Adhesive Force of a Single Gecko Foot-Hair. *Nature* **2000**, *405* (6787), 681–685. https://doi.org/10.1038/35015073.

(149) Filippov, A. E.; Gorb, S. N. Modelling of the Frictional Behaviour of the Snake Skin Covered by Anisotropic Surface Nanostructures. *Sci. Rep.* **2016**, *6*, 23539. https://doi.org/10.1038/srep23539.

(150) Alamri, S.; Aguilar-Morales, A. I.; Lasagni, A. F. Controlling the Wettability of Polycarbonate Substrates by Producing Hierarchical Structures Using Direct Laser Interference Patterning. *Eur. Polym. J.* **2018**, *99*, 27–37. https://doi.org/10.1016/j.eurpolymj.2017.12.001.

(151) Roessler, F.; Lasagni, A. F. Protecting Sub-Micrometer Surface Features in Polymers from Mechanical Damage Using Hierarchical Patterns. *J. Laser Micro Nanoeng.* **2018**, *13* (2), 68–75. https://doi.org/10.2961/jlmn.2018.02.0004.

(152) Cardoso, J. T.; Alamri, S.; Lasagni, A. F.; Aguilar-Morales, A. I.; Huerta-Murillo, D.; Cordovilla, F.; Ocaña, J. L. Superhydrophobicity on Hierarchical Periodic Surface Structures Fabricated via Direct Laser Writing and Direct Laser Interference Patterning on an Aluminium Alloy. *Opt. Lasers Eng.* **2018**, *111*, 193–200. https://doi.org/10.1016/j.optlaseng.2018.08.005.

(153) Martínez-Calderon, M.; Rodríguez, A.; Dias-Ponte, A.; Morant-Miñana, M. C.; Gómez-Aranzadi, M.; Olaizola, S. M. Femtosecond Laser Manufacturing of Highly Hydrophobic Hierarchical Structures Fabricated by Combining Surface Microstructures and LIPSS. *Appl. Surf. Sci.* **2016**, *374*, 81–89.

(154) Neděla, O.; Slepička, P.; Sajdl, P.; Veselý, M.; Švorčík, V. Surface Analysis of Ripple Pattern on PS and PEN Induced with Ring-Shaped Mask Due to KrF Laser Treatment. *Surf. Interface Anal.* **2017**, *49* (1), 25–33. https://doi.org/10.1002/sia.6054.

(155) Rao, J. P.; Geckeler, K. E. Polymer Nanoparticles: Preparation Techniques and Size-Control Parameters. *Prog. Polym. Sci.* **2011**, *36* (7), 887–913. https://doi.org/10.1016/j.progpolymsci.2011.01.001.

(156) Li, J.; Rao, J.; Pu, K. Recent Progress on Semiconducting Polymer Nanoparticles for Molecular Imaging and Cancer Phototherapy. *Biomaterials* **2018**, *155*, 217–235. https://doi.org/10.1016/j.biomaterials.2017.11.025.

(157) Feng, L.; Zhu, C.; Yuan, H.; Liu, L.; Lv, F.; Wang, S. Conjugated Polymer Nanoparticles: Preparation, Properties, Functionalization and Biological Applications. *Chem. Soc. Rev.* **2013**, *42* (16), 6620-6633. https://doi.org/10.1039/c3cs60036j.

(158) Crucho, C. I. C. Stimuli-Responsive Polymeric Nanoparticles for Nanomedicine. *ChemMedChem* **2015**, *10* (1), 24–38. https://doi.org/10.1002/cmdc.201402290.

(159) Tran, N. T. D.; Truong, N. P.; Gu, W.; Jia, Z.; Cooper, M. A.; Monteiro, M. J. Timed-Release Polymer Nanoparticles. *Biomacromolecules* **2013**, *14* (2), 495–502. https://doi.org/10.1021/bm301721k.

(160) Rose, S.; Prevoteau, A.; Elzière, P.; Hourdet, D.; Marcellan, A.; Leibler, L. Nanoparticle Solutions as Adhesives for Gels and Biological Tissues. *Nature* **2014**, *505* (7483), 382–385. https://doi.org/10.1038/nature12806.

(161) Vogel, N.; Weiss, C. K.; Landfester, K. From Soft to Hard: The Generation of Functional and Complex Colloidal Monolayers for Nanolithography. *Soft Matter* **2012**, *8* (15), 4044–4061. https://doi.org/10.1039/c1sm06650a.

(162) Pecher, J.; Mecking, S. Nanoparticles of Conjugated Polymers. *Chem. Rev.* **2010**, *110* (10), 6260–6279. https://doi.org/10.1021/cr100132y.

(163) Gehan, T. S.; Bag, M.; Renna, L. A.; Shen, X.; Algaier, D. D.; Lahti, P. M.; Russell, T. P.; Venkataraman, D. Multiscale Active Layer Morphologies for Organic Photovoltaics through Self-Assembly of Nanospheres. *Nano Lett.* **2014**, *14* (9), 5238–5243. https://doi.org/10.1021/nl502209s.

(164) Nagarjuna, G.; Baghgar, M.; Labastide, J. A.; Algaier, D. D.; Barnes, M. D.; Venkataraman, D. Tuning Aggregation of Poly(3-Hexylthiophene) within Nanoparticles. *ACS Nano* **2012**, *6* (12), 10750–10758. https://doi.org/10.1021/nn305207b.

(165) Millstone, J. E.; Kavulak, D. F. J.; Woo, C. H.; Holcombe, T. W.; Westling, E. J.; Briseno, A. L.; Toney, M. F.; Fréchet, J. M. J. Synthesis, Properties, and Electronic Applications of Size-Controlled Poly(3-Hexylthiophene) Nanoparticles. *Langmuir* **2010**, *26* (16), 13056–13061. https://doi.org/10.1021/la1022938.

(166) Satapathi, S.; Gill, H. S.; Li, L.; Samuelson, L.; Kumar, J.; Mosurkal, R. Synthesis of Nanoparticles of P3HT and PCBM for Optimizing Morphology in Polymeric Solar Cells. *Appl. Surf. Sci.* **2014**, *323*, 13–18. https://doi.org/10.1016/j.apsusc.2014.07.175.

(167) Kang, S. J.; Bae, I.; Shin, Y. J.; Park, Y. J.; Huh, J.; Park, S. M.; Kim, H. C.; Park, C. Nonvolatile Polymer Memory with Nanoconfinement of Ferroelectric Crystals. *Nano Lett.* **2011**, *11* (1), 138–144. https://doi.org/10.1021/nl103094e.

(168) Edqvist, E.; Hedlund, E. Design and Manufacturing Considerations of Low-Voltage Multilayer P(VDF-TrFE) Actuators. *J. Micromechanics Microengineering* **2009**, *19* (11), 115019. https://doi.org/10.1088/0960-1317/19/11/115019.

(169) Xiao, Z.; Dong, Q.; Sharma, P.; Yuan, Y.; Mao, B.; Tian, W.; Gruverman, A.; Huang, J. Synthesis and Application of Ferroelectric P(VDF-TrFE) Nanoparticles in Organic Photovoltaic Devices for High Efficiency. *Adv. Energy Mater.* **2013**, *3* (12), 1581–1588. https://doi.org/10.1002/aenm.201300396.

Chapter 2. Techniques and experimental conditions

This chapter contains a description of all the experimental techniques used throughout this Thesis, separated in three sections, and another section with the experimental conditions.

- Deposition techniques: deposition techniques are those by which a solution or dispersion of a material is deposited onto a substrate and by different methods, the solvent is allow to evaporate, leaving a solid residue of the sample, generally in the form of film. This section outlines the three employed approaches to fabricate thin films.

- Nanostructuring techniques: this section describes in detail the three methods to nanostructure the materials of study.

- Characterization techniques: once the sample is prepared and/or nanostructured, it must be characterized by several procedures depending on the functionality of the material. The characterization methods used in this Thesis are described, together with some physical basis of them, some technical features and purpose to this Thesis.

- Experimental conditions: in this section, the experimental details used to fabricate the samples investigated during this Thesis are listed, including the protocols for the preparation of substrates, the characteristics of the materials, the preparation of solutions, and experimental parameters for sample deposition.

2.1 Substrate-deposition techniques

2.1.1 Drop-casting

A droplet of the material solution or dispersion is pipetted over a substrate (Figure 2.1), leaving it to dry, either at ambient temperature or at a particular temperature, depending on the requirement for the drying rate or the boiling point of the solvent. This technique has been used for example for depositing samples that hardly attach to the substrate like polymeric aqueous colloids. By drop-casting, deposits with thickness in the range of microns are obtained. Drop-casted samples usually show visually ring-like shapes due to capillary flows that cause recirculation of the material to the edges of the droplet where evaporation is enhanced (coffee-

stain effect). Nevertheless, the evaporation of a droplet over a surface is a complex process that involves several mechanisms[1,2].

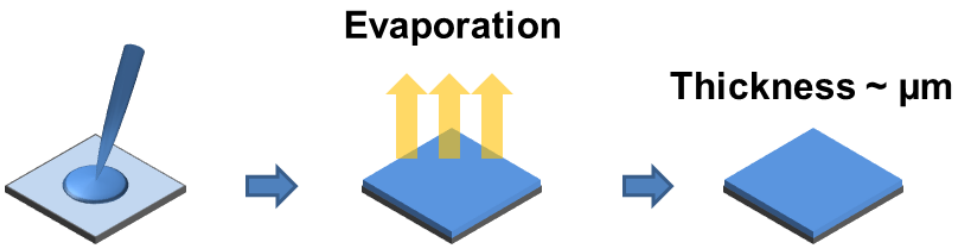

Figure 2.1 Drop-casting deposition method.

2.1.2 Spin-coating

The substrate is placed on top of a plate that has the capability to rotate at high speed. The substrate is hold in place by vacuum, through a hole in the rotating plate connected to a vacuum pump. A volume of the solution or dispersion is pipetted over it and then the rotation program is started. The rotation program has been previously designed taking in consideration the rotation time, the rotational speed and the acceleration applied to reach the target velocity. This particular technique is called "static" spin-coating (Figure 2.2), which is the method employed in this Thesis. On the other hand, "dynamic" spin-coating eliminates the acceleration parameter by depositing the dispersion over the rotating substrate once it has achieved the required speed. The quality and the thickness of the film depend on many factors like the rotational speed, the solvent of the solution, the concentration and the wettability of the solvent on the substrate used[3].

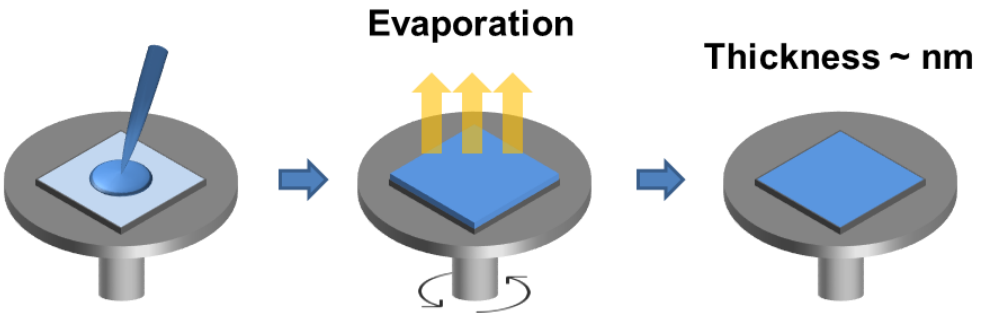

Figure 2.2 Spin-coating deposition method.

The thickness of the film (t) usually presents an inverse proportional relation with the rotational speed (ω_{cyc})[4]: $t \propto \frac{1}{\sqrt{\omega_{cyc}}}$. The thickness of polymeric films can strongly determine the crystallinity degree and the crystal orientation and consequently influences the properties of the devices that

use thin-film architectures like OSCs[5] or OFETs[6], for example. A different deposition technique, and therefore a different drying rate, can yield to a different preferential crystalline orientation[7].

In this Thesis, most of the samples from polymeric dispersions and solutions were deposited by spin-coating. This method allows a good reproducibility and easy tenability of the sample thickness by varying mainly the treatment of the substrate surface, the solution concentration and the rotational speed of the program. In this Thesis, a spin-coater from Laurell Technologies, Model WS-650HZB-23NPPB/ED3 was used.

2.1.3 Inkjet printing

Inkjet printing is one of the most useful and versatile techniques to deposit polymers[8–10], metallic oxides[11] and ceramics[12] among others[13]. Inkjet printing is a layer-by-layer depositing technique, that forms films by the arrangement of consecutive ejected droplets from a mobile reservoir filled with the liquid of study. This liquid is commonly a colloid or a dissolution, named as ink. By solvent evaporation, the material typically solidifies via either crystallization or vitrification after the deposition process[14]. The ink is previously injected inside a cartridge and then installed in the printer. The droplets are ejected through a nozzle –or a bunch of nozzles- whose aperture is controlled by a piezoelectric element. Therefore, the electric potential applied to the piezo controls the inkjet deposition rate. Upon reaching the substrate, the droplet forms a deposit by spreading, wetting and drying of the solvent on the substrate surface. The printed droplets form lines of typically about tens of microns[15]. The final film is formed by the assembly of printed lines (Figure 2.3).

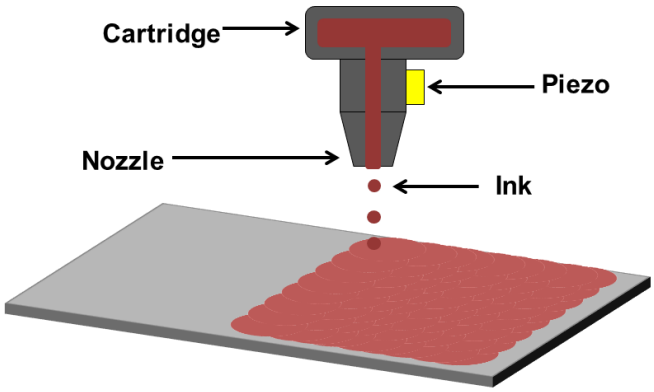

Figure 2.3 Scheme of the working principle of the film formation by inkjet printing.

This technique has several advantages over spin coating: it allows the impression of large areas, with customizable shapes by automatic routines, which is useful for printed electronics for instance. The process is scalable, i.e. it is possible to print large areas and also controlling the number of layers printed. This process has been applied to create a wide variety of organic

electronic devices including OSCs[8,16], electrochemical transistors[15,17,18], read-only memories[19] and sensors[20,21] among others. However, it has some drawbacks like the previous preparation of a cartridge, the bead-on-a-string effect[22] and the optimization of the liquid viscosity to avoid pouring problems due to low viscosity or, in the other extreme, obstruction issues due to high viscosity.

In this Thesis, inkjet printing was used as an alternative deposition method for aqueous dispersions of PEDOT:PSS. Inkjet impressions were made at the Departament d'Enginyeria Electrònica i Biomèdica (Universitat de Barcelona), using an Inkjet printer Dimatix 2831, Fujifilm, USA.

2.2 Nanostructuring techniques

2.2.1 Laser Induced Periodic Surface Structures (LIPSS)

There are different ways to create submicrometric size patterns in materials by means of laser irradiation. Among them, Laser Induced Periodic Surface Structures (LIPSS) is a widely used technique to create periodical structures over material surfaces. LIPSS produced over semiconductors using a Ruby laser were first reported by Birnbaum[23]. Since then, LIPSS have been fabricated using nanosecond[24] and femtosecond[25] lasers over metals[26,27], semiconductors and dielectrics with wavelengths from ultraviolet to near-infrared[28]. Figure 2.4 shows an example of LIPSS created on a soft matter surface.

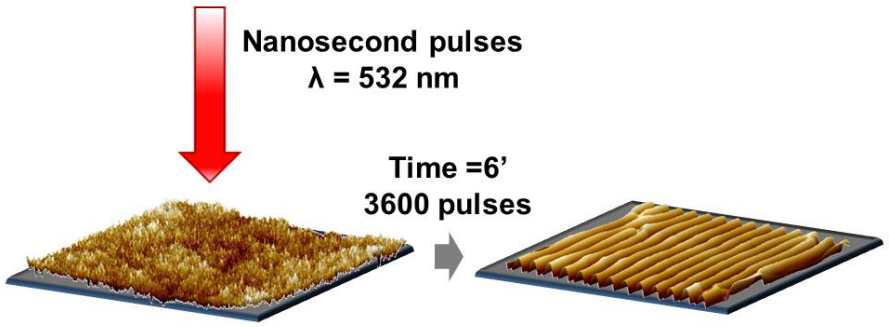

Figure 2.4 LIPSS over a $PC_{71}BM$ thin film.

The mechanism involved in LIPSS formation is complex; it includes optical, chemical and thermal processes. The model used to explain the formation of LIPSS could be very different between distinct materials or variable laser pulse rate. The first extensive theoretical model was developed by Sipe et al[29]. Regarding LIPSS formation in polymers, the models have included photolysis with migration of the material upon partial melting[30], photooxidation[31,32], rubbing[33], formation of granules or droplets from dewetting[34] that act as nucleants of ripples[35] or

reorientation of polymer chains[36], but the general model is yet incomplete. A standard explanation for LIPSS formation in polymers in the nanosecond regime involves redistribution of superficial molten slices of material induced by interference between incoming waves and waves scattered by inhomogeneities in the surface. All these mechanisms run below the ablation threshold of the material, so there is no removal of material, or it is insignificant. A necessary condition, but not sufficient, is that the material must absorb at the wavelength of the laser used. Quality and morphology parameters of the nanostructures, or even the formation itself[37], will be influenced by the thermal conductivity of the material, the substrate, the film thickness and the roughness. The timeline of the LIPSS formation can be separated into: (1) the formation of an interference pattern over the surface, and (2) the response of the material to it. The second phase begins when the material starts to flow, generally depending upon the material temperature. When the material absorbs the laser photons of the first pulse, its temperature starts to rise. If the second pulse reaches the material before the temperature drops to the initial value, the temperature will keep rising. The material is going beyond a certain temperature where the molecules flow and move one respect to the other: a glass transition temperature if the material is amorphous or a melting temperature if it is semicrystalline. As an example, when polystyrene (PS) is irradiated with λ=266 nm at a certain fluence below the ablation threshold, the surface temperature rises to a maximum during several nanoseconds. When the pulse is over, the temperature decreases. The next pulse reaches the material 0.1 second later -when a repetition of 10 Hz is used-, where the temperature still keeps slightly higher than the initial value. Therefore, the pulsed cycle implies a fast heating-cooling treatment of the material. An offset temperature is accumulated in each cycle so after several hundreds of laser pulses, the temperature of amorphous PS is above its glass transition temperature (Figure 2.5).

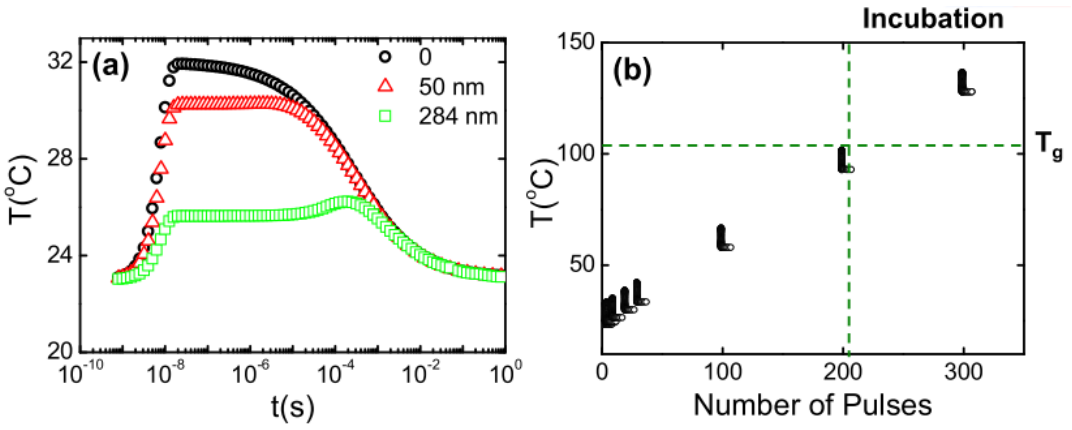

Figure 2.5 (a) Calculated time dependence of the surface temperature of PS after irradiation with the first pulse at 266 nm at a fluence of 10 mJ·cm^{-2} at the indicated depths. **(b)** Temperature estimation of polymer surface upon irradiation with successive laser pulses. Dashed line corresponds to the T_g of PS. Figure adapted from reference[37].

However, it has to be remarked that this is only a straightforward model to explain some aspects of the system and that it just gives an estimation. In addition, the heating of the material after each pulse could induce chemical modifications and changes on its absorption coefficient, giving rise to incubation effects. Thus, LIPSS mechanism cannot be explained totally only considering the temperature increase by using a one-dimensional heat conduction equation model[36].

The interference between the incoming laser waves and the ones scattered by the material surface will produce a heterogeneous intensity distribution that together with a feedback mechanism results in the enhancement of the modulation intensity. The shape of the generated nanostructure depends on the laser polarization. If the laser is linearly polarized, a grating-like pattern parallel to the laser polarization vector will grow in the surface (dots could be grown if the polarization is circular), with its period close to the laser wavelength[38] (Equation 2.1).

$$\Lambda = \frac{\lambda}{\boldsymbol{n} - \sin\Theta} \qquad (\mathbf{2.1})$$

Λ is the period or pitch of the emerged grating, λ is the wavelength of the laser, $\boldsymbol{n}$ is the refractive index of the material and Θ is the angle of incidence between the incoming wave and the normal vector of the substrate. This Equation could be obtained assuming interference between scattered waves parallel to the substrate and incoming waves at an angle θ from the normal vector, and calculating the projection of the interference pattern over the substrate[35]. A scheme of LIPSS formation with experimental parameters from Equation 2.1 is shown in Figure 2.6.

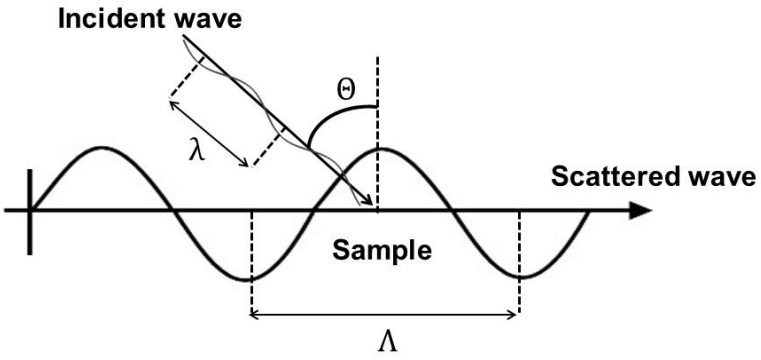

Figure 2.6 Scheme of LIPSS formation with parameters from Equation 2.1.

In summary, this technique is a free-template, reproducible, quick nanostructuring approach, allowing the fabrication of grating-like patterns over polymer films by means of irradiation at room conditions, in a matter of minutes and avoiding the use of clean rooms and the fabrication of complex masks.

In this Thesis, we fabricated LIPSS by irradiating with a Nd:YAG laser (neodymium-doped yttrium aluminium garnet). Nd:YAG is a solid-state laser, i.e. a solid material (Nd:$Y_3Al_5O_{12}$) is excited, in this case by an optical source, and emits photons at a particular wavelength: 1064 nm. This emission is amplified inside an optical cavity until it is emitted in a pulse by a technique called Q-switching. We irradiate with laser pulses linearly polarized of a Q-switched Nd:YAG laser (Lotis TII LS-2131M). The pulse duration is 8 nanoseconds and the frequency used is 10 Hz. Depending on the material, we used the second (λ=532nm) or the fourth harmonic (λ=266 nm) of the laser. The optical system used during this Thesis is shown in Figure 2.7.

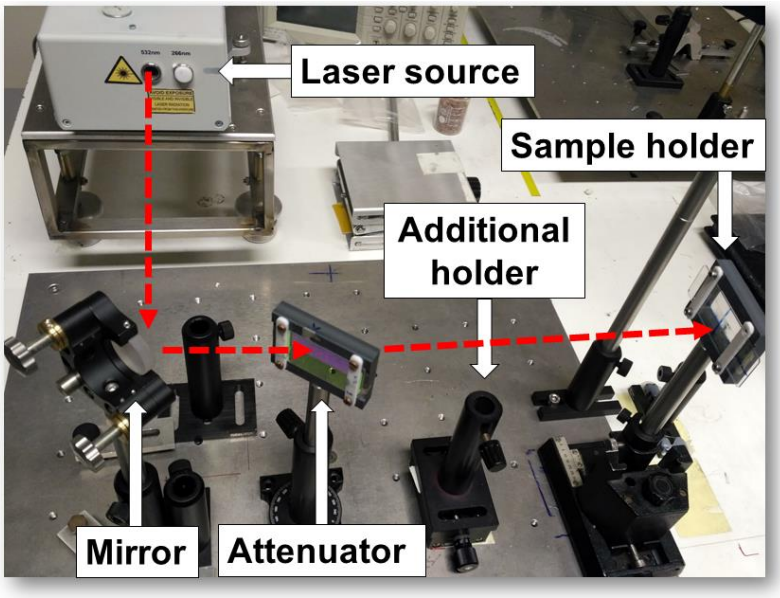

Figure 2.7 Optical system used to irradiate the samples. Red dotted lines indicate the path of the laser beam.

The laser beam is initially reflected on a mirror, then passes through an attenuator that allows us to tune the fluence and finally reaches the sample. The irradiation fluences were determined by measuring the laser energy in front of the sample. In some of the sections of this Thesis, an additional holder placed before the sample holder is used to insert an iris or a half-wave plate.

2.2.2 Nanoimprint Lithography (NIL)

Nanoimprint Lithography (NIL) is a straightforward, efficient, versatile high-resolution technique to fabricate micro and nanostructures[39]. It was developed by Chou and coworkers[40], who achieved nanometric trenches and dots of PMMA printed with a silicon stamp. The principle is essentially the replication of a mold, already structured, over a surface material, leaving the negative of the mold through a process with high temperatures and pressures previously fixed depending on the thermal properties of the material. High temperature and pressure allow polymer chain mobility

followed by the filling of the mold cavities. Therefore, the material needs to be heated over a glass transition temperature or a melting temperature depending on the amorphous or semicrystalline nature of the polymer. When the filling process is over, the temperature drops and the material is released from the pressure applied by the press, allowing the mold removal (Figure 2.8).

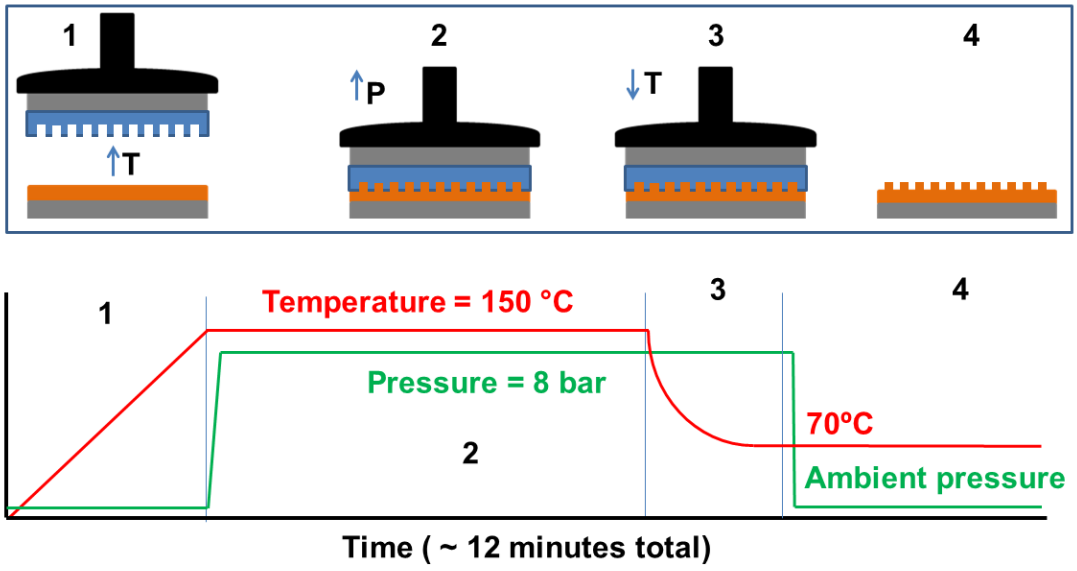

Figure 2.8 Scheme of a NIL process. The values of temperature, pressure and time correspond to our experiments.

NIL allows a large production of nanostructured samples in the same process and there are not limitations regarding the size of the structures, avoiding diffraction issues which can occur when using laser techniques. In addition, the successive mold choices allow producing scalable-step micro/nanostructures over large film areas. The drawbacks are the need of a clean room, the complex reproducibility in certain systems, the degradation/accumulation of material in the mold and the delicate removal of the mold.

In this Thesis, we use NIL to nanostructure PEDOT:PSS thin films deposited by spin-coating over silicon. NIL experiments have been carried out at the clean room of IMDEA Nanoscience (Campus de Cantoblanco, Madrid): air quality ISO5 (maximum of 100.000 particles bigger than 0.1 µm per m^3 of air). A press by NIL technologies (NILT) was used (Figure 2.9).

Molds of polydimethylsiloxane (PDMS) are used to nanoimprint PEDOT:PSS thin films. A master mold of silicon is used to fabricate the PDMS mold. First, the silicon mold is replicated on an intermediate polymer stamp (IPS). Then, the IPS pattern is replicated on PDMS, that is fabricated with a thin layer of hard-PDMS (with high Young modulus) and a thick layer of soft-PDMS (with lower Young modulus)[41]. Firstly, a layer of hard-PDMS (Gellest Inc.) is drop-casted on the IPS and is kept under vacuum conditions for 5-10 minutes. After that, a spin-coating step

is performed in order to decrease the thickness of the hard-PDMS layer. Then, it is pre-cured at 70ºC for 5 minutes. After that, soft-PDMS (Sylgard-184) is drop-casted over the hard-PDMS layer and cured for 3 hours at 70ºC. Finally, the PDMS mold is removed and cured at 120ºC for 30 minutes.

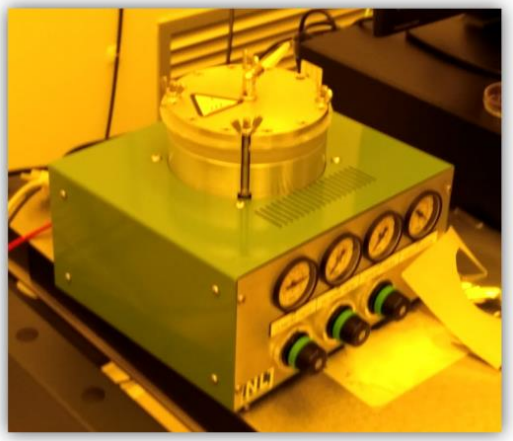

Figure 2.9 Press (NILT) used for Nanoimprint Lithography.

2.2.3 Polymer nanoparticles

Another nanostructuring approach used consists in precipitating polymers by exchanging a good organic solvent with a bad solvent, i.e. through the addition of an antisolvent[42]. To obtain conjugated polymer nanoparticles, the most typical antisolvent used is water. Sometimes, alcohols are used. Polymer chains in good solvents are unfolded, exposing the largest area to the environment, minimizing the interaction between monomers in the same molecule and between molecules depending on the solute concentration. The ideal situation would be the 'ideal chain' model[43]. A decrease in the solubility produced by the addition of the antisolvent will produce the folding and aggregation of the chains, reducing the effective interfacial area between solid and liquid, leading to total separation of phases if the solute is insoluble. However, if the good and the bad solvents are miscible –or immiscible but a surfactant is added- it is possible to induce a stable dispersion of the polymer in the bad solvent, water in this case, in the form of globules with diameters in the range of 10-1000 nanometers[44] (Figure 2.10).

Polymeric nanoparticles have found applications in many scientific fields: photonic systems[45], adhesives[46], biomedical applications like targeting[47], molecular imaging[48] and drug delivery activated by external stimuli[49,50], and organic electronics[51]. Polymer nanoparticles offer high effective area, the tuning of the size through the preparation conditions and the possibility of having a dispersion in water, avoiding, during the deposition process, the handling of toxic

organic solvents, or allowing the incorporation of the polymers into the human body for different medical applications.

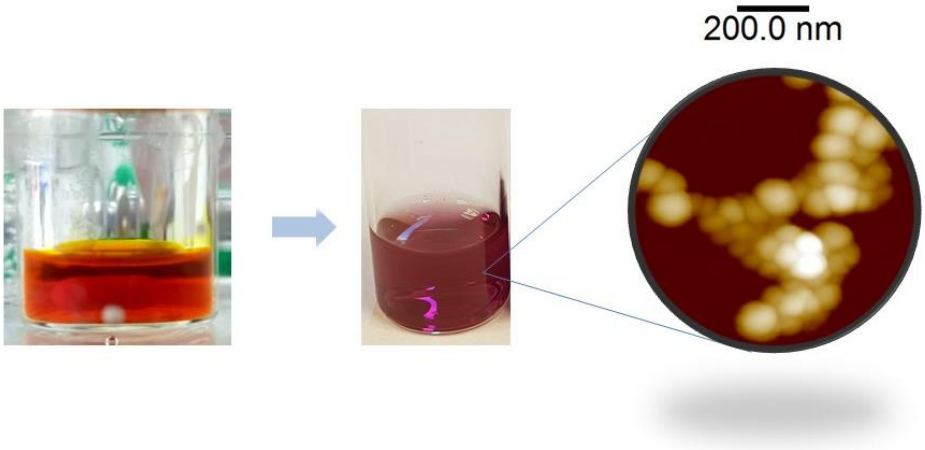

Figure 2.10 Polymer solved in an organic solvent **(left)** and later dispersed in water **(center)**. **Right** image is a topographical image of polymer nanoparticles taken by AFM (see section 2.3.1.1).

In this Thesis, several polymers are processed into nanoparticles. There are many ways to produce polymer nanoparticles[44]. Three techniques have been used in this Thesis, all of them starting from preformed polymers: the dialysis technique[52], the miniemulsion technique[53] and the flash, or reprecipitation technique[54].

2.2.3.1 Dialysis technique

In the dialysis approach, the nanoprecipitation is achieved by an exchange of solvent and water through the walls of a dialysis membrane with a molecular weight cut-off, so liquid molecules will pass through it but polymer chains above the threshold will not. The polymer is first dissolved in a good organic solvent: the solvent used must be miscible with water. The membrane is stored in the fridge, floating inside a saline solution. Previous to the experiment, a portion of the membrane is extracted from the saline solution and rinsed three times in deionized water. Then, with the aid of a funnel, the inner walls of the membrane are rinsed with the same solvent in which the polymer is dissolved. After that, the membrane is closed by one of its ends with a magnetic clamp and then the polymer solution is poured inside the membrane. Finally, another clamp seals the other end and the membrane is placed inside a beaker with two liters of deionized water and stirred at low speed with a magnet, where the magnetic clamp is attached. Due to the miscibility of the liquids and the molecular weight threshold of the membrane walls, the solvent molecules will be leaving the membrane into the water bath, and the water molecules will replace them until total removal of the original organic solvent. This displacement will produce a continuous aggregation of the polymer caused by the decrease of solubility until obtaining a homogeneous

colloid of the polymer in water. The mechanism has been described as a first nucleation step where small aggregates are formed, followed by the aggregation of the nuclei, increasing their sizes until achieving a stable state[55]. This dialysis step will spend around twenty-four hours; the water will be changed periodically. Visking membranes were used (Visking DTV by Medicell Int Ltd. Cut-off range 12000-14000 $g \cdot mol^{-1}$, diameter=25.5 mm), previously cleaned and rinsed in deionized water. Figure 2.11 summarizes the main steps of the dialysis procedure.

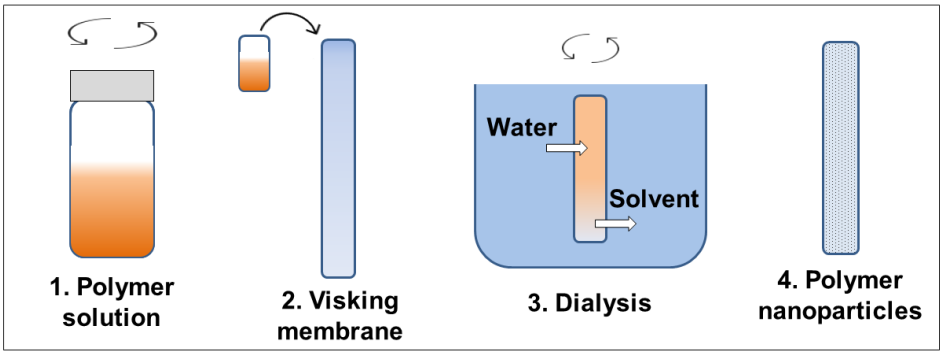

Figure 2.11 Scheme of dialysis approach steps.

In this Thesis, the dialysis approach has been used to fabricate PVDF nanoparticles.

2.2.3.2 Miniemulsion technique

In the miniemulsion approach, a surfactant aids the precipitation of the polymer between two immiscible liquids. In this process, both liquids are immiscible and the boiling point of the organic solvent must be lower than the one corresponding to water. Initially the polymer is dissolved in a good solvent. The surfactant used is solved in water at 1 wt. %. In this Thesis, the surfactant was sodium dodecyl sulfate (SDS), which has a hydrophilic anionic extreme and a hydrophobic alkyl tail. The next step is creating a macroemulsion, mixing both solutions and stirring vigorously for two hours. The final miniemulsion will be produced by sonication for fifteen minutes. Then, the sonicated mixture is stirred and heated to 70ºC for around one hour to evaporate the $CHCl_3$. The result is a colloid formed with polymer nanoparticles in water. However, an excess of SDS is still solved in the water. To remove the surfactant, the colloid is dialyzed against pure water by pouring the dispersion into a Visking membrane and stirring it in a beaker with two liters of water during three to five days. Water is removed twice a day. The final result will be the polymer nanoparticles with a SDS coating but without SDS remaining in the water. Figure 2.12 summarizes the main steps of the miniemulsion procedure.

In this Thesis, the miniemulsion approach has been used to fabricate P3HT nanoparticles. The solvent used in every experiment was $CHCl_3$ (>99.98%), purchased from Quimipur S.L.U.

(Campo Real, Madrid, Spain). SDS powder was purchased from Sigma-Aldrich (ACS reagent ≥99.0%).

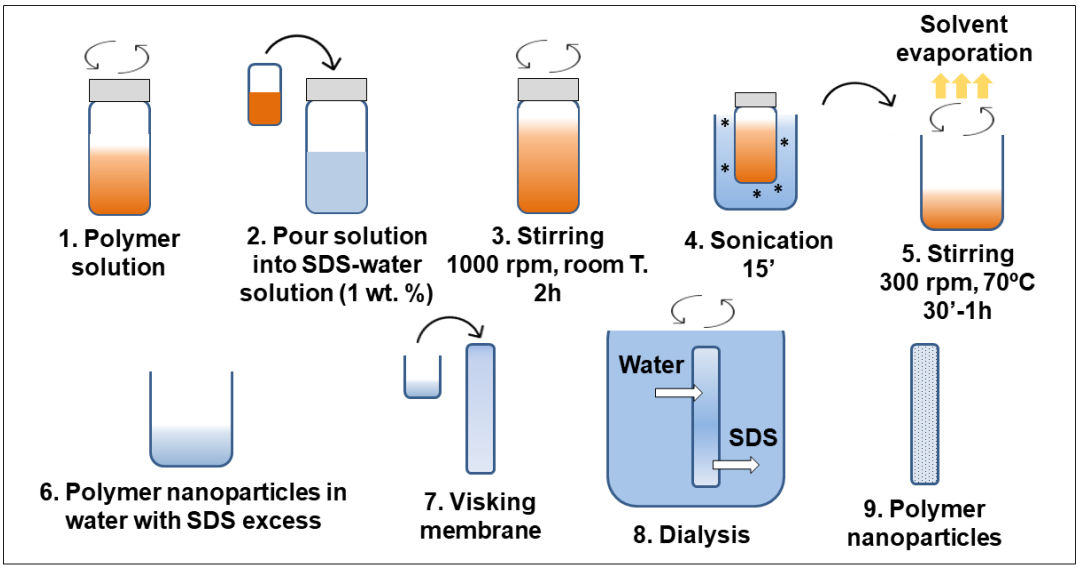

Figure 2.12 Scheme of miniemulsion approach steps.

2.2.3.3 Flash technique

Flash or reprecipitation technique is the simplest of the three methods to fabricate nanoparticles. The two liquids are rapidly mixed together with an external energy supply, in this case stirring, inside a vessel. Initially, the polymer is solved in a good solvent, miscible with water and with a boiling point below 100ºC. Then, the solution is injected into water (ten times the volume of the solution) and immediately the mixture is stirred at 900 rpm during fifteen to thirteen minutes, depending on the polymer (15' for P3HT and 30' for P(VDF-TrFE)). A rapid displacement of the solvents could be seen as in the first moments of the stirring the final color of the colloid is achieved. As a result of the mixed liquids, the polymer, i.e. the solute is above its saturation limit, thus a state of supersaturation is achieved[42,56]. In this state, the nucleation of polymer chains is promoted. The nucleation step is followed by aggregation and growth of the already formed particles. To achieve a narrow distribution of particles with nanometric diameters, it is important that the nucleation rate is favored over the growth rate. The high speed of stirring induces turbulent flows in the liquids, and provides the supersaturation conditions[57]. After the initial stirring step, a slow stirring rate at 70ºC is maintained to remove the solvent for thirteen minutes to one hour. Figure 2.13 summarizes the main steps of the flash procedure.

In this Thesis, flash precipitation approach has been carried out to fabricate nanoparticles of P3HT and P(VDF-TrFE) using tetrahydrofuran (THF) ($(CH_2)_4O$) as solvent. THF is miscible with water and its boiling point is 65-66ºC. THF (≥99.5%, EMPARTA® ACS) was purchased from Merck.

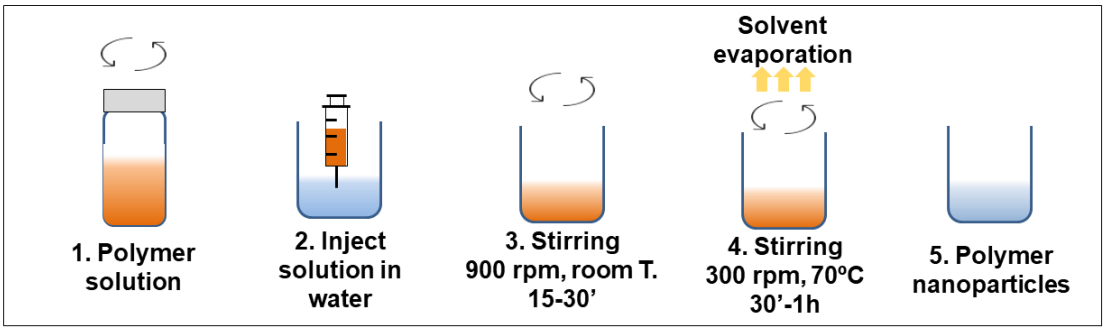

Figure 2.13 Scheme of flash approach steps.

In order to perform calorimetric and X-ray scattering experiments on the nanoparticles, the resulting colloid produced by any of the three methods previously described must be dried. This was achieved by using a vacuum centrifuge (Speed Vac. Plus SC110A, Savant). Through vacuum drying technique, the water is removed by sublimation of frozen water at high vacuum conditions.

2.3 Characterization techniques

2.3.1 Microscopy techniques

2.3.1.1 Atomic Force Microscopy (AFM)

The Atomic Force Microscope[58] was invented in 1986 at the Stanford University in collaboration with IBM San Jose Research Laboratory, as an alternative to the Scanning Tunneling Microscope (STM), developed in 1981 at IBM Zürich[59], which was only able to picture conductive surfaces. AFM is a probe method; it maps the topography of a surface by measuring the deflection of a cantilever with a tip coupled at its end (Figure 2.14). The tip is usually a metallic tetrahedron whose peak has a nanometric size.

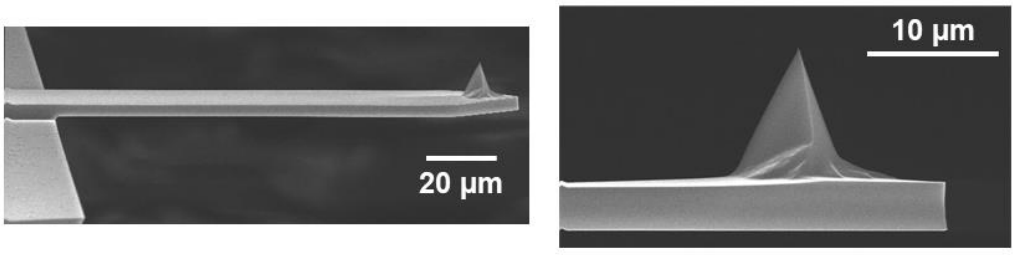

Figure 2.14 Shape of a conventional probe for tapping mode: the cantilever **(left)** and the tip **(right)**. Adapted figure from Bruker website[60].

The mechanism moves the tip repetitively all along the surface of the sample, making topographical lines until a complete 3D image of the surface is mapped. The working scheme of image mapping of AFM is shown in Figure 2.15.

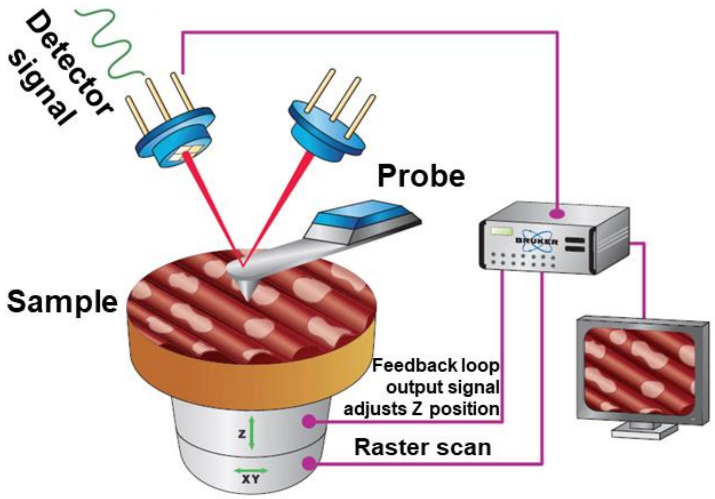

Figure 2.15 Working scheme of AFM[61].

There are several modes of measuring the topography, besides the modes that scan other physical parameters like electric current, Young Modulus or piezoelectric deformation. A classical way of taking topographical information is the contact mode: the tip is touching the surface in every moment so height differences will deflect the cantilever that holds the tip. To quantify this movement, a laser is pointing to the upper surface of the cantilever, so the deflection of the latter will produce an oscillation of the reflected beam, which is collected by a photodiode that transforms the light contrast in voltage contrast, and this in a height contrast. Essentially, the cantilever-laser-photodiode mechanism is the same in the modes we used in this Thesis. We deal with soft matter samples, and in contact mode, it is easy to have dragging effects over the surface sample due to higher mechanical modulus of the metallic tip than soft matter samples modulus. This is the reason why we used tapping mode instead of contact mode.

In this Thesis, we have used a Multimode 8 AFM (Bruker) with a Nanoscope V controller (Bruker). The different modes used in this Thesis are described hereunder.

2.3.1.1.1 Tapping mode

In order to measure topographical profiles of our samples, we use the tapping mode which is optimal for soft matter. In the tapping mode, a Bruker patented technique, a piezo induces an oscillation into the cantilever close to its resonant frequency. It is also called intermittent contact mode since the tip is alternatively touching the sample, thus minimizing the effect from the tip on the sample and eliminating lateral forces during mapping. The information is not collected

through the cantilever deflection (as in contact mode) but through its amplitude[62]. If the tip finds an obstacle in the surface of the sample (a hole or a mountain), the distance between tip and sample will increase or decrease, both varying the force on the tip (Figure 2.16). This gradient of forces will affect the frequency and the amplitude of the cantilever oscillation. For example, if the tip goes too close to the surface, the repulsive force will be higher and the oscillation frequency will increase as well. On the other side, an increment of the attractive force to the tip will reduce the frequency.

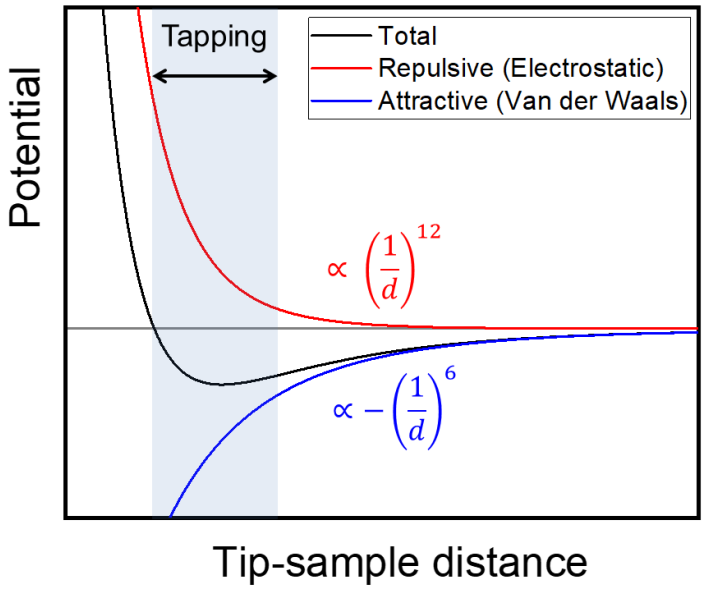

Figure 2.16 Plot of forces as a function of tip-sample distance using the Lennard-Jones potential[62].

The feedback mechanism in tapping mode keeps constant the original value of frequency and amplitude of the oscillation by moving the cantilever along the z-axis the same distance as the surface features of the sample. Therefore, the topographic picture of the sample is mapped line by line.

In this Thesis, the morphology and topography of most of the studied systems were characterized by AFM in tapping mode. Tapping images were collected using gold-coated silicon probes (Tap300GB-G probes by BudgetSensors).

2.3.1.1.2 Conductive-AFM (C-AFM)

In the conductive mode of the AFM (C-AFM), the equipment acts essentially as an ammeter of a circuit where the sample is the resistance and the tip probe, the substrate and the rest of the electronics of the AFM is the rest of the circuit. It is used to measure the electric current when a DC voltage is applied between the tip probe and a conductive substrate. This mode works in contact. It measures simultaneously the vertical current through the sample and the topography

through contact mode. The tip and the substrate must be electrically conducting to engage the circuit with the top and the bottom of the sample respectively. The sample is often attached to the scanner with a metallic tape or conducting paste. The current, that is usually in the order of picoampere to tens of nanoamperes, is detected with a current-to-voltage pre-amplifier. This technique provides us local (nanometric) variations in the conductivity of a sample. The working scheme of C-AFM is presented in Figure 2.17.

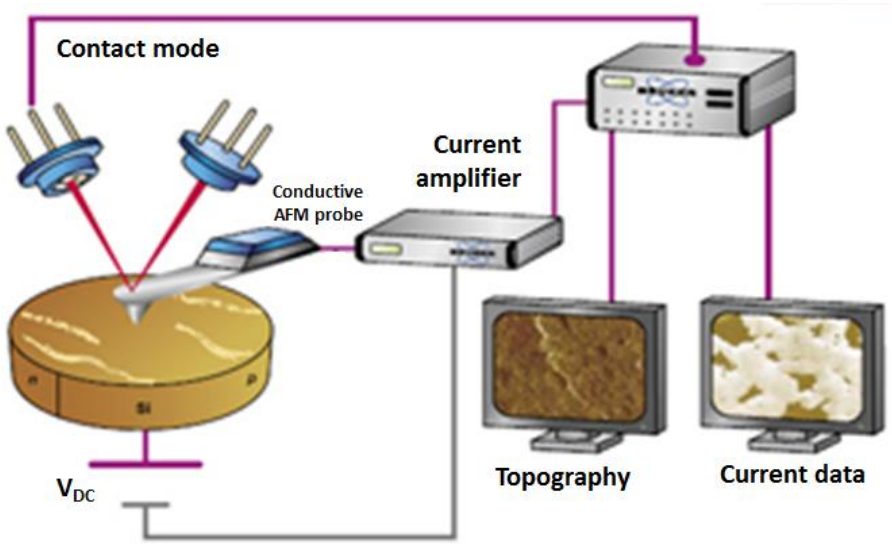

Figure 2.17 Working scheme of the C-AFM[64].

In this Thesis, the C-AFM mode was used to detect values and local changes of electrical current on thin films of $PC_{71}BM$, P3HT, PCDTBT and PEDOT:PSS. Electrical current measurements were performed applying a relatively low force on the tip in order to minimize the damage on the samples. Pt-Ir covered Si conductive tips were used, with a spring constant of $k=0.2\ N\cdot m^{-1}$, (SCM-PIC by Bruker). The sample substrates were attached to iron supports through conductive silver epoxy (CW2400, Chemtronics).

2.3.1.1.3 Piezoresponse Force Microscopy (PFM)

Another application consists of applying an alternating current (AC) voltage to reveal the polarization nature of the sample and local variations of polarization. As C-AFM, this mode[65] also works in contact and measures the inverse piezoelectric effect in ferroelectric materials (see section 1.2). The AC voltage must be low enough to reveal the ferroelectric nature of the sample without disturbing the original state while measuring it. When the polarization vector of a particular point of the sample has a vertical component, the AC voltage will induce a vertical oscillation, in the order of picometers, that will be detected as out-of-plane piezoelectric amplitude (Figure 2.18). On the other hand, the lateral component of the polarization vector is detected as

long as it will be orthogonal to the cantilever axis, so that elongation will excite the torsional mode of the cantilever as in-plane amplitude. However, a polarization vector parallel to the cantilever axis do not excite the torsional mode of the cantilever but can produce a "buckling" movement on it, inducing an out-of-plane amplitude that sometimes can lead to misinterpretation of the signal. In addition, PFM measures the piezoelectric phase as a way to distinguish different polarization orientation in the same direction, e.g. pointing up and down in the vertical direction.

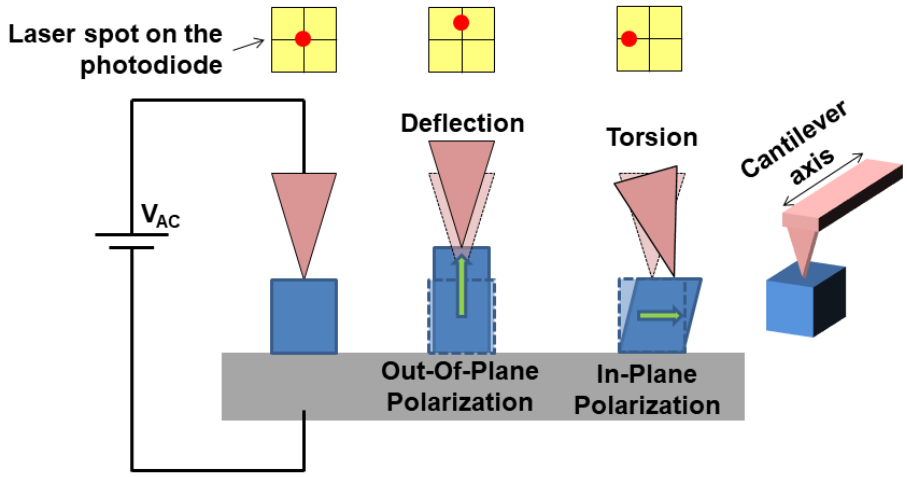

Figure 2.18 Working scheme of the PFM mode.

PFM mode also allows applying increasing and decreasing DC voltage ramps over a single point at the sample to measure the phase and register hysteresis cycles if the local zone under influence is ferroelectric.

In this Thesis, PFM is used to characterize piezoelectric behavior in several systems involving the ferroelectric copolymer P(VDF-TrFE). PFM measurements were performed applying a relatively low force on the tip in order to avoid damaging the samples and by using Pt-Ir covered Si conducting tips with a spring constant of k=3 $N \cdot m^{-1}$, (SCM-PIT by Bruker). The sample substrates were attached to iron supports through conducting silver epoxy (CW2400, Chemtronics) or through double sided carbon conducting tape (Ted Pella).

2.3.1.1.4 Quantitative Nanomechanical Mapping (QNM)

PeakForce QNM measures mechanical properties by making nanoindentations with the tip in every point of the sample, so it is also a contact mode. The process of tracing and retracing the sample with the tip is registered in a force curve (Figure 2.19). The red curve (trace) represents the force experienced by the tip along the approaching way to the sample surface: starting with a zero value, following by an attractive-force zone applied by the sample adhesion and ending with the applying force (repulsive) of the tip. The behavior of the material when the tip withdrawal

(retrace, black curve) is started will give us its elastic modulus, then a consequent enhancement of the adhesion force before final disengagement between tip and sample. Applying a mechanical model to this system, and having calibrated before the physical parameters of the tip (radius and spring constant), it is possible to extract mechanical parameters of the sample: Young Modulus, adhesion, deformation and dissipation (Figure 2.19), while it is mapping the topography in PeakForce mode.

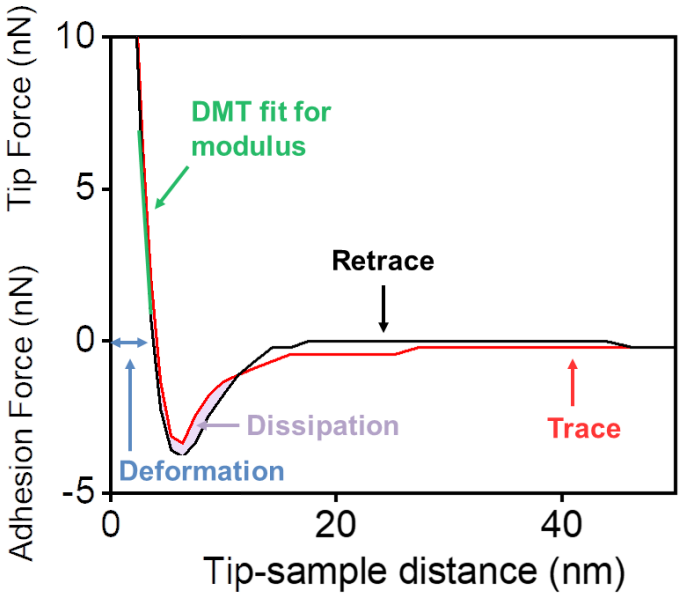

Figure 2.19 Typical force curve obtained at every point of the sample.

The model by Derjaguin, Muller and Toporov[66] (DMT) gives us a mathematical relation between the force experienced by the tip and the separation between the tip and the sample (Equation 2.2) assuming a Hertzian (spherical) contact between tip and sample. Therefore, a force-distance curve is obtained at every point of the sample, that fitted with Equation 2.2, gives us particular values of the adhesion force and the reduced Young Modulus (E_r).

$$F_{tip} = \frac{4}{3} E_r \sqrt{R {d_{ts}}^3} + F_{adhesion} \qquad (\mathbf{2.2})$$

R is the radius of the tip, d_{ts} is the distance between the tip and the sample, F_{tip} is the force applied by the tip and $F_{adhesion}$ is the attractive adhesion force between tip and sample. E_r represents the elastic deformation of the material-tip system so a deconvolution must be applied to get an exclusive-material parameter. Equation 2.3 gives us a relation between the separated Young Modulus and the respective Poisson ratio (ν) of tip and sample. Poisson ratio is the negative relation between transverse strain and axial strain.

$$E_r = \left(\frac{1 - {\nu_s}^2}{E_s} + \frac{1 - {\nu_{tip}}^2}{E_{tip}} \right)^{-1} \qquad (\mathbf{2.3})$$

However, it is usually considered that the Young Modulus of the tip is much higher than the sample one, so the second term of Equation 2.3 is rounded to zero. Therefore, the Young Modulus of the sample is calculated as a function of the DMT Reduced Young Modulus and the Poisson ratio of the sample (Equation 2.4).

$$E_s = (1 - {\nu_s}^2) E_r \qquad (\mathbf{2.4})$$

In this Thesis, QNM mode has been used to measure the mechanical properties of various layers of PEDOT:PSS deposited by inkjet printing. The measurements were performed by using Al covered Si tips (RTESPA-300, Bruker) with a nominal spring constant k=40 $N \cdot m^{-1}$. Spring constant was measured by the thermal tune method and found to be around 15-30 $N \cdot m^{-1}$. Tip radius was calibrated against a polystyrene standard provided by Bruker. The measured value of the tip radius was around 6-15 nm.

2.3.1.2 Scanning Electron Microscopy (SEM)

SEM is also a technique that allows visualization of the real space at the nanometer scale. A source produces a beam of electrons that are collimated and focused on the sample. The scattered electrons are recollected and form an image of the sample, with textures, depth and even with compositional information of the sample. SEM can be used as a complementary technique with AFM because they are approximately in the same level of resolution. AFM usually implies a lower impact on the sample and gives also an accurate mapping of the surface height. However, SEM achieves more textured images of nanometric objects and also can take larger images, scanning areas of square millimeters.

In this Thesis, SEM is used to visualize fresh PEDOT:PSS samples nanostructured by nanoimprint lithography to elucidate the quality of the nanostructures in large areas and detect surface imperfections. SEM images were taken at IMDEA Nanociencia, Campus de Cantoblanco, Madrid using a SEM Auriga (Carl Zeiss) with applied voltages and intensities in the order of 1 kV and 10 pA respectively.

2.3.1.3 Optical microscopy

The classical optical microscope uses light in the visible range and a series of lenses to magnify images until a resolution slightly below 1 μm.

In this Thesis, an optical microscope has been used to visualize $PC_{71}BM$ thin films that were irradiated by laser using an iris of 1.2 mm of diameter, thus the diameter of the irradiated spot is around that value. Microscope images were taken using a polarizing microscope (Laborlux 12 Pol, Leitz), illuminating with a halogen optical fiber illuminator (Motic MLC-150C), through a 10X objective (Leitz Wetzlar 10X/0.25 160/-) and with the software Motic Images Plus 2.0.

2.3.2 Differential Scanning Calorimetry (DSC)

DSC allows analyzing the thermal behavior of the material, for example, localizing the temperature of the phase transitions and how much material is involved in the process. It measures the difference of heat flow between a sample of material and a reference when both are being heated or cooled at the same rate: 0.1-100 ºC per minute. The sample consists of 1-20 mg of material that is sealed in a capsule. The reference is usually an empty capsule. The relation between the absorbed heat and the increase of temperature is called the heat capacity ($C = \frac{Q}{\Delta T}$). At certain temperatures, the material experiments phase transition (thermal events) that will affect its heat capacity and consequently, the heat rate provided by the calorimeter. DSC can reveal the presence and the nature of thermal events experimented by polymers: glass transition, melting, crystallization, aging, curing, polymerization, etc.

Thermal events can be either endothermic or exothermic, if the heat is required or released, respectively. The glass transition and crystal melting are endothermic processes. The glass transition is detected in the DSC as an upward step in the heat flow-temperature diagram. This means that the system requires more heat than before to keep rising the temperature at the same rate. Therefore, a liquid system has a higher heat capacity than a glassy one. Crystallization, on the other hand, is an exothermic process, thus the system will release heat. An amorphous polymer that can be arranged in an ordered structure will form a semicrystalline system when it is within a temperature window between the glass transition temperature and the melting temperature. The molecules will have mobility enough to arrange themselves in an ordered periodic array that will low their entropy, releasing the excess of heat to the environment. In this case, the heat needed to keep rising the temperature in the DSC will drop and it its detected as an exothermic peak in the heat flow-temperature diagram. When the temperature is high enough, the energy of the molecules acts against the integrity of the crystals and they will melt. Melting is another endothermic process that affects only to the crystalline regions of the polymer. It can be seen as the energy payback of the previous crystallization; the heat released before is now required to melt the crystals. Melting is a first order transition, so the temperature will not rise until the transition is completed, meanwhile the system will need enough heat to melt all the crystals and the diagram will show an endothermic peak. Figure 2.20 shows the DSC heating and cooling ramps from a sample of PVDF.

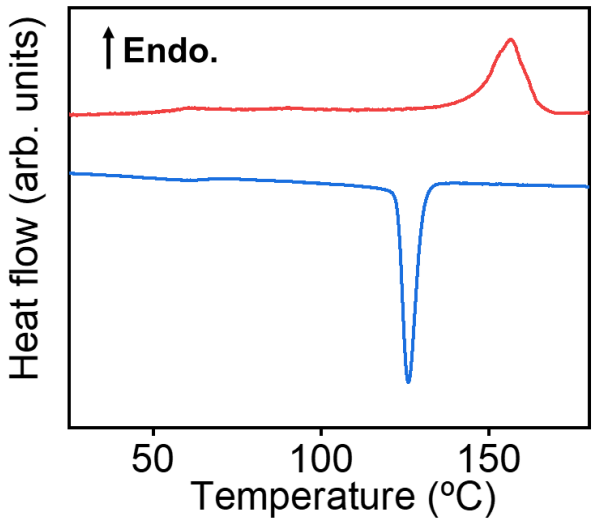

Figure 2.20 DSC of PVDF, the red curve corresponds to the heating ramp and the blue curve to the cooling ramp. Rate= 10°C·min^{-1}. The arrow indicates the direction of the endothermic peaks.

In this Thesis the convention is using upwards peaks to represent endothermic transitions. PVDF is a semicrystalline polymer and thus the endothermic peak located at 160°C in the heating ramp is associated with the melting of the crystals and the exothermic peak at 125°C in the cooling ramp is associated with the crystallization.

In this Thesis, calorimetric experiments were performed in a DSC 8500 (PerkinElmer) using aluminum pans of 10µL volume. Heating rates of 10ºC·min^{-1} were used.

2.3.3 Ultraviolet-Visible-Infrared Spectroscopy techniques

2.3.3.1 Absorption

In section 1.1.1, it was mentioned that conjugated polymers are particularly sensitive to light near the visible range because their electronic gap usually lies in this range of the electromagnetic spectrum. An analysis of how conjugated polymers absorb through the VIS and UV spectra provides information about the conformations of the conjugated chains.

In this Thesis, UV-VIS absorption technique is used both to identify maximums of absorption that could be associated with the choice of the appropriate laser wavelength to nanostructure PEDOT:PSS and to study different conformations in nanoparticles of P3HT. Absorption experiments were carried out using a UV-3600 Shimadzu Spectrophotometer (Duisburg, Germany) on liquids poured into quartz cuvettes with path lengths of 10 mm (Sugelabor, S.A.) and on thin films deposited on quartz substrates.

2.3.3.2 Spectrofluorometry

A complementary characterization technique to UV-VIS absorption is the emission spectra when the material is excited with photons at a particular wavelength. The emission spectrum shape reveals the decay mechanisms of electrons from the excited state (fluorescence). As with absorption, emission spectra provide information about the interactions and arrangement of the conjugated polymer chains. Figure 2.21 shows a simplified diagram for photoabsorption and photoemission.

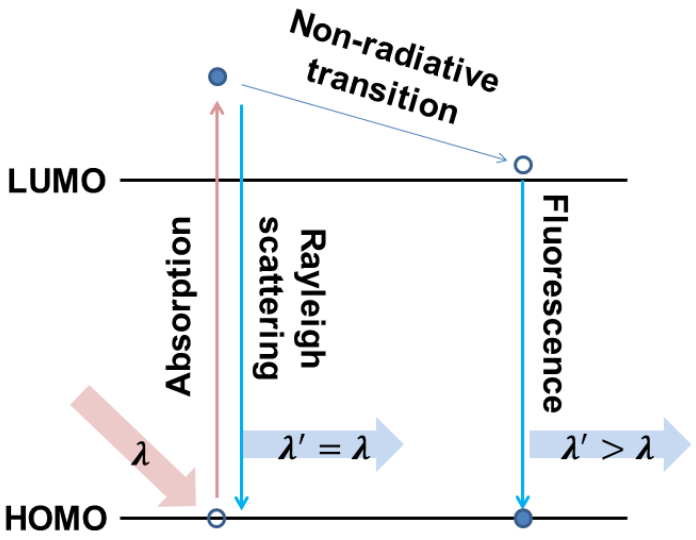

Figure 2.21 Scheme of the absorption and emission mechanisms.

In this Thesis, photoluminescence experiments in water-colloids were carried out with a Spectrofluorometer FluoroMax 4 (HORIBA Jovin Yvon) at Rocasolano Physical Chemistry Institute.

2.3.4 Raman spectroscopy

Raman spectroscopy is a chemical sensitive technique based on the inelastic scattering of photons by molecules that provides information about vibrational, rotational and other modes when the material is excited with low frequency laser pulses. Unlike infrared absorption that implies a change in the dipole moment, Raman scattering consists of an inelastic scattering of light, starting with a molecule excitation to a higher virtual level and subsequent emission of a different wavelength photon. If the emitted photon has a lower energy than the original, the process is called Stokes Raman Scattering. If, on the other hand, the molecule is excited from an already excited state and the emitted photon is more energetic than the original, is called Anti-Stokes Raman Scattering. Rayleigh scattering would be the elastic interaction (Figure 2.22). Raman

spectroscopy is a valuable technique to identify materials or particular conformations by characteristic phonon modes with a certain Raman shift, among other excitations as plasmons.

In this Thesis, Raman spectroscopy was used to elucidate chemical and conformational modifications on nanostructured systems of $PC_{71}BM$ and PEDOT:PSS. Raman spectroscopy was performed by using a Renishaw Raman InVia Reflex Spectrophotometer, equipped with a Leica Microscope, and an electrically refrigerated CCD camera. The excitation wavelength was the second harmonic (λ=532 nm) of the Nd:YAG laser. The spectra were acquired with a spectral resolution of 2 cm^{-1} using a 50x magnification objective to a spot with a diameter < 1μm on the samples.

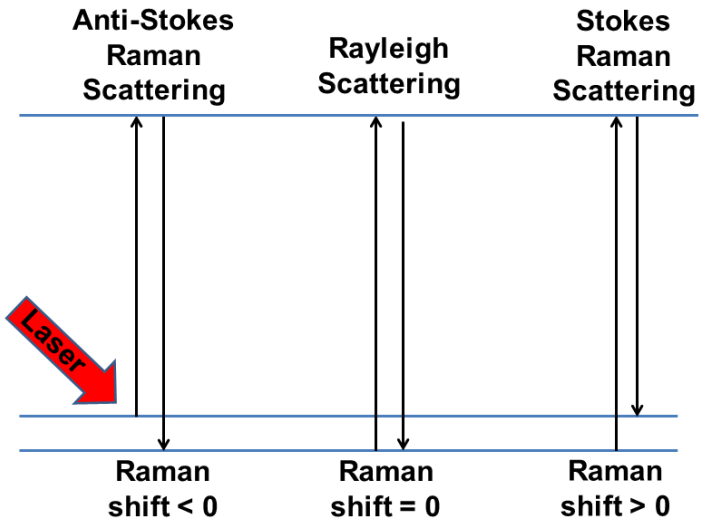

Figure 2.22 Scheme of Raman scattering mechanism.

2.3.5 X-ray techniques using synchrotron light

2.3.5.1 Synchrotron light sources

X-ray characterization occupies a large part of this Thesis so this section will describe in detail the concepts related with this technique. In this Thesis, all the experiments involving X-ray have been carried out in synchrotron facilities. Synchrotron radiation presents peculiar characteristics that differ from those of conventional X-ray sources. Synchrotron light is very brilliant, several orders of magnitude higher than X-ray produced in conventional X-ray tubes. Synchrotron light is very polarized (linear, elliptical or circular) and it is highly collimated (small angular divergence of the beam). It also has low emittance, i.e. the product of source cross section and solid angle of emission is small. Furthermore, synchrotron radiation covers the electromagnetic spectrum from nearly γ-rays to far infrared[67], and therefore , its energy (wavelength) can be tuned by appropriate monochromatization.

The synchrotron studies presented in this Thesis have been performed at third-generation synchrotron facilities. First-generation synchrotrons were dependent of original particle accelerators facilities. The second generation was the first built exclusively for synchrotron light production. The third generation implemented a new type of magnets to induce wiggle movement in the electrons in order to produce brighter light beams. Nowadays, third-generation of synchrotrons achieve around 10^{12} brighter beams of light than in early sources[68]. The fourth generation of synchrotrons will achieve ultra-low emittance of the electrons, yielding to higher brightness[69]. The ESRF-EBS in Grenoble (France), MAX IV laboratory in Lund (Sweden) and SIRIUS in Campinas (Brazil) will be some examples of the 4th-generation synchrotrons. Figure 2.23 shows a scheme with the main parts of a synchrotron facility.

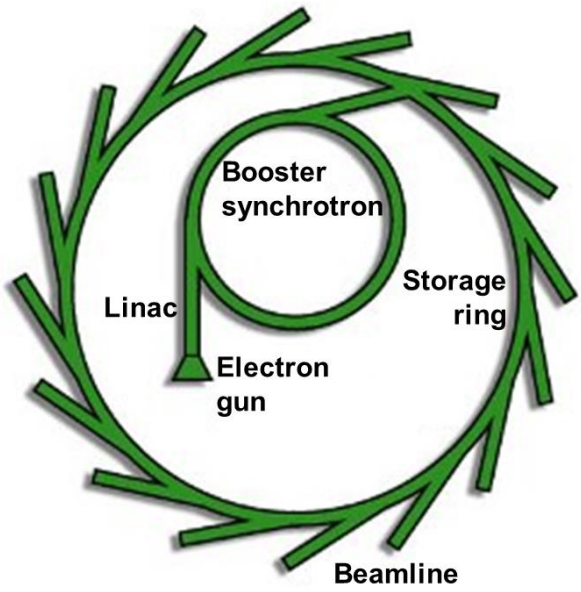

Figure 2.23 Main parts of a synchrotron radiation source. Adapted figure from Diamond synchrotron website[70].

The light generated in the synchrotron is radiated by electrons moving close to the speed of light inside the storage ring. These electrons are generated inside the "Electron gun" by heating a metal (tungsten impregnated of barium oxide (BaO)[71]). Then, they are first accelerated in a linear accelerator (LinAc) up to 100 MeV[71] and then injected to a first synchrotron, the booster ring, to be accelerated up to 3 GeV in the case of ALBA synchrotron, when they are injected into the larger storage ring. Different synchrotrons have different energy thresholds. The storage ring contains straight sections with a lattice of magnets, called insertion devices. There are two kinds of insertion devices: wigglers and undulators, both are composed of two matrix of magnets vertically separated. When the electrons pass between the magnets, they meander describing a small-amplitude oscillation in the horizontal plane. The radiation emitted by an electron in the first oscillation is in phase with the radiation from the next oscillations. Therefore, they emit a

cone of intense radiation beam towards the velocity vector tangent to the ring[68]. The emitted spectrum can be tuned by modifying the insertion devices[67].

The user-dedicated spaces, the beamlines, are built as branches tangent to the storage ring (Figure 2.23). Before the radiation reaches to the user's sample, the beam is channeled through monochromators, slits and different optic systems as X-ray mirrors and refractive Fresnel lenses located at the "optic hutch" (Figure 2.24) to obtain preferential features of the beam as a function of the different services of the beamline and the desired targets of the user.

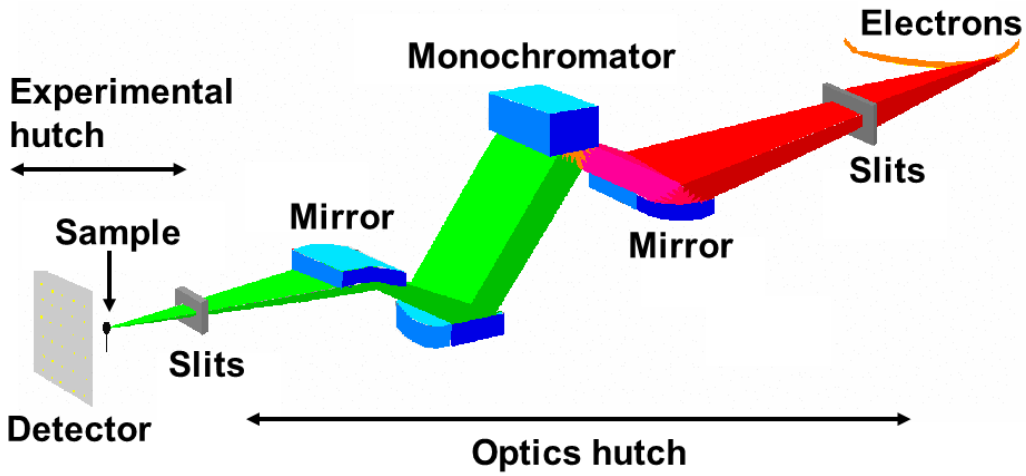

Figure 2.24 Scheme of the synchrotron radiation beam, through the optics hutch until it reaches the sample. Figure adapted from ESRF website[72].

For this Thesis, X-ray experiments have been carried out in two different synchrotron facilities. X-ray scattering measurements have been performed at ALBA synchrotron (Cerdanyola del Vallès, Barcelona, Spain) at beamline BL11 (NCD-SWEET) and at European Synchrotron Radiation Facililty (ESRF, Grenoble, France) at BM26 (DUBBLE, Dutch-Belgian Beamline). X-ray absorption experiments have been performed at ALBA synchrotron, at beamline BL29 (BOREAS).

2.3.5.2 Wide Angle and Small Angle X-ray Scattering (WAXS & SAXS)

Photons interact with matter by means of absorption or scattering. Scattering refers to the interaction of waves with atoms in which the wave is redirected in many directions[73]. Particles in the earth atmosphere scatter the sun light. The blue color in the sky is the result of selective scattering at a particular wavelength after absorption of the continuous of wavelengths emitted by the sun. Following classical electrodynamics, the incoming wave transfers energy to an electron, which oscillates and emits a new wave with the original energy (elastic scattering). According to

quantum mechanics, the new photon has not necessarily the same energy and is emitted with a certain scattering angle set by Compton equation (inelastic scattering). However, elastic scattering is usually a valid approximation in the study of matter through X-rays. The atoms of a material sample scatter the X-ray waves, primarily through the atoms' electrons, generating new waves with the same wavelength (λ). So the modulus of the wavenumber **k** is constant in the elastic scattering process (Equation 2.5).

$$|\boldsymbol{k}| = |\boldsymbol{k}'| = \frac{2\pi}{\lambda} \qquad (\mathbf{2.5})$$

The scattering vector **q** or wavevector transfer is defined as the difference between the incoming and the scattered wave vectors, which form an angle named as 2θ, i.e. the scattering angle (Equation 2.6 and Equation 2.7).

$$\boldsymbol{q} = \boldsymbol{k} - \boldsymbol{k}' \qquad (\mathbf{2.6})$$

$$|\boldsymbol{q}| = \sqrt{(\boldsymbol{k}-\boldsymbol{k}')(\boldsymbol{k}-\boldsymbol{k}')} = \sqrt{2|\boldsymbol{k}|^2(1-\cos 2\theta)} == \sqrt{2|\boldsymbol{k}|^2(1-1-2sin^2\theta)}$$
$$= \sqrt{4|\boldsymbol{k}|^2 sin^2\theta} = 2|k|\sin\theta = \frac{4\pi}{\lambda}\sin\theta \qquad (\mathbf{2.7})$$

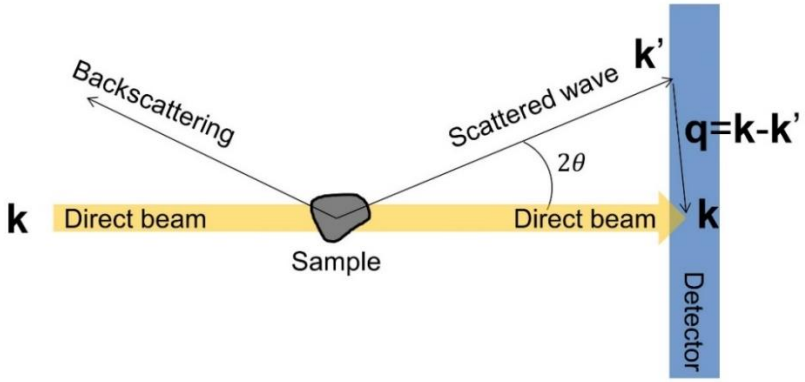

Figure 2.25 Scheme of scattering process between an electromagnetic wave and matter.

The meaning of scattering vector **q** is represented in Figure 2.25. Depending on their phase shift, these waves can cancel each other or add constructively. The requirement to the latter is that the atoms of the material are arranged in a periodical way: a crystal. The Bragg law[74], proposed by Bragg father and Bragg son in 1913, establishes a geometric condition for constructive interference between scattered waves (Equation 2.8).

$$n_I\lambda = 2d\sin\theta \qquad (\mathbf{2.8})$$

In Bragg equation (Equation 2.8), *d* is the distance between adjacent periodic planes in a crystal lattice, 2θ is the angle formed between the incoming wave and the scattered wave (Figure 2.25)

and n_I is an integer number. Through Bragg law, it is possible to know the characteristic periodic distance between atoms that makes constructive interference possible. Therefore, there is constructive interference if the Bragg condition is fulfilled, i.e. if the additional paths travelled by waves reflected by underlying periodic planes is equivalent to an integer number of wavelengths (Figure 2.26). A diffracted beam is composed of a huge number of scattered waves that reinforce between them.

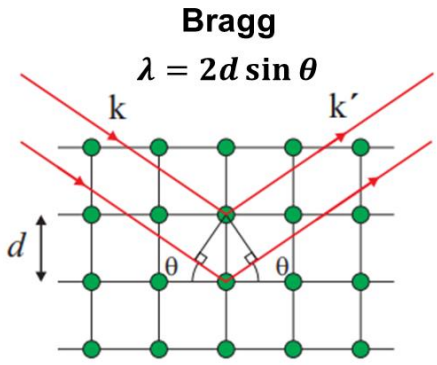

Figure 2.26 Condition for constructive interference between scattered waves as described by Bragg law. Figure adapted from reference[68].

Crystalline materials will concentrate the diffracted beams at particular angles related to crystallographic distances. Fluctuations of these distances due to crystalline defects will affect the scattering angles, giving rise to a distribution of intensity around the average angle related to the average distance. Therefore, the perfection of a crystal will be determined by the width of its scattering peaks, called Bragg peaks (Figure 2.27).

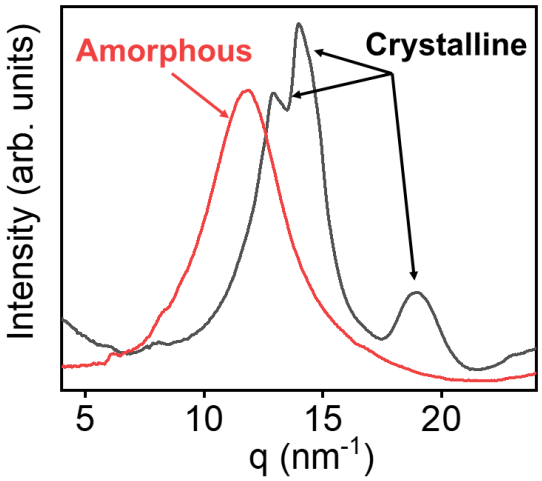

Figure 2.27 Diffractograms from a semicrystalline sample of PVDF (black curve) and from its corresponding amorphous molten state (red curve).

Amorphous materials, on the other hand, can be seen as an extreme deviation of a crystal and will show a broad maximum of scattering intensity (Figure 2.27) that corresponds to an average distance between the centers of mass of the scattering objects.

The position of a detected Bragg peak in the axis x, y or z of q is determined by the orientation and crystallographic distances of the multiple atomic layers that are scattering waves in a constructive way. This information –the average distance value between atoms and its orientation- can be packed through Fourier transform. Therefore, the Fourier transform of all real space coordinates of a crystal (known as the reciprocal space) contains a summary, so to speak, of the average distance between crystalline planes and orientations. This is the information present in a diffraction pattern. There is constructive interference between scattered waves when a point of the reciprocal space is at a distance of $|\mathbf{k}|$ from the sample (only elastic scattering is considered), i.e. when the sphere with center in the sample and radius $|\mathbf{k}|$ intersects with one point of the reciprocal space (associated with certain crystallographic indexes). Briefly, the information about the periodic arrangement of atoms inside a crystal is encoded mathematically in the reciprocal space. X-rays reveal the coordinates of the reciprocal space by projecting them over the surface of an abstract sphere called the Ewald sphere (Figure 2.28), which is itself projected over the detector.

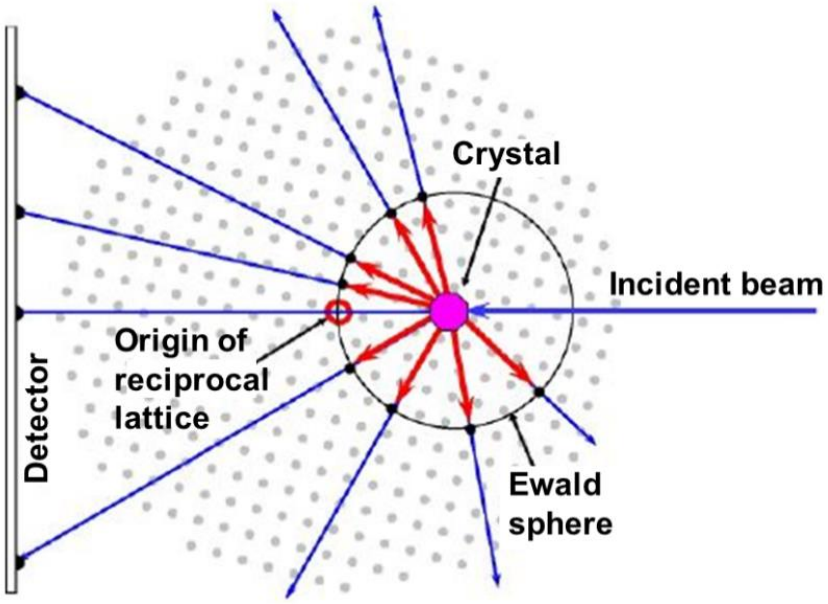

Figure 2.28 Representation of Ewald sphere. Figure adapted from website[75].

X-ray scattering experiments have been historically separated into wide-angle scattering angle range ($2\theta>1^{o}$) and small-angle ($2\theta<1^{o}$). It can be seen directly from Bragg law (Equation 2.8) that scattered angles 2θ and interplanar distances d follow an inverse relation. In WAXS experiments, scattered peaks are directly associated to correlations of the orders of a few Angstroms (0.01 nm

-1 nm). At small angle experiments (SAXS), lengths are associated with longer distances (1 nm - 500 nm). WAXS has been historically used to detect and analyze crystalline materials, whereas SAXS has been mostly related with the study of liquid dispersions, the shape and size of particles in colloids and in the case of polymers, the nanoscopic arrangement of the crystalline lamella in semicrystalline polymers, the study of block copolymers, gels and liquid crystals among others[67,76].

The scattered intensity is collected in a detector, in the form of a 2-dimensional map of pixels. The pixel coordinate basis can be transformed into scattered angles using simple trigonometry and knowing the pixel coordinates of the non-scattered beam (called the direct beam, which will be the origin in angles), the sample-detector distance (sdd) and the pixel size. Finally, the basis in angles can be transformed into scattered vector **q** by using the Bragg equation (Equation 2.9).

$$2\theta = atan\left(\frac{pixelsize \cdot \left(x_p - x_0\right)}{sdd}\right) \qquad (\mathbf{2.9})$$

In Equation 2.9, x_p is the coordinate of the pixel correspondent to 2θ and x_0 is the pixel of the direct beam. In transmission experiments, the incoming wave path is perpendicular to the sample, i.e. the beam passes through the sample.

In this Thesis, transmission X-ray experiments were performed on dispersions of PEDOT:PSS with different additives (see section 3.2) poured in glass capillaries and on nanoparticles of P3HT (see section 6.1). Dried nanoparticles from aqueous colloids were collected into an aluminum envelope, which was placed in the beam path.

2.3.5.3 X-ray scattering at Grazing-Incidence geometry (GIWAXS & GISAXS)

In this Thesis, a significant part of the samples were prepared over rigid substrates (e.g. silicon) and grazing-incidence geometry, instead of transmission geometry was used. In this geometry, the X-ray beam reaches the sample at an incident angle, usually between 0.15º and 0.4º from the substrate plane, because ~0.15º is the critical angle of the silicon at the wavelength used (~0.1 nm), and below this angle there is an excess of photons from the reflected beam. On the other hand, if we use a large incident angle (>0.4º), there could be an excess of photons scattered by the substrate itself. Therefore, intermediate angles are used, so that the beam can penetrate and be scattered by the material film but minimizing the penetration through the substrate. Figure 2.29 shows typical grazing-incidence geometry. α_i is the incident angle, i.e. the angle between the X-ray beam and the substrate plane of the sample.

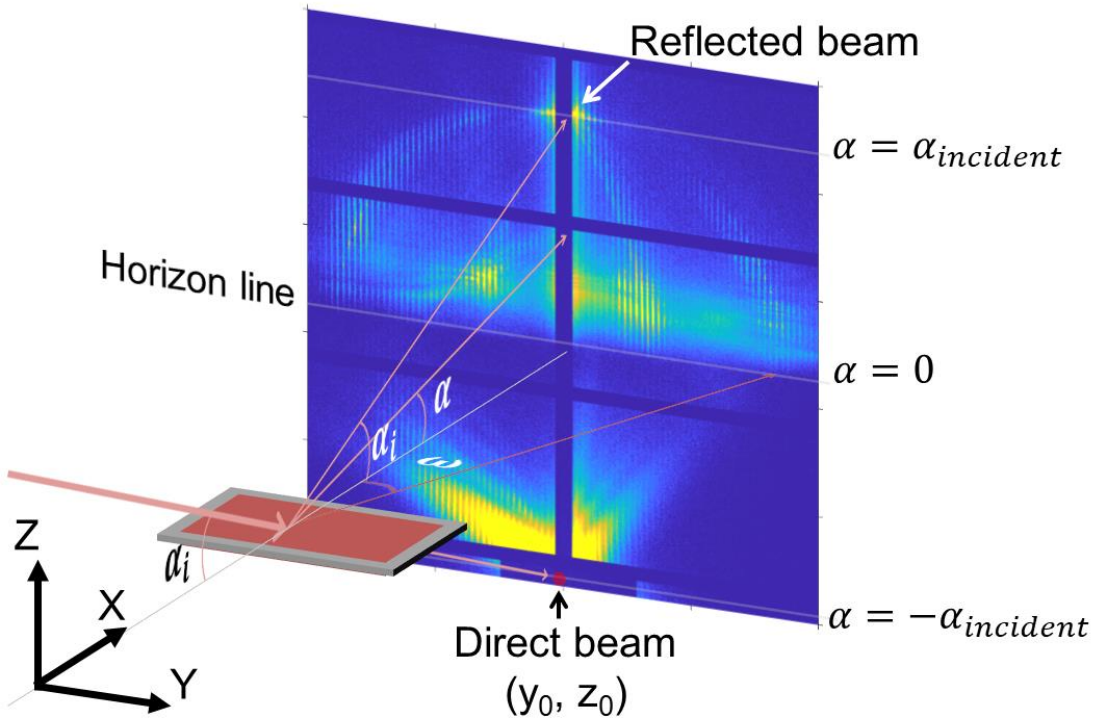

Figure 2.29 Typical geometry of a grazing incidence X-ray scattering experiment.

Exit angles α and ω can be inferred the same way as Equation 2.9 but taking the horizon line marked by the substrate as the origin α=0 (Equation 2.10).

$$\alpha = atan\left(\frac{pixelsize \cdot (z_p - z_0)}{sdd} - \tan\alpha_i\right) \cong atan\left(\frac{pixelsize \cdot (z_p - z_0)}{sdd}\right) - \alpha_i \quad (\mathbf{2.10})$$

pixelsize refers to the dimensions of the pixels of the detector. The approximation used in Equation 2.10 is valid for incident angles α_i=0.1-1º. For exit angle ω there is no offset angle (Equation 2.11).

$$\omega = atan\left(\frac{pixelsize \cdot (y_p - y_0)}{sdd}\right) \quad (\mathbf{2.11})$$

Finally, the Bragg law allows transforming the exit angles into **q**-vector 3D coordinates[67] (Equation 2.12).

$$\begin{pmatrix} q_x \\ q_y \\ q_z \end{pmatrix} = \frac{2\pi}{\lambda}\begin{pmatrix} \cos\alpha\cos\omega - \cos\alpha_i \\ \cos\alpha\sin\omega \\ \sin\alpha + \sin\alpha_i \end{pmatrix} \quad (\mathbf{2.12})$$

Equation 2.12 relates the three Cartesian components of the **q** vector with the angles α (scattering along the vertical direction –orthogonal from the polarization vector at synchrotrons-) and ω (scattering angle along the polarization vector direction –horizontal-). Obviously, flat detectors

generate flat patterns that are described with only two Cartesian components. However, in all the cases in this Thesis, pixel maps are transformed into 3D maps with q-components using Equation 2.12 and then projected into flat pictures with the wedge-shaped zones typical from an atlas (Figure 2.30).

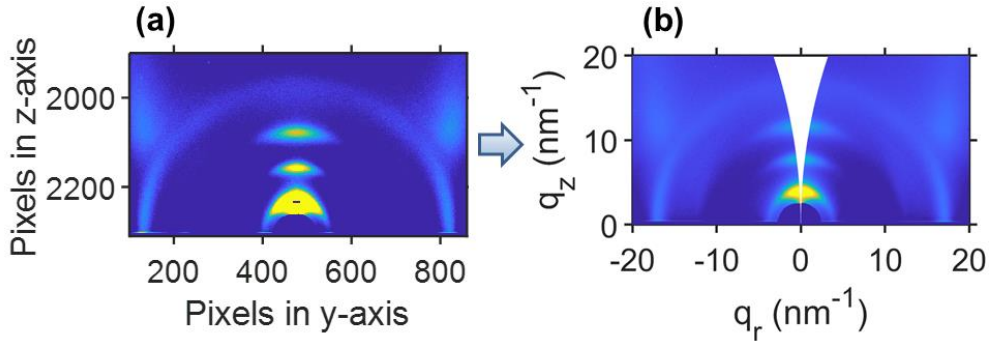

Figure 2.30 (a) GIWAXS pattern as pixel map and **(b)** transformed into q-coordinates using the 3D-transformation from Equation 2.12. $\boldsymbol{q_r} = \sqrt{\boldsymbol{q_x}^2 + \boldsymbol{q_y}^2}$.

As it was pointed out in section 2.3.5.2, in an X-ray scattering experiment, the information collected with a detector is a flat projection of the intersection between the Ewald sphere and the points of the reciprocal space. This effect must be taken into account during the processing of data. Other corrections are commonly used[77]. The solid angle correction corresponds to the higher sample-detector distances at higher scattered angles; this is another consequence of using flat detectors. The beam in a synchrotron facility is, in general, horizontally polarized and this influences the angular distribution of the scattered intensity. This is considered in the polarization correction[78].

2.3.5.4 Near Edge X-ray Absorption Fine Structure (NEXAFS)

NEXAFS is a technique that measures the absorption features of the material as a function of the incoming energy wave. The spectrum is taken near the edge of absorption of the core electron of a particular atom. The electrons that occupy the closest shell to the nucleus of an atom have a particular binding energy, called the K-edge. The absorption spectrum near the K-edge presents several peaks and features associated with electronic transitions from the core to an empty state near the photo-ionization threshold. This technique is sensitive to the chemical structure and to molecular orientation. In the case of polymers, absorption near the K-edge of carbon (~285eV), oxygen (~535 eV) or sulphur (~2474 eV) is a quite useful technique to identify different atomic bonds associated with a specific energy. NEXAFS is also called X-ray Absorption Near Edge Structure (XANES). The term NEXAFS is typically used for soft X-ray absorption spectra

(surface science, organic materials, etc) and XANES for hard X-ray spectra (coordination chemistry, metal atoms, etc). The soft X-ray spectrum covers from ~50 eV (25 nm) to 3000 eV (0.41 nm). In this range, the cross section of carbon photoabsorption dominates over scattering process[79]. The electric field vector **E** of synchrotron radiation produced by most bending magnets and undulator devices is linearly polarized in the plane of the storage ring. NEXAFS spectra show absorption peaks whose intensity is proportional to the cosine of the angle (**δ**) between the polarization vector of the beam (**E**) and the transition dipole vector (**O**)[80,81] (Equation 2.13).

$$I \propto (E \cdot O)^2 \propto cos^2\delta \qquad (\mathbf{2.13})$$

The **O** vector is oriented differently depending on the molecular orbital at which the core electron is excited. Single bonds between carbon atoms yield to σ molecular orbitals. The **O** vector of a transition to the unoccupied antibonding σ* molecular orbital is oriented parallel to the bond. However, carbon double bonds generate σ and π molecular orbitals. A transition to π* molecular orbital has its dipole vector oriented perpendicular to the bond, because the electronic cloud of π orbital is located out of the bonding plane. For instance, in a thiophene ring, the dipole vector **O** associated with this transition is oriented perpendicular to the aromatic ring (Figure 2.31). For this reason, NEXAFS is a very useful technique to analyze orientations in conjugated polymer thin films[82].

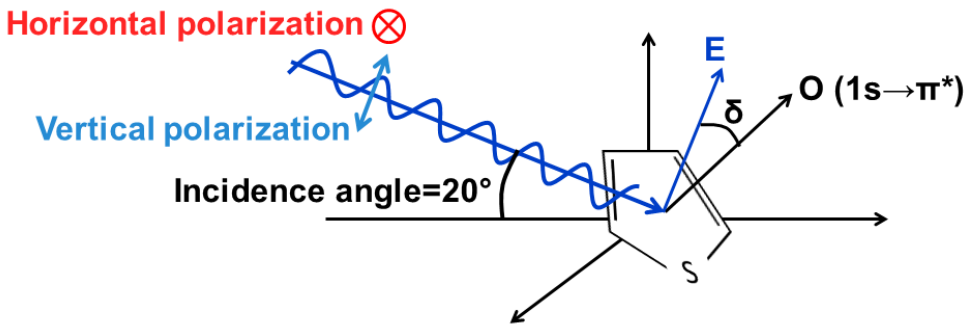

Figure 2.31 Scheme of incident polarization vector and transition dipole vector of the π* transition in P3HT.

Polarized soft X-ray allows visualizing and measuring the degree of linear dichroism in the surface sample. If the direction of a transition dipole vector is known, the dichroism can be used to infer a preferential molecular orientation. In this Thesis, the followed protocol consisted in measuring the NEXAFS spectra of the thin films using two polarizations of the beam (Figure 2.31). The incident angle between the beam and the substrate was set to 20º. Therefore, when the beam is horizontally polarized, the electric field vector lies in the substrate plane; and when the beam is vertically polarized, it means that the electric field vector is rotated 20º from the normal vector of the substrate.

In this Thesis, NEXAFS is used in electron yield mode: in this mode, the absorbed X-ray are not measured directly but instead the photoelectrons created by the absorbed X-ray. Specifically, we used the Total Electron Yield (TEY) mode, in which all the electrons that leave the sample are collected. These include Auger electrons created by the decay of other electrons into the empty core levels left by the original absorption, and all the secondary electrons with lower kinetic energy, as a consequence of loses due to scattering within the sample[80]. In this Thesis, TEY mode of NEXAFS technique is used to detect the linear dichroism of conjugated polymers (P3HT and PCDTBT) in thin films before and after laser structuring of the materials.

2.3.6 Contact Angle (CA)

Contact Angle (CA) technique quantifies the wettability of a surface. The degree of affinity between a solid and a certain liquid can be seen as the angle (φ) formed by one drop of the liquid over the solid surface. If there is a strong attractive interaction between both, the drop will spread maximizing the interfacial area, yielding to a low angle. A neutral or a repulsive interaction will avoid the spreading and the angle will be ninety degrees or higher (Figure 2.32).

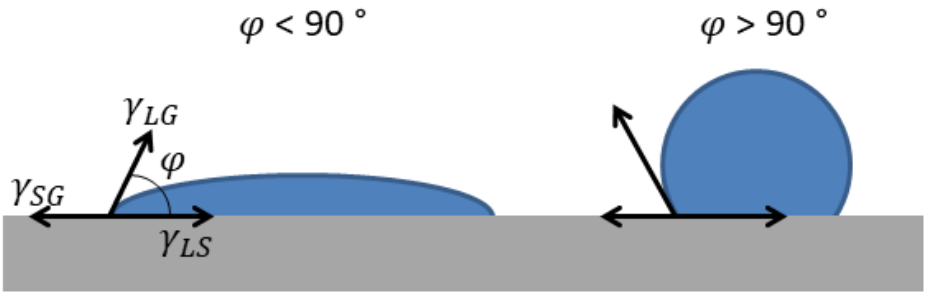

Figure 2.32 Scheme of interaction between solid and a probe liquid droplet.

The energy surface parameters of the solid are related to the contact angles through the Young equation (Equation 2.14).

$$\gamma_{SG} - \gamma_{SL} - \gamma_{LG}\cos\varphi = 0 \qquad (\mathbf{2.14})$$

In Equation 2.14, γ is the interfacial energy: SG solid-gas interface, LG liquid-gas interface and SL solid-liquid interface. From the contact angle measurements, it is possible to calculate the surface free energy by using different methodologies. In this Thesis, the Young-Dupre theory, later improved by van Oss, Chaudhury and Good[83,84], was used. This model gives information on the Liftshitz-van der Waals and electron-donor components, allowing the assessment of both apolar and polar interactions respectively. To that purpose, Equation 2.15 is used.

$$\gamma_l(1+\cos\varphi) = 2\sqrt{\gamma_s{}^d\gamma_l{}^d} + 2\sqrt{\gamma_s{}^+\gamma_l{}^-} + 2\sqrt{\gamma_s{}^-\gamma_l{}^+} \qquad (\mathbf{2.15})$$

γ_s^+ and γ_l^+ are the electron-acceptor, while γ_s^- and γ_l^- are the electron-donor components of the surface free energy of solid and liquid respectively. The term γ_s^d of a solid surface is calculated using the CA value of an apolar liquid as a probe. The total liquid free energy is the sum of the apolar component and the polar one. Since for apolar liquids $\gamma_l^+=\gamma_l^-=0$, then $\gamma_l=\gamma_d$. In this case, Equation 2.15 can be rewritten as Equation 2.16.

$$\gamma_s{}^d = \gamma_l(1+\cos\varphi)^2/4 \qquad (\mathbf{2.16})$$

In order to calculate the surface energy values, the contact angle of at least three different liquids over the material must be measured. In this Thesis, the use of paraffin oil as apolar liquid allows to calculate the apolar component of the solid γ_s^d in first term, employing the values of the surface free energy components compiled in Table 2.1. Once γ_s^d is known, the unknown values of γ_s^+ and γ_s^- are calculated by solving Equation 2.15 for the pair water-glycerol, using again the corresponding parameters compiled in Table 2.1. Finally, to determine the total surface energy of the sample film (γ_s), Equation 2.17 and Equation 2.18 are used, which relate the total surface energy with dispersion (γ_s^d) and acid-base (γ_s^p) components.

$$\gamma_s = \gamma_s{}^d + \gamma_s{}^p \qquad (\mathbf{2.17})$$

$$\gamma_s{}^p = 2\sqrt{\gamma_s{}^+\gamma_s{}^-} \qquad (\mathbf{2.18})$$

Table 2.1 Surface free energy components of the liquid probes. The units are $mJ\cdot m^{-2}$. γ_l is the total surface energy, γ_l^d is the apolar component, γ_l^p is the polar component, γ_l^+ is the electron-acceptor component and γ_l^- is the electron-donor component of the surface free energy.

Liquid	γ_l	γ_l^d	γ_l^p	γ_l^+	γ_l^-
Water	72.8	21.8	51	25.5	25.5
Glycerol	64	34	30	3.92	57.4
Paraffin Oil	28.9	28.9	0	0	0

In this Thesis, contact angle experiments have been approached to evaluate or to reinforce proposed models related to ferroelectric behavior in ferroelectric-semiconductor bilayer systems. CA measurements were carried out at room temperature and ambient humidity using a pocket goniometer PG2 (FIBRO system)[85]. The CA values were determined by the sessile drop technique. Two polar liquids, water and glycerol, and one apolar liquid, paraffin oil, were chosen. During measurements, a droplet of each liquid probe with a volume of around 5 µL was deposited on a dry and clean polymer surface. Static CA values were measured immediately after the formation of sessile drops of liquid on the surface.

2.4 Experimental details

2.4.1 Preparation of substrates

Two rigid substrates were used to deposit the materials: silicon and ITO-coated glass. Properties of the substrates and suppliers are compiled in Table 2.2.

Table 2.2 Substrates used in this Thesis including their supplier and thickness.

Substrate	Supplier	Thickness
Silicon n-doped (arsenic) (100) double-side polished	Neyco (France)	525 ± 20 µm
Unpatterned ITO-covered glass	Ossila Ltd. (UK)	100 nm (ITO) + 1 mm (glass)

The sample is deposited on the substrate from a solution or from an aqueous dispersion. Depending on the substrate used and the solvent, different protocols are followed to clean the substrate surface and to improve the thin film formation.

Materials solved in organic solvents have been deposited on silicon substrates. Before deposition procedure, in order to remove residual organic particles, silicon substrates were cleaned following the protocol described in Table 2.3. In the case of aqueous dispersions deposited over ITO, the same cleaning protocol is performed.

Table 2.3 Protocol for cleaning of silicon and ITO substrates.

Steps	
1	Sonication: 10’ in acetone
2	Sonication: 10’ in isopropyl alcohol (IPA)
3	Rinsing with deionized water
4	Drying with nitrogen blow

Prior to depositing aqueous dispersions over silicon, the substrates are cleaned and submerged in piranha solution in order to enhance their wettability (i.e. the compatibility between the substrate surface and water). Piranha solution adds hydroxyl groups (OH) to the surface of silicon, enhancing its hydrophilicity. The cleaning and treatment protocol with piranha solution for silicon substrates are included in Table 2.4.

Table 2.4 Protocol for cleaning and piranha treatment of silicon substrates.

Steps	
1	Sonication: 10’ in acetone
2	Sonication: 10’ in IPA
3	Rinsing with deionized water
4	30’ in piranha solution: H_2SO_4:H_2O_2 (3:1)
5	Rinsing with deionized water
6	Drying with nitrogen blow

2.4.2 Material details

The functional materials investigated in this Thesis are presented in section 1.4: four semiconducting materials (P3HT, PCDTBT, $PC_{71}BM$ and PEDOT:PSS) and two ferroelectric polymers (PVDF and P(VDF-TrFE)). Material properties and supplier of P3HT, PCDTBT and $PC_{71}BM$ are listed in Table 2.5. Similar and additional useful information exclusively about PEDOT:PSS is included in Table 2.6. Material properties and supplier of PVDF and P(VDF-TrFE) are compiled in Table 2.7.

Table 2.5 Details of P3HT, PCDTBT and $PC_{71}BM$ including weight average molecular weight (M_w), number average molecular weight (M_n), polydispersity index (PDI) and regioregularity (RR).

Material	P3HT		PCDTBT	$PC_{71}BM$
Company	Ossila Ltd. (UK)			
Batch	M102	M106	M139	M114
M_w (g·mol^{-1})	65200	34100	35400	-
M_n (g·mol^{-1})	29600	19500	14750	1031
PDI	2.20	1.75	2.4	-
RR	95.7 %	94.7 %	-	-
Others	-	-	-	Purity > 99 %

Table 2.6 Details of PEDOT:PSS including D_{90} and D_{50} values (D_x corresponds to the upper value of a colloidal distribution in which x % of the particles have diameters below D_x)

Material	PEDOT:PSS
Company	Ossila Ltd. (UK)
Batch	AI 4083
Resistivity (Ω·cm)	500-5000
Weight in water (% wt)	1.3-1.7
Viscosity (mPa·s)	5-12
PEDOT/PSS ratio	0.167
D_{90} (nm)	100
D_{50} (nm)	80
Work function (eV)	5.0-5.2

Table 2.7 Details of ferroelectric polymers including weight average molecular weight (M_w), glass transition temperature (T_g), melting temperature (T_m).

Material	PVDF	P(VDF-TrFE)
Company	Sigma-Aldrich	Piézotech S.A.S.
Batch	182702	-
M_w (g·mol^{-1})	534000	367000
T_g (ºC)	-38	~ -30ºC [86]
T_m (ºC)	171	150
Others	-	VDF/TrFE ratio ≈ 76/24

2.4.3 Preparation of solutions

Most of the samples studied in this Thesis consist of deposits of the material of study on a rigid substrate. The materials have been previously solved in organic solvents or, in the case of PEDOT:PSS, it is supplied in the form of an aqueous dispersion (see section 1.4.4). Conditions

for preparations of solutions of P3HT, PCDTBT, $PC_{71}BM$, PVDF and P(VDF-TrFE) employed to fabricate either supported thin films or nanoparticles (NPs) are displayed in Table 2.8.

Table 2.8 Details for preparation of solutions of P3HT, PCDTBT, $PC_{71}BM$, PVDF and P(VDF-TrFE) used to fabricate thin films or nanoparticles together with the section of this Thesis in which the corresponding system is studied. The organic solvents used in this Thesis are chloroform ($CHCl_3$), chlorobenzene (C_6H_5Cl), tetrahydrofuran (THF), methyl ethyl ketone (MEK) and N,N-Dimethylacetamide (DMA).

Solution						
Solute	**Batch**	**Solvent**	**Concentration ($g \cdot L^{-1}$)**	**Stirring time and temperature**	**Sample form**	**Section**
P3HT	M102	$CHCl_3$	8-20	1 h – 40 ºC	Supported thin film	3.1
	M102	$CHCl_3$	16	1 h – 40 ºC	Supported thin film	4.3
	M106	C_6H_5Cl	24	1 h - Room T.	Supported thin film	4.2
	M102	$CHCl_3$	3	1 h – 40 ºC	Miniemulsion NPs	6.1
	M102	THF	3	2 h – 66 ºC	Flash NPs	6.1
PCDTBT	M139	C_6H_5Cl	24	1 h - Room T.	Supported thin film	4.2
$PC_{71}BM$	M114	C_6H_5Cl	40	1 h - Room T.	Supported thin film	4.4
P(VDF-TrFE)	-	MEK	5	3 h – 72 ºC	Supported thin film	3.1 4.3
		THF	1	2 h – 60 ºC	Flash NPs	6.3
PVDF	182702	DMA	2	1 h - Room T.	Dialysis NPs	6.2

Before the deposition, the PEDOT:PSS dispersion is treated following the protocols described in Table 2.9.

Table 2.9 Details for preparation of dispersions of PEDOT:PSS with the original concentration, blended with additives and concentrated, together with the section of this Thesis that deals with the corresponding PEDOT:PSS system.

PEDOT:PSS dispersions			
Dispersion	**Concentration (wt. % in water)**	**Preparation**	**Section**
PEDOT:PSS original	1.3 – 1.7	1. Filtration through 0.2 µm cellulose filter. 2. Sonication for 5'.	3.2 3.3 4.1
PEDOT:PSS blended with additives	1.3 – 1.7 + x wt. % between the water and the additive	1. Filtration through 0.2 µm cellulose filter. 2. Mixing with the additive. 3. Sonication for 5'.	3.2
PEDOT:PSS concentrated	2.6 - 3.4	1. Filtration through 0.2 µm cellulose filter. 2. Stirring at 100 ºC until getting half of the original volume. 3. Storage in the fridge for 24 hours.	4.1
PEDOT:PSS concentrated with glycerol	2.6 - 3.4 + x wt. % between the water and glycerol	1. Filtration through 0.2 µm cellulose filter. 2. Stirring at 100 ºC until getting half of the original volume. 3. Storage in the fridge for 24 hours. 4. Mixing concentrated PEDOT:PSS with glycerol. 5. Sonication for 5'.	Chapter 5

2.4.4 Spin-coating conditions

The spin-coating conditions employed for the deposition of samples are listed in Table 2.10.

Table 2.10 Spin-coating parameters used for the preparation of thin films, along with the substrate used for every system, the approximated value of the thickness of the resulting thin film and the section of the Thesis where the corresponding system is studied. The additives blended with PEDOT:PSS are ethylene glycol (EG), glycerol (G) and dimethyl sulfoxide (DMSO).

Spin-coating						
Solution/Dispersion	**Time (s)**	**Speed (rpm)**	**Acceleration (rpm·s^{-1})**	**Substrate**	**Thickness (nm)**	**Section**
P3HT in $CHCl_3$	120	2400	11300	Silicon	≈ 70-170*	3.1, 4.3
P3HT in C_6H_5Cl				Silicon	≈ 150	4.2
PCDTBT				Silicon	≈ 180	4.2
$PC_{71}BM$				Silicon	80-100	4.4
P(VDF-TrFE)				Silicon / P3HT thin film†	≈ 20	3.1, 4.2
PEDOT:PSS original	60	3000	3000	Silicon / ITO	60 ± 10	3.2, 4.1
PEDOT:PSS + EG	60	2000	2000	Silicon	≈**	3.2
PEDOT:PSS + G	60	3000	3000		≈**	3.2
PEDOT:PSS + G + DMSO	60	2000	2000		≈**	3.2
PEDOT:PSS concentrated	60	3000	3000		160 ± 10	4.1
PEDOT:PSS concentrated + G					≈***	Chapter 6

†The solvent for P(VDF-TrFE), MEK, had not any effect on P3HT[87].

*The thicknesses of P3HT thin films fabricated from solution in $CHCl_3$ prepared following the protocol from Table 2.8 and using spin-coating conditions from Table 2.10 are displayed in Table 2.11.

**The concentrations of the additives blended with PEDOT:PSS and the thickness of their corresponding thin films are part of the discussed results in section 3.2. The boiling points of the different additives mixed with PEDOT:PSS dispersions are compiled in Table 2.12.

***The concentrations of G blended with concentrated PEDOT:PSS and their corresponding thin films are part of the discussed results in Chapter 5.

Table 2.11 Thickness obtained for P3HT thin films using solution and spin-coating conditions included in Table 2.8 and Table 2.10 respectively.

Concentration ($g \cdot L^{-1}$)	Thickness (nm)
8	67 ± 5
12	112 ± 8
16	131 ± 8
20	171 ± 9

Table 2.12 Boiling point of additives mixed with PEDOT:PSS dispersions and investigated in section 3.2.

Solvent	EG	G	DMSO
Boiling point (ºC)	198	290	189

The boiling temperature of the additive is determinant because it may resist the spin-coating step and remain in the film. Thermal annealing at T=140 ºC for 10 minutes was performed for each sample in order to remove the remains of the solvent after spin-coating.

2.4.5 Inkjet printing conditions

Furthermore, as presented in section 3.3, PEDOT:PSS is also deposited by inkjet printing. The PEDOT:PSS dispersion was injected in a cartridge of an Inkjet printer (Dimatix 2831, Fujifilm, USA). The viscosity of the dispersion was 4.32 cP at 10 rpm as determined by a Cone/Plate (CPE-40) version of a Brookfield DV-I Prime Viscosimeter at room temperature. Taking into account the specifications of the printer, the viscosity value was suitable for the formation and ejection of stable droplets at room temperature. No additives were added. The droplet volume was fixed at 10 pL. Continuous lines patterns of about 25 µm width were printed forming squared layers of approximately 1x1 cm^2, covering the whole substrate surface. The number of layers deposited was 1, 2, 3 and 4. After inkjet printing process the samples were heat treated at 50ºC for two hours to eliminate the water. The relative humidity (RH) and temperature were measured using a

temperature and RH data logger (EL-USB-2-LCD, Lascar Electronics). The values obtained are 28 ± 1% and 21 ± 0.5ºC respectively.

2.5 References

(1) Deegan, R. D.; Bakajin, O.; Dupont, T. F.; Huber, G.; Nagel, S. R.; Witten, T. A. Contact Line Deposits in an Evaporating Drop. *Phys. Rev. E - Stat. Physics, Plasmas, Fluids, Relat. Interdiscip. Top.* **2000**, *62* (1 B), 756–765. https://doi.org/10.1103/PhysRevE.62.756.

(2) Yunker, P. J.; Still, T.; Lohr, M. A.; Yodh, A. G. Suppression of the Coffee-Ring Effect by Shape-Dependent Capillary Interactions. *Nature* **2011**, *476* (7360), 308–311. https://doi.org/10.1038/nature10344.

(3) Hall, D. B.; Underhill, P.; Torkelson, J. M. Spin Coating of Thin and Ultrathin Polymer Films. *Polym. Eng. Sci.* **1998**, *38* (12), 2039–2045. https://doi.org/10.1002/pen.10373.

(4) https://www.ossila.com/pages/spin-coating#spin-coating-general-theory.

(5) Ludwigs, S. *P3HT Revisited – From Molecular Scale to Solar Cell Devices*; 2014; Vol. 265. https://doi.org/10.1007/978-3-662-45145-8.

(6) Gburek, B.; Wagner, V. Influence of the Semiconductor Thickness on the Charge Carrier Mobility in P3HT Organic Field-Effect Transistors in Top-Gate Architecture on Flexible Substrates. *Org. Electron. physics, Mater. Appl.* **2010**, *11* (5), 814–819. https://doi.org/10.1016/j.orgel.2010.01.023.

(7) Yang, H.; Lefevre, S. W.; Ryu, C. Y.; Bao, Z. Solubility-Driven Thin Film Structures of Regioregular Poly(3-Hexyl Thiophene) Using Volatile Solvents. *Appl. Phys. Lett.* **2007**, *90* (17), 1–4. https://doi.org/10.1063/1.2734387.

(8) Eom, S. H.; Senthilarasu, S.; Uthirakumar, P.; Yoon, S. C.; Lim, J.; Lee, C.; Lim, H. S.; Lee, J.; Lee, S. H. Polymer Solar Cells Based on Inkjet-Printed PEDOT:PSS Layer. *Org. Electron. physics, Mater. Appl.* **2009**, *10* (3), 536–542. https://doi.org/10.1016/j.orgel.2009.01.015.

(9) Sirringhaus, H.; Kawase, T.; Friend, R. H.; Shimoda, T.; Inbasekaran, M.; Wu, W.; Woo, E. P. High-Resolution Inkjet Printing of All-Polymer Transistor Circuits. *Science.* **2000**, *290* (5499), 2123–2126. https://doi.org/10.1126/science.290.5499.2123.

(10) De Gans, B. J.; Duineveld, P. C.; Schubert, U. S. Inkjet Printing of Polymers: State of the Art and Future Developments. *Adv. Mater.* **2004**, *16* (3), 203–213. https://doi.org/10.1002/adma.200300385.

(11) Vescio, G.; López-Vidrier, J.; Leghrib, R.; Cornet, A.; Cirera, A. Flexible Inkjet Printed High-k HfO2-Based MIM Capacitors. *J. Mater. Chem. C* **2016**, *4* (9), 1804–1812. https://doi.org/10.1039/c5tc03307a.

(12) Calvert, P. Inkjet Printing for Materials and Devices. *Chem. Mater.* **2001**, *13* (10), 3299–3305. https://doi.org/10.1021/cm0101632.

(13) Vaezi, M.; Seitz, H.; Yang, S. A Review on 3D Micro-Additive Manufacturing Technologies. *Int. J. Adv. Manuf. Technol.* **2013**, *67* (5–8), 1721–1754. https://doi.org/10.1007/s00170-012-4605-2.

(14) Hoth, C. N.; Choulis, S. A.; Schilinsky, P.; Brabec, C. J. High Photovoltaic Performance of Inkjet Printed Polymer:Fullerene Blends. *Adv. Mater.* **2007**, *19* (22), 3973–3978. https://doi.org/10.1002/adma.200700911.

(15) Basiric, L.; Cosseddu, P.; Scidà, A.; Fraboni, B.; Malliaras, G. G.; Bonfiglio, A. Electrical Characteristics of Ink-Jet Printed, All-Polymer Electrochemical Transistors. *Org. Electron. physics, Mater. Appl.* **2012**, *13* (2), 244–248. https://doi.org/10.1016/j.orgel.2011.11.010.

(16) Eom, S. H.; Park, H.; Mujawar, S. H.; Yoon, S. C.; Kim, S. S.; Na, S. I.; Kang, S. J.; Khim, D.; Kim, D. Y.; Lee, S. H. High Efficiency Polymer Solar Cells via Sequential Inkjet-Printing of PEDOT:PSS and P3HT:PCBM Inks with Additives. *Org. Electron. physics, Mater. Appl.* **2010**, *11* (9), 1516–1522. https://doi.org/10.1016/j.orgel.2010.06.007.

(17) Mannerbro, R.; Ranlöf, M.; Robinson, N.; Forchheimer, R. Inkjet Printed Electrochemical Organic Electronics. *Synth. Met.* **2008**, *158* (13), 556–560. https://doi.org/10.1016/j.synthmet.2008.03.030.

(18) Afonso, M.; Morgado, J.; Alcácer, L. Inkjet Printed Organic Electrochemical Transistors with Highly Conducting Polymer Electrolytes. *J. Appl. Phys.* **2016**, *120* (16), 165502. https://doi.org/10.1063/1.4966651.

(19) Jung, S.; Sou, A.; Gili, E.; Sirringhaus, H. Inkjet-Printed Resistors with a Wide Resistance Range for Printed Read-Only Memory Applications. *Org. Electron. physics, Mater. Appl.* **2013**, *14* (3), 699–702. https://doi.org/10.1016/j.orgel.2012.12.034.

(20) Seekaew, Y.; Lokavee, S.; Phokharatkul, D.; Wisitsoraat, A.; Kerdcharoen, T.; Wongchoosuk, C. Low-Cost and Flexible Printed Graphene-PEDOT:PSS Gas Sensor for Ammonia Detection. *Org. Electron. physics, Mater. Appl.* **2014**, *15* (11), 2971–2981. https://doi.org/10.1016/j.orgel.2014.08.044.

(21) Borghetti, M.; Serpelloni, M.; Sardini, E.; Pandini, S. Mechanical Behavior of Strain Sensors Based on PEDOT:PSS and Silver Nanoparticles Inks Deposited on Polymer Substrate by Inkjet Printing. *Sensors Actuators, A Phys.* **2016**, *243*, 71–80. https://doi.org/10.1016/j.sna.2016.03.021.

(22) Mun, R. P.; Byars, J. A.; Boger, D. V. The Effects of Polymer Concentration and Molecular Weight on the Breakup of Laminar Capillary Jets. *J. Nonnewton. Fluid Mech.* **1998**, *74* (1–3), 285–297. https://doi.org/10.1016/S0377-0257(97)00074-8.

(23) Birnbaum, M. Semiconductor Surface Damage Produced by Ruby Lasers. *J. Appl. Phys.* **1965**, *36* (11), 3688–3689. https://doi.org/10.1063/1.1703071.

(24) Rebollar, E.; Castillejo, M.; Ezquerra, T. A. Laser Induced Periodic Surface Structures on Polymer Films: From Fundamentals to Applications. *Eur. Polym. J.* **2015**, *73*, 162–174. https://doi.org/10.1016/j.eurpolymj.2015.10.012.

(25) Rebollar, E.; Vázquez de Aldana, J. R.; Martín-Fabiani, I.; Hernández, M.; Rueda, D. R.; Ezquerra, T. A.; Domingo, C.; Moreno, P.; Castillejo, M.; Pereira, A.; et al. Assessment of Femtosecond Laser Induced Periodic Surface Structures on Polymer Films. *Phys. Chem. Chem. Phys.* **2013**, *15* (27), 11287. https://doi.org/10.1039/c3cp51523k.

(26) Young, J. F.; Preston, J. S.; Van Driel, H. M.; Sipe, J. E. Laser-Induced Periodic Surface Structure. II. Experiments on Ge, Si, Al, and Brass. *Phys. Rev. B* **1983**, *27* (2), 1155–1172. https://doi.org/10.1103/PhysRevB.27.1155.

(27) Guosheng, Z.; Fauchet, P. M.; Siegman, A. E. Growth of Spontaneous Periodic Surface Structures on Solids during Laser Illumination. *Phys. Rev. B* **1982**, *26* (10), 5366–5381. https://doi.org/10.1103/PhysRevB.26.5366.

(28) Rebollar, E.; Vázquez De Aldana, J. R.; Pérez-Hernández, J. A.; Ezquerra, T. A.; Moreno, P.; Castillejo, M. Ultraviolet and Infrared Femtosecond Laser Induced Periodic Surface Structures on Thin Polymer Films. *Appl. Phys. Lett.* **2012**, *100* (4), 041106. https://doi.org/10.1063/1.3679103.

(29) Sipe, J. E.; Young, J. F.; Preston, J. S.; Van Driel, H. M. Laser-Induced Periodic Surface Structure. I. Theory. *Phys. Rev. B* **1983**, *27* (2), 1141–1154. https://doi.org/10.1103/PhysRevB.27.1141.

(30) Bolle, M.; Lazare, S. Submicron Periodic Structures Produced on Polymer Surfaces with Polarized Excimer Laser Ultraviolet Radiation. *Appl. Surf. Sci.* **1992**, *65–66*, 349–354. https://doi.org/10.1016/0169-4332(93)90684-4.

(31) Bolle, M.; Lazare, S. Large Scale Excimer Laser Production of Submicron Periodic Structures on Polymer Surfaces. *Appl. Surf. Sci.* **1993**, *69* (1–4), 31–37. https://doi.org/10.1016/0169-4332(93)90478-T.

(32) Bolle, M.; Lazare, S. Characterization of Submicrometer Periodic Structures Produced on Polymer Surfaces with Low-Fluence Ultraviolet Laser Radiation. *J. Appl. Phys.* **1993**, *73* (7), 3516–3524. https://doi.org/10.1063/1.352957.

(33) Lazare, S.; Drilhole, D. Submicrometre Ablation on Polymer Surfaces. *J. Photochem. Photobiol. A Chem.* **1997**, *106* (1–3), 15–20. https://doi.org/10.1016/S1010-6030(97)00032-4.

(34) Csete, M.; Marti, O.; Bor, Z. Laser-Induced Periodic Surface Structures on Different Poly-Carbonate Films. *Appl. Phys. A Mater. Sci. Process.* **2001**, *73* (4), 521–526. https://doi.org/10.1007/s003390100973.

(35) Csete, M.; Bor, Z. Laser-Induced Periodic Surface Structure Formation on Polyethylene-Terephthalate. *Appl. Surf. Sci.* **1998**, *133* (1–2), 5–16. https://doi.org/10.1016/S0169-4332(98)00192-5.

(36) Glynn, T.; Sherlock, R.; Prendergast, Ú.; Kudzma, S.; O'Connell, C. TEM Investigation of Laser-Induced Periodic Surface Structures on Polymer Surfaces. *Phot. Process. Microelectron. Photonics VI* **2007**, *6458*, 64581V. https://doi.org/10.1117/12.699999.

(37) Cui, J.; Nogales, A.; Ezquerra, T. A.; Rebollar, E. Influence of Substrate and Film Thickness on Polymer LIPSS Formation. *Appl. Surf. Sci.* **2017**, *394*, 125–131. https://doi.org/10.1016/j.apsusc.2016.10.045.

(38) Bäuerle, D. Laser Processing and Chemistry: Recent Developments. *Appl. Surf. Sci.* **2002**, *186* (1–4), 1–6.

(39) Guo, L. J. Nanoimprint Lithography: Methods and Material Requirements. *Adv. Mater.* **2007**, *19* (4), 495–513. https://doi.org/10.1002/adma.200600882.

(40) Chou, S. Y.; Krauss, P. R.; Renstrom, P. J. Imprint of Sub-25 Nm Vias and Trenches in Polymers. *Appl. Phys. Lett.* **1995**, *67*, 3114. https://doi.org/10.1063/1.114851.

(41) Michel, B.; Schmid, H. Siloxane Polymers for High-Resolution, High-Accuracy Soft Lithography. *Macromolecules* **2000**, *33* (8), 3042–3049. https://doi.org/10.1021/ma982034l.

(42) D'Addio, S. M.; Prud'homme, R. K. Controlling Drug Nanoparticle Formation by Rapid Precipitation. *Adv. Drug Deliv. Rev.* **2011**, *63* (6), 417–426. https://doi.org/10.1016/j.addr.2011.04.005.

(43) Flory, P. J.; Volkenstein, M. Statistical Mechanics of Chain Molecules. Wiley Online Library 1969.

(44) Rao, J. P.; Geckeler, K. E. Polymer Nanoparticles: Preparation Techniques and Size-Control Parameters. *Prog. Polym. Sci.* **2011**, *36* (7), 887–913. https://doi.org/10.1016/j.progpolymsci.2011.01.001.

(45) Fudouzi, H.; Xia, Y. Photonic Papers and Inks: Color Writing with Colorless Materials. *Adv. Mater.* **2003**, *15* (11), 892–896. https://doi.org/10.1002/adma.200304795.

(46) Rose, S.; Prevoteau, A.; Elzière, P.; Hourdet, D.; Marcellan, A.; Leibler, L. Nanoparticle Solutions as Adhesives for Gels and Biological Tissues. *Nature* **2014**, *505* (7483), 382–385. https://doi.org/10.1038/nature12806.

(47) Kamaly, N.; Xiao, Z.; Valencia, P. M.; Radovic-Moreno, A. F.; Farokhzad, O. C. Targeted Polymeric Therapeutic Nanoparticles: Design, Development and Clinical Translation. *Chem. Soc. Rev.* **2012**, *41* (7), 2971–3010. https://doi.org/10.1039/c2cs15344k.

(48) Li, J.; Rao, J.; Pu, K. Recent Progress on Semiconducting Polymer Nanoparticles for Molecular Imaging and Cancer Phototherapy. *Biomaterials* **2018**, *155*, 217–235. https://doi.org/10.1016/j.biomaterials.2017.11.025.

(49) Crucho, C. I. C. Stimuli-Responsive Polymeric Nanoparticles for Nanomedicine. *ChemMedChem* **2015**, *10* (1), 24–38. https://doi.org/10.1002/cmdc.201402290.

(50) Tran, N. T. D.; Truong, N. P.; Gu, W.; Jia, Z.; Cooper, M. A.; Monteiro, M. J. Timed-Release Polymer Nanoparticles. *Biomacromolecules* **2013**, *14* (2), 495–502. https://doi.org/10.1021/bm301721k.

(51) Xiao, Z.; Dong, Q.; Sharma, P.; Yuan, Y.; Mao, B.; Tian, W.; Gruverman, A.; Huang, J. Synthesis and Application of Ferroelectric P(VDF-TrFE) Nanoparticles in Organic Photovoltaic Devices for High Efficiency. *Adv. Energy Mater.* **2013**, *3* (12), 1581–1588. https://doi.org/10.1002/aenm.201300396.

(52) Zhang, C.; Chung, J. W.; Priestley, R. D. Dialysis Nanoprecipitation of Polystyrene Nanoparticles. *Macromol. Rapid Commun.* **2012**, *33* (20), 1798–1803. https://doi.org/10.1002/marc.201200335.

(53) Landfester, K.; Montenegro, R.; Scherf, U.; Güntner, R.; Asawapirom, U.; Patil, S.; Neher, D.; Kietzke, T. Semiconducting Polymer Nanospheres in Aqueous Dispersion Prepared by a Miniemulsion Process. *Adv. Mater.* **2002**, *14* (9), 651–655. https://doi.org/10.1002/1521-4095(20020503)14:9<651::AID-ADMA651>3.0.CO;2-V.

(54) Zhang, C.; Pansare, V. J.; Prud'homme, R. K.; Priestley, R. D. Flash Nanoprecipitation of Polystyrenenanoparticles. *Soft Matter* **2012**, *8* (1), 86–93. https://doi.org/10.1039/C1SM06182H.

(55) Aubry, J.; Ganachaud, F.; Cohen-Addad, J. P.; Cabane, B. Nanoprecipitation of PMMA by Solvent Shifting: 1. Boundaries. *Langmuir* **2009**, *25* (4), 1970–1979. https://doi.org/10.1021/la803000e.

(56) Saad, W. S.; Prud'Homme, R. K. Principles of Nanoparticle Formation by Flash Nanoprecipitation. *Nano Today* **2016**, *11* (2), 212–227. https://doi.org/10.1016/j.nantod.2016.04.006.

(57) Johnson, B. K.; Prud'homme, R. K. Chemical Processing and Micromixing in Confined Impinging Jets. *AIChE J.* **2003**, *49* (9), 2264–2282. https://doi.org/10.1002/aic.690490905.

(58) Binnig, G.; Quate, C. F.; Gerber, C. Atomic Force Microscope. *Phys. Rev. Lett.* **1986**, *56* (9), 930–933. https://doi.org/10.1103/PhysRevLett.56.930.

(59) G. Binnig; Rohrer, H. Scanning Tunneling Microscopy. *Surf. Sci.* **1983**, *126*, 236–244. https://doi.org/10.1016/0039-6028(83)90716-1.

(60) https://www.brukerafmprobes.com/Product.aspx?ProductID=3907

(61) https://www.bruker.com/products/surface-and-dimensional-analysis/atomic-force-microscopes/campaigns/afm-microscopes.html

(62) Schönherr, H.; Vancso, G. J. *Scanning Force Microscopy of Polymers*; Springer, **2010**.

(63) Kittel, C.; McEuen, P.; McEuen, P. *Introduction to Solid State Physics*; Wiley New York, **1976**; Vol. 8.

(64) https://www.bruker.com/products/surface-and-dimensional-analysis/atomic-force-microscopes/modes/modes/nanoelectrical-modes/c-afm.html

(65) Simões, A. Z.; Onofre, T. B.; Moura, F. Piezoresponse Force Microscopy. *J. Adv. Microsc. Res.* **2010**, *5* (2), 129–136. https://doi.org/10.1166/jamr.2010.1034.

(66) Derjaguin, B.; Muller, V.; Toporov, Y. Effect of Contact Deformation on the Adhesion of Elastic Solids. *J. Colloid. Interface Sci* **1975**, *53* (2), 314–326. https://doi.org/10.1016/j.ijsolstr.2016.01.021.

(67) Ezquerra, T. A.; Garcia-Gutierrez, M. C.; Nogales, A.; Gomez, M. *Applications of Synchrotron Light to Scattering and Diffraction in Materials and Life Sciences*; Springer, **2009**; Vol. 776.

(68) Als-Nielsen, J.; McMorrow, D. *Elements of Modern X-Ray Physics*; John Wiley & Sons, **2011**.

(69) Raimondi, P. ESRF-EBS: The Extremely Brilliant Source Project. *Synchrotron Radiat. News* **2016**, *29* (6), 8–15. https://doi.org/10.1080/08940886.2016.1244462.

(70) https://www.diamond.ac.uk/Public/How-Diamond-Works.html

(71) https://www.cells.es/en/accelerators/linac

(72) http://www.esrf.eu/UsersAndScience/Experiments/CRG/BM02/optic

(73) Cebe, P.; Hsiao, B. S.; Lohse, D. J. Scattering from Polymers. *ACS symposium Series*; **1999**; Vol. 739.

(74) Cullity, B. D.; Stock, S. R. *Elements of X-Ray Diffraction*; Pearson Education, **2014**.

(75) https://www.physics.byu.edu/faculty/campbell/x-ray_diffraction.aspx

(76) Chu, B.; Hsiao, B. S. Small-Angle X-Ray Scattering of Polymers. *Chem. Rev.* **2001**, *101* (6), 1727–1761. https://doi.org/10.1021/cr9900376.

(77) Müller-Buschbaum, P. The Active Layer Morphology of Organic Solar Cells Probed with Grazing Incidence Scattering Techniques. *Adv. Mater.* **2014**, *26* (46), 7692–7709. https://doi.org/10.1002/adma.201304187.

(78) Baker, J. L.; Jimison, L. H.; Mannsfeld, S.; Volkman, S.; Yin, S.; Subramanian, V.; Salleo, A.; Alivisatos, A. P.; Toney, M. F. Quantification of Thin Film Cristallographic Orientation Using X-Ray Diffraction with an Area Detector. *Langmuir* **2010**, *26* (11), 9146–9151. https://doi.org/10.1021/la904840q.

(79) https://www.nist.gov/

(80) Stöhr, J. *NEXAFS Spectroscopy*; Springer Science & Business Media, 2013; Vol. 25.

(81) Nahid, M. M.; Gann, E.; Thomsen, L.; McNeill, C. R. NEXAFS Spectroscopy of Conjugated Polymers. *Eur. Polym. J.* **2016**, *81*, 532–554. https://doi.org/10.1016/j.eurpolymj.2016.01.017.

(82) Ade, H.; Hitchcock, A. P. NEXAFS Microscopy and Resonant Scattering: Composition and Orientation Probed in Real and Reciprocal Space. *Polymer (Guildf).* **2008**, *49* (3), 643–675. https://doi.org/10.1016/j.polymer.2007.10.030.

(83) Van Oss, C. J.; Good, R. J. Prediction of the Solubility of Polar Polymers by Means of Interfacial Tension Combining Rules. *Langmuir* **1992**, *8* (12), 2877–2879. https://doi.org/10.1021/la00048a006.

(84) Van Oss, C. J.; Chaudhury, M. K.; Good, R. J. Interfacial Lifshitz-van Der Waals and Polar Interactions in Macroscopic Systems. *Chem. Rev.* **1988**, *88* (6), 927–941. https://doi.org/10.1021/cr00088a006.

(85) Domingo, C.; Castillejo, M.; Rebollar, E.; Hernández, M.; García-Ruiz, J. P.; Pérez, S.; Martín, M.; Ezquerra, T. A. Physicochemical Modifications Accompanying UV Laser Induced Surface Structures on Poly(Ethylene Terephthalate) and Their Effect on Adhesion of Mesenchymal Cells. *Phys. Chem. Chem. Phys.* **2014**, *16* (33), 17551. https://doi.org/10.1039/c4cp02434f.

(86) Teyssèdre, G.; Lacabanne, C. Study of the Thermal and Dielectric Behavior of P(VDF-TrFE) Copolymers in Relation with Their Electroactive Properties. *Ferroelectrics* **1995**, *171* (1), 125–144. https://doi.org/10.1080/00150199508018427.

(87) Martínez-Tong, D. E.; Rodríguez-Rodríguez, Á.; Nogales, A.; García-Gutiérrez, M. C.; Pérez-Murano, F.; Llobet, J.; Ezquerra, T. A.; Rebollar, E. Laser Fabrication of Polymer Ferroelectric Nanostructures for Nonvolatile Organic Memory Devices. *ACS Appl. Mater. Interfaces* **2015**, *7* (35), 19611–19618. https://doi.org/10.1021/acsami.5b05213.

Chapter 3. Thin films of functional polymers: analysis of structure and properties at the nanoscale

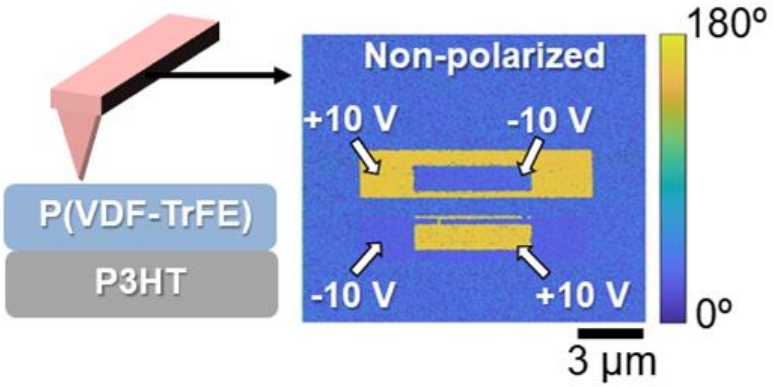

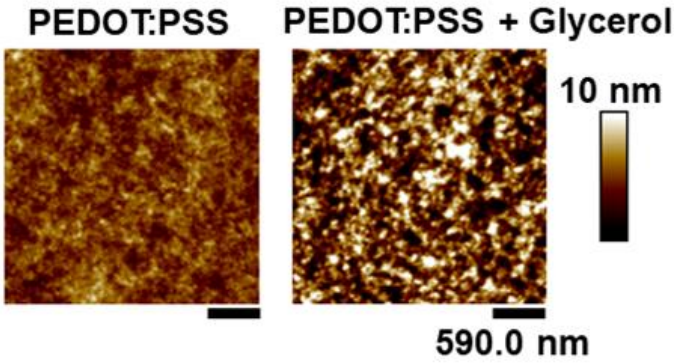

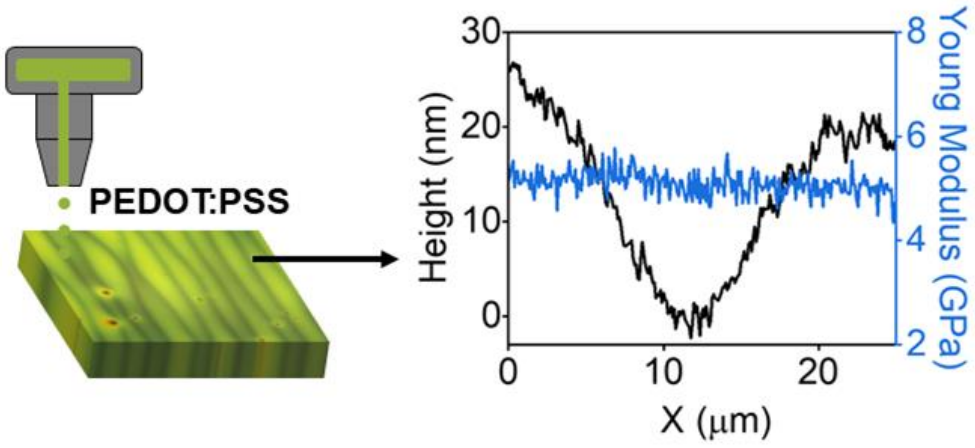

The functional electronic component in many organic electronic devices is a thin film of the functional material of interest. The most common method of fabricating a thin layer of a particular polymer consists essentially in depositing a polymeric solution or dispersion over a substrate followed by a removal of the continuous liquid phase. As the solvent is removed, the organic material remains as a solid film via crystallization or vitrification. Since thin films consist of layers with thicknesses below 1000 nm (mostly below 100 nm), they can be seen as nanostructured samples already.

This chapter contains three sections, each one dealing with a different functional polymeric system prepared in the form of thin films by different techniques.

- The first section describes a combined, semiconducting-ferroelectric system prepared by sequential spin-coating. We analyze the impact of a P3HT layer within a P3HT/P(VDF-TrFE) (semiconducting-ferroelectric) bilayered system. It is demonstrated that P3HT is able to stabilize the switching polarization of the upper-ferroelectric layer. In-plane and out-of-plane polarization of the ferroelectric layer is analyzed elucidating the impact of the thickness and crystallinity of the P3HT layer.

- The second section deals with thin films of PEDOT:PSS previously mixed with several polar liquids with high boiling point. These additives are mostly used to increase the conductivity though the real impact of them on PEDOT:PSS either in the dispersion or in the film is yet not completely understood. Morphological and structural analyses have been made in order to stablish differences and equivalences in the influence that the different additives has on PEDOT:PSS thin films.

- In the third section, the deposition of samples of PEDOT:PSS by inkjet printing is presented. We performed a morphological and structural analysis of these thin film samples, with special interest on the local electrical and mechanical properties of the films as a function of the number of deposited layers.

3.1 Morphology and ferroelectric properties on semiconducting/ferroelectric bilayers

In section 1.5.1 it was described the potential application on organic electronics of synergetic systems that combine ferroelectric and semiconducting behavior through the inclusion of two functional polymers.

In this section, we study the optimum conditions for preparing stable stacked semiconducting/ferroelectric polymer films where it is possible to write information via ferroelectricity. Bilayered samples were prepared by sequential spin-coating, that consists in depositing the second (upper) layer on top of the first one. The requirement for sequential spin-coating is that the solvent used for the second material does not affect the already deposited material. Conditions for preparation of solutions of P3HT in $CHCl_3$ and P(VDF-TrFE) are included in Table 2.9. Spin-coating conditions for sample deposition are detailed in Table 2.10.

3.1.1 Thickness characterization by AFM.

The thicknesses of the P3HT samples prepared from solutions with different concentration were obtained by making a scratch on the film with a razor and measuring by AFM in tapping mode the height profile of the scratch. Thickness of P3HT as a function of concentration in $CHCl_3$ is represented in Figure 3.1.

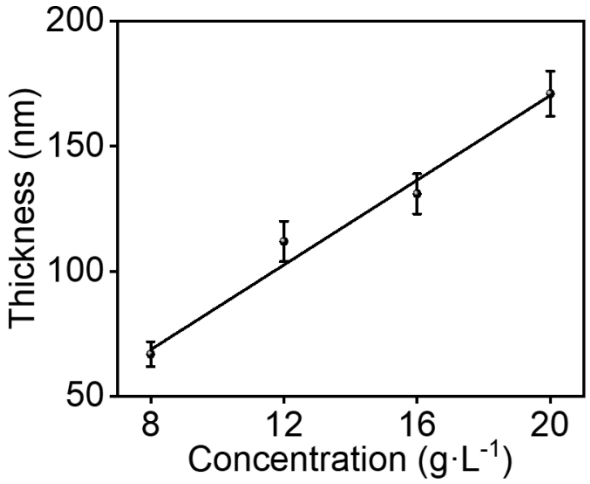

Figure 3.1 Thickness of spin-coated P3HT thin film as a function of the concentration in solution. Line added as a visual guide.

As can be seen in Figure 3.1, the thickness of P3HT thin films increases with increasing concentration following a linear progression.

3.1.2 Effect of the semiconducting polymer layer on the ferroelectric character of the upper film

The ferroelectric properties of the polymer stacked films formed by a bottom layer of P3HT with varying thickness and top layer of P(VDF-TrFE) with thickness ≈20 nm have been studied. Previous works have demonstrated that for particular combination of thicknesses of the P3HT layer and P(VDF-TrFE) layer, the stack preserves the ferroelectric nature[1]. In this Thesis we have

evaluated the effect of the P3HT thickness. The topographical image in contact mode of P(VDF-TrFE) layer deposited on silicon (Figure 3.2.a, left) shows holes indicating some degree of dewetting. On the contrary, the ferroelectric polymer film on a 130 nm thick P3HT film is continuous (Figure 3.2.a, right), with a roughness R_q, calculated as the root means square of height deviations from the average height value, around 1 nm, producing a more continuous P(VDF-TrFE) film.

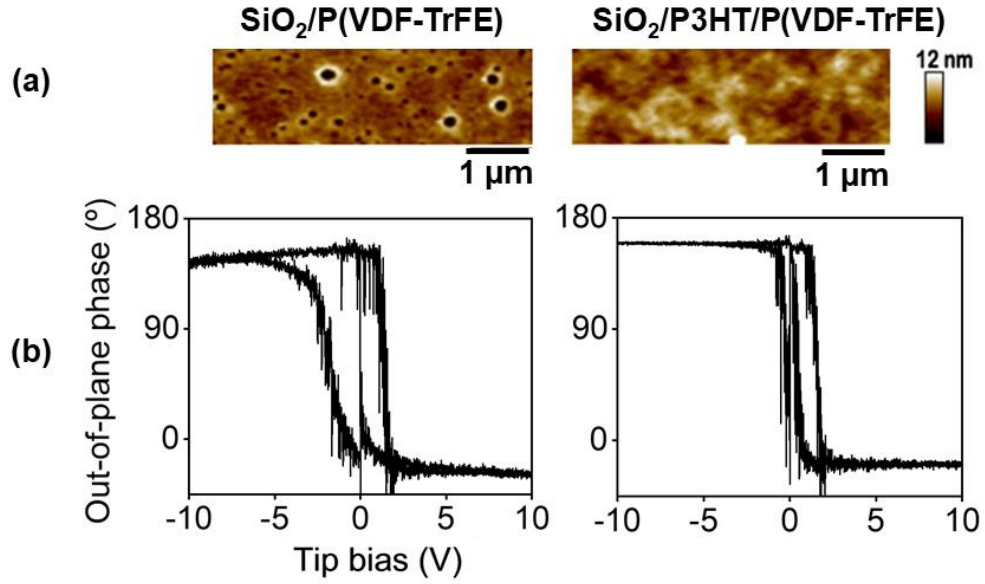

Figure 3.2 (a) Topographical image in contact mode of a P(VDF-TrFE) layer with thickness ≈20 nm on top of an n-doped silicon wafer with its native oxide layer **(left)** and on top of a P3HT layer with thickness ≈130 nm **(right)**. **(b)** Piezoresponse loops obtained on the samples above by applying a DC voltage to the AFM tip.

By using the AFM tip as top electrode the ferroelectricity of the samples was probed (see section 2.3.1.1.3). Ferroelectric hysteresis is observed in the out-of-plane (OOP) phase as a function of the applied voltage as shown in Figure 3.2.b for the ferroelectric layer on silicon (Figure 3.2.b, left) and on P3HT (Figure 3.2.b, right). These loops were obtained by applying a DC voltage to the tip following the sequence: 0V → 10V, 10V → -10V, -10V → 0V. For both cases, a phase switch of nearly 180º was observed at a critical voltage (coercive voltage V_c). In the case of doped silicon as substrate, the initial value of OOP phase is between 0 and 90º, the hysteresis cycle is wide and exhibits a $V_c \approx 2.5$ V, and the cycle is centered on 0V. However, when the layer of 130 nm thick P3HT is placed in between, the initial value of the OOP phase is close to 180º, the hysteresis loop becomes narrower, with a $V_c \approx 2$ V and slightly shifted towards positive voltages. Similar shifts of the hysteresis cycle have been observed in layers of P(VDF-TrFE) on semiconducting polymer layers as polypyrrole[2] and polyethylenedioxythiophene[3]. In these works, the shifted hysteresis loop is attributed to the fact that the semiconducting layer supplies the

amount of charges needed to stabilize the ferroelectric dipoles and prevent depolarization, suggesting a homogeneous orientation of the P(VDF-TrFE) dipoles. This phenomenon is called self-polarization and it has been reported in Langmuir-Blodgett films of P(VDF-TrFE)[4] and PVDF[5]. Self-polarization is due to a preferential alignment of the dipoles on the substrate. Fu et al.[6] reported similar shifts in capacitance-voltage curves obtained from bilayered ferroelectric polymer/semiconducting structures. In general, it has been shown that the polarization switching is very sensitive to the electric environment especially at the interface with the substrate[7,8]. These particular electric conditions at the interface produce a built-in field (E_0) that depending on its magnitude may modify the polarization switching behavior of the ferroelectric. In general, if the polarization behavior of the ferroelectric is represented by a double well potential, the presence of a built-in field at the interface destabilizes the double well and one of the polarization states might be thermodynamically favoured[8]. A larger external field with different sign to E_0 would be required to flip the polarization in one direction whereas, helped by E_0, the switching would be easier in the opposite direction. Yuan et al.[9] have estimated that the magnitude of E_0 at the interface between a P(VDF-TrFE) and a semiconducting polymer can be obtained from:

$$E_0 = \frac{t_f \sigma_p}{\varepsilon_0 \varepsilon_{FE} t_s} \qquad (\mathbf{3.1})$$

σ_p is the polarization charge density, t_f is the thickness of the P(VDF-TrFE) film, ε_{FE} is the relative dielectric constant of the ferroelectric layer, t_s is the thickness of the semiconducting layer and ε_0 is the dielectric constant in vacuum. The presence of this built-in field can be explained by the increase of electric static potential due to the presence of a large charge density in the interface between the semiconducting and ferroelectric layers, assuming that the polarization is perpendicular to the layer plane. It is possible to estimate the magnitude of this field: one may consider the nominal remnant polarization of 100 $mC \cdot m^{-2}$ of P(VDF-TrFE) and ε_{FE}=7.5[9]. The order of magnitude of the built-in field is around several hundred $V \cdot \mu m^{-1}$ for the thicker P3HT film and even ~2000 $V \cdot \mu m^{-1}$ for the thinner P3HT film. These values are overestimated since the remnant polarization value is obtained for a monolayer of P(VDF-TrFE) molecules forming a perfect crystal with perpendicular polarization to the layer and covering completely the semiconducting polymer. However, this estimation provides a hint on the high magnitude of the built-in field.

Since the semiconducting/ferroelectric polymer structures keep the ferroelectric character when stacking, as shown in Figure 3.2, it may be possible to selectively orient their permanent polarization by an electric field. The scheme of the writing procedure is shown in Figure 3.3.a and the geometry of the proven polarization with respect to the cantilever axis of the AFM is shown in Figure 3.3.b. Figure 3.3.c and Figure 3.3.d show the OOP PFM phase obtained for a

written region of P(VDF-TrFE) thin film on doped silicon and on a P3HT thin film with thickness=110 nm. The OOP signal is related to the vertical component of the polarization vector (P_z in Figure 3.3.b).

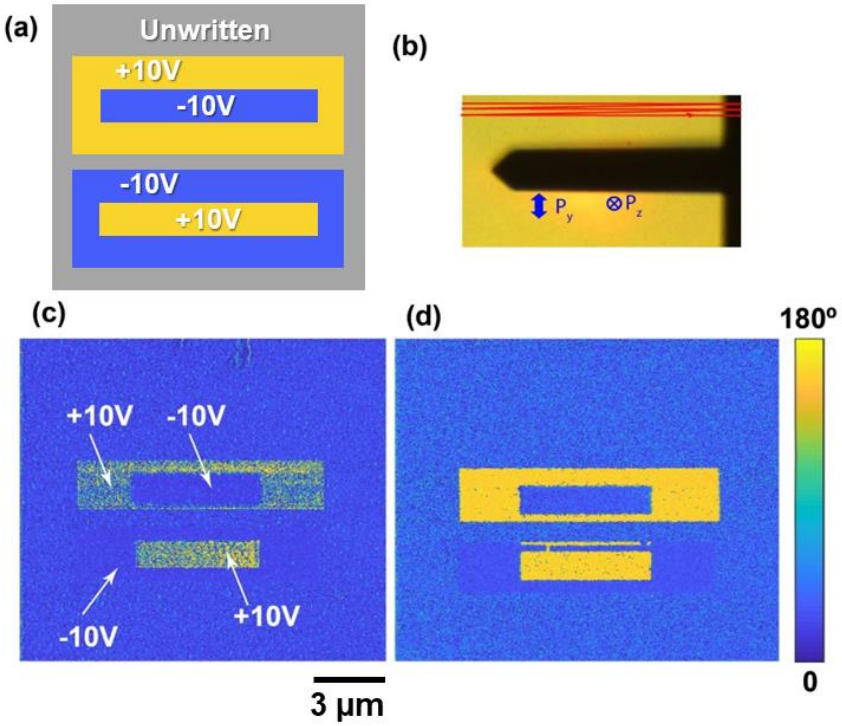

Figure 3.3 (a) Schematics of the ferroelectric domain writing on P(VDF-TrFE) films with different poled regions. First, a 10x2 µm^2 region was poled with +10 V applied to the substrate, then an inner central region of 5x1 µm^2 was poled with -10V. A bottom region was poled with opposite DC bias (region of 10x2 µm^2 with -10V and an inner region of 5x1 µm^2 with +10V). **(b)** Geometry of the PFM experiment indicating the direction of polarization vector components. Red lines indicate the scanning direction of writing and reading PFM processes, which is also the cantilever axis. **(c)** and **(d)** PFM-phase image in the out-of-plane direction by applying an AC voltage while the tip is grounded in a P(VDF-TrFE) thin film over doped silicon **(c)** and over a P3HT thin film **(d)**.

The DC voltages used for writing will produce a vertical field with positive sign (pointing upwards) if the voltage sign is positive and pointing downwards if the sign of the voltage is negative. The PFM response is probed by an AC voltage applied to the tip. With this reading setup, the OOP phase will be 180º shifted if the P_z component of the polarization vector points upwards (yellow regions), and it will be in phase with the reading voltage when P_z is pointing downwards (blue regions). The presence of a thin P3HT layer between the doped silicon and the ferroelectric polymer produces a more homogeneous shifting of the polarization when the sample is written with a positive sign voltage.

The P3HT interlayer between silicon and P(VDF-TrFE) decreases the coercive voltage for polarization switching and produces a more homogeneous switching of the polarization with the writing bias. These results are in line with those obtained by Naber et al[10]. By employing a conducting polymeric bottom electrode, they demonstrate that the coercive field, the switching time and the remnant polarization are improved for thin ferroelectric films.

3.1.3 Role of thickness of the P3HT thin film on the polarization switching mechanism as revealed by PFM

Figure 3.4.a shows the complete PFM response of written regions in a ferroelectric polymer thin film deposited on P3HT with different thickness.

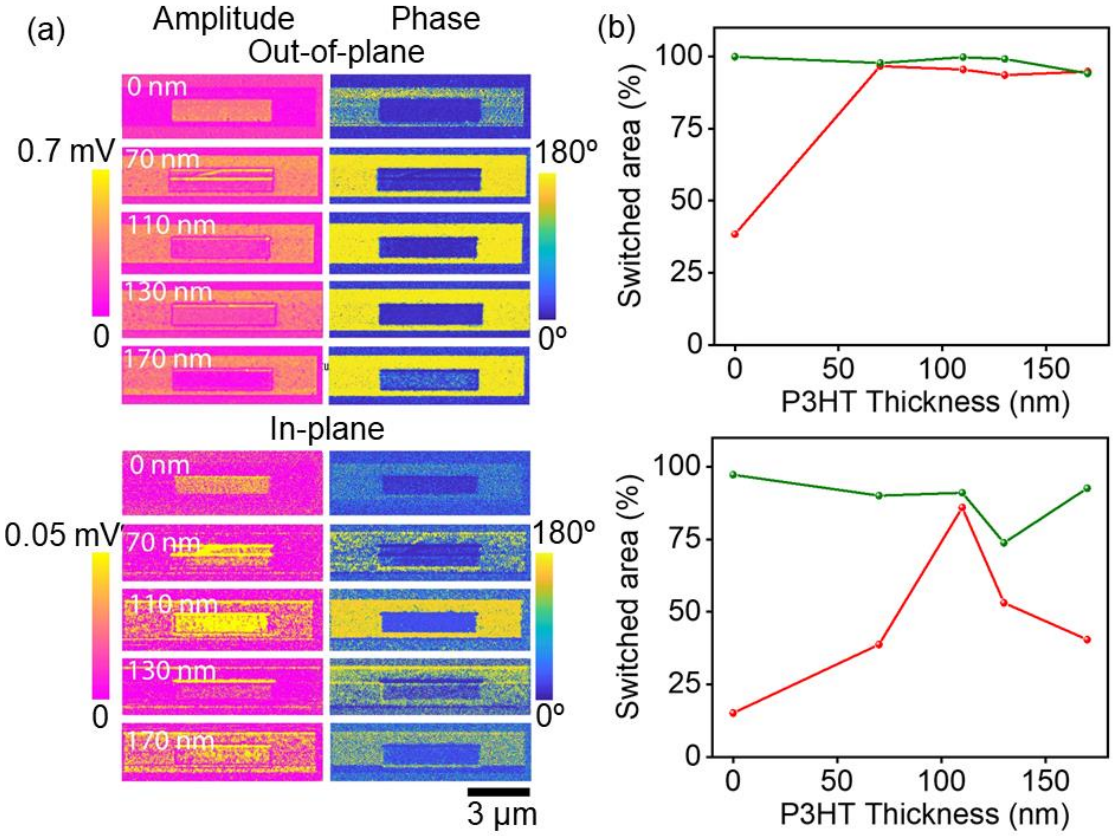

Figure 3.4 (a) PFM amplitude and PFM phase in the out-of-plane and in-plane direction of samples with a P(VDF-TrFE) thin film over silicon and over a P3HT thin film with different thicknesses, white-labelled in every row. **(b)** Percentage of areas exhibiting out-of-plane **(up)** and in-plane **(down)** polarization switching when applying positive voltage (red dots) and negative voltage (green dots).

Qualitatively, the vertical polarization switching behaves in a similar way for all the P3HT thicknesses as revealed by the OOP PFM amplitude (Figure 3.4.a). To quantify the writing properties as a function of the P3HT interlayer thickness, the protocol by Roth et al.[11] is followed,

estimating the percentage of biased area that undergoes a vertical polarization switch in the positive and negative polarized regions. In Figure 3.4.b, the obtained percentages as a function of P3HT layer thicknesses are presented. The results indicate that the presence of the P3HT layer stabilizes efficiently the vertical switch of the polarization in the ferroelectric layer under positive voltage. This efficiency seems to be slightly lower when the P3HT thickness is higher. In the case of regions written with a negative bias, the switch is almost perfect regardless the P3HT thickness. Again, the sample with thicker P3HT layer exhibits less efficiency in the switching.

The in-plane (IP) or lateral PFM results are also presented in Figure 3.4. Compared with the results obtained for the vertical or OOP PFM component, the changes in amplitude are weaker and noisier. However, the IP phase exhibits a clear dependence with the thickness of the P3HT substrate. When the sample is written with positive bias, the IP amplitude is very weak with the exception of the samples with P3HT thickness=110 nm and 170 nm. The IP phase contrast, as in the case of the OOP phase, is enhanced for the samples with a P3HT layer. However, the contrast is not as homogeneous. In this case, the sample with thickness=110 nm exhibits the most homogeneous shift of the IP phase. The percentage of area of shifted IP phase is maximum for the sample with thickness=110 nm (Figure 3.4.b). Different crystals orientations of the P(VDF-TrFE) or P3HT crystals may be responsible for the different PFM responses obtained as a function of the P3HT layer thicknesses.

3.1.4 Crystallinity and orientation of bilayers as revealed by GIWAXS and its influence on ferroelectric behavior

To elucidate the role of the crystal orientation in the PFM results of the previous subsection, the orientation of the crystalline phase of both layers has been studied by means of GIWAXS (see section 2.3.5.3).

Figure 3.5.a shows the GIWAXS patterns of the monolayer of P(VDF-TrFE) on silicon and the bilayer system with two different thicknesses of P3HT. In every sample P(VDF-TrFE) presents the same orientation, with the characteristic (110) and (200) reflections of the β phase being more intense in the meridian (q_z-axis). This orientation is typical of "edge-on" lamella[12], where the polymer chain (c-axis) lies parallel to the substrate. Two possible orientations of the unit cell produce meridional (110) and (200) reflections. In one case, the a and b crystallographic axis lay perpendicular and parallel to the substrate respectively (Figure 3.5.b, left). In the other case, the a and b axis form 30º and 60º angle with the substrate plane respectively (Figure 3.5.b, right)[11]. These two orientations are not distinguished by GIWAXS. According to the geometry of the β phase of P(VDF-TrFE), dipoles in the crystalline structure are oriented along the b axis, i.e. perpendicular to the c axis. Therefore, in "edge-on" lamellas they can be either parallel to the

substrate or forming 60º angle with it. If the orientation of the P(VDF-TrFE) lamella were preferentially with the (100) direction perpendicular to the sample plane, it would be not possible to pole it with a vertical bias.

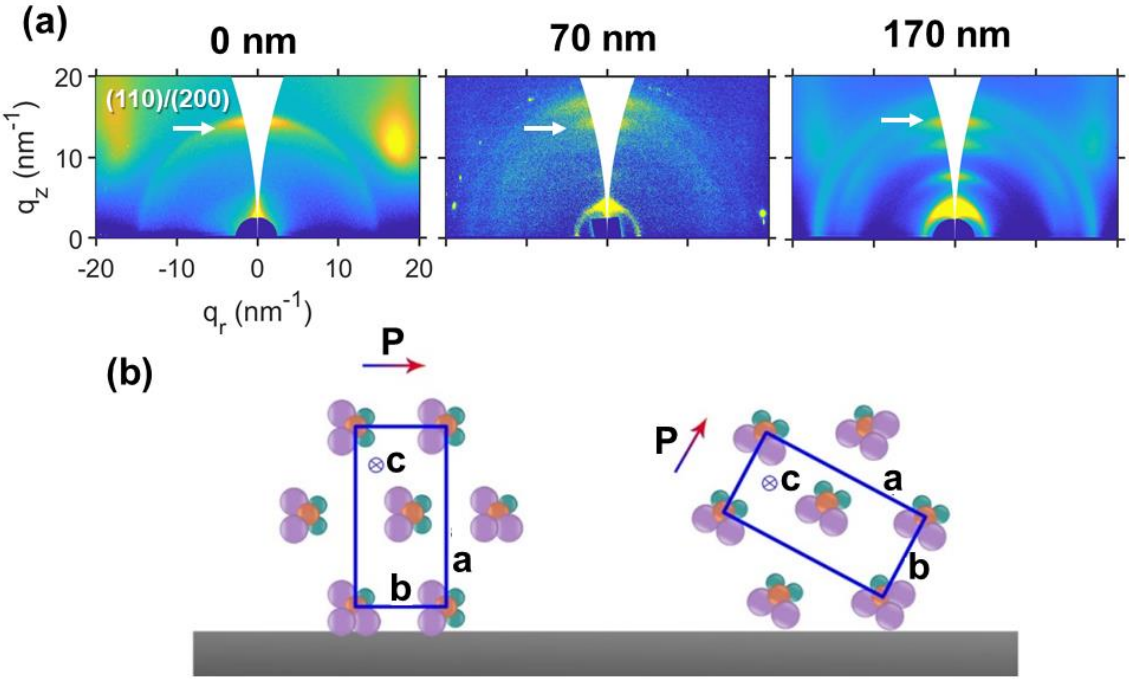

Figure 3.5 (a) GIWAXS patterns of a 20 nm thick film of P(VDF-TrFE) on doped silicon **(left)** and on a P3HT thin film with thickness 70 nm **(center)** and 170 nm **(right)**. The arrow indicates the (110/200) reflection of the β phase of P(VDF-TrFE). **(b)** Scheme of the different orientations of the chains in the "edge-on" lamellas of P(VDF-TrFE) and schematics of its crystalline structure with an indication of the dipole vector direction: in the **left** scheme the b direction of the unit cell is parallel to the substrate and also the polarization vector whereas in the **right** scheme the b direction is rotated 60º relative to the substrate plane, and thus the polarization vector is also rotated 60º, having non-zero horizontal and vertical components. Intensity of GIWAXS patterns is in logarithmic scale.

As observed in Figure 3.3 and Figure 3.4, the ferroelectric polymer deposited directly on a silicon wafer exhibits an inhomogeneous OOP phase shift under positive bias, which might be a hint of the presence of both types of orientations in the P(VDF-TrFE) lamellas. On the contrary, the P(VDF-TrFE) deposited onto a P3HT layer exhibits a homogeneous switching of the OOP component of the polarization vector, indicating that the "edge-on" lamellas show primarily the (110) orientation (Figure 3.5.b, right). Under a vertical poling bias, these dipoles rotate freely around the c axis (the molecular chain axis) to try to align with the poling field.

In the case of (110) orientation of the P(VDF-TrFE) crystals under vertical poling, three different switching angles of the polarization are possible: 180º, 120º and 60º. In a 180º switching of the dipole, both vertical and lateral components of the PFM should be active, since it would imply

that both P_y and P_z will change their sign. The 120º switching implies that only reversal of P_z would occur, and therefore, only OOP PFM contribution would be detected. In the 60º switching, only P_y would change the sign, and then only IP PFM signal would be detected. It has been reported before that, at large tip voltages, 180º switching is predominant and lower voltages values yield 120º switchings[11,13]. In view of the PFM results, introducing a P3HT layer underneath the ferroelectric layer promotes the 180º dipole switching. Sharma et al.[13] explain this effect considering that the tip generated field has an in-plane component that would be more important for larger voltages. In this case, however, the tip applied voltage is the same for all samples. Therefore, the variations should be related to the presence of P3HT. GIWAXS measurements on monolayers of P3HT with different thicknesses have been done. Figure 3.6.a-d shows the GIWAXS results obtained in P3HT bottom layers with different thicknesses, labelled in every image.

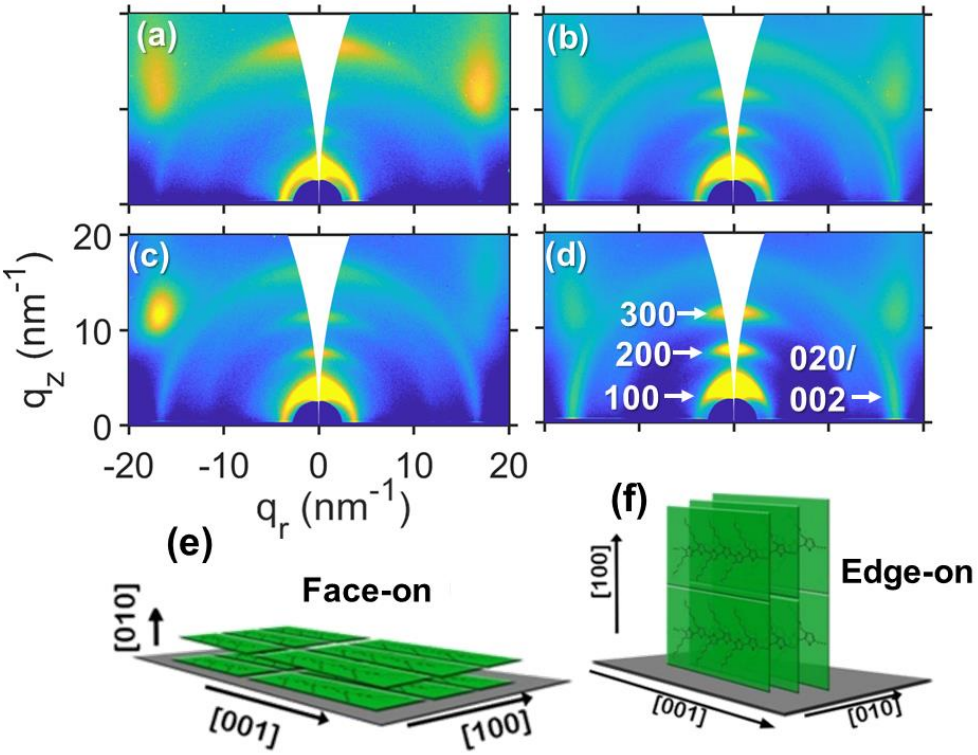

Figure 3.6 (a-d) GIWAXS patterns of spin-coated P3HT thin films with different thicknesses: **(a)** 70 nm, **(b)** 110 nm, **(c)** 130 nm and **(d)** 170 nm. Main reflections of P3HT labelled in **(d)**. **(e-f)** Schematic drawing of the molecular orientation of P3HT in different crystals orientations. Intensity of GIWAXS patterns is in logarithmic scale.

The X-ray results show that there is a clear dependence on the crystallinity and especially on the orientation of the crystals in P3HT with its thickness. The thinnest P3HT film (Figure 3.6.a) exhibits a complete different preferential orientation than the thickest one (Figure 3.6.d). The crystallinity of the thinnest sample is relatively lower, as revealed by the absence of higher orders

of the (100) reflection. Regarding orientation, in the thinnest sample, the (020) reflection is more intense in the meridian, indicating that the π-π stacking direction is perpendicular to the layer plane. This orientation corresponds to the "face-on" P3HT lamella, sketched in Figure 3.6.e (or see section 1.4.1, Figure 1.8). Thicker layers exhibit the characteristic meridional reflections (h00) of the crystalline phase of P3HT. In this case, the (020) reflection is more intense in the equator, indicating that the π-π stacking direction is preferentially parallel to the layer surface, associated with the "edge-on" orientation of the lamellas, as in Figure 3.6.f. It is generally assumed that the thermodynamically favored texture is the one with "edge-on" oriented chains whereas the "face-on" orientation of the P3HT is considered as a kinetically trapped morphology[14]. In this sense, crystals in the thinner P3HT layer grow in a more confined environment that promotes the "face-on" orientation for the P3HT lamella.

The variation in the orientation of P3HT lamella can be responsible for the different type of P(VDF-TrFE) dipole switching under positive bias. P3HT chains have an intrinsic surface dipole along the conjugated backbone. The electronic cloud in the π molecular orbitals, located above and below the backbone, is negatively charged; whereas in the backbone plane, positive charges compensate the negative-charged cloud[15]. This produces a surface dipole whose magnitude depends on the orientation of molecules relative to the surface[16]. Considering this effect, the thinner P3HT layers studied in this work, whose chains are mostly lying in the surface plane, would have a strong built-in dipole perpendicular to the surface in contact with the ferroelectric layer. The built-in field induced by this dipole in the "face-on" lamella would point upwards and it will add up to the applied external field, producing an effective higher polarizing field. Because of that, and in line with the literature[13], a 180º dipole switch is more predominant in the P(VDF-TrFE) layer when it is deposited onto P3HT with majority of "face-on" lamella. In the other extreme, in thicker P3HT layers with majority of lamella with "edge-on" orientations, the dipole would appear parallel to the surface, but somehow screened due to the presence of aliphatic chains as observed in the IP response.

3.1.5 Impact of the surface energy components of P3HT measured by contact angle

The presence of this dipolar effect in the P3HT lamella is also reflected in the components of the surface energy obtained for the P3HT substrates of different thicknesses. The contact angle technique is described in section 2.3.6, and essentially consists in depositing droplets of different liquids over the solid substrate investigated. Higher affinity between the solid and the liquid produces spreading of the droplet and lower contact angle measured. Higher contact angle reflects low affinity. The surface energy and its different components have been calculated by means of

the Young-Dupre theory modified by van Oss, Chaudhury and Good[17,18]. The protocol and equations used to calculate the components of surface energy from the contact angle value are described in section 2.3.6. Contact angles measurements on the different samples with every liquid are listed in Table 3.1.

Table 3.1 Measured contact angles with every liquid.

Material	Thickness (nm)	CA Water (º)	CA Glycerol (º)	CA Paraffin Oil (º)
Silicon	-	63 ± 5	69 ± 2	18 ± 4
P3HT	70	107 ± 1	83 ± 1	35 ± 1
	110	107 ± 0	80 ± 6	38 ± 1
	130	107 ± 1	81 ± 4	37 ± 1
	170	107 ± 1	93 ± 6	43 ± 1

Calculated components of the surface energy are presented in Table 3.2. Additionally, the polarity P is included, as the ratio in % between the polar component and the total surface free energy:

$$P = 100 \cdot \frac{{\gamma_S}^p}{\gamma_S} \qquad (\mathbf{3.2})$$

Table 3.2 Calculated components of the surface free energy and polarity for every sample.

Material	Thickness (nm)	γ_s^d	γ_s^-	γ_s^+	γ_s^p	γ_s	P (%)
Silicon	-	27.5	28.3	0.1	3.36	30.7	10.9
P3HT	70	23.91	0.27	1.24	1.19	25.10	4.7
	110	23.10	0.66	2.16	2.40	25.50	9.4
	130	23.37	0.52	1.83	1.95	25.32	7.7
	170	21.66	0.23	1.65	1.24	22.90	5.4

The non-polar surface of P3HT can be explained by the tendency to form lamellar structures with alkyl chains oriented perpendicular to the substrate (i.e. the “edge-on” stacking). In this configuration, it is expected that the top surface will be rich in hydrophobic alkyl groups, leading to its non-polar nature. The amount of “edge-on” crystallites was calculated following the same

protocol as Petsagkourakis et al[19]. First the GIWAXS patterns were integrated along the whole azimuthal range. Then, the Bragg peaks and the amorphous halo were fitted to Voigt or Gaussian functions. A value of relative crystallinity for every sample was calculated as the relation between the area of fitted Bragg peaks and the total area. Then, a radial integration of the (100) peak of P3HT between the azimuthal angle χ= 0º (the out-of-plane axis) and χ=90º (in-plane axis) was done. Integration limits are schematized in Figure 3.7.a-b. The value of the relative amount of "edge-on" crystallites was calculated as the relation between the integral of I (χ)·sin (χ) between χ=0º and χ=45º, and the same integral between χ=0º and χ=90º. I (χ) is the intensity function calculated by radial integration of the 100 peak of P3HT (Figure 3.7.c-d).

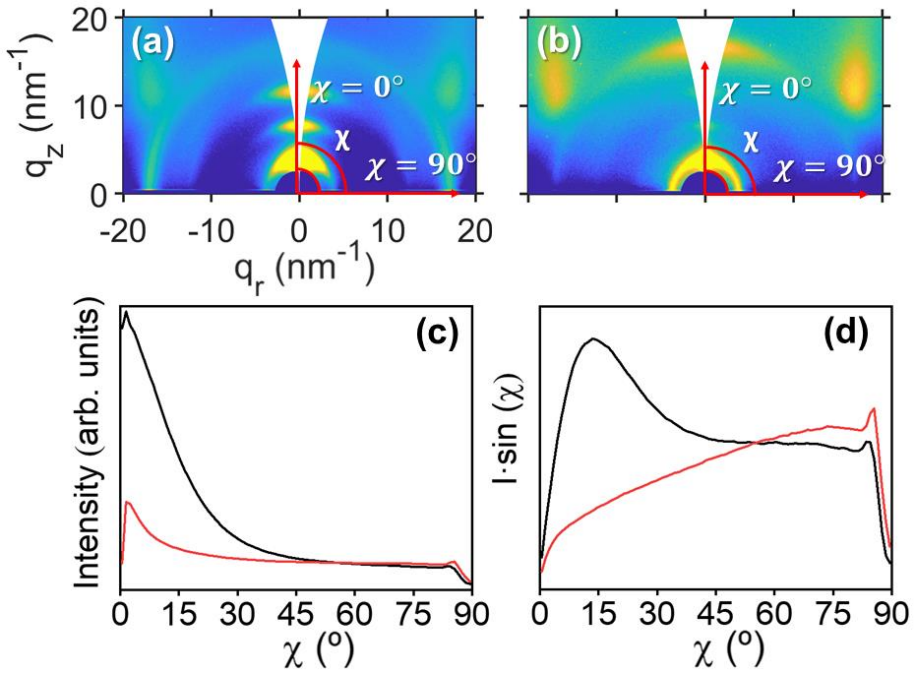

Figure 3.7 GIWAXS pattern of **(a)** P3HT thin film (thickness=170 nm), **(b)** thickness=70 nm, **(c)** intensity profiles of GIWAXS as a function of azimuthal angle χ (º), P3HT thickness=170 nm (black curve), 70 nm (red curve), **(d)** I·sin (χ) profile, P3HT thickness=170 nm (black curve), 70 nm (red curve).

Finally, the real value comparable between samples is the total amount of "edge-on" crystallites that is obtained by multiplying the relative amount of "edge-on" crystallites by the relative crystallinity of the sample (Equation 3.3). The amount of "edge-on" crystallites are compiled in Table 3.3.

$$amount\ of\ "edge-on"\ crystallites = \left[\frac{\int_{\chi=0°}^{\chi=45°} I(\chi)\cdot\sin\chi}{\int_{\chi=0°}^{\chi=90°} I(\chi)\cdot\sin\chi}\right]\cdot\left[\frac{area\ of\ Bragg\ peaks}{total\ area}\right] \quad (3.3)$$

Table 3.3 Amount of "edge-on" crystallites in every sample of P3HT.

Thickness of P3HT (nm)	Amount of "edge-on" crystallites
70	0.24
110	0.36
130	0.36
170	0.47

For thicker P3HT films the amount of "edge-on" crystallites increases and this fact can explain that both the polar component and the polarity decrease. However, to explain the different behavior of the thinnest P3HT film, we have to consider its lower crystallinity (Figure 3.7.b). As it has been previously reported for amorphous P3HT films, to minimize the interfacial energies, the hexyl side chains, which are apolar, come to the surface[20]. The increase of surface polarity, due to high values of γ_s^+ in thinner samples of P3HT can be responsible for the stabilization of the dipole in the poled P(VDF-TrFE) over P3HT.

3.2 Structural and morphological changes of dispersions and thin films of PEDOT:PSS with high boiling point additives

As it is described in section 1.4.4, the structure of PEDOT:PSS is mostly explained in terms of colloidal particles with a core rich in PEDOT and shell rich in PSS. This structure could be tuned by different methods being the mixing with an additive of high boiling point or 'secondary dopant' one of the most interesting for potential applications.

Many works are focused on the study of properties of deposited thin films of PEDOT:PSS treated with these kind of additives[21–23]. However, as far as we know, few studies are done to support and stablish correlations between structural changes in the dispersion and the final properties of the film[24–26]. In this work, PEDOT:PSS dispersions are mixed with high boiling point additives: ethylene glycol (EG), glycerol (G), dimethyl sulfoxide (DMSO) and the blend (G+DMSO). The effect of the additives on PEDOT:PSS on both dispersions and thin films is described, in terms of the proposed models.

The additives were added to the pristine dispersion of PEDOT:PSS and thin films were prepared by spin-coating. Experimental details for the preparation of dispersions blended with additives were described in Table 2.9, and the spin-coating conditions in Table 2.10. Thermal annealing was performed at T=140ºC for 10 minutes to remove the additives from the films.

3.2.1 Additive effect on the structure of PEDOT:PSS dispersions

SAXS experiments (see section 2.3.5.2) were carried out over PEDOT:PSS aqueous dispersions, pristine and with additives at different concentrations. Figure 3.8 presents the intensity profiles as a function of q, obtained by azimuthal integration of the SAXS patterns in the whole range.

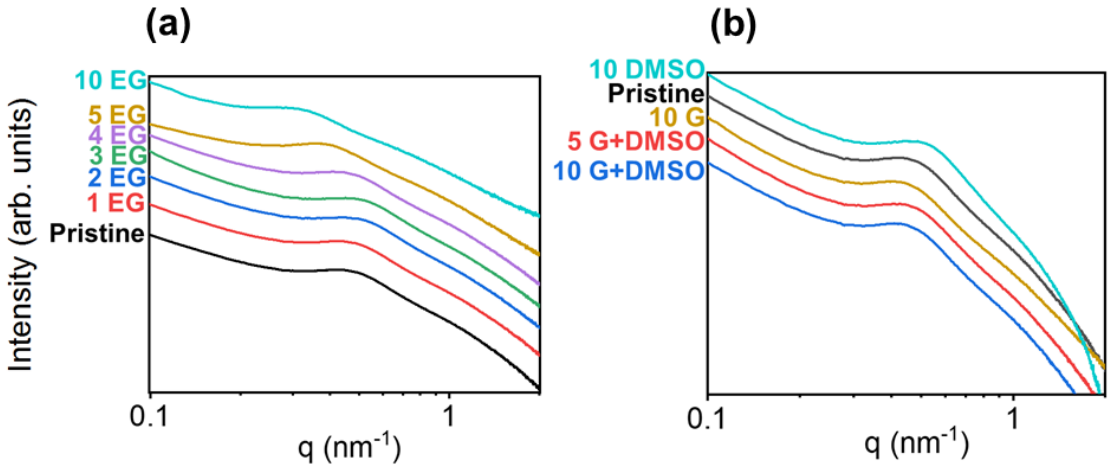

Figure 3.8 SAXS intensity profiles of **(a)** PEDOT:PSS with EG and **(b)** PEDOT:PSS with G, with DMSO and G+DMSO at different wt. %. X-axis and Y-axis in logarithmic scale.

The shape of SAXS profiles from PEDOT:PSS dispersions shows the same features as the reported profile by Takano et al[27]. In this kind of profiles, the component at low q (~0.1 nm^{-1}) with a high negative slope comes from aggregation of colloidal particles[27], whereas the peak-like feature at q≈0.4 nm^{-1} (d≈15 nm) comes from a correlation length within the particles. The PEDOT:PSS colloid used here is formed by particles whose diameter is 90% under 100 nm, and 50% under 80 nm (see Table 2.6). The peak is located nearly at the same q value in all PEDOT:PSS batches[27] so we consider that the correlation distance is located within the PEDOT:PSS 'grains', being the grains formed by a PEDOT-rich core and a PSS-rich shell. Murphy et al. suggest that the peak is related to the known polyelectrolyte peak, which arises from interchain electrostatic repulsions[25].

At a first glance, a shift of the peak maximum to either lower or higher q values depending on the EG concentration (Figure 3.8.a) can be observed. This effect is less evident in the case of G and

DMSO (Figure 3.8.b). The SAXS data are presented in the form of Kratky plots (Figure 3.9) to highlight the impact of additive on the structure of PEDOT:PSS.

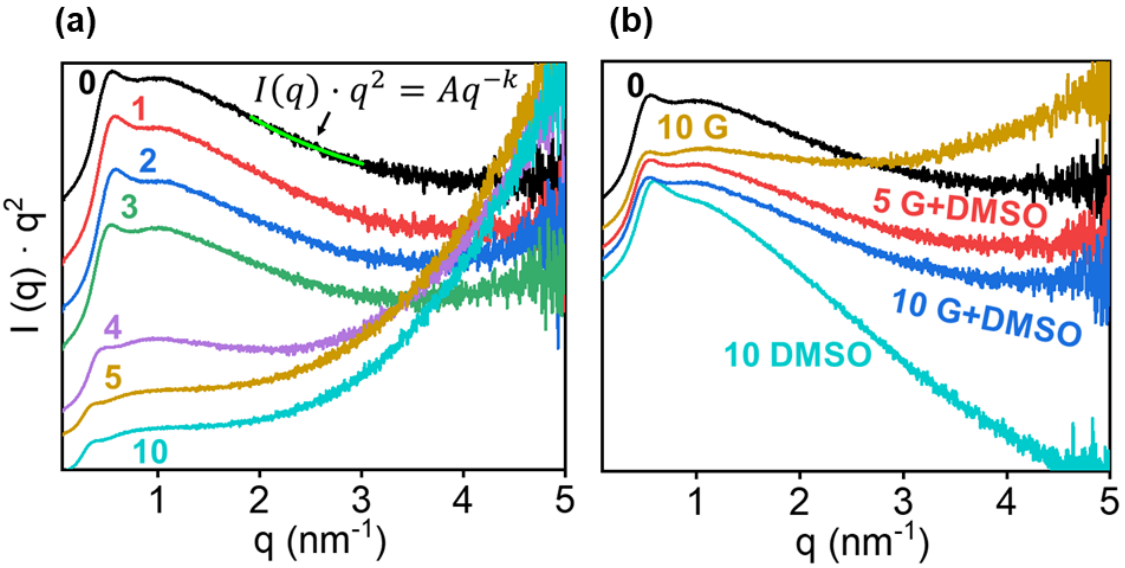

Figure 3.9 Kratky plots [I(q)·q^2 vs q] obtained from the SAXS intensity profiles of **(a)** PEDOT:PSS with EG and **(b)** PEDOT:PSS with G, with DMSO and G+DMSO. The different wt. % are labelled. As an example, it is shown the fitting of the range q=2-3 nm^{-1} of Kratky plot from pristine PEDOT:PSS dispersion in **(a)** with the function labelled. The resulting fitting is the green curve indicated with an arrow.

The Kratky plot from pristine dispersion (Figure 3.9.a-b, black curves) shows an initial peak, followed by a small plateau and a decay. A similar result for aqueous dispersion of PEDOT:PSS has been associated with a compact coil structure[24]. The decay can be separated in two regions: the first at q≈1.25–2 nm^{-1} (d≈5-3.1 nm), where the distances are comparable to reported values of radius of gyration[24] of PEDOT:PSS, and the second region at q>>1/R_g, where the intensity can be modelled with the generalized Porod's law (Equation 3.4)[28], where *s* is the dimensionality of the system.

$$I(q) \propto q^{-(6-s)} \qquad (\mathbf{3.4})$$

The region q≈2-3 nm^{-1} (d≈2-3.1 nm) from Kratky plot of pristine PEDOT:PSS dispersion was fitted with the function q^2·I(q)=A·q^{-k} and represented as a green curve in Figure 3.9.a, highlighted with an arrow. A is a constant and k≈0.56. Therefore, at this q-range, the SAXS intensity decays as $I(q) \propto q^{-2.56}$, which is close to reported values[26]. Following Equation 3.4, the dimensionality of the system is around s≈3.4. This means that the system at length ranges of ≈2-3 nm behaves as compact spheres with rough surface (fractal-like)[28]. This result can be correlated with the size of coils of individual PEDOT:PSS chains in the pristine dispersion[26,29].

Addition of EG in the dispersion does not change much the Kratky plot for concentrations of 1-3 wt. % EG. Higher concentrations yield qualitative differences. Kratky plots at 4 wt. % and higher EG concentrations (Figure 3.9.a) present an extended plateau region followed by an upturn at high q. The presence of an extended plateau is characteristic of Gaussian chains[30]. At high q, Gaussian chains show a decrease of intensity with q^{-2}. Therefore, its Kratky plot ($I(q)\cdot q^2$) is nearly a constant function. The upturn is explained in terms of worm-like chain model, or persistent chain model[30]. In this model, under a certain length range, consecutive segments of the chain form small angles so the chain defines a continuous curvature. This relative rigidity is quantified as the persistence length *a*. The higher persistence length, the more rigid is the chain. Therefore, the scattering object is close to a cylinder; when q is large enough, the scattered intensity is proportional to q^{-1}. Therefore, in the Kratky plot, $I(q)\cdot q^2$ would be proportional to q, this is the origin of the upturn at high q in Kratky plots. In these curves, the transition point q* between the plateau and the upturn is related to the persistence length through Equation 3.5[30].

$$a = \frac{1.91}{q^*} \qquad (\mathbf{3.5})$$

In the Kratky plot from PEDOT:PSS dispersion with 4 wt. % EG (Figure 3.9.a), the transition point is at $q\approx2.4$ nm^{-1} ($a\approx0.796$ nm). In the Kratky plots from PEDOT:PSS dispersions with 5 and 10 wt. % EG, the transition points are at $q\approx2$ nm^{-1} ($a\approx0.955$ nm). The Kratky plot from PEDOT:PSS dispersion with 10 wt. % G (Figure 3.9.b) shows also an extended plateau and an upturn around $q=3$ nm^{-1}, thus in this system the persistence length is $a\approx0.64$ nm. Interestingly, DMSO (Figure 3.9.b) seems to induce the opposite effect than EG and G. The more pronounced decay in Kratky plot suggests a more compact structure of PEDOT:PSS chains when DMSO is added. This effect is compensated in dispersions with blended additives G+DMSO, whose Kratky plots (Figure 3.9.b) are quite similar to the one from pristine dispersion (Figure 3.9.b).

Conclusions from Kratky plot analysis are that EG does not seem to induce a notable effect on the structure of PEDOT:PSS within the dispersion until a concentration of 4 wt. %. At this value, PEDOT:PSS chains, which initially arrange in a compact coil structure, present an extended plateau characteristic of Gaussian chains over a length range of ≈9-2.6 nm, followed by an upturn. The upturn characteristic of worm-like chains is indicative of unfolded, more extended and rigid chains of PEDOT:PSS. Higher concentrations of EG reinforce this acquired rigidity. Since EG is polar, the more extended and rigid chains are likely to be induced by the interaction of EG through hydrogen bonding between charged PEDOT and PSS. The additive screens the Coulombic interaction between charged segments, which are able to adopt less constrained and more planarized conformations of the chains. This is the model used to explain conductivity

improvements in PEDOT:PSS thin films with EG and other additives[31,32]. G seems to induce the same effect, as opposed to DMSO that induces more compact structures.

In order to obtain physical parameters that can be matched with real structural changes of PEDOT:PSS within the dispersion, the intensity profiles have been fitted following the same procedure as Murphy et al[25]. They adjust the SAXS profile to the Broad Peak model, or polyelectrolyte model, which is an empiric model used for electrolytic systems[33] (Equation 3.6).

$$I(q) = \frac{A_0}{q^n} + \frac{A_1}{1 + (L \cdot |q - q_{max}|)^m} + A_2 \qquad (\mathbf{3.6})$$

In Equation 3.6 A_0, A_1 and A_2 are scaling factors, *n* and *m* are the low-q and high-q scaling exponents, respectively, that is, a parameter of the dimensionality of the scattering object at different distances: *n* for distances of tens of nanometers (in the order of PEDOT:PSS grains) and *m* for distances around 1-10 nm (in the range of interchain interactions)[25]. q_{max} is the peak position. As it was said at the beginning of the subsection, the peak is often treated as a result of a correlation distance $\xi = \frac{2\pi}{q_{max}}$ between charged chains due to electrostatic repulsions[25]. If PEDOT:PSS grains are seen as cores of PEDOT with a shell of PSS, ξ could be seen as an average distance between the center of the core (positive region) and the middle of the PSS shell (negative region). L is treated as the screening length of the interchain interaction[25]. Our data were adjusted in the region q=0.09-1 nm^{-1} (d≈70-6 nm). Figure 3.10 shows, as an example, the SAXS intensity profile of the pristine PEDOT:PSS dispersion and the curve fitted with Equation 3.6.

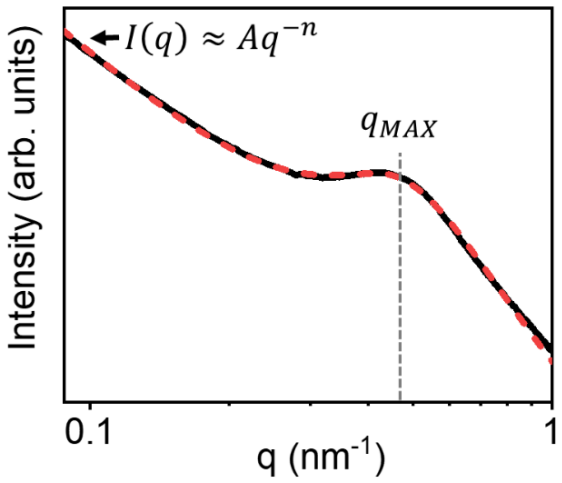

Figure 3.10 SAXS intensity profile of the pristine PEDOT:PSS dispersion (black curve) and its corresponding fitting with Equation 3.6 (red dashed line). The grey dashed line indicates the q-position of the peak (q_{max}). At q ≈ 0.1 nm^{-1}, the curve is mainly determined by the first factor of Equation 3.6, labelled in the Figure. X-axis and Y-axis in logarithmic scale.

Figure 3.11 shows the fitted values of *n* and *m* from Equation 3.6.

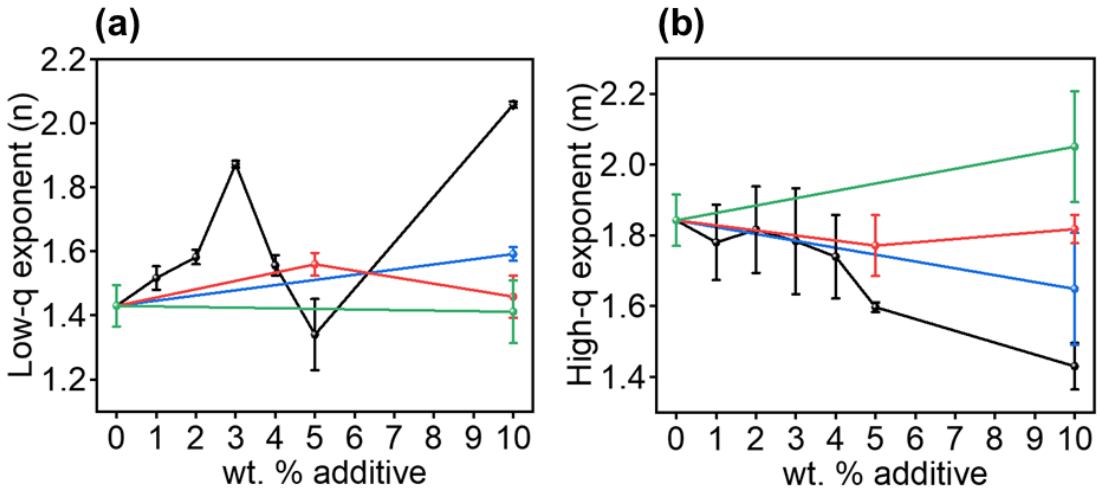

Figure 3.11 (a) Low-q exponent *n* and **(b)** high-q exponent *m* of PEDOT:PSS dispersions with different concentrations of EG (black data), G (blue data), G+DMSO (red data), and DMSO (green data).

The low-q exponents from dispersions of PEDOT:PSS with EG (Figure 3.11.a, black data) show a tendency to increase in most of the concentrations with respect to the pristine value. The values corresponding to 5 wt. % and 10 wt. % EG are probably not accurate due to the broadening of the peak in SAXS intensity profiles (Figure 3.8.a) which is screening the real slope from the aggregations at this q-range. The high-q exponent of samples with EG (Figure 3.11.b, black data) presents values systematically lower than the pristine one. The same trend for both *n* and *m* is found in the dispersion with 10 wt. % of G (Figure 3.11.a-b, blue data). Dispersion with 10 wt. % of DMSO (Figure 3.11.a-b, green data) maintains the same low-q exponent as pristine dispersion but shows an increase of the high-q exponent. Regarding both parameters, in dispersions with blended additives G+DMSO (Figure 3.11.a-b, red data), the values change in an intermediate way between the additives separately.

The increase of *n* is associated with denser aggregates in the dispersions. On the other hand, a reduction of high-q exponent (*m*) can be attributed to a transition of chains from a coil-like to a more-rigid conformation in the dispersion[25,26]. Fitted data from dispersions with EG and G present this behavior. These results support the ideas extracted from Kratky plots concerning the addition of EG to the PEDOT:PSS dispersion (Figure 3.9.a). Similar conclusion can be suggested for PEDOT:PSS with G, bearing in mind the differences mentioned from Kratky plots (Figure 3.9.a-b) and considering that the results can be associated to the high polarity of G that can interact between the charged segments of PSS and PEDOT[26], screening the Coulombic force and inducing a more-extended chain conformation, as it is suggested to be the effect of EG[32]. However, DMSO seems to induce another effect on the dispersion, which affects at the range of interchain distances,

and at the nanometer range as it was seen with Kratky plots analysis (Figure 3.9.b) but does not affect remarkably at the PEDOT:PSS grain level.

The screening length of the interchain interaction L[25] is obtained in every system with a value of 4.5 ± 0.5 nm. Regarding the correlation distance $\xi = \frac{2\pi}{q_{max}}$, the trends for every additive concentration are presented in Figure 3.12.

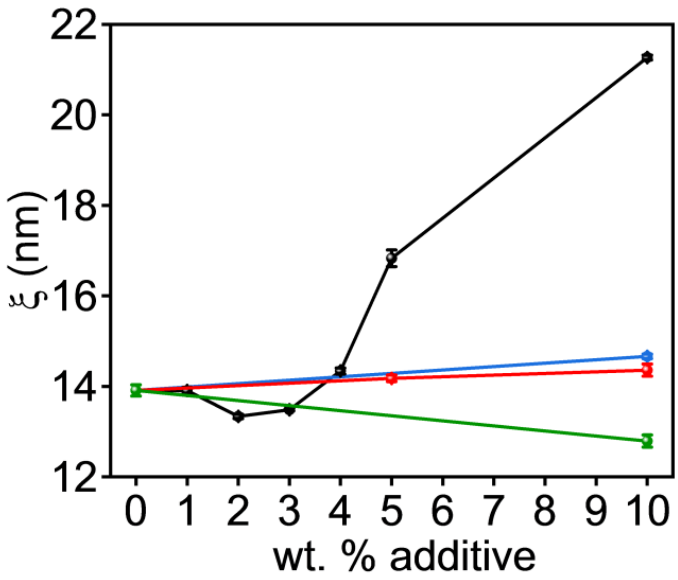

Figure 3.12 Correlation length (ξ) as a function of different concentrations of EG (black data), G (blue data), G+DMSO (red data), and DMSO (green data).

In the case of PEDOT:PSS with EG (Figure 3.12, black data), ξ drops slightly from the initial value of ξ≈14 nm for low concentrations (in the range of 1-3 wt. %) and then it increases in the range of 4-10 wt. %, reaching a value of ξ≈21 nm for the maximum concentration. In the case of PEDOT:PSS with 10 wt. % of G (Figure 3.12, blue data), ξ increases slightly compared to the pristine value, whereas in the case of 10 wt. % of DMSO (Figure 3.12, green data), ξ decreases. Data from dispersions with blended additives G+DMSO (Figure 3.12, red data) show an intermediate situation between G and DMSO separately, presenting a slight increase with increasing concentration.

It is clear from Figure 3.12 that EG has a stronger impact on ξ than the other additives. The reduction of ξ at low concentrations of EG can be explained as a compaction of the PEDOT:PSS grains, as seen in other polylelectrolyte systems[34]. It has been reported that spin-coated thin films of PEDOT:PSS with EG present lower amount of PSS compared with pristine PEDOT:PSS thin films because the EG interacts with the excess of PSS and it is washed away during spin-coating process[35]. We suggest that this is occurring in our PEDOT:PSS dispersions with 1-3 wt. % of EG.

At these low concentrations, EG could be interacting mainly with the PSS shells of PEDOT:PSS grains, removing it partially from the shells. The lower amount of PSS within PEDOT:PSS grains would induce a stronger Coulombic interaction between unbalanced charged regions that would collapse the structure. This will reduce the correlation length between charged zones ξ (Figure 3.12.a, black data) and also could explain the densification of the larger aggregates, as related with the increased value of the low-q exponent *n* in Figure 3.11.a (black data).

The increase of ξ from 4-5 and higher wt. % of EG points toward the swelling of the PEDOT:PSS grains. We can explain this two-stage mechanism of EG effect considering that PEDOT:PSS grains are seen as cores of PEDOT with a shell of PSS. A schematic view is shown in Figure 3.13. After the reduction of ξ at low EG concentrations, at concentrations equal and higher than 4 wt. %, the additive interacts between PEDOT and PSS charged segments, inducing more extended chains at the nanometer scale and a swelling of the PEDOT:PSS grains at the scale of tens of nanometers. This analysis agrees also with the treatment of the SAXS data in the frame of the Kratky plots analysis (Figure 4.9.a, black data). This model is coherent with reported dynamic light scattering (DLS) results, that show larger PEDOT:PSS grains when poly(ethylene glycol) is added in the pristine PEDOT:PSS dispersion[36].

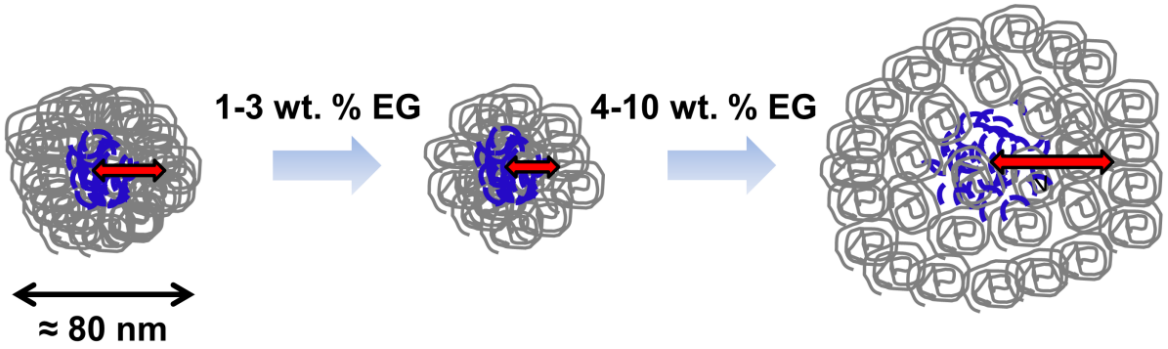

Figure 3.13 Scheme of the effect of EG on the PEDOT:PSS grains. Red arrows represent the correlation length ξ. Scales are not proportional.

G seems to follow the same path as EG, though the effect is less pronounced (Figure 3.12, blue data). The trend of ξ in the case of DMSO is the opposite as effects reported by Bagchi et al[26]. In our work, the correlation distance ξ is reduced upon the addition of DMSO. However, it must be taken into account that there is only one concentration data regarding the system with DMSO, and it is a quite lower concentration compared with the work by Bagchi et al[26], who used around 300 wt. % of DMSO. On the other hand, Murphy et al[25] used similar concentrations of DMSO as ours (10-15 wt. %) and they reported almost no change in the SAXS profile.

3.2.2 Morphology of PEDOT:PSS thin films with additives

The dispersions studied in section 3.2.1 were deposited by spin-coating in order to obtain thin films. Spin-coating details were compiled in Table 2.10. It was found that PEDOT:PSS with EG concentrations higher than 4 wt. % and did not form continuous film with any concentration of DMSO. The addition of glycerol did not affect the film formation. Therefore, thin films were prepared from dispersions of pristine PEDOT:PSS, PEDOT:PSS+EG, PEDOT:PSS+G and PEDOT:PSS+G+DMSO.

Figure 3.14 shows topographical images of PEDOT:PSS thin films, pristine and treated with the different additives.

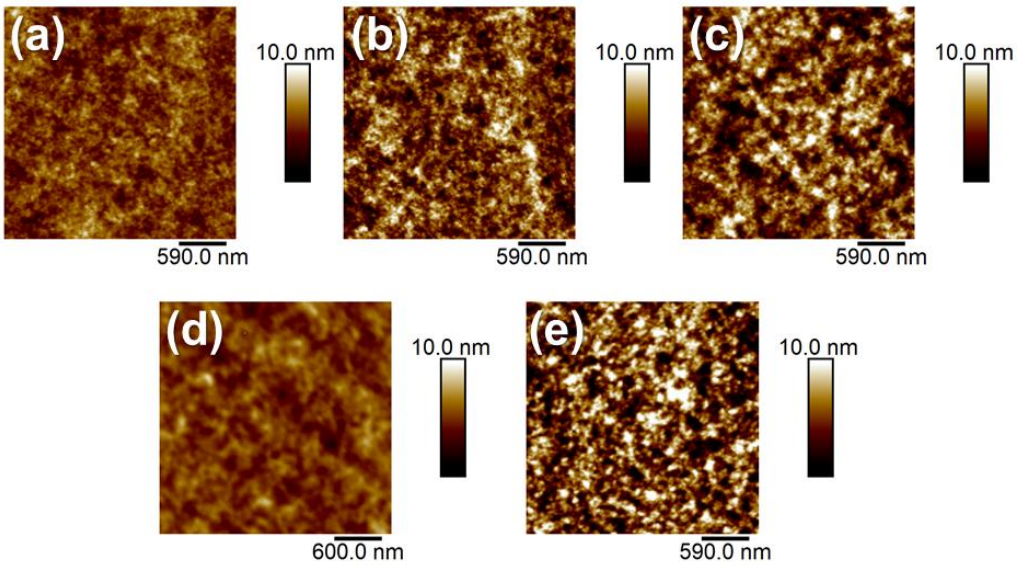

Figure 3.14 Topographical images taken by AFM in tapping mode of **(a)** pristine PEDOT:PSS spin-coated at 2000 rpm, **(b)** PEDOT:PSS with 4 wt.% EG spin-coated at 2000 rpm, **(c)** PEDOT:PSS with 5 wt. % (G+DMSO) spin-coated at 2000 rpm, **(d)** pristine PEDOT:PSS spin-coated at 3000 rpm, **(e)** PEDOT:PSS with 10 wt. % G spin-coated at 3000 rpm.

Samples with EG and (G+DMSO) were spin-coated at a rotational speed of 2000 rpm, so they can be compared with pristine PEDOT:PSS deposited with the same spin-coating conditions. Sample with G was spin-coated at 3000 rpm so it should be compared with pristine PEDOT:PSS thin film deposited at 3000 rpm as well. Both pristine PEDOT:PSS thin films spin-coated at different speeds (Figure 3.14.a,d) present smooth surfaces, with roughness R_q around 1 nm. Thin films prepared from dispersions with additives present higher roughness. In the case of EG-additive (Figure 3.14.b), $R_q \approx 1.5$ nm; this higher roughness seems to appear from sharper narrow domains. In the cases where G and G+DMSO are added (Figure 3.14.c and Figure 3.14.e respectively), $R_q \approx 2$ nm and 2.5 nm respectively, and their surfaces present higher protuberances

and larger domains. A clearer vision of this effect is shown in Figure 3.15 where the sections of AFM images of Figure 3.14 are presented.

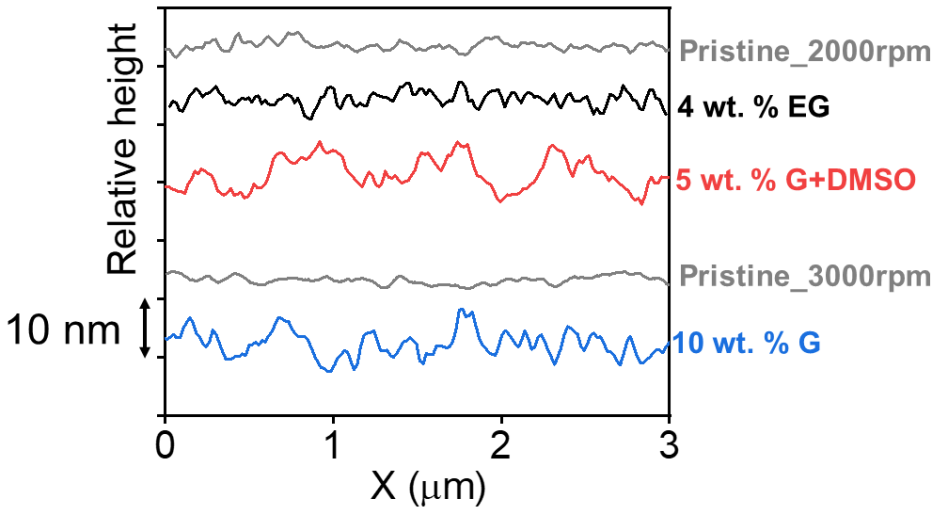

Figure 3.15 Height profiles of AFM images from Figure 3.14.

It is clear that all the additives increase the surface roughness in different ways. By the addition of EG, sharper and small domains are detected. With (G+DMSO), higher and larger domains are clearly seen. PEDOT:PSS mixed with G was deposited at a rotational speed of 3000 rpm. The comparison with pristine PEDOT:PSS spin-coated at this rotational speed shows also higher and larger domains.

Increase of roughness in PEDOT:PSS films doped with EG has been attributed to thinning or removal of PSS segments within PEDOT:PSS grains[37–39]. Smaller domains have been detected by AFM in micrometric-thickness PEDOT:PSS films with EG[40], and attributed to the reduction of PSS shells during spin-coating. Interestingly, an increase in grain size has been also detected by AFM[41], in this case, in spin-coated thin films, and it has been attributed to the coalescence of PEDOT:PSS grains with lower amount of PSS. It is possible that different thermal treatments over the film leads to the coalescence of the grains and a consequent increment of the roughness.

In the case of G and G+DMSO, the larger detected globules by AFM can be explained by the swelling of PEDOT:PSS grains after addition of glycerol, as explained in section 3.2.1. Although the effect of G and G+DMSO in the dispersions was lower than the effect of EG, the higher impact on the thin films morphology upon addition of G and G+DMSO could be related with the higher boiling point of G, that lasts longer times in the film than EG during spin-coating and thermal annealing. This would provide more time to the PEDOT:PSS chains to arrange before the additive is removed and the film stays in a rigid, vitrified state.

The thickness and roughness of PEDOT:PSS thin films with additives have been studied. Figure 3.16 shows the trend of thickness and roughness as a function of additive concentrations. The thickness was measured by making a scratch on the film with a razor and taking an AFM image of the scratch profile in several points of the sample.

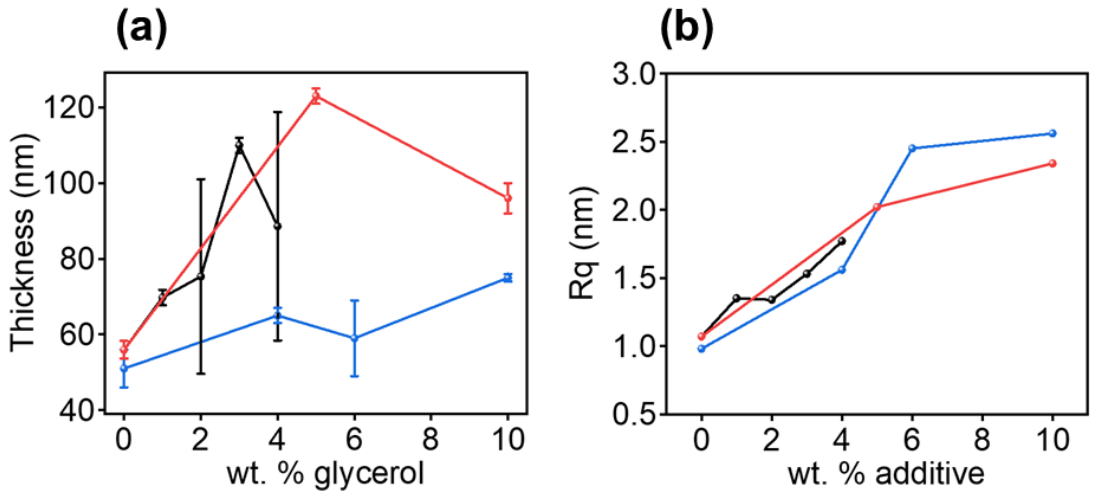

Figure 3.16 (a) Thickness and **(b)** roughness (R_q) of PEDOT:PSS thin films with EG (black data), G (blue data) and G+DMSO (red data).

The thickness of PEDOT:PSS with EG (Figure 3.16.a, black data) increases with increasing additive concentration although the film becomes more irregular, indicated by the error bars. For concentrations higher than 4 wt. % the films are not continuous. Thicknesses of PEDOT:PSS films with G (Figure 3.16.a, blue data) are also increasing with increasing concentration. In the case of films with PEDOT:PSS blended with G+DMSO (Figure 3.16.a, red data), the thickness increases initially until around 110 nm at 5 wt. % and decreases at higher concentrations. The R_q of thin films with additive is always higher than the R_q from pristine PEDOT:PSS thin films (Figure 3.16.b), increasing, as it was mentioned before, from the initial value of ~1 nm in the pristine PEDOT:PSS film to ~2.5 nm in films with 10 wt. % of G and G+DMSO (Figure 3.16.b, blue and red data respectively). The roughness of PEDOT:PSS films with EG (Figure 3.16.b, black data) also increases in the range of concentration in which films are formed.

It should be pointed out that, for the pristine sample (0 wt. %) different values of R_q and thickness are obtained for different spin-coating conditions. For the spin-coating conditions used to prepare the series of PEDOT:PSS with G (3000 rpm) the thicknesses of the pristine PEDOT:PSS thin films (Figure 3.16.a, blue data) is ≈47 nm. Addition of the G additive produces an increase of thickness. The series of PEDOT:PSS with EG and PEDOT:PSS with G + DMSO have been spin-coated at 2000 rpm. The thickness of the pristine film prepared under this conditions is ≈55 nm, and again, the additives produce an increase of thickness.

Taken into account that the additive is removed from the film by thermal annealing, the enhanced thickness suggests a reorganization of the material induced by the additive once it is deposited in the film. Thermal annealing removes the additive but the PEDOT:PSS retains the effect of the additives that we have explained in the previous section. In the case of PEDOT:PSS with EG, the two-stage mechanism described in section 3.2.1 provides an explanation of why PEDOT:PSS grains in thin films can be observed either without size variations but sharper as in our case (Figure 3.15) or with larger globules by other groups[41]. Densification of grains at low EG concentration may provide a rougher, more granulated morphology, whereas swelling at higher concentrations would support larger globules. Here, globules are referred to the structures detected by AFM, in the range of 100 nm, which are composed of agglomerated PEDOT:PSS grains. In Figure 3.12, the increase of correlation distance ξ at high concentrations of EG and G was associated with the swelling of PEDOT:PSS grains. Continuous thin films of PEDOT:PSS with high concentrations of EG were not formed. However, the swelling induced by G can be related with the larger domains detected by AFM (Figure 3.14 and Figure 3.15). This is applicable also for thin films of PEDOT:PSS with G+DMSO.

3.2.3 Additive effect on the thin film internal structure as revealed by GIWAXS

GIWAXS experiments were performed to elucidate structural changes on PEDOT:PSS thin films mixed with additives and after thermal annealing. Figure 3.17 shows GIWAXS patterns from selected samples.

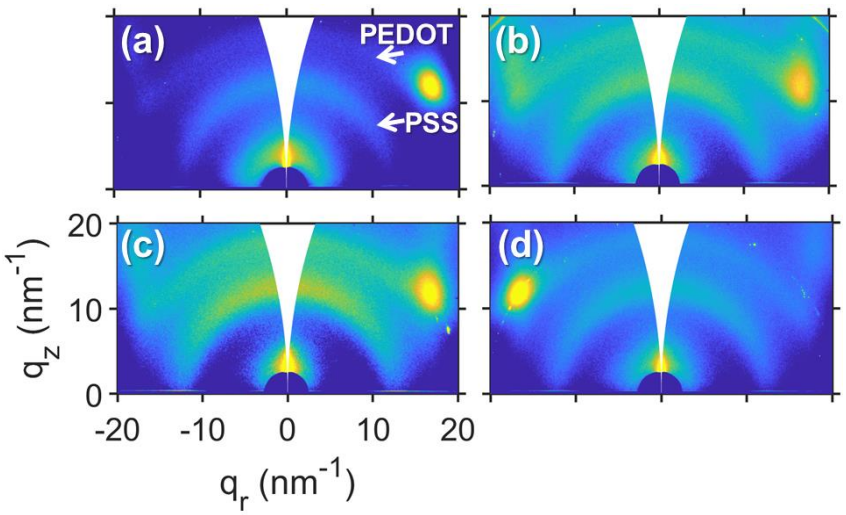

Figure 3.17 GIWAXS patterns of thin films deposited from dispersion of PEDOT:PSS pristine **(a)**, with 4 wt. % EG **(b)**, with 10 wt. % G **(c)**, and with 10 wt. % G+DMSO **(d)**. High intensity dots around the same q as PEDOT reflection come from scattering from silicon substrate. Intensity of patterns is in logarithmic scale.

GIWAXS patterns of pristine PEDOT:PSS (Figure 3.17.a) and with additives (Figure 3.17.b-d) share the same features: two broad reflections at q≈12.5 nm^{-1} and at q≈18.2 nm^{-1}. The one at q=12.5 nm^{-1} is associated with the amorphous halo of PSS[27] although other works refer to the π-π stacking of PSS[42]. The peak at q=18.2 nm^{-1} is the reflection from π-π stacking of PEDOT chains[42], which is partially oriented in the q_z axis.

Further analysis has been done by comparing the ratios between the area of the peak associated with the PSS reflection and the area of the peak associated with the PEDOT reflection. It has been reported that the selective interaction of the additive with PSS induces a phase segregation, and therefore, a decrease of PSS in the surface of spin-coated films[32,35]. This would modify the ratio of areas of GIWAXS peaks. Azimuthal integrations of GIWAXS patterns of Figure 3.17 were done over a large range centered at q_z, avoiding the contributions from the silicon substrate. The intensity profiles were corrected from background scattering and normalized to the maximum of PSS peaks, as shown in Figure 3.18.

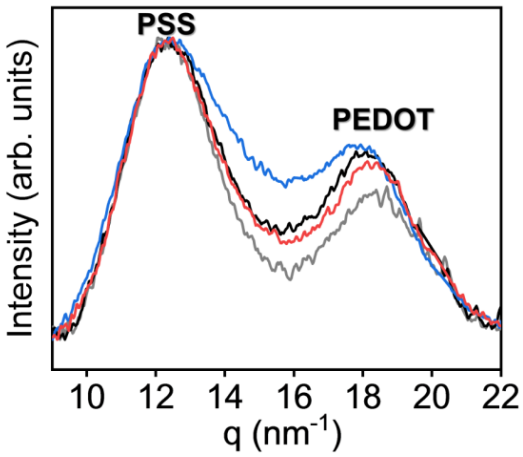

Figure 3.18 Azimuthal integrations in a broad range centered at q_z of GIWAXS patterns from thin films deposited from dispersion of PEDOT:PSS pristine (gray curve), with 4 wt. % EG (black curve), with 10 wt. % G (blue curve) and with 10 wt. % G+DMSO (red curve).

The peaks from Figure 3.18 were adjusted to Voigt functions and the relation between calculated areas (A_{PSS}/A_{PEDOT}) are included in Table 3.4.

Table 3.4 Relation between areas of peaks in Figure 3.18.

Ratio PSS Peak area / PEDOT Peak area			
Pristine	**4 wt. % EG**	**10 wt. % G**	**10 wt. % G+DMSO**
0.98 ± 0.04	0.79 ± 0.08	0.80 ± 0.01	0.91 ± 0.05

The ratio from PEDOT:PSS thin films with additives is lower than from pristine PEDOT:PSS thin film. This may suggests a decrease of PSS during spin-coating, due to interaction of PEDOT:PSS with the additives, either by hydrophilic interaction with PSS or by phase segregation between PEDOT and PSS. The decrease of the ratio A_{PSS}/A_{PEDOT} with additives compared to the pristine PEDOT:PSS could indicate also an increase of the order of PEDOT chains.

3.3 Quantitative assessment of mechanical and electrical properties by local probe methods of inkjet printed PEDOT:PSS

Inkjet printing technology is described in section 2.1.3 as an attractive deposition technique to produce flexible organic-based electronic devices like water-dispersed PEDOT:PSS. The mechanical stability of the film, as for the case of fused deposition additive manufacturing[43], may vary on the welding zones between adjacent lines. The QNM mode of AFM (see section 2.3.1.1.4) offers a versatile approach to study local mechanical properties of materials. In addition, it was pointed out in section 1.4.4 the influence of deposited PEDOT:PSS film thickness uniformity[44,45] and roughness[46,47] over its electrical properties. Thus, due to the great influence of preparation variables on the features and morphology of PEDOT:PSS[29,46], it is pertinent to evaluate the mechanical and electrical properties of inkjet deposited PEDOT:PSS films by local probe methods.

In this section, we present a study of the mechanical and electrical properties of inkjet printed PEDOT:PSS films on ITO-coated glass substrates, by employing QNM-AFM (see section 2.3.1.1.4) in combination with C-AFM (see section 2.3.1.1.2). Protocol for the preparation of the PEDOT:PSS dispersion was included in Table 2.8. Inkjet printing details were described in section 2.4.5.

3.3.1 Topography, electrical and mechanical properties of the inkjet printed films as a function of number of layers

Figure 3.19.a shows the AFM tapping topography image of an area of 500x500 nm^2 of one layer of PEDOT:PSS. R_q calculated from Figure 3.19.a is less than 1 nm. The surface is quite smooth with a texture of distributed grains of 40-70 nanometers diameter. The phase image (Figure 3.19.b) presents a relatively high contrast among 10-50 nanometers grains and the rest of the material.

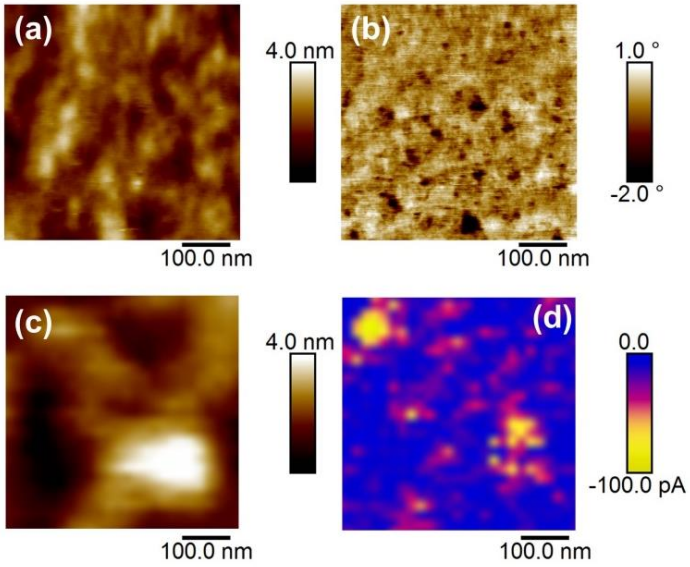

Figure 3.19 (a) AFM topography image in tapping mode, **(b)** corresponding AFM phase image. **(c)** Topography contact AFM image and **(d)** C-AFM (DC voltage applied=-3 V) for one layer of PEDOT:PSS film inkjet deposited on ITO.

Since AFM phase imaging can be sensitive to material composition, these results are compatible with the general proposed model for spin-coated PEDOT:PSS thin films[29]. As it was mentioned in section 1.4.4 and treated along section 3.2, the general model for PEDOT:PSS consists of localized PEDOT-rich domains surrounded by a PSS shell, forming grains with an average diameter of about 30-80 nm[42,48,49]. Additional information about the morphology of the PEDOT:PSS films can be obtained by C-AFM. Figures 3.19.c and d show a topography image in contact mode and its electrical current mapping respectively. The C-AFM current image (Figure 3.19.d) is consistent with the previous model and exhibits conducting dot-like domains of 30-80 nanometers size randomly distributed within a less-conducting continuous phase. A similar morphology is observed for inkjet deposited PEDOT:PSS films with more layers (Figure 3.20).

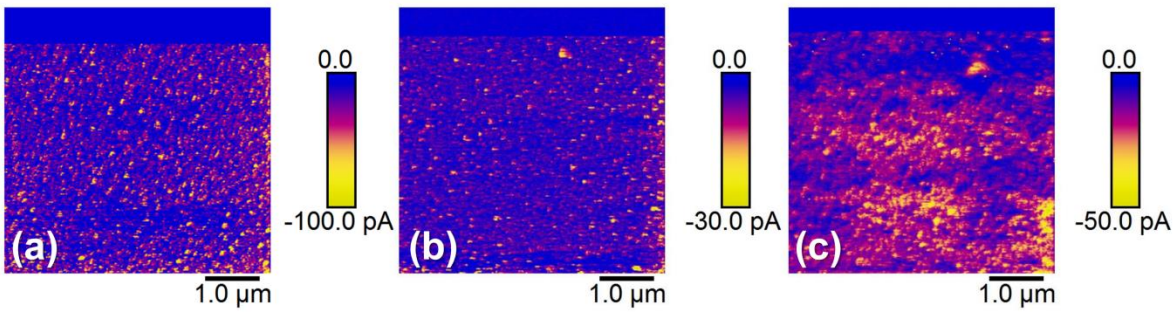

Figure 3.20 Current C-AFM images of inkjet deposited PEDOT:PSS on ITO: **(a)** 1 layer, DC voltage applied=-3V, **(b)** 2 layers, DC voltage applied=-3V, **(c)** 3 layers, DC voltage applied=-5V. The blue upper band in each image corresponds to DC voltage applied=0 V.

According to Figure 3.19.d and Figure 3.20, the surface sample suggests a far more abundant PSS phase domain than conducting PEDOT, which is consistent with the initial PEDOT/PSS ratio of 1/6 (see Table 2.6). Moreover, it has been reported that during film deposition PSS tends to segregate to the surface, being enhanced after exposing to a thermal annealing[50].

Figure 3.21 shows, in the upper row (a-d), optical microscope images of the different number of layers (1-4) of PEDOT:PSS deposited by inkjet onto ITO. A characteristic topography consisting of continuous lines is observed. The width of the lines is ≈ 25 µm, which is close to the diameter of the ejected droplets. In the middle row (Figure 3.21.e-h) AFM topographic images in tapping mode are shown. They are magnifications of 30x30 µm^2 of the corresponding images above them. The size and position of the image was chosen to measure a complete height profile of the printed line. The height profiles are shown in the bottom row of Figure 3.21.i-l.

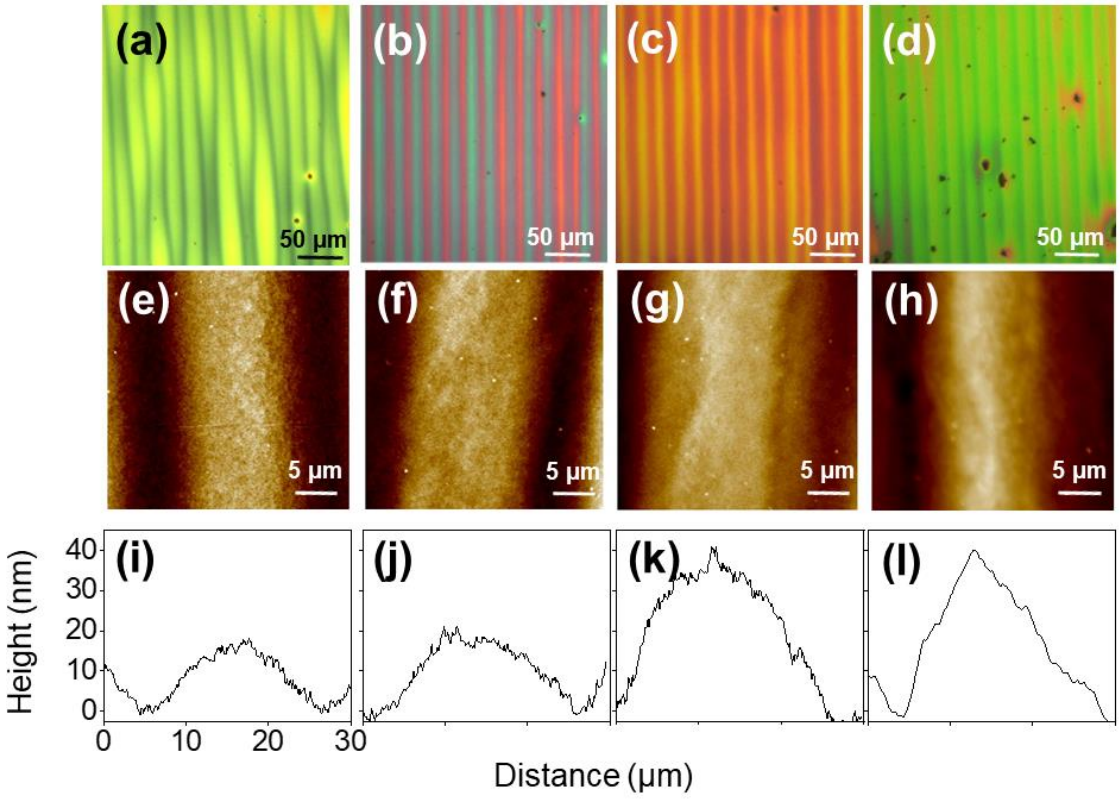

Figure 3.21 (Upper row) Optical microscope images for: **(a)** 1, **(b)** 2, **(c)** 3 and **(d)** 4 layers of PEDOT:PSS inkjet deposited on ITO. **(Middle row)** AFM topography images for 1 **(e)** to 4 **(h)** PEDOT:PSS layers in an area of 30x30 µm^2. **(Bottom row)** AFM height profiles across the corresponding images shown in the intermediate row.

AFM reveals that the lines are rather homogeneous with a roughness of about 1 nm estimated in an area of 1x1 µm^2 from the AFM topography images taken at the top of one line. The thickness of the PEDOT:PSS films scales linearly with the number of inkjet deposited layers as it is shown

in Figure 3.22. These results emphasize the additive character of the inkjet deposition forming PEDOT:PSS thin films. From Figure 3.21.i to Figure 3.21.l a curious effect in the surface of the films can be seen; the height of the printed lines seems to increase with the number of layers deposited beneath. The average distances between the maximum and the minimum point of every horizontal line of Figure 3.21.e-h are represented in Figure 3.22. Taking into account that the quantity of material deposited in every layer is the same, the increase of the height of these lines suggests a worst compactness between layers due to the appearance of interfacial capsules of air or water remaining during printing process.

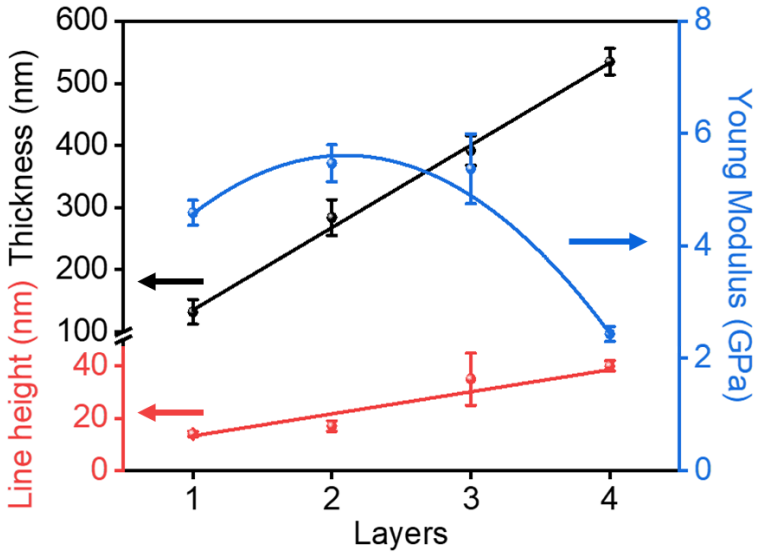

Figure 3.22 (●, left y-axis) Thickness of the film, (●, left y-axis) height of the printed line and (●, right y-axis) Young modulus versus the number of PEDOT:PSS inkjet deposited layers over ITO. Lines and parabola for the Young Modulus data are guides for the eye.

3.3.2 Homogeneity of mechanical and electrical properties of the inkjet printed films

Nanomechanical properties of the inkjet printed PEDOT:PSS films were studied following the method described in section 2.3.1.1.4. PeakForce-QNM gives information on the Young Modulus of the material by using the Dejarguin-Muller Toporov (DMT) model. Figures 3.23.a and b show PF-QNM images of topography and DMT modulus respectively for one PEDOT:PSS layer deposited onto ITO. The measurements were done between two consecutive inkjet printed lines including the joint region. It is clear that in spite of the relatively discontinuous topographical profile (Figure 3.23.c, black curve), the DMT modulus (blue curve) remains almost constant. This result indicates that the welding between two consecutive lines of inkjet deposited PEDOT:PSS

is rather good providing a homogeneous behavior from the perspective of its mechanical properties. This behavior is essentially similar for PEDOT:PSS films with more layers.

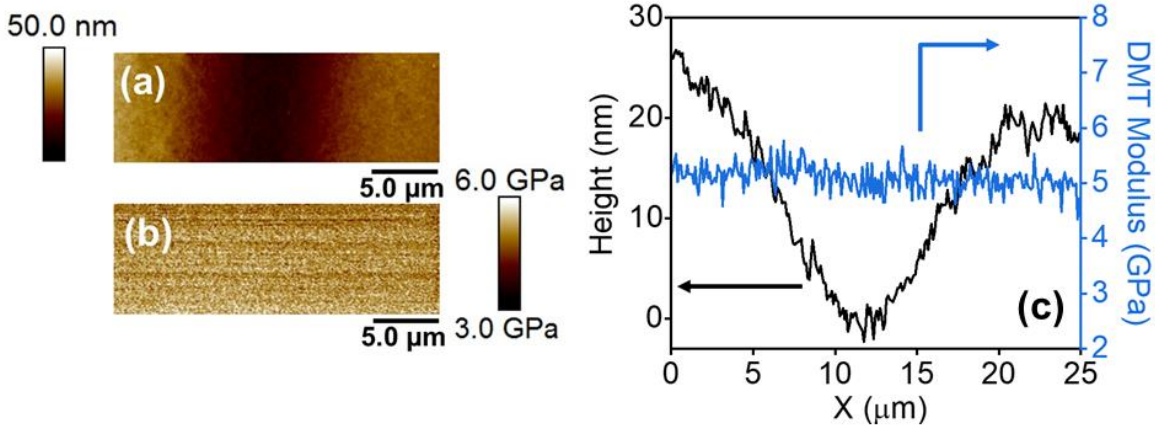

Figure 3.23 (a) Peak Force-QNM topography image and **(b)** DMT elastic modulus for one layer PEDOT:PSS film inkjet deposited on ITO. **(c)** Topographical (black curve) and DMT modulus profile (blue curve) across a perpendicular direction to the printed lines.

Data for Young's modulus measured for films with a different number of layers are reported in Figure 3.22. The modulus values range from 4.6 ± 0.2 GPa for the 1-layer system to 2.4 ± 0.1 GPa for the 4-layers one reaching a maximum of around 5.5 GPa for intermediate thick samples. These values measured for inkjet deposited PEDOT:PSS films compare well with the theoretical values of 3.79 GPa ± 0.45 GPa and of 4.23 GPa ± 0.50 GPa for PEDOT and PSS respectively[51]. However, they are higher than those in the 1-3 GPa range reported for free-standing films[29,48,49,52], microfibers of 10 µm in diameter[53] and for supported films 50 nm thick. The overall higher values obtained here suggest that the intrinsic additive nature of the inkjet deposited films leads to a higher ionic interaction between PEDOT and PSS segments that results in a more entangled structure, with enhanced mechanical properties. This effect has been previously observed for polyelectrolyte multilayers and has been proposed to be due to the ionic bonding between the layers[54]. Due to the relatively high thickness of the films, PEDOT:PSS grains are expected to organize themselves into a pancake-like structure with improved mechanical properties[29,55]. According to Greco et al[49], ultra-thin films with thicknesses between 30 and 80 nm have poorer mechanical properties than thicker ones because less PEDOT:PSS grains can pile up along the film thickness, yielding lower values of Young Modulus (≈1 GPa). In thicker films, however, grains can distribute forming a layered 'pancake-like' structure[56], yielding improved mechanical properties and a higher Young Modulus value. Another reason to be taken into account is that in previous reports, PEDOT-to-PSS ratios of 0.4-0.8 were used[53,57], while in our case this ratio is of 0.17 (see Table 2.6). Since the Young Modulus theoretical value of PSS is larger than PEDOT one[51], it is reasonable that more PSS content in the sample renders to a higher Young Modulus

average value. As the number of layers increases there is a decrease of Young Modulus (Figure 3.22) that can be related with a less mechanical stability caused by a lack of compaction between layers, an effect previously hypothesized in Figure 3.21.i-l and Figure 3.22 where an increase in the height of the printed lines suggested a lack of compactness between layers. This effect leads to a decrease of the modulus once it can counterbalance that of the ionic interaction previously described.

Considering the characteristic continuous lines texture of the inkjet PEDOT:PSS (Figure 3.21.a-d), additional C-AFM measurements were carried out between two consecutive printed lines including joint region in between them. The results are shown in Figure 3.24. Similarly as for the previously discussed case of mechanical properties, here it is also clear that in spite of the relatively discontinuous topographical profile (Figure 3.24.c, black curve), the C-AFM current displays a nearly constant value. This behavior is qualitative similar to thicker PEDOT:PSS films with more layers. This result, in conjunction with the similar one related to the mechanical properties (Figure 3.23), further supports that the welding between two consecutive lines of inkjet deposited PEDOT:PSS is rather efficient and provides homogeneous both mechanical and electrical properties.

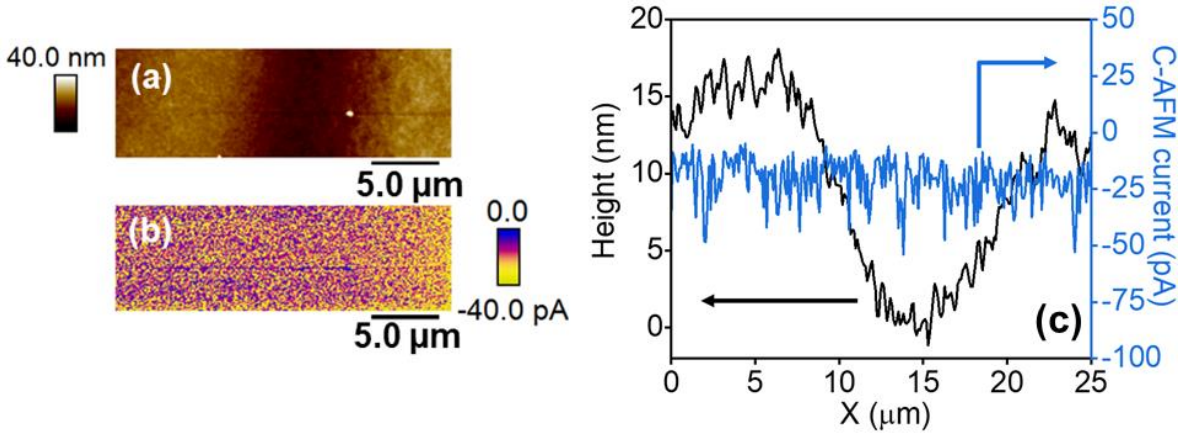

Figure 3.24 (a) Contact mode AFM topography image and **(b)** electrical current C-AFM image for one layer PEDOT:PSS film inkjet deposited on ITO. **(c)** Topographical (black curve) and electrical current profile (blue curve) across a perpendicular direction to the printed lines. DC voltage applied=-3V

3.3.3 Internal order of PEDOT:PSS films as revealed by GIWAXS

The inner structure of the inkjet deposited PEDOT:PSS films was examined by GIWAXS. The measurements were performed with incident angles between 0.1º and 0.2º which are below the critical angle of ITO[58]. One of the issues upon investigating these kind of samples by GIWAXS

comes from the strong diffraction features exhibited by ITO as shown in Figure 3.25.b and the weak scattering of the PEDOT:PSS (Figure 3.25.a).

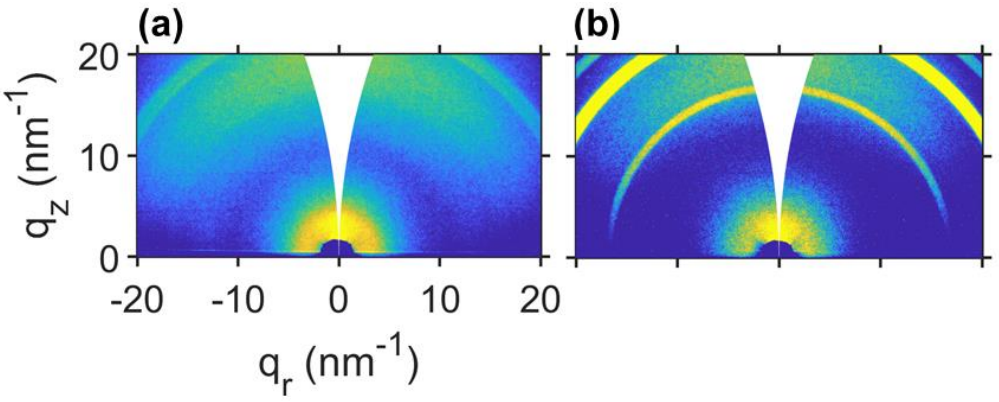

Figure 3.25 GIWAXS intensity patterns of **(a)** 4 layers of inkjet deposited PEDOT:PSS, **(b)** ITO substrate. Air background has been subtracted. Intensity is in logarithmic scale.

Therefore, at q>10 nm^{-1} the scattered intensity by PEDOT:PSS films cannot be separated from scattered intensity from the substrate. Therefore, the low-q range (q<10 nm^{-1}) from GIWAXS patterns was investigated. At this range, the intensity from the substrate is negligible but the scattered intensity by the air is important. Therefore, the GIWAXS patterns for the PEDOT:PSS samples were corrected for air background scattering. Figure 3.26 shows background subtracted GIWAXS patterns for ITO substrate and selected inkjet deposited PEDOT:PSS samples.

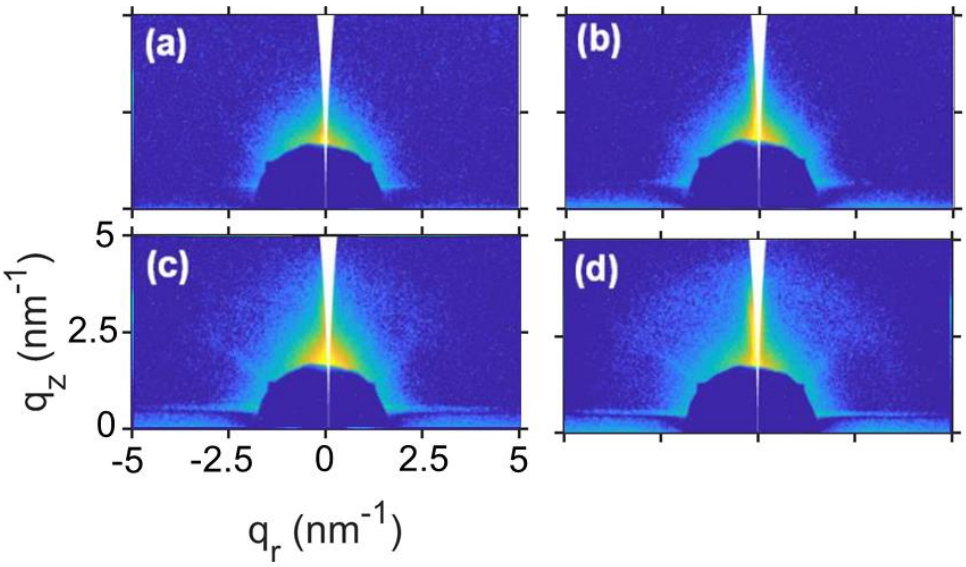

Figure 3.26 GIWAXS intensity patterns taken at an incident angle of 0.2° of **(a)** ITO-covered glass, **(b)** 1, **(c)** 2 and **(d)** 4 inkjet deposited layers of PEDOT:PSS. Air background has been subtracted. Intensity is in logarithmic scale.

Patterns of ITO substrate (Figure 3.26.a) and one layer of PEDOT:PSS (Figure 3.26.b) exhibit no significant scattering aside from an intense spike from the reflected beam around the beamstop which is characteristic of this type of samples[56]. When the films contain more than one layer (Figure 3.26.c-d) a scattering arc located in the meridional region starts to be detected. GIWAXS patterns were analyzed using azimuthal integrations to obtain intensity profiles as a function of q. Figure 3.27 shows the plots of these intensity profiles for films with one to four PEDOT:PSS layers and for ITO substrate.

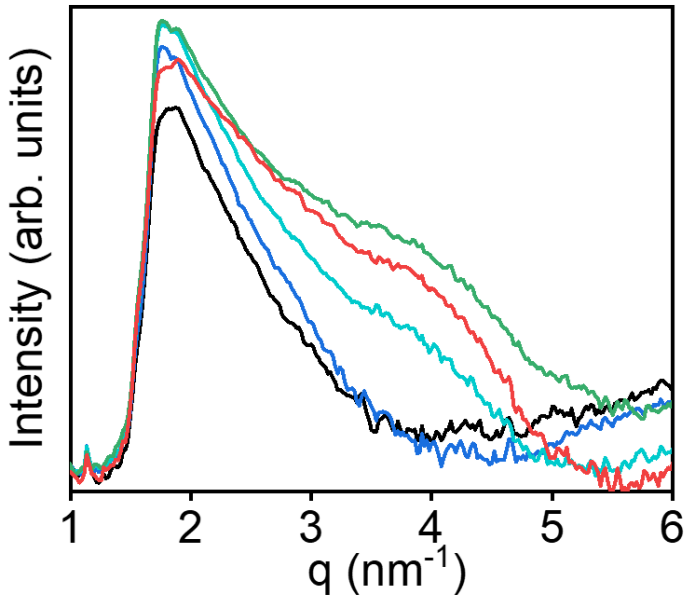

Figure 3.27 Integrated scattered intensity as a function of the module of the scattering vector q for the subtracted GIWAXS patterns of ITO (black curve) and 1 (blue curve), 2 (cyan curve), 3 (green curve) and 4 (red curve) inkjet deposited layers of PEDOT:PSS on ITO.

From two to four layers, the plot exhibits an excess of scattered intensity between q≈2.5 nm^{-1} and 5 nm^{-1} (Figure 3.27) corresponding to real space distances between d≈2.5 nm and 1.3 nm. This excess of scattering could be composed of different reflections. The one corresponding to the stacking distance between lamellas of alternating PEDOT and PSS segment chains d_{100} has been reported to be d≈2.2 nm (q=2.8 nm^{-1}), coherent with the chain widths of PEDOT (0.75 nm) and PSS (1.55 nm)[59]. In addition, reflections proposed to be associated with PSS interdigitation packing (d= 1.37 nm, q= 4.6 nm^{-1}) and with PEDOT lamellar stacking (d= 1.4 nm, q= 4.5 nm^{-1}) also have been localized within this range[60].

Radial integrations of the GIWAXS patterns in the whole azimuthal range and between q=3 nm^{-1} and q=5 nm^{-1} show an excess of intensity in the out-of-plane direction in comparison to that in the in-plane direction (Figure 3.28). This result suggests a slightly preferential “edge-on” disposition of the PEDOT:PSS lamellae.

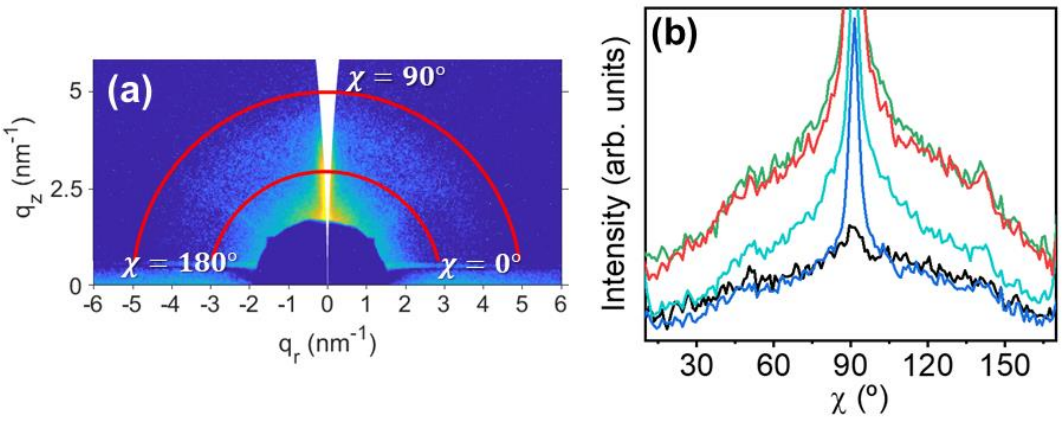

Figure 3.28 (a) GIWAXS of 4 layers of PEDOT:PSS indicating the cake used for the radial integration. **(b)** Intensity profile as a function of azimuthal angle χ of inkjet printed PEDOT:PSS samples with different layers: 1 layer (blue curve), 2 layers (cyan curve), 3 layers (green curve), 4 layers (red curve) and ITO (black curve). Intensity is in logarithmic scale.

3.4 Conclusions

In this chapter, different polymeric systems in the form of thin films have been studied. It is clear from each particular system that the deposition method and the conditions during film formation are able to change the material features in the films like crystallinity, molecular orientation or film morphology at the nanoscale. The conclusions extracted for each of the studied systems are the following:

- In the first section, we have proved the suitability of P3HT/P(VDF-TrFE) bilayers as PFM writable surfaces. The role of the P3HT layer thickness and its crystalline orientation in the observed polarization switching has been discussed. It has been observed that the presence of the P3HT layer produces an enhancement of the PFM contrast on the upper layer of P(VDF-TrFE), that is related with a stabilization of the vertical component of the polarization of the P(VDF-TrFE) crystals. The in-plane switching depends on the orientation of the P3HT crystals. A decrease in the switching voltage when a P3HT thin film is implemented between the doped silicon and the ferroelectric layer is observed and can be attributed to the built-in field in the interphase between the semiconducting and the ferroelectric polymer.

- In the second section, the structural and morphological changes of dispersions and thin films of PEDOT:PSS with high boiling point additives have been investigated. Ethylene glycol (EG) has a strong impact on the PEDOT:PSS dispersion considering that PEDOT:PSS grains are formed by cores of PEDOT with a shell of PSS. We have found

a two-stage mechanism of the EG effect on the PEDOT:PSS dispersions. First, at low EG concentrations, a compaction of PEDOT:PSS grains and thinning of their shells is observed. In a second stage, at larger EG concentrations, the additive acts as an intermediate layer between PEDOT-core and PSS-shell producing a swelling of the grains and also a phase segregation induced by the screening effect of the additive between PEDOT and PSS segments. Glycerol (G) follows the same path as EG, though the effect is less pronounced. DMSO seems to have an opposite effect than EG and G, while the effects of G and DMSO almost compensates each other when adding blended G+DMSO to the PEDOT:PSS dispersion. The effect produced by the additives in the dispersion is also reflected in the PEDOT:PSS thin films. An increase of film thickness and roughness with increasing additive concentration is observed for all the additives investigated. The highest roughness is obtained for high concentrations of G and G+DMSO; we assign this result to the higher boiling point of G, allowing it to act longer on the PEDOT:PSS thin films after processing.

- In the third section, the mechanical and electrical properties of inkjet deposited PEDOT:PSS on ITO substrates have been investigated by local probe methods. Large areas with a broad range of thicknesses of PEDOT:PSS on ITO can be obtained by inkjet printing with both homogeneous electrical and mechanical properties. The Young modulus of the PEDOT:PSS deposited films as revealed by QNM mode of the AFM approaches the theoretical value. In spite of the line texture observed under optical microscopy in the inkjet films, the welding between lines is very efficient, providing across the junction of consecutive lines both homogeneous Young Modulus and electrical current values. These results provide support for the use of inkjet methods for the extensive area processing of PEDOT:PSS in the form of thin films with adequate electrical conductivity and mechanical stability.

3.5 References

(1) Martínez-Tong, D. E.; Rodríguez-Rodríguez, Á.; Nogales, A.; García-Gutiérrez, M. C.; Pérez-Murano, F.; Llobet, J.; Ezquerra, T. A.; Rebollar, E. Laser Fabrication of Polymer Ferroelectric Nanostructures for Nonvolatile Organic Memory Devices. *ACS Appl. Mater. Interfaces* **2015**, *7* (35), 19611–19618. https://doi.org/10.1021/acsami.5b05213.

(2) Xu, H.; Zhong, J.; Liu, X.; Chen, J.; Shen, D. Ferroelectric and Switching Behavior of Poly(Vinylidene Fluoride-Trifluoroethylene) Copolymer Ultrathin Films with Polypyrrole Interface. *Appl. Phys. Lett.* **2007**, *90* (9), 88–91. https://doi.org/10.1063/1.2710477.

(3) Xu, H.; Liu, X.; Fang, X.; Xie, H.; Li, G.; Meng, X.; Sun, J.; Chu, J. Domain Stabilization Effect of Interlayer on Ferroelectric Poly(Vinylidene Fluoride-Trifluoroethylene) Copolymer Ultrathin Film. *J. Appl. Phys.* **2009**, *105* (3). https://doi.org/10.1063/1.3075897.

(4) Zhao, X. L.; Tian, B. B.; Liu, B. L.; Wang, J. L.; Han, L.; Sun, J. L.; Meng, X. J.; Chu, J. H. Self-Polarization in Ultrathin Langmuir-Blodgett Polymer Films. *Thin Solid Films* **2014**, *551*, 171–173. https://doi.org/10.1016/j.tsf.2013.11.106.

(5) Chen, S.; Li, X.; Yao, K.; Tay, F. E. H.; Kumar, A.; Zeng, K. Self-Polarized Ferroelectric PVDF Homopolymer Ultra-Thin Films Derived from Langmuir-Blodgett Deposition. *Polymer (Guildf).* **2012**, *53* (6), 1404–1408. https://doi.org/10.1016/j.polymer.2012.01.058.

(6) Fu, Z.; Zhang, J.; Weng, J.; Chen, W.; Jiang, Y.; Zhu, G. Piezoresponse Force Microscopy Study on Ferroelectric Polarization of Ferroelectric Polymer Thin Films with Various Structural Configurations. *AIP Adv.* **2015**, *5* (9). https://doi.org/10.1063/1.4931998.

(7) Stengel, M.; Vanderbilt, D.; Spaldin, N. A. Enhancement of Ferroelectricity at Metal-Oxide Interfaces. *Nat. Mater.* **2009**, *8* (5), 392–397. https://doi.org/10.1038/nmat2429.

(8) Yang, M.; Kc, A.; Garcia-Castro, A. C.; Borisov, P.; Bousquet, E.; Lederman, D.; Romero, A. H.; Cen, C. Room Temperature Ferroelectricity in Fluoroperovskite Thin Films. *Sci. Rep.* **2017**, *7* (1), 1–9. https://doi.org/10.1038/s41598-017-07834-0.

(9) Yuan, Y.; Reece, T. J.; Sharma, P.; Poddar, S.; Ducharme, S.; Gruverman, A.; Yang, Y.; Huang, J. Efficiency Enhancement in Organic Solar Cells with Ferroelectric Polymers. *Nat. Mater.* **2011**, *10* (4), 296–302. https://doi.org/10.1038/nmat2951.

(10) Naber, R. C. G.; Blom, P. W. M.; Marsman, A. W.; De Leeuw, D. M. Low Voltage Switching of a Spin Cast Ferroelectric Polymer. *Appl. Phys. Lett.* **2004**, *85* (11), 2032–2034. https://doi.org/10.1063/1.1788885.

(11) Roth, R.; Koch, M.; Schaab, J.; Lilienblum, M.; Syrowatka, F.; Band, T.; Thurn-Albrecht, T.; Dörr, K. Aligning In-Plane Polarization Multiplies Piezoresponse in P(VDF-TrFE) Films on Graphite. *New J. Phys.* **2018**, *20* (10), 103044. https://doi.org/10.1088/1367-2630/aae8b6.

(12) Lee, J. S.; Prabu, A. A.; Kim, K. J. Annealing Effect upon Chain Orientation, Crystalline Morphology, and Polarizability of Ultra-Thin P(VDF-TrFE) Film for Nonvolatile Polymer Memory Device. *Polymer (Guildf).* **2010**, *51* (26), 6319–6333. https://doi.org/10.1016/j.polymer.2010.10.053.

(13) Sharma, P.; Wu, D.; Poddar, S.; Reece, T. J.; Ducharme, S.; Gruverman, A. Orientational Imaging in Polar Polymers by Piezoresponse Force Microscopy. *J. Appl. Phys.* **2011**, *110* (5). https://doi.org/10.1063/1.3623765.

(14) Tremel, K.; Ludwigs, S. Morphology of P3HT in Thin Films in Relation to Optical and Electrical Properties. In *P3HT Revisited–From Molecular Scale to Solar Cell Devices*; Springer, 2014; pp 39–82.

(15) Heimel, G.; Salzmann, I.; Duhm, S.; Rabe, J. P.; Koch, N. Intrinsic Surface Dipoles Control the Energy Levels of Conjugated Polymers. *Adv. Funct. Mater.* **2009**, *19* (24), 3874–3879. https://doi.org/10.1002/adfm.200901025.

(16) Duhm, S.; Heimel, G.; Salzmann, I.; Glowatzki, H.; Johnson, R. L.; Vollmer, A.; Rabe, J. P.; Koch, N. Orientation-Dependent Ionization Energies and Interface Dipoles in Ordered Molecular Assemblies. *Nat. Mater.* **2008**, *7* (4), 326–332. https://doi.org/10.1038/nmat2119.

(17) Van Oss, C. J.; Good, R. J. Prediction of the Solubility of Polar Polymers by Means of Interfacial Tension Combining Rules. *Langmuir* **1992**, *8* (12), 2877–2879. https://doi.org/10.1021/la00048a006.

(18) Van Oss, C. J.; Chaudhury, M. K.; Good, R. J. Interfacial Lifshitz-van Der Waals and Polar Interactions in Macroscopic Systems. *Chem. Rev.* **1988**, *88* (6), 927–941. https://doi.org/10.1021/cr00088a006.

(19) Hadziioannou, G.; Fleury, G.; Pavlopoulou, E.; Dilhaire, S.; Petsagkourakis, I.; Portale, G.; Kuropatwa, B. A. Structurally-Driven Enhancement of Thermoelectric Properties within Poly(3,4-Ethylenedioxythiophene) Thin Films. *Sci. Rep.* **2016**, *6* (1). https://doi.org/10.1038/srep30501.

(20) Yimer, Y. Y.; Yang, B.; Bhatta, R. S.; Tsige, M. Interfacial and Wetting Properties of Poly(3-Hexylthiophene)-Water Systems. *Chem. Phys. Lett.* **2015**, *635*, 139–145. https://doi.org/10.1016/j.cplett.2015.06.055.

(21) Ouyang, J. "Secondary Doping" Methods to Significantly Enhance the Conductivity of PEDOT:PSS for Its Application as Transparent Electrode of Optoelectronic Devices. *Displays* **2013**, *34* (5), 423–436. https://doi.org/10.1016/j.displa.2013.08.007.

(22) Palumbiny, C. M.; Heller, C.; Schaffer, C. J.; Körstgens, V.; Santoro, G.; Roth, S. V.; Müller-Buschbaum, P. Molecular Reorientation and Structural Changes in Cosolvent-Treated Highly Conductive PEDOT:PSS Electrodes for Flexible Indium Tin Oxide-Free Organic Electronics. *J. Phys. Chem. C* **2014**, *118* (25), 13598–13606. https://doi.org/10.1021/jp501540y.

(23) Ouyang, L.; Musumeci, C.; Jafari, M. J.; Ederth, T.; Inganäs, O. Imaging the Phase Separation between PEDOT and Polyelectrolytes during Processing of Highly Conductive PEDOT:PSS Films. *ACS Appl. Mater. Interfaces* **2015**, *7* (35), 19764–19773. https://doi.org/10.1021/acsami.5b05439.

(24) Choudhury, P. K.; Bagchi, D.; Sangeeth, C. S. S.; Menon, R. Modified Conformation and Physical Properties in Conducting Polymers Due to Varying Conjugation and Solvent Interactions. *J. Mater. Chem.* **2011**, *21* (5), 1607–1614. https://doi.org/10.1039/c0jm02304c.

(25) Murphy, R. J.; Weigandt, K. M.; Uhrig, D.; Alsayed, A.; Badre, C.; Hough, L.; Muthukumar, M. Scattering Studies on Poly(3,4-Ethylenedioxythiophene)-Polystyrenesulfonate in the Presence of Ionic Liquids. *Macromolecules* **2015**, *48* (24), 8989–8997. https://doi.org/10.1021/acs.macromol.5b02320.

(26) Bagchi, D.; Menon, R. Conformational Modification of Conducting Polymer Chains by Solvents: Small-Angle X-Ray Scattering Study. *Chem. Phys. Lett.* **2006**, *425* (1–3), 114–117. https://doi.org/10.1016/j.cplett.2006.05.014.

(27) Takano, T.; Masunaga, H.; Fujiwara, A.; Okuzaki, H.; Sasaki, T. PEDOT Nanocrystal in Highly Conductive PEDOT:PSS Polymer Films. *Macromolecules* **2012**, *45* (9), 3859–3865. https://doi.org/10.1021/ma300120g.

(28) Roe, R.-J.; Roe, R. J. *Methods of X-Ray and Neutron Scattering in Polymer Science*; Oxford university press New York, 2000; Vol. 739.

(29) Lang, U.; Muller, E.; Naujoks, N.; Dual, J. Microscopical Investigations of PEDOT:PSS Thin Films. *Adv. Funct. Mater.* **2009**, *19* (8), 1215–1220. https://doi.org/10.1002/adfm.200801258.

(30) Feigin, L. A.; Svergun, D. I. *Structure Analysis by Small-Angle X-Ray and Neutron Scattering*; Springer, 1987; Vol. 1.

(31) Ouyang, J.; Xu, Q.; Chu, C. W.; Yang, Y.; Li, G.; Shinar, J. On the Mechanism of Conductivity Enhancement in Poly(3,4- Ethylenedioxythiophene):Poly(Styrene Sulfonate) Film through Solvent Treatment. *Polymer (Guildf).* **2004**, *45* (25), 8443–8450. https://doi.org/10.1016/j.polymer.2004.10.001.

(32) Alemu Mengistie, D.; Wang, P. C.; Chu, C. W. Effect of Molecular Weight of Additives on the Conductivity of PEDOT:PSS and Efficiency for ITO-Free Organic Solar Cells. *J. Mater. Chem. A* **2013**, *1* (34), 9907–9915. https://doi.org/10.1039/c3ta11726j.

(33) Horkay, F.; Hammouda, B. Small-Angle Neutron Scattering from Typical Synthetic and Biopolymer Solutions. *Colloid Polym. Sci.* **2008**, *286* (6–7), 611–620. https://doi.org/10.1007/s00396-008-1849-3.

(34) Danielsen, S. P. O.; Sanoja, G. E.; McCuskey, S. R.; Hammouda, B.; Bazan, G. C.; Fredrickson, G. H.; Segalman, R. A. Mixed Conductive Soft Solids by Electrostatically Driven Network Formation of a Conjugated Polyelectrolyte. *Chem. Mater.* **2018**, *30* (4), 1417–1426. https://doi.org/10.1021/acs.chemmater.7b05303.

(35) Yan, H.; Okuzaki, H. Effect of Solvent on PEDOT/PSS Nanometer-Scaled Thin Films: XPS and STEM/AFM Studies. *Synth. Met.* **2009**, *159* (21–22), 2225–2228. https://doi.org/10.1016/j.synthmet.2009.07.032.

(36) Soleimani-Gorgani, A. Co-Solvents Roles in PEDOT:PSS Ink-Jet Inks. *Adv. Nat. Sci. Nanosci. Nanotechnol.* **2018**, *9* (2), 25009. https://doi.org/10.1088/2043-6254/aac2a0.

(37) Pasha, A.; Khasim, S.; Al-Hartomy, O. A.; Lakshmi, M.; Manjunatha, K. G. Highly Sensitive Ethylene Glycol-Doped PEDOT-PSS Organic Thin Films for LPG Sensing. *RSC Adv.* **2018**, *8* (32), 18074–18083. https://doi.org/10.1039/c8ra01061g.

(38) Xiao, T.; Cui, W.; Anderegg, J.; Shinar, J.; Shinar, R. Simple Routes for Improving Polythiophene:Fullerene-Based Organic Solar Cells. *Org. Electron. physics, Mater. Appl.* **2011**, *12* (2), 257–262. https://doi.org/10.1016/j.orgel.2010.11.008.

(39) Rahman, Z. A.; Sulaiman, K.; Shuhaimi, A.; Rusop, M. PEDOT:PSS Thin Film as Transparent Electrode in ITO-Free Organic Solar Cell. *Adv. Mater. Res.* **2012**, *501* (April), 252–256. https://doi.org/10.4028/www.scientific.net/amr.501.252.

(40) Unuma, T.; Yoshikawa, M.; Nakamura, A.; Kishida, H. Segmentation of Conducting Domains in PEDOT:PSS Films Induced by an Additive for Conductivity Enhancement. *Appl. Phys. Express* **2016**, *9* (5), 51601. https://doi.org/10.7567/APEX.9.051601.

(41) Singh, V.; Arora, S.; Arora, M.; Sharma, V.; Tandon, R. P. Characterization of Doped PEDOT: PSS and Its Influence on the Performance and Degradation of Organic Solar Cells. *Semicond. Sci. Technol.* **2014**, *29* (4), 45020. https://doi.org/10.1088/0268-1242/29/4/045020.

(42) Palumbiny, C. M.; Liu, F.; Russell, T. P.; Hexemer, A.; Wang, C.; Müller-Buschbaum, P. The Crystallization of PEDOT:PSS Polymeric Electrodes Probed in Situ during Printing. *Adv. Mater.* **2015**, *27* (22), 3391–3397. https://doi.org/10.1002/adma.201500315.

(43) Davis, C. S.; Hillgartner, K. E.; Han, S. H.; Seppala, J. E. Mechanical Strength of Welding Zones Produced by Polymer Extrusion Additive Manufacturing. *Addit. Manuf.* **2017**, *16*, 162–166. https://doi.org/10.1016/j.addma.2017.06.006.

(44) Natori, A. Y.; Canestraro, C. D.; Roman, L. S.; Ceschin, A. M. Modification of the Sheet Resistance of Ink Jet Printed Polymer Conducting Films by Changing the Plastic Substrate. *Mater. Sci. Eng. B Solid-State Mater. Adv. Technol.* **2005**, *122* (3), 231–235. https://doi.org/10.1016/j.mseb.2004.11.026.

(45) Wilson, P.; Lekakou, C.; Watts, J. F. A Comparative Assessment of Surface Microstructure and Electrical Conductivity Dependence on Co-Solvent Addition in Spin Coated and Inkjet Printed Poly(3,4-Ethylenedioxythiophene):Polystyrene Sulphonate (PEDOT:PSS). *Org. Electron. physics, Mater. Appl.* **2012**, *13* (3), 409–418. https://doi.org/10.1016/j.orgel.2011.11.011.

(46) Eom, S. H.; Senthilarasu, S.; Uthirakumar, P.; Yoon, S. C.; Lim, J.; Lee, C.; Lim, H. S.; Lee, J.; Lee, S. H. Polymer Solar Cells Based on Inkjet-Printed PEDOT:PSS Layer. *Org. Electron. physics, Mater. Appl.* **2009**, *10* (3), 536–542. https://doi.org/10.1016/j.orgel.2009.01.015.

(47) Eom, S. H.; Park, H.; Mujawar, S. H.; Yoon, S. C.; Kim, S. S.; Na, S. I.; Kang, S. J.; Khim, D.; Kim, D. Y.; Lee, S. H. High Efficiency Polymer Solar Cells via Sequential Inkjet-Printing of PEDOT:PSS and P3HT:PCBM Inks with Additives. *Org. Electron. physics, Mater. Appl.* **2010**, *11* (9), 1516–1522. https://doi.org/10.1016/j.orgel.2010.06.007.

(48) Lang, U.; Naujoks, N.; Dual, J. Mechanical Characterization of PEDOT:PSS Thin Films. *Synth. Met.* **2009**, *159* (5–6), 473–479. https://doi.org/10.1016/j.synthmet.2008.11.005.

(49) Greco, F.; Zucca, A.; Taccola, S.; Menciassi, A.; Fujie, T.; Haniuda, H.; Takeoka, S.; Dario, P.; Mattoli, V. Ultra-Thin Conductive Free-Standing PEDOT/PSS Nanofilms. *Soft Matter* **2011**, *7* (22), 10642. https://doi.org/10.1039/c1sm06174g.

(50) Jukes, P. C.; Martin, S. J.; Higgins, A. M.; Geoghegan, M.; Jones, R. A. L.; Langridge, S.; Wehrum, A.; Kirchmeyer, S. Controlling the Surface Composition of Poly(3,4-Ethylene Dioxythiophene)–Poly(Styrene Sulfonate) Blends by Heat Treatment. *Adv. Mater.* **2004**, *16* (910), 807–811. https://doi.org/10.1002/adma.200306487.

(51) Tank, D.; Lee, H. H.; Khang, D. Y. Elastic Moduli of Organic Electronic Materials by the Buckling Method. *Macromolecules* **2009**, *42* (18), 7079–7083. https://doi.org/10.1021/ma900137k.

(52) Lang, U.; Dual, J. Mechanical Properties of the Intrinsically Conductive Polymer Poly(3,4-Ethylenedioxythiophene) Poly(Styrenesulfonate) (PEDOT/PSS). *Key Eng. Mater.* **2007**, *345–346*, 1189–1192. https://doi.org/10.4028/www.scientific.net/KEM.345-346.1189.

(53) Okuzaki, H.; Ishihara, M. Spinning and Characterization of Conducting Microfibers. *Macromol. Rapid Commun.* **2003**, *24* (3), 261–264. https://doi.org/10.1002/marc.200390038.

(54) Pavoor, P. V; Bellare, A.; Strom, A.; Yang, D.; Cohen, R. E. Mechanical Characterization of Polyelectrolyte Multilayers Using Quasi-Static Nanoindentation. *Macromolecules* **2004**, *37*, 4865–4871. https://doi.org/10.1021/ma049777t.

(55) Nardes, A. M.; Kemerink, M.; Janssen, R. A. J.; Bastiaansen, J. A. M.; Kiggen, N. M. M.; Langeveld, B. M. W.; Van Breemen, A. J. J. M.; De Kok, M. M. Microscopic Understanding of the Anisotropic Conductivity of PEDOT:PSS Thin Films. *Adv. Mater.* **2007**, *19* (9), 1196–1200. https://doi.org/10.1002/adma.200602575.

(56) Wang, G.; Huang, W.; Eastham, N. D.; Fabiano, S.; Manley, E. F.; Zeng, L.; Wang, B.; Zhang, X.; Chen, Z.; Li, R.; et al. Aggregation Control in Natural Brush-Printed Conjugated Polymer Films and Implications for Enhancing Charge Transport. *Proc. Natl. Acad. Sci.* **2017**, *114* (47), E10066–E10073. https://doi.org/10.1073/pnas.1713634114.

(57) Borghetti, M.; Serpelloni, M.; Sardini, E.; Pandini, S. Mechanical Behavior of Strain Sensors Based on PEDOT:PSS and Silver Nanoparticles Inks Deposited on Polymer Substrate by Inkjet Printing. *Sensors Actuators, A Phys.* **2016**, *243*, 71–80. https://doi.org/10.1016/j.sna.2016.03.021.

(58) Yang, L. L.; Ge, D. T.; He, X. D.; He, F.; Li, Y. B.; Zhang, S. Grazing Incidence X-Ray Scattering Study of Sol-Gel Derived Indium Tin Oxide Thin Films. *Thin Solid Films* **2009**, *517* (17), 5151–5156. https://doi.org/10.1016/j.tsf.2009.03.047.

(59) Kim, N.; Lee, B. H.; Choi, D.; Kim, G.; Kim, H.; Kim, J. R.; Lee, J.; Kahng, Y. H.; Lee, K. Role of Interchain Coupling in the Metallic State of Conducting Polymers. *Phys. Rev. Lett.* **2012**, *109* (10), 1–5. https://doi.org/10.1103/PhysRevLett.109.106405.

(60) Massonnet, N.; Carella, A.; de Geyer, A.; Faure-Vincent, J.; Simonato, J.-P. Metallic Behaviour of Acid Doped Highly Conductive Polymers. *Chem. Sci.* **2015**, *6* (1), 412–417. https://doi.org/10.1039/C4SC02463J.

Chapter 4. Nanostructuring organic semiconducting thin films by pulsed nanosecond laser

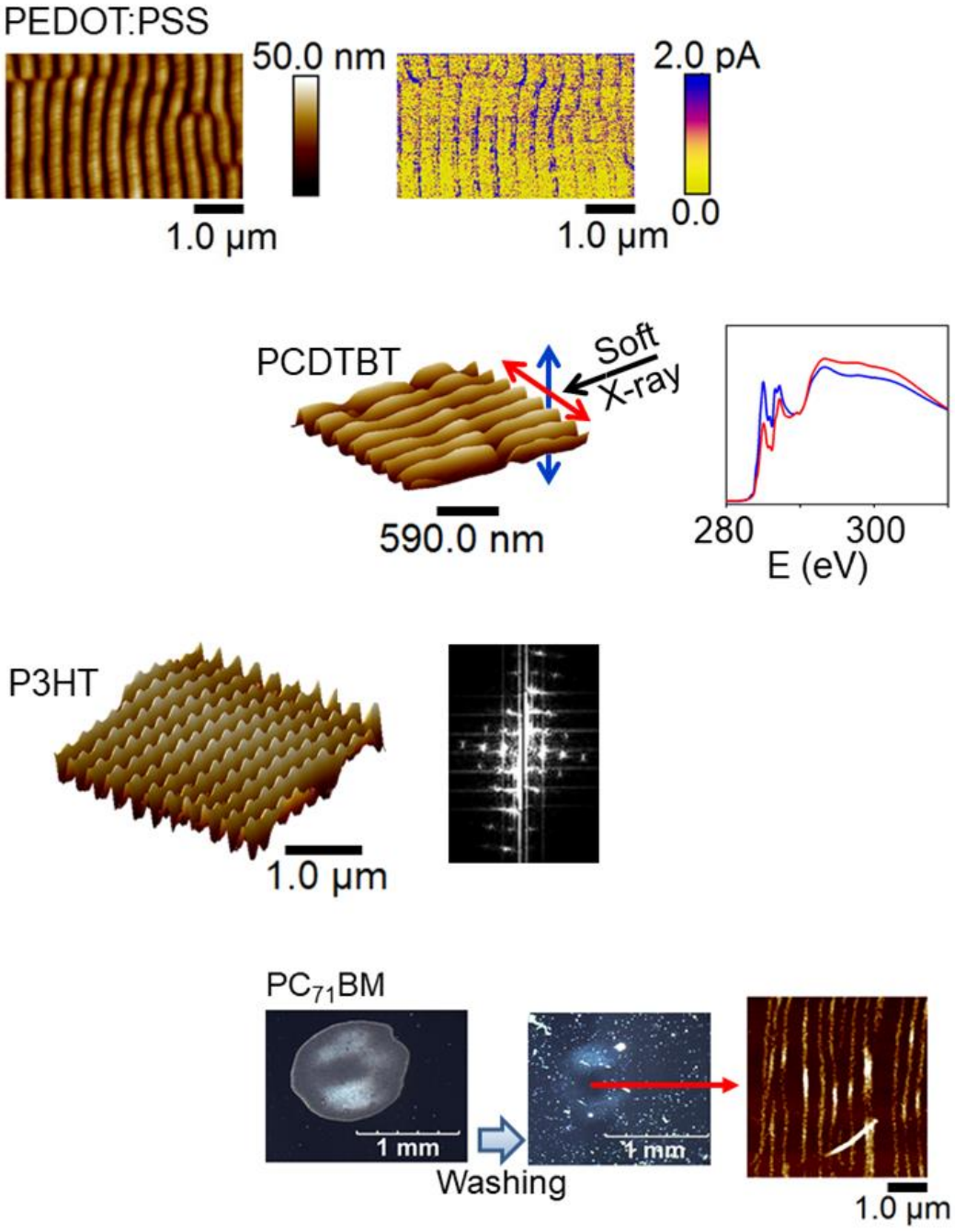

The field of organic electronics demands straightforward methods to produce micro and nanostructured material surfaces[1–3]. In section 2.2.1 we presented a method to nanostructure polymer surfaces using nanosecond laser pulses. Laser irradiation is a free-template procedure; it does not need the fabrication of masks and it can be performed at ambient conditions. In short, the mechanism formation of Laser Induced Periodic Surface Structures (LIPSS) implies the absorption of the laser light by the material at the irradiation wavelength and an interference process supported by a feedback mechanism.

This chapter contains four sections; each one is centered in a certain material or multi-material system that is nanostructured by laser.

- The first section describes the laser nanostructuring process on PEDOT:PSS thin films. A study of the optimal conditions for nanostructuration is given. Also, a systematic study of the morphology and the impact of the irradiation over the electrical properties of this material is presented.

- The second subsection shows a characterization study of P3HT and PCDTBT LIPSS (irradiated in vacuum and air) by TEY-NEXAFS in order to see a direct proof of the impact of laser irradiation over chain orientation in thin films.

- In the third section, we describe the process of obtaining complex patterns by sequential laser irradiation on functional polymer thin films (P3HT and P3HT/P(VDF-TrFE) bilayer system), with a characterization of the patterns and the properties of interest of the material.

- The fourth subsection deals with irradiations as a function of fluence of $PC_{71}BM$ thin films with two harmonics of the same laser, followed by a systematic characterization of the pattern morphology and a post-irradiation process consisting in solvent-washing, leaving a residue in the laser spot with enhanced electrical properties.

4.1 Nanostructuring of PEDOT:PSS thin films by laser and its influence on its electrical properties

In section 1.5.1, it was introduced the technological interest in producing nanostructures of PEDOT:PSS, mainly motivated towards implementation in organic solar cells (OSCs). Several methods to nanostructure PEDOT:PSS have already been reported: by nanoimprint lithography (NIL)[4], by electro-spinning[5] and also by laser methods as Direct Laser Interference Patterning

(DLIP)[6] and selective ablation patterning[7,8]. The laser techniques reported imply an ablation of the material.

In this work we produce for the first time LIPSS in PEDOT:PSS surfaces. LIPSS, as it is described in section 2.2.1, is a non-ablative method to produce nanostructures on polymers through absorption by the material at the wavelength used. Thin films of PEDOT:PSS were prepared by spin-coating. Conditions for preparation of PEDOT:PSS dispersions, either with the original concentration or concentrated, were listed in Table 2.9. Spin-coating conditions were included in Table 2.10.

4.1.1 Ultraviolet and visible absorption of PEDOT:PSS and irradiation conditions

One of the most interesting features of PEDOT:PSS thin films is the high transmittance in the visible region. Figure 4.1 shows the absorption spectrum of a thin film of PEDOT:PSS in the ultraviolet and visible region.

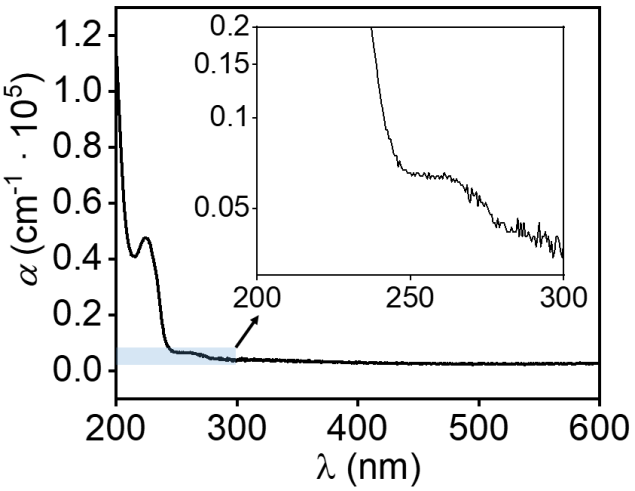

Figure 4.1 Absorption coefficient (***α***) in the UV-VIS range of PEDOT:PSS thin film. The inset is a magnification of the spectrum around λ=250 nm.

PEDOT:PSS is practically transparent in the measured visible range (λ=380-600 nm). In the ultraviolet range various absorption components appear that are associated with the benzene rings of PSS[9], although the thiophene aromatic rings also presents absorption at this region[10]. To form LIPSS, the material must absorb at the wavelength used. For this reason, we use the 4th harmonic of the Nd:YAG laser (λ=266 nm) to irradiate PEDOT:PSS, as long as it presents a window of absorption around 260 nm (see inset of Figure 4.1). The absorption coefficient of PEDOT:PSS at λ=266 nm is $\alpha=6\cdot10^5$ m^{-1}. The fluence chosen was 12.4 mJ·cm^{-2}. Pulses were varied to perform a

systematic study of LIPSS formation. Irradiations were performed at ambient conditions and at normal incidence. Table 4.1 shows the irradiation parameters.

Table 4.1 Irradiation parameters for PEDOT:PSS thin films.

λ (nm)	266			
Fluence (mJ · cm^{-2})	12.4			
Pulses	4800	6000	7200	8400

4.1.2 Formation and morphology of LIPSS on thin films of PEDOT:PSS. Period and depth characterization by AFM and GISAXS

The formation of LIPSS is promoted or limited by several experimental factors. The substrate, through its thermal conductivity and other physical parameters, could be crucial for the efficient growth of LIPSS[11]. Therefore, to compare the effect of the substrate on LIPSS formation, two substrates were used: silicon, as being the typical substrate used in other LIPSS systems investigated in this chapter, and indium-tin oxide (ITO) coated on glass substrates, since ITO is the paradigmatic transparent electrode used in OSCs (see Figure 1.9 of section 1.4.1). Figure 4.2 shows a series of LIPSS on silicon irradiated at a fluence=12.4 mJ·cm^{-2} with various numbers of pulses, and below each AFM image, its corresponding FFT image is shown.

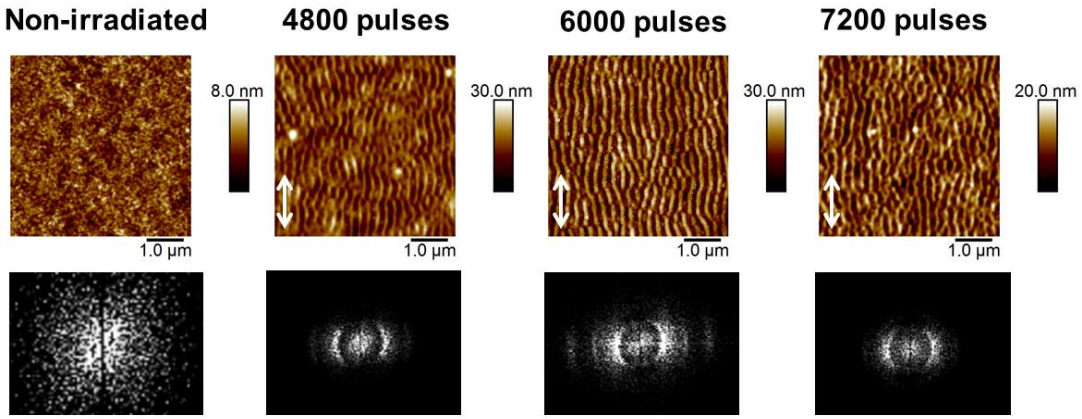

Figure 4.2 Upper row: AFM tapping images of PEDOT:PSS LIPSS on silicon, irradiated with different nanosecond pulses at λ=266 nm, fluence=12.4 mJ·cm^{-2}. The double arrow indicates the laser polarization. **Bottom row**: corresponding FFT images.

It can be seen in Figure 4.2 that at 4800 pulses LIPSS are already formed and the FFT image presents two intensity maxima, at 6000 pulses the order is increased by the appearance of another

additional intensity maximum. However, at 7200 pulses, the order of LIPSS is decreased as its FFT image is similar as the one associated with 4800 pulses. Nanostructures are oriented in the direction of the laser polarization vector (see double arrows) though some bifurcations can be seen between consecutive ripples.

Periods and depths of the samples were obtained from AFM images (Figure 4.2) and represented in Figure 4.3.a.

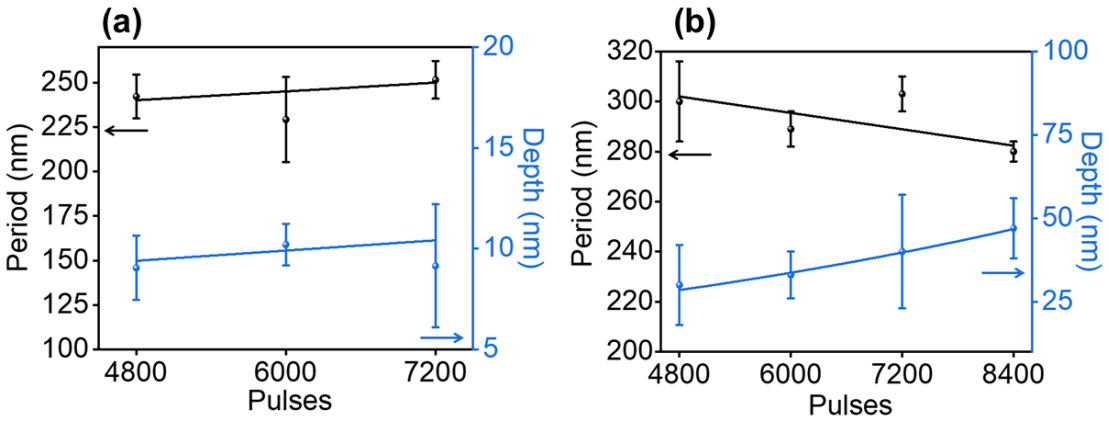

Figure 4.3 Period and depth of LIPSS of PEDOT:PSS deposited on silicon, fluence= 12.4 mJ·cm^{-2}. **(a)** Original PEDOT:PSS, **(b)** concentrated PEDOT:PSS. Lines are added as visual guides.

The period of LIPSS in PEDOT:PSS on silicon (Figure 4.3.a, blue data) is around 230 nm, with a slight tendency to increase with the number of pulses. The depth (black data) slightly increases from the sample irradiated with 4800 pulses to the one irradiated with 6000 pulses. However, taking into account the error value, in the three samples the depth is around the same value (≈10 nm). The only clear difference is the maximized order of the LIPSS in the sample irradiated with 6000 pulses, as shown in the FFT images from Figure 4.2.

It is known that thin films of PS with low enough thickness do not develop well ordered LIPSS when irradiated[11]. It is suggested that a low thickness enhances the effect of heat dissipation through the substrate below the sample whereas a higher thickness reduces this effect and promotes the formation of deeper and better ordered LIPSS. The thickness of these PEDOT:PSS thin films are 60±10 nm (Table 2.10). It is possible that the thickness of these PEDOT:PSS thin films is not high enough to further allow deeper LIPSS.

Considering this suggested coupled effect between the substrate and low thickness samples, thicker PEDOT:PSS films were prepared. Concentrated PEDOT:PSS thin films were prepared following the protocol included in Table 2.9 and the same spin-coating conditions as used for thinner samples (Table 2.10). Figure 4.4 shows AFM topographical images in tapping mode of a

series of LIPSS of concentrated PEDOT:PSS (thickness=160±10 nm) on silicon at a constant fluence and varying the number of pulses.

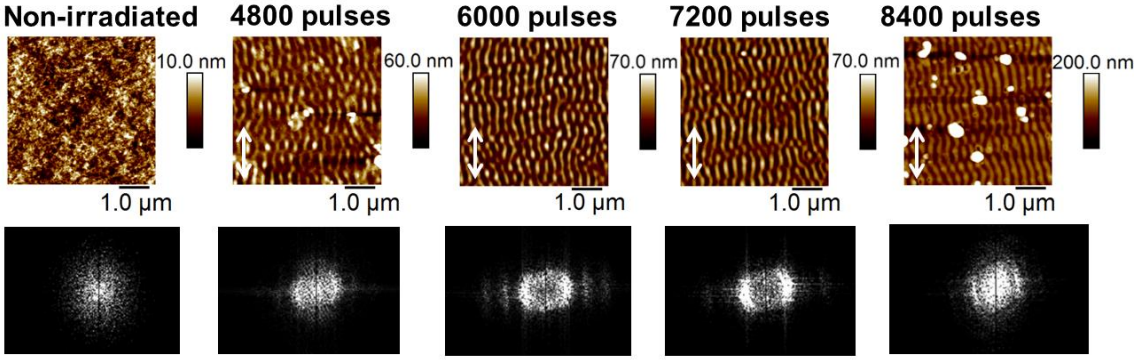

Figure 4.4 Upper row: concentrated PEDOT:PSS LIPSS on silicon, irradiated with different nanosecond pulses at λ=266 nm, fluence=12.4 mJ·cm^{-2}. The double arrow indicates the laser polarization. **Bottom row**: corresponding FFT images.

By using thicker films of PEDOT:PSS, deeper LIPSS are formed. At first glance, the morphology of the LIPSS is well oriented in the direction of the laser polarization vector (see double arrows) and, as in Figure 4.2, they present some degree of bifurcations between ripples and also a droplet-like morphology in some zones of the images, especially in the samples irradiated with 4800 and 6000 pulses. The order of the LIPSS is based on the corresponding FFT images (Figure 4.4, bottom row). Concentrated PEDOT:PSS sample irradiated with 4800 pulses shows two intensity maxima and a slight less intense third one. Samples irradiated with 6000 and 7200 pulses show three intensity maxima whereas the sample irradiated with 8400 pulses starts to lose order, as its FFT shows only two maxima. However, in this sample irradiated with 8400 pulses, the FFT image is affected by the protuberances of the AFM image. The protuberances could be a sign of material degradation. Below these protuberances in the AFM image, it can be seen that the morphology and order of the LIPSS are similar to those in the sample irradiated with 7200 pulses, well oriented and even with lower level of bifurcations.

LIPSS on thicker samples of PEDOT:PSS on silicon depict their higher order over a more extended ranges of pulses since FFT from samples irradiated with 6000 and 7200 pulses show three intensity maxima, whereas on thinner films, only the FFT of the sample irradiated with 6000 pulses shows three maxima.

The period and the depth of this series were measured from AFM images in Figure 4.4 and represented in Figure 4.3.b. The depth of the LIPSS is increased to more than the double compared with the values of Figure 4.3.a and it enhances with the number of pulses until around 50 nm. This suggests that in thinner films on silicon, the lower thickness has a limiting role in the LIPSS

growth. Interestingly enough, the period of the gratings is also increased, (~300 nm), surpassing the wavelength of the laser (λ=266 nm). Longer distances from the silicon would slow down the heat dissipation through the substrate, allowing the LIPSS to grow deeper and more isolated. The final drop of the period could be associated with complete nanostructures, without empty spaces that reduce the average period. A similar effect was observed on PS thin films, in which higher thickness induces an increase in the period and the LIPSS depth[11].

As it was said before, LIPSS in PEDOT:PSS were also fabricated on ITO-coated glass substrates. Figure 4.5 shows AFM tapping images of a series of LIPSS in PEDOT:PSS thin films deposited on ITO as a function of number of pulses; below each AFM image its corresponding Fast Fourier Transform (FFT) is displayed.

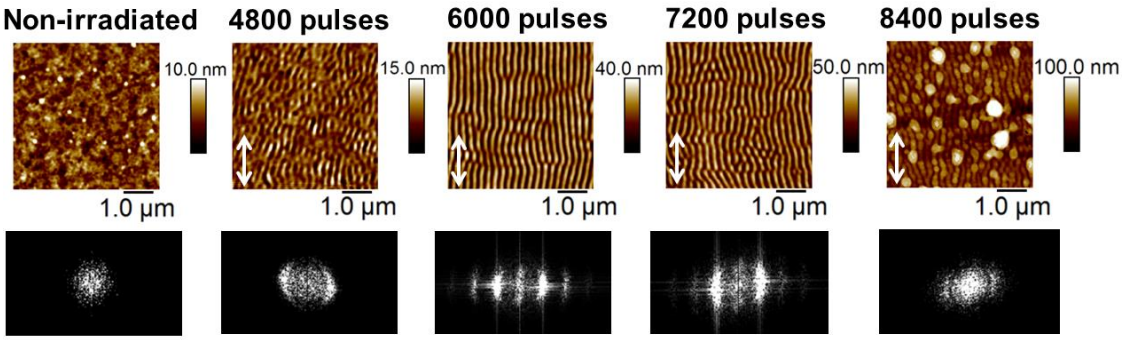

Figure 4.5 Upper row: AFM tapping images of PEDOT:PSS LIPSS on ITO irradiated with different nanosecond pulses at λ=266 nm, fluence=12.4 mJ·cm^{-2}. The double arrow indicates the laser polarization. **Bottom row**: corresponding FFT images.

The AFM image of the sample irradiated with 4800 pulses shows linearly oriented precursors of grating, with low depth. Its FFT presents one intensity maximum. Samples irradiated with 6000 and 7200 pulses present uniformly oriented LIPSS and their corresponding FFT present three intensity maxima. The sample irradiated with 8400 pulses presents protuberances possibly associated with degradation of the material. Its FFT only presents one intensity maxima.

In the case of LIPSS of PEDOT:PSS deposited on ITO, the order follows a similar trend as LIPSS in concentrated PEDOT:PSS on silicon (Figure 4.4), with low ordered LIPSS in the sample irradiated with 4800 pulses, maximizing the order in the sample irradiated with 6000-7200 pulses and with signals of degradation of the material in the sample irradiated with 8400 pulses. The depth and period of the LIPSS were measured from AFM images in Figure 4.5 and represented in Figure 4.6. The depth of LIPSS on ITO (blue data) increases from around 10 nm in the sample irradiated with 4800 pulses until a plateau of around 25±5 nm for the rest of the irradiation conditions. On the other hand, the period of LIPSS (black data) is around ≈240 nm. The period

of the sample irradiated with 8400 pulses is lower, although this value is affected by the degradation of the material shown in the corresponding AFM image (Figure 4.5).

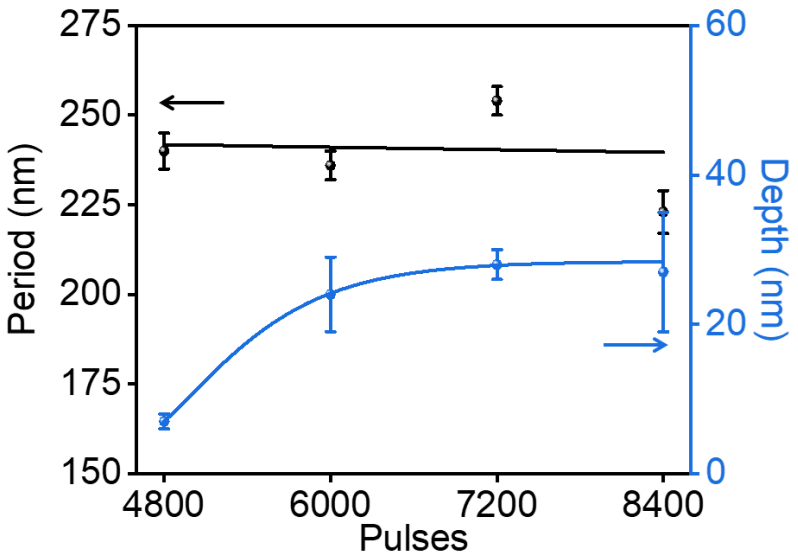

Figure 4.6 Period and depth of LIPSS of PEDOT:PSS spin-coated on ITO as a function of number of pulses, fluence= 12.4 mJ·cm^{-2}. Lines are added as visual guides.

This series of PEDOT:PSS deposited on ITO have similar thicknesses as the thinner films deposited on silicon (≈60 nm). However, LIPSS on ITO are deeper and present better order over a wider range of irradiated pulses, similar as the series of LIPSS on thicker samples deposited on silicon. The substrate has a clear impact on the growth of LIPSS on PEDOT:PSS.

The influence of the substrate on LIPSS formation and growth has been previously studied in terms of thermal and optical parameters[11] of the material and the substrate. We follow the Beer-Lambert law (Equation 4.1) using the absorption coefficient of PEDOT:PSS at 266 nm ($\alpha \approx 6 \cdot 10^5$ m^{-1}) extracted from Figure 4.1.

$$I(z) = I_0 e^{(-\alpha z)} \qquad (\mathbf{4.1})$$

I(z) is the intensity of light at a certain depth (z) from the substrate, I_0 is the intensity of incident light and α is the absorption coefficient of the material at the laser wavelength used. In thinner films of PEDOT:PSS on silicon and ITO, around the 97% of the incident intensity will reach the substrate and around the 91% for the thicker films on silicon. Therefore, the thermal properties of the substrate can be relevant for LIPSS formation. A percentage of this transmitted light is absorbed at the substrate and induced a temperature increase determined by Equation 4.2[11].

$$\Delta T = \frac{F\alpha}{c\rho} = \frac{F\alpha}{C} \qquad (\mathbf{4.2})$$

In Equation 4.2, F is the fluence of the laser, $\boldsymbol{\alpha}$ is the absorption coefficient of the substrate, c the specific heat, ρ the density and C the heat capacity. Thermal and optical properties at λ=266 nm of ITO and silicon are compiled in Table 4.2 together with their references.

Table 4.2 Thermal and optical parameters of ITO and silicon, including the absorption coefficient $\boldsymbol{\alpha}$ at λ=266 nm, heat capacity C and thermal conductivity κ; with references in parentheses.

Substrate	$\boldsymbol{\alpha}$ **(m^{-1})**	**C ($J \cdot m^{-3} \cdot K^{-1}$)**	**κ ($W \cdot m^{-1} \cdot K^{-1}$)**
ITO	$2 \cdot 10^7$ ([12])	$2.58 \cdot 10^6$ ([13])	≈ 4 ([14])
Silicon	$1.97 \cdot 10^8$ ([15])	$1.64 \cdot 10^6$ ([16])	163.3 ([16])

Using Equation 4.2 with F=12.4 $mJ \cdot cm^{-2}$ and the parameters from Table 4.2, the temperature increase on ITO is estimated at 961 K, whereas on silicon was estimated at $1.5 \cdot 10^4$ K. The temperature increase in silicon is higher than in ITO due to its higher absorption coefficient at 266 nm and its lower heat capacity. After this increase of temperature, the heat is dissipated in a time scale depending on the thermal conductivity (Equation 4.3)[17].

$$t_d = \frac{1}{D\alpha^2} = \frac{C}{\kappa\alpha^2} \qquad (\mathbf{4.3})$$

In Equation 4.3, t_d is the thermal diffusion time and D is the thermal diffusivity ($D = \frac{\kappa}{C}$). t_d for ITO substrate was estimated at 1.6 ns, whereas in silicon $t_d \approx 2.6 \cdot 10^{-4}$ ns. According to these estimations, the heat is released from the system much faster in silicon than in ITO. This could explain the deeper LIPSS in PEDOT:PSS on ITO compared with PEDOT:PSS films on silicon with similar thicknesses. If the substrate releases the heat too fast, LIPSS on the surface of the upper film cannot develop deeper structures even irradiating with more pulses (Figure 4.3.a, blue data). On the other hand, ITO substrate is able to retain the heat longer times, thus the gradient of temperature through the PEDOT:PSS films is lower than in PEDOT:PSS on silicon. Therefore, the surface of the film maintains higher temperatures during longer times, allowing the enhancement in depth of developed ripples.

The order of the LIPSS can be inferred by means of GISAXS, as this technique reveals information of an area of square millimeters (see section 2.3.5.3). Figure 4.7.a-c shows the GISAXS patterns of LIPSS irradiated on concentrated PEDOT:PSS thin films deposited on silicon and the horizontal cuts from the GISAXS patterns (Figure 4.7.d), transformed to q_y (nm^{-1}) using Equation 2.12 (section 2.3.5.3).

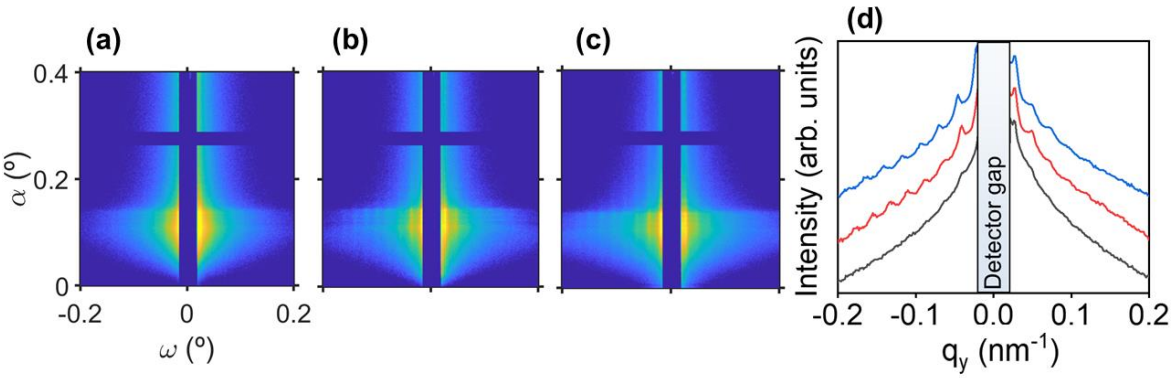

Figure 4.7 GISAXS patterns of concentrated PEDOT:PSS spin-coated on silicon irradiated at a fluence=12.4 mJ·cm^{-2} with **(a)** 4800 pulses, **(b)** 6000 pulses and **(c)** 8400 pulses. **(d)** Horizontal cuts of sample irradiated with 4800 pulses (black curve), 6000 pulses (red curve) and 8400 pulses (blue curve). GISAXS patterns taken at an incident angle α_i=0.4º. Intensity in logarithmic scale.

Only a few diffraction maxima are observed in the GISAXS pattern of the sample irradiated with 4800 pulses (Figure 4.7.a and Figure 4.7.d, black curve). For larger number of pulses (6000 and 8400, Figure 4.7.b and c), the diffraction pattern exhibits more maxima. Although the sample irradiated with 8400 pulses shows well ordered LIPSS as revealed by GISAXS, it was possible to observe in the AFM image some protuberances related with material degradation (Figure 4.4). Periods obtained from horizontal cuts in GISAXS patterns (Figure 4.7.d) are 290±15 nm, 287±14 nm and 266±15 nm for samples irradiated with 4800, 6000 and 8400 pulses respectively. These values are coherent with periods measured in AFM images (Figure 4.3.b), though the periods obtained from GISAXS are systematically lower than those obtained from AFM images, taking into account the error bars. This discrepancy has been previously found in LIPSS fabricated with other polymers[18] and it is explained considering that LIPSS are not perfect periodical structures. The ripples grow into a grating structure but sometimes two consecutive ripples that are not completely parallel may melt into one during growing, and present a final periodical structure with some degree of ramifications, decreasing the average pitch of the structure measured by GISAXS in a large area. LIPSS on concentrated PEDOT:PSS deposited on silicon (Figure 4.4), as well as LIPSS on original PEDOT:PSS deposited on ITO (Figure 4.5) show a slight degree of ramifications as revealed by the AFM images.

Figure 4.8 shows the GISAXS patterns of LIPSS irradiated on PEDOT:PSS thin films deposited on ITO. LIPSS obtained by irradiating with 4800 pulses and 6000 pulses yield to gratings with many diffraction maxima (Figure 4.8.d, black and red curves respectively). Although in the sample with 4800 pulses the depth of the nanostructures is considerably smaller (Figure 4.6), the nanostructures are already well ordered. The sample irradiated with 8400 pulses does not show any diffraction maxima, indicating lost order (Figure 4.8.c and Figure 4.8.d, blue curve). This

matches well with its corresponding AFM and FFT image (Figure 4.5). Periods obtained from horizontal cuts in GISAXS patterns are 227 nm and 226 nm for samples irradiated with 4800 and 6000 pulses respectively. As in GISAXS from LIPSS on concentrated PEDOT:PSS deposited on silicon (Figure 4.7), the period detected by GISAXS is lower than the one extracted from AFM images (Figure 4.6).

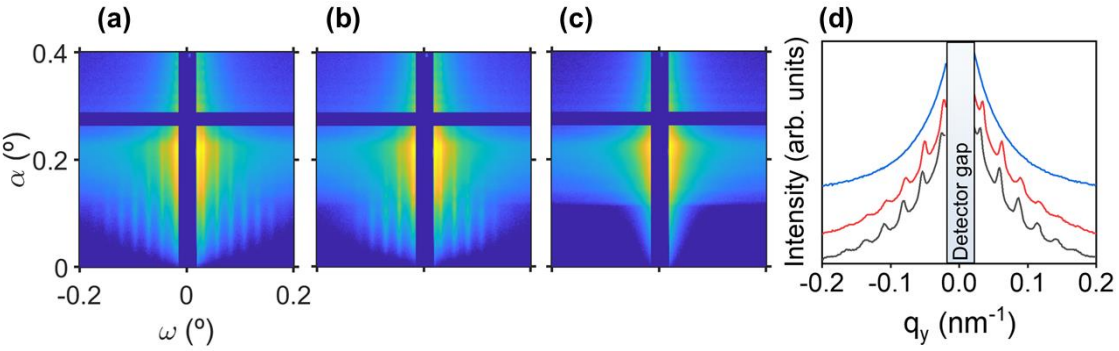

Figure 4.8 GISAXS patterns of PEDOT:PSS LIPSS on ITO irradiated at fluence=12.4 mJ·cm^{-2} with **(a)** 4800 pulses, **(b)** 6000 pulses and **(c)** 8400 pulses. **(d)** Horizontal cuts from irradiated PEDOT:PSS on ITO with 4800 pulses (black curve), 6000 pulses (red curve) and 8400 pulses (blue curve). GISAXS patterns taken at an incident angle α_i=0.4º. Intensity in logarithmic scale.

4.1.3 Modification of the inner structure as revealed by GIWAXS and Raman scattering

GIWAXS measurements were carried out to see whether the inner structure is significantly affected by laser treatment. Figure 4.9 shows a series of GIWAXS patterns obtained for LIPSS fabricated on concentrated PEDOT:PSS thin films deposited by spin-coating on silicon. The GIWAXS pattern of the non-irradiated sample (Figure 4.9.a) reveals a conventional PEDOT:PSS diffraction pattern with two characteristic broad peaks at q=12.2 nm^{-1} (d=0.52 nm) and q=18.2 nm^{-1} (d=0.34 nm), which correspond to π-π stacking PSS and π-π stacking of PEDOT[19], respectively. GIWAXS patterns of irradiated samples show a series of narrow rings with granulated textures, suggesting the appearance of a polycrystalline phase induced by laser treatment.

The patterns were azimuthally integrated over a wide arc centered in the q_z axis to avoid the intensity contribution from the silicon reflections. Intensity profiles of the samples from Figure 4.9 are represented in Figure 4.10. The new Bragg peaks are located at q=11.9 nm^{-1} (0.53 nm), at q=14.3 nm^{-1} (0.44 nm), at q=16 nm^{-1} (d=0.39 nm) and several peaks around q=20 nm^{-1} that can be confused with the reflections from the silicon substrate. The peaks do not correspond with any reported crystallographic distance for PEDOT[20,21] or PEDOT:PSS. However, the peaks at

q=14.3 nm^{-1} and q=16 nm^{-1} matches with the reflections of a reported crystallization of PSS achieved by mixing PSS with an ionic liquid[22]. The laser irradiation could take part on enhancing the temperature of PEDOT:PSS that leads to separation of phases between PEDOT and PSS, thus promoting the crystallization of PSS. In addition, the broad peaks from PEDOT and PSS in the profile from the non-irradiated sample decrease in intensity in the profiles from irradiated samples.

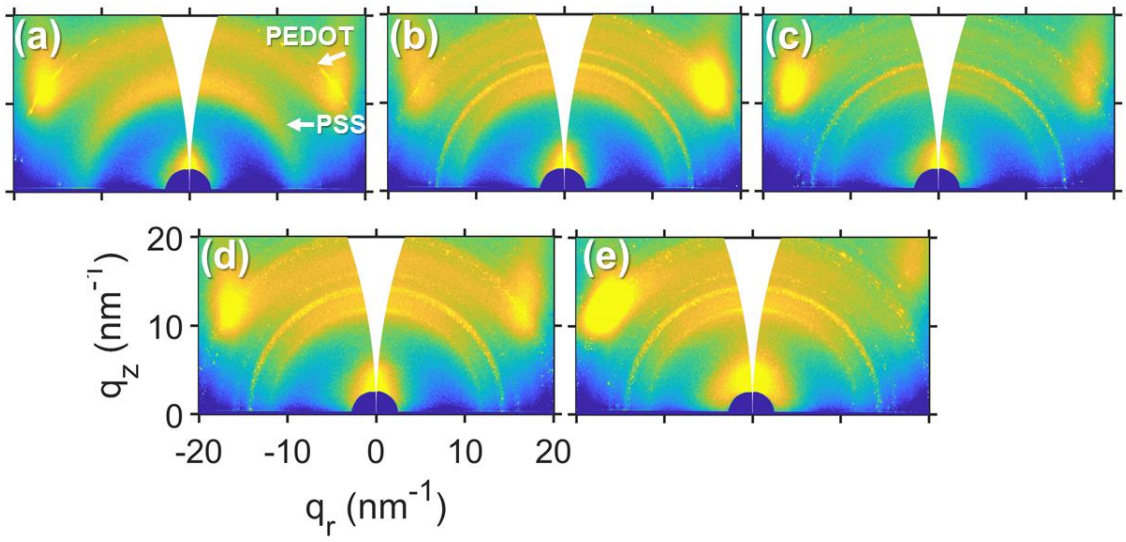

Figure 4.9 GIWAXS patterns of concentrated PEDOT:PSS thin films on silicon, **(a)** non-irradiated, and irradiated at λ=266 nm, fluence=12.4 $mJ \cdot cm^{-2}$ with **(b)** 4800 pulses, **(c)** 6000 pulses, **(d)** 7200 pulses and **(e)** 8400 pulses. Intense spots at the side of the patterns and the narrow ring near the PEDOT reflection located also in the non-irradiated sample pattern **(a)** come from scattering of silicon substrate. Intensity in logarithmic scale.

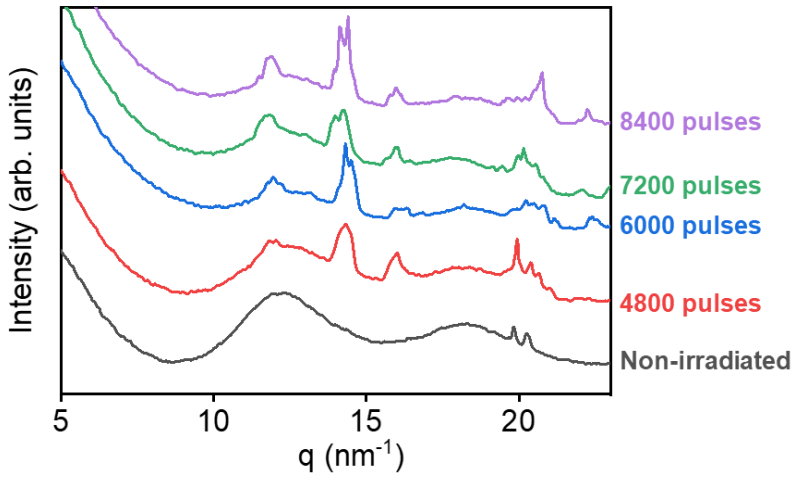

Figure 4.10 Azimuthal integrations of GIWAXS patterns from concentrated PEDOT:PSS films on silicon non-irradiated and irradiated at fluence=12.4 $mJ \cdot cm^{-2}$. Number of irradiation pulses labelled. Peaks at q≈20 nm^{-1} come from scattering of silicon substrate.

In order to see this effect in other substrate, GIWAXS measurements were performed on PEDOT:PSS LIPSS on ITO (Figure 4.11).

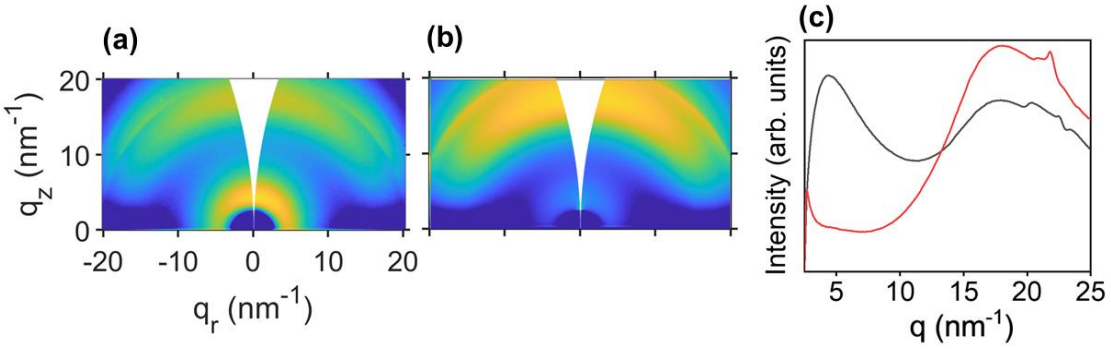

Figure 4.11 GIWAXS patterns of **(a)** ITO-coated glass, **(b)** PEDOT:PSS thin film on ITO irradiated at fluence=12.4 mJ·cm^{-2} with 6000 pulses. **(c)** Azimuthal integration of ITO (black curve) and PEDOT:PSS LIPSS on ITO (red curve). Intensity of GIWAXS patterns is in logarithmic scale.

As can be seen, GIWAXS patterns of samples deposited on ITO are contaminated with scattering from ITO and from glass substrate and this prevents a clear analysis of the broad peaks from PEDOT:PSS at q=12.2 nm^{-1} and q=18.2 nm^{-1}. However, none of the intense peaks localized in the GIWAXS patterns from LIPSS on PEDOT:PSS deposited on silicon (Figure 4.9) was found in the patterns from LIPSS on PEDOT:PSS on ITO (Figure 4.11.c), not even the peak located at q=11.9 nm^{-1} which is limiting with the beginning of the broad halo from the substrate. For this reason, this crystallization effect is likely to be occurring in irradiated samples deposited on silicon but not on ITO.

This idea of the silicon substrate acting as a nucleation surface for the irradiated material connects directly with section 4.4 of this chapter, in which irradiated $PC_{71}BM$ thin films spin-coated on silicon is affected by laser irradiation, on one side by enhancing the amorphous part of the material on the surface but inducing large crystallites close to the silicon surface.

In order to elucidate chemical and conformational changes on the PEDOT:PSS, Raman experiments (see section 2.3.4) were performed on non-irradiated and irradiated PEDOT:PSS samples over silicon and ITO (Figure 4.12). Raman spectra present several bands associated with molecular modes from PEDOT. The bands at 1250 cm^{-1} and 1365 cm^{-1} are assigned to C_α-C_α' inter-ring stretching vibration and C_β-C_β' stretching vibration respectively of the PEDOT thiophene ring[23]. The most intense band at 1450 cm^{-1} is associated to the symmetric stretching modes of C_α=C_β. The bands around 1510 cm^{-1} and 1570 cm^{-1} are identified as asymmetric stretching modes of C_α=C_β[23]. No signs of graphitization after laser irradiation are detected that would produce the appearance of the characteristic D (1350 cm^{-1}) and G (1584 cm^{-1}) bands of graphene oxide[24–26]. The most intense peak is centered at 1450 cm^{-1} in the spectrum from non-

irradiated sample (Figure 4.12.b, black curve), and is shifted to 1441 cm^{-1} in both spectra from irradiated samples over silicon and over ITO (Figure 4.12.b, red and blue curve respectively). This shift has been associated with a conformational transition of PEDOT chains from benzoid to quinoid structure[27], since the peak associated with symmetric stretching mode of C_α=C_β of the benzoid structure is located at higher Raman shift (Figure 4.12.b)[28]. The quinoid structure of PEDOT:PSS has been identified with extended chain conformations and the benzoid structure with coil-like conformation[27]. This transition has been achieved for instance by mixing PEDOT:PSS with ethylene glycol[27], by mixing with ionic liquids[22] and by thermal annealing[28]. In our case, the transition of PEDOT chains from benzoid to quinoid structure may be induced by the temperature enhancement of the material during laser irradiation.

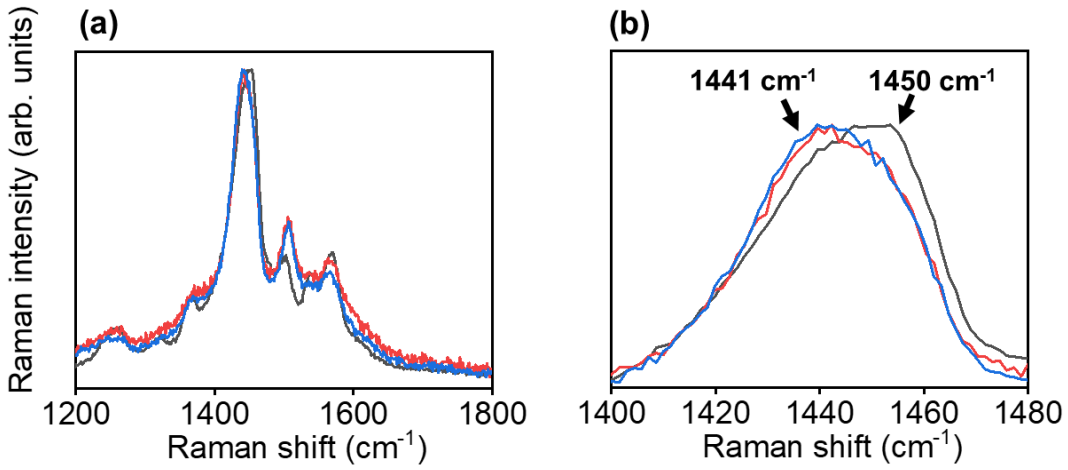

Figure 4.12 (a) Raman spectra of concentrated PEDOT:PSS thin film on silicon (black curve), LIPSS of concentrated PEDOT:PSS deposited on silicon, irradiated at fluence=12.4 $mJ \cdot cm^{-2}$ with 4800 pulses (red curve) and LIPSS of PEDOT:PSS deposited on ITO, irradiated at fluence=12.4 $mJ \cdot cm^{-2}$ with 6000 pulses (blue curve). **(b)** Magnification of the region of **(a)** associated to the symmetric stretching modes of C_α=C_β. Spectra have been baseline corrected and normalized to the maximum of each spectrum. Labelled at 1441 cm^{-1} and 1450 cm^{-1} the position of the components of the symmetric stretching of C_α=C_β from the quinoid and benzoid structure of PEDOT, respectively.

4.1.4 Calculation of temperature increase of PEDOT:PSS during laser irradiation

In order to gain insights about the impact of laser irradiation on PEDOT:PSS, the evolution of the temperature of the material with time is estimated. As it was described in section 2.2.1, the mechanism by which LIPSS are formed involves the interference between incoming and scattered waves and an enhancement of temperature in the surface of the film. When the temperature is high enough –above the glass transition or the melting point- the polymer chains can diffuse and

reorganize at a higher spatial level. However, PEDOT:PSS is a polymeric system which does not present a defined glass transition temperature due to the strong electrostatic interaction between oxidized PEDOT and reduced PSS[29]. It does neither present a melting temperature, reaching degradation before. For these reasons, the evolution of the morphology of PEDOT:PSS with temperature is studied indirectly by other properties like changes in conductivity and Young Modulus[29]. Estimations of the temperature using physical parameters of PEDOT:PSS can give insights about the temperature achieved by the material. Considering laser irradiation as the only heating source of the polymer film, the corresponding temperature increase can be estimated by solving the heat equation for one spatial dimension[18,30] (Equation 4.4). For simplification, the temperature dependence of the polymer physical parameters and the possible changes in the thermal properties during the process were not taken into account in the calculation.

$$\frac{\partial^2 T(z,t)}{\partial z^2} - \left(\frac{\rho c}{\kappa}\right)^2 \frac{\partial T(z,t)}{\partial t} = -\frac{\alpha}{\kappa} P(t) e^{-\alpha z} F \qquad (\mathbf{4.4})$$

In Equation 4.4, among the parameters already introduced for Equation 4.2 and 4.3, *T* is the temperature, *z* is the depth through the film, *t* is the time and P(t) is the function that describes the temporal shape of the laser pulse, considered to be as a modified Gaussian beam (Equation 4.5).

$$P(t) = \frac{2t}{{\tau_p}^2} e^{-\left(\frac{t}{\tau_p}\right)^2} \qquad (\mathbf{4.5})$$

In Equation 4.5, τ_p is the pulse duration: 8 ns in this work. The other physical parameters used are included in Table 4.3.

Table 4.3 Physical parameters of PEDOT:PSS: absorption coefficient (*α*) at 266 nm, specific heat (c), density (ρ), thermal conductivity (κ) and refractive index (*n*) at 266 nm.

α (m^{-1})	c ($J \cdot kg^{-1} \cdot K^{-1}$) [31]	ρ ($kg \cdot m^{-3}$) [32]	κ ($W \cdot m^{-1} \cdot K^{-1}$) [31]	*n* [33]
$6 \cdot 10^5$	1500	1011	0.3	~1

The results of this equation are presented in Figure 4.13 and Figure 4.14. According to the estimation, the PEDOT:PSS thin film is heated up to 70ºC before 20 ns in the surface and then the cooling until the original temperature is nearly recovered in the range of milliseconds (Figure 4.13). The maximum temperature reached in underlying layers of the film has also been calculated and it is represented in Figure 4.14. It can be seen that the maximum estimated temperature at the surface film during the first pulse is nearly 70ºC and 68.6 ºC at a depth of 100 nm. This estimation shows that in this case there is no significant difference in temperature between the surface and

the bottom of a film. However, it should be remembered that this temperature estimation does not consider the effect of the substrate, which plays an important role on the LIPSS formation as described in section 4.1.2.

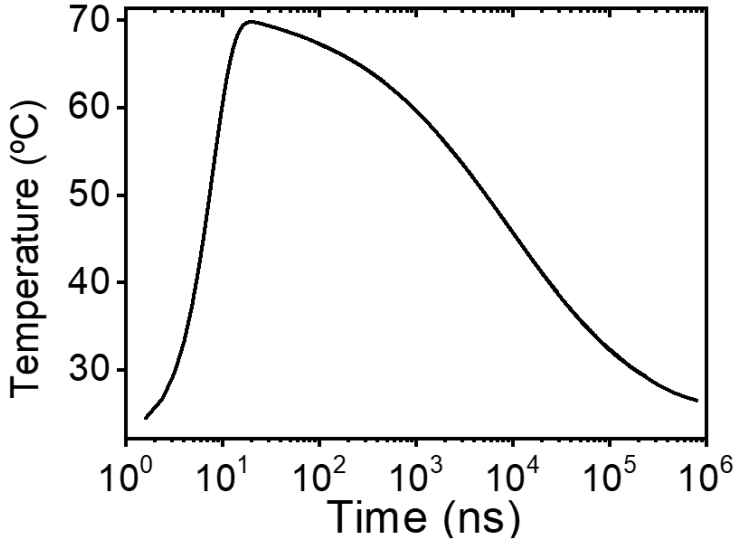

Figure 4.13 Estimation of the temperature evolution at the surface of a PEDOT:PSS thin film upon absorption of one irradiated pulse.

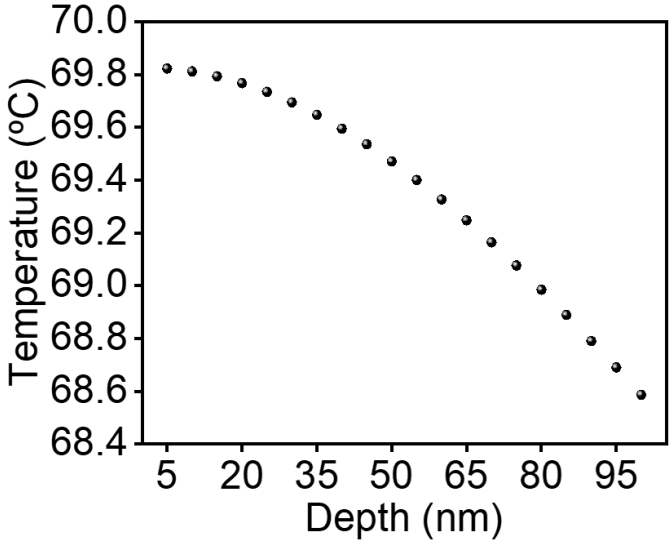

Figure 4.14 Simulation of the maximum temperature achieved in a film of 100 nm of thickness as a function of the depth.

As it is said before, the morphology and mobility of PEDOT:PSS cannot be simply explained in terms of glass transition temperature and melting temperature. The mobility of PEDOT:PSS has been analyzed through the strength of hydrogen bonds between water molecules and PSS^-, a parameter that can be tuned through the relative humidity[34] and the temperature[29]. Vitoratos et

al[35] proposed the rupture of the ionic bond between charged segments of PEDOT and PSS from 120ºC. In the present case, it is estimated that the PEDOT:PSS goes to 70ºC during the first pulse and cools down to room temperature before the next pulse arrives. However, this is only an estimation. Other considerations like the fact that after the first pulse, the optical properties of the material might be different[18] has not been taken into account. Therefore, it is coherent to suppose that PEDOT:PSS will surpass the 120ºC barrier with the thousands of laser pulses used and PEDOT-PSS bonding will be affected, allowing the reorganization of the material, which has been revealed by GIWAXS (Figure 4.9) and Raman spectroscopy (Figure 4.12).

4.1.5 Influence of laser irradiation on the electric current through PEDOT:PSS as revealed by C-AFM

To see how the irradiation treatment affects the electrical properties of PEDOT:PSS, C-AFM mode of the AFM was used. Figure 4.15.a-b show a topographic image in contact mode of a PEDOT:PSS thin film (non-irradiated) deposited over ITO and its corresponding current C-AFM mapping.

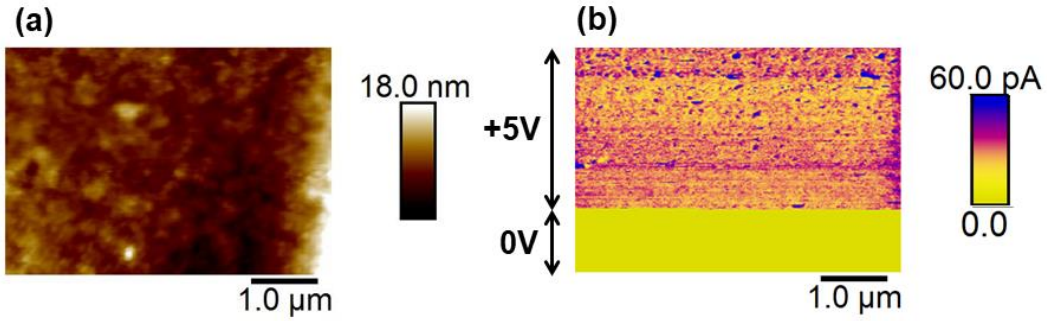

Figure 4.15 (a) Topographic image in contact mode of PEDOT:PSS thin film over ITO, **(b)** current C-AFM image. DC voltages applied in different regions of the sample are labelled.

The electrical current image (Figure 4.15.b) shows two regions, one with a DC voltage applied and a lower band with no voltage applied as a reference. PEDOT:PSS thin film shows many dot-like regions with high conductivity and a continuous phase with relatively low conductivity. Similar results were shown in section 3.3 of this Thesis for PEDOT:PSS films deposited by inkjet printing. The dot-like regions are likely to be rich in PEDOT.

The electrical behavior of a LIPSS sample of PEDOT:PSS deposited on ITO is shown in Figure 4.16. It can be seen in Figure 4.16.b that the conducting regions in the PEDOT:PSS LIPSS, associated with blue-like colors, are partially segregated in stripe-like zones, slightly concentrated in the valley of the nanostructures, as it is emphasized in the docking image (Figure 4.16.c). PEDOT:PSS LIPSS show a similar electrical behavior as LIPSS in P3HT[36], in PCDTBT (see

section 4.2) and in $PC_{71}BM$ (see section 4.4). In these cases, the mapping of electrical current shows also segregation of the conducting domains to the trenches of the gratings although the ridges show no current. In PEDOT:PSS LIPSS, the ridges of the gratings also show electrical response (Figure 4.16.c). In P3HT[36] and $PC_{71}BM$ (section 4.4)[37], the non-conducting regions in LIPSS have been associated with lower crystallinity regions. Laser irradiation induces fast heating and cooling processes that allows the material to flow but the initial crystallinity is not recovered; the result is a more amorphous material. In the case of PEDOT:PSS, if the heat treatment of the laser is enough to break the bonding between the PEDOT and PSS, the reorganization of the material could be inducing a segregation of the PEDOT (with high conductivity) to the valleys of the LIPSS. On the other hand, the ridges of the LIPSS could be rich in insulating PSS.

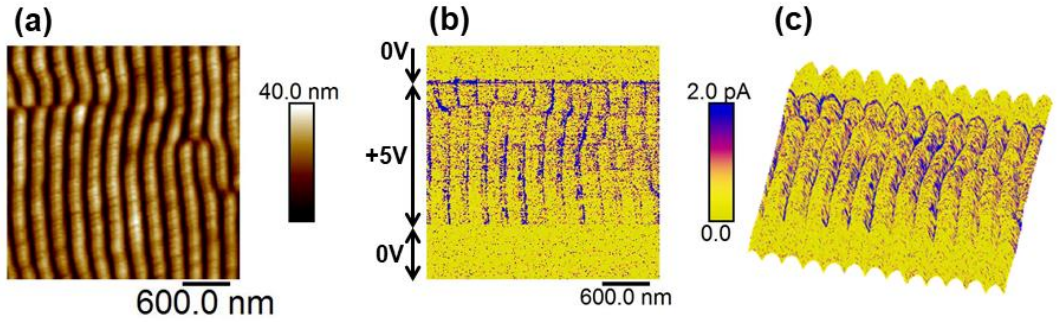

Figure 4.16 (a) Topographic image in contact mode of PEDOT:PSS LIPSS over ITO irradiated at fluence=12.4 mJ·cm^{-2} with 7200 pulses, **(b)** current C-AFM image, **(c)** docking of the topography and current images. DC voltages applied in different regions of the sample are labelled**.**

4.2 Chain orientation in LIPSS of photovoltaic polymers as revealed by TEY-NEXAFS

The performance of OPVs highly depends on the electronic properties of the bulk heterojunction, mainly determined by the crystallinity and orientation of the conjugated materials in the active layer. TEY-NEXAFS (see section 2.3.5.4) is a powerful technique to reveal surface orientation in thin films of conjugated polymers, since the intensity of the absorption peaks depends on the angle between beam polarization and transition dipole vector of the molecule, revealing dichroism effects. In addition, TEY-NEXAFS is a surface-sensitive technique and provides information of the first 10 nm of a film surface.

In this work, we study the linear dichroism revealed by TEY-NEXAFS of thin films of conjugated polymers P3HT and PCDTBT (section 1.4.2) before and after irradiation by laser. The ambient conditions strongly influence the final morphology of the nanostructures. For this reason, we

combine the study of LIPSS fabricated under air conditions and under vacuum conditions. Thin films of P3HT and PCDTBT were prepared by spin-coating. Conditions for preparation of solutions of P3HT and PCDTBT, both in C_6H_5Cl, were defined in Table 2.8. Spin-coating conditions were included in Table 2.10.

4.2.1 Irradiation under air and vacuum conditions

Irradiations of both polymers were performed at λ=532 nm, at normal incidence at air or vacuum conditions. However, in the latter case, LIPSS were obtained only in PCDTBT thin films. The idea behind using vacuum is to achieve LIPSS minimizing the impact of the active gases in the ambient. Regarding the vacuum set-up, the energy coming from the laser was set taking into account a reduction of 10% of the energy absorbed by the window of the vacuum chamber. Therefore, the final fluence on the sample is the same in both set-ups. Irradiation conditions are compiled in Table 4.4.

Table 4.4 Irradiation conditions for P3HT and PCDTBT thin films.

λ=532 nm			
Material	**Atmosphere**	**Fluence (mJ·cm^{-2})**	**Pulses**
P3HT	Air	25.9	3600
PCDTBT	Air	25.9	9000
	Vacuum ($4\cdot10^{-2}$ mbar)	25.9	9000

4.2.2 LIPSS visualization by AFM

Figure 4.17 shows the morphology of the LIPSS in P3HT and PCDTBT obtained using irradiation conditions from Table 4.4. P3HT LIPSS under vacuum conditions at λ=532 nm are not formed. P3HT LIPSS formed at λ=532 nm under air conditions (Figure 4.17.a) show a period of around 450 nm and depth of 100 ± 10 nm. LIPSS in PCDTBT formed under air conditions (Figure 4.17.b) have a period around 390 nm and a depth of 60 ± 10 nm. On the other side, LIPSS in PCDTBT formed under vacuum conditions (Figure 4.17.c) have a period around 430 nm and a depth of 70 ± 5 nm. These values are closed to reported ones for LIPSS in P3HT and PCDTBT irradiated under air conditions[36,38]. LIPSS of PCDTBT irradiated under vacuum conditions are slightly deeper and have a larger period than the PCDTBT LIPSS formed under air conditions. In addition, PCDTBT LIPSS irradiated under both conditions (Figure 4.17.b-c) are narrower (~200 nm) than P3HT LIPSS irradiated under air conditions (Figure 4.17.a) that have a width measured at the half

of the height of around 270 nm. Geometrical features of the LIPSS developed in distinc materials are different due to varying optical and thermal properties. The atmosphere conditions during irradiation have also impact on the LIPSS growth.

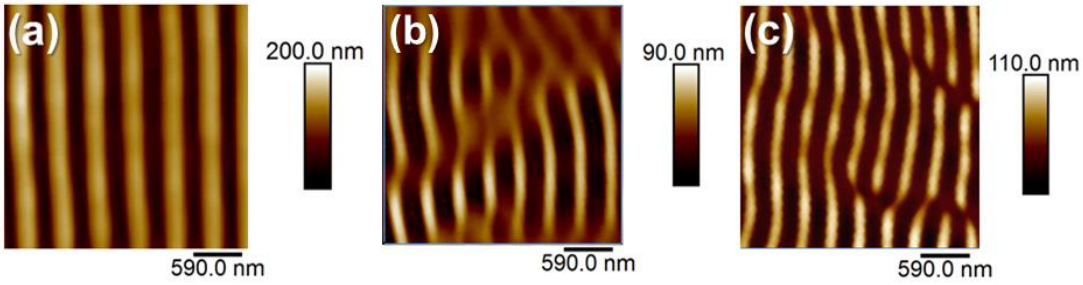

Figure 4.17 AFM topography images taken in contact mode of **(a)** P3HT LIPSS obtained under air conditions, **(b)** PCDTBT LIPSS obtained under air conditions, **(c)** PCDTBT LIPSS obtained under vacuum conditions.

4.2.3 Linear dichroism in P3HT and PCDTBT as revealed by TEY-NEXAFS

Geometry of TEY-NEXAFS experiment is described in detail in section 2.3.5.4. Two polarizations of the beam are used: horizontal (parallel to the substrate) and vertical (20º degrees from the normal vector of the substrate). Figure 4.18 shows the TEY-NEXAFS spectra of a P3HT thin film and an irradiated P3HT thin film with both polarizations. The spectra were normalized by setting the pre-edge range (<280 eV) to 0 and the post-edge range (>320 eV) to 1. This region is considered to be sufficiently above the photoionization threshold so there are not any resonant transitions affected by dichroism[39].

Figure 4.18.a shows marked differences between the intensity of the peaks comparing the horizontal (red curve) and vertical polarization (blue curve). The lowest energy peak corresponds to the transition to the molecular orbital π*. As it was described in section 2.3.5.4, the intensity of the peaks depends on the angle between beam polarization and the transition dipole vector associated with each transition. The transition dipole vector of the C=C π* transition is perpendicular to the thiophene ring of P3HT, therefore the difference in intensity between both polarizations is a direct indicator of a predominant orientation in the surface of the film. In Figure 4.18.a, horizontal polarization yields higher intensity of the π* transition peak, thus the thiophene rings in the P3HT thin film are predominantly disposed perpendicular to the substrate. This is coherent with an "edge-on" orientation (see section 1.4.1), usually obtained in solution casted thin films with thickness≈150 nm[36].

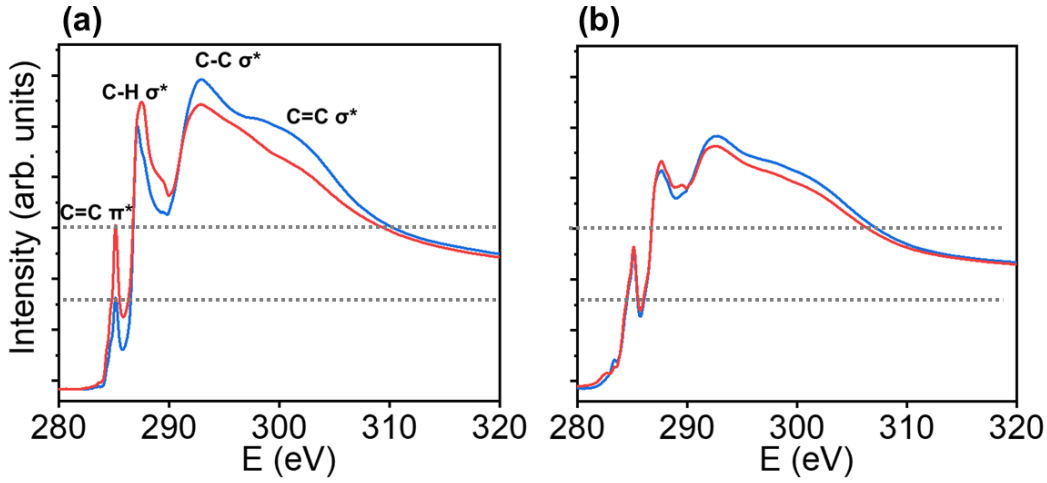

Figure 4.18 Normalized TEY-NEXAFS spectra of **(a)** P3HT thin film and **(b)** P3HT LIPSS sample. Blue curve=vertical polarization, red curve=horizontal polarization of the X-ray beam. Gray dotted lines mark the intensity of the C=C π* in the P3HT non-irradiated thin film spectra at both polarizations. Peaks associated with electronic transitions are labelled in **(a)**.

Figure 4.18.b shows the TEY-NEXAFS spectra of irradiated P3HT thin film with the irradiation conditions from Table 4.4. Two features are clearly induced by irradiation. The intensity of π* transition peak is equal in both polarizations; this indicates a loss of preferential orientation at the film surface. Comparing Figure 4.18.a and Figure 4.18.b looking at the dotted gray lines, the π* transition peak from vertical polarization (blue curves) increases from the spectrum of non-irradiated sample to the spectrum of LIPSS. On the other hand, this peak measured with horizontal polarization (red curves) is reduced from the spectrum of non-irradiated sample to the spectrum of LIPSS. This could suggest a decrease of "edge-on" orientation on LIPSS accompanied with an increase of the "face-on" orientation, with the thiophene rings parallel to the substrate. However, GIWAXS results[36] do not support this effect, possibly due to the fact that GIWAXS is not a surface-sensitive technique and it averages the nanostructured surface and the rest of the non-structured film. TEY-NEXAFS, on the other side, averages a few nanometers of the sample surface. In addition, TEY-NEXAFS gives information about global molecular orientation while GIWAXS gives information of mainly crystalline orientation. The other feature is a reduction of the dichroism of the transition at ~288 eV (C-H σ*) (Figure 4.18.b), which is associated with the hexyl chains of P3HT, thus could be related with modifications of the orientations of the lateral chains upon laser irradiation.

Figure 4.19 shows the TEY-NEXAFS spectra of PCDTBT thin film non-irradiated and irradiated under ambient or vacuum conditions.

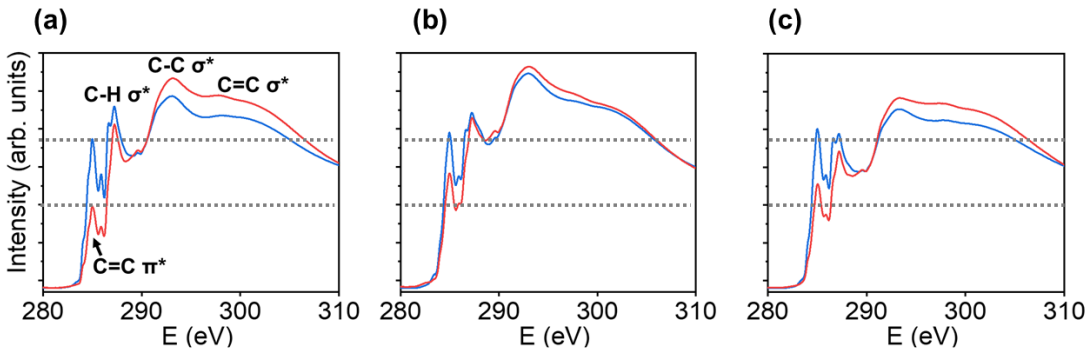

Figure 4.19 Normalized TEY-NEXAFS spectra of **(a)** PCDTBT thin film, **(b)** PCDTBT LIPSS irradiated in air and **(c)** PCDTBT LIPSS irradiated in vacuum. Blue curve=vertical polarization, red curve=horizontal polarization of the X-ray beam. Gray dotted lines mark the intensity of the C=C π* in the PCDTBT non-irradiated thin film spectra at both polarizations. Peaks associated with electronic transitions are labelled in **(a)**.

In Figure 4.19.a, linear dichroism is clear in PCDTBT thin film, though the effect is the opposite as in P3HT (Figure 4.18.a). The first resonant peaks around 285 eV are shifted to lower energy (~284.95 eV) than P3HT (~285.15 eV), a feature associated to the different heteroatoms in the aromatic structures[40]. This peak is more intense when using vertical polarization of the beam, thus indicating a perpendicular orientation of the transition dipole vector with respect to the film surface, suggesting a "face-on" disposition of the PCDTBT molecules. While PCDTBT thin films are largely amorphous[41], the preference of the chains to arrange in a "face-on" disposition induced by the intermolecular interaction (π-π stacking) has already been suggested[42,43]. The peak associated with the C-H σ*, which is related to the alkyl chains attached to the carbazole group of PCDTBT, also shows enhanced intensity using vertical polarization.

Spectra from irradiated PCDTBT under both conditions, air and vacuum, (Figure 4.19.b-c) show almost the same intensity for the peak of C=C π* transition using vertical polarization as in the spectrum from non-irradiated PCDTBT (Figure 4.19.a). However, the intensity of this peak is enhanced using horizontal polarization in both spectra from irradiated samples, being this enhancement higher in the case of PCDTBT irradiated in air. Therefore, the dichroism showed in the spectra from non-irradiated PCDTBT thin film (Figure 4.19.a) is reduced in the spectra from irradiated PCDTBT (Figure 4.19.b-c) but not removed, as in the case of P3HT (Figure 4.18.b). In the case of PCDTBT irradiated in air (Figure 4.19.b), the peak associated with the C-H σ* transition is almost equal in intensity comparing both polarizations. However, the spectrum from PCDTBT irradiated in vacuum (Figure 4.19.c) still show dichroism in this peak, related to the alkyl chains, similar as the spectrum from non-irradiated PCDTBT (Figure 4.19.a).

To quantify the effect of the irradiation in all the systems, a dichroism parameter LD has been calculated using the intensity of the maximum resonant peak associated with the π* transition of each polarization measurement (Equation 4.6).

$$LD = I_H - I_V \qquad (\mathbf{4.6})$$

The values of linear dichroism for every sample are presented in Figure 4.20.

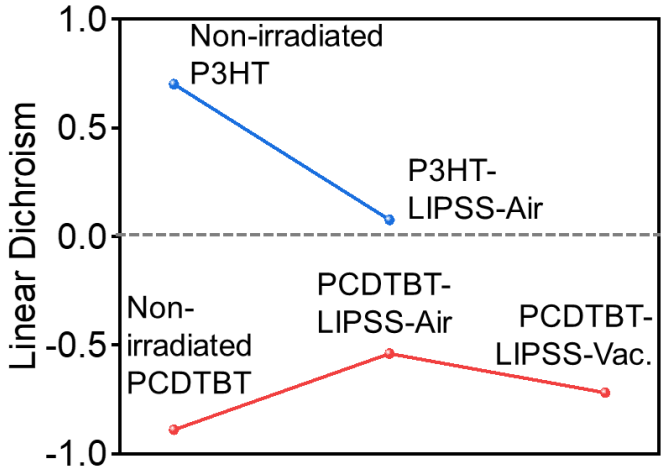

Figure 4.20 Linear dichroism in the different systems before and after laser irradiation. Blue data correspond to P3HT systems. Red data correspond to PCDTBT systems. Gray dotted line indicates the zero.

It is clear from Figure 4.20 that the irradiation process has an impact on the chain orientation in the polymer film surface. It was previously reported that laser irradiation could impact on the polymer chains orientation[44], specifically, it is reported that femtosecond irradiation promotes "face-on" orientation of P3HT[45]. In our case, using nanosecond irradiation, TEY-NEXAFS results from P3HT LIPSS (Figure 4.18) show loss of preferential "edge-on" orientation but it has been pointed out that the enhancement of the peak associated with C=C π* transition using vertical polarization on P3HT LIPSS sample could also be indicating an enhancement of "face-on" orientation of the molecules at the surface probed by TEY-NEXAFS experiments. For PCDTBT films (Figure 4.20, red data), the linear dichroism is negative since the intensity measured with vertical polarization is higher than the one measured with horizontal polarization. Its absolute value is reduced to around a half when irradiated under air conditions whereas in P3HT the linear dichroism is almost vanished when irradiated (Figure 4.20, blue data). This could be explained by the more rigid PCDTBT backbone in comparison with P3HT, and its higher glass transition temperature (see section 1.4.2). Looking at the TEY-NEXAFS spectrum from PCDTBT samples irradiated under vacuum conditions (Figure 4.19.c), it is clear that the atmosphere has an influence on the LIPSS formation and the structural modification of the polymer. First of all, under vacuum

conditions, P3HT LIPSS do not grow at the same irradiation conditions as under air conditions. In the case of PCDTBT, LIPSS are formed in both atmospheres with some morphological differences between them (Figure 4.17) and the TEY-NEXAFS spectrum corresponding to vacuum shows higher dichroism than the one corresponding to air (Figure 4.20, red data).

Another fact that should be taken into account is that PCDTBT has a peculiar behavior against temperature. It has been reported[43] that side-chain packing and π-π stacking in PCDTBT have opposite mechanisms as the temperature rises. During thermal annealing over the T_g, π-π stacking order decreases and side-chain order increases. Although the heating and cooling processes induced by laser are quite fast, a competition between side-chain and π-π packing could be involved. In Figure 4.19.c, corresponding to PCDTBT irradiated in vacuum, the vertical polarization (blue curve) presents a higher intensity C=C π* peak than C-H σ* peak, suggesting that side chains lose more orientation than the backbone. This is the opposite situation to that found in the non-irradiated PCDTBT and the irradiated PCDTBT in air (Figure 4.19.a-b). Under a more active atmosphere, i.e. in air, PCDTBT molecules are more exposed to faster heat dissipation and chains are finally more disoriented, leading to an almost complete overlap between spectra taken at both polarizations (Figure 4.19.b), except for the C=C π* peak.

In summary, irradiation induces disorientation of the molecules in the LIPSS. However, irradiation under vacuum conditions does not only affect the growth of the ripples (as in P3HT) but it affects the segmental movements of the chains during heating and cooling processes, partially avoiding the total disorientation of the chains and driving them to a partially modified orientation.

4.2.4 Impact of atmosphere on the LIPSS electric current

Figure 4.21 shows the electric current maps taken in C-AFM mode corresponding to the topographical images shown in Figure 4.17.

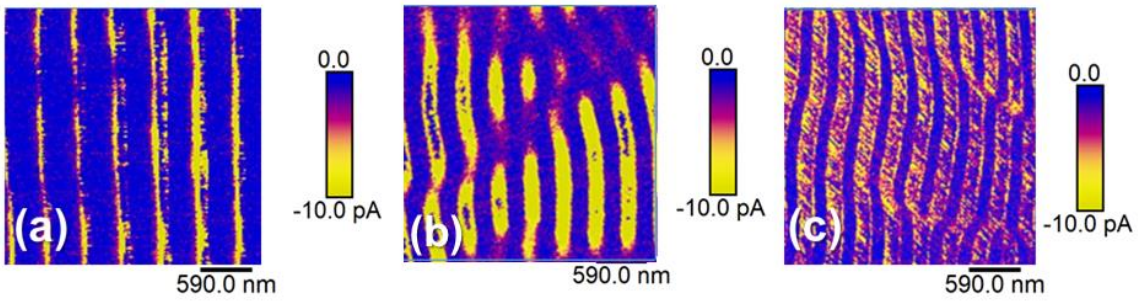

Figure 4.21 C-AFM current images of **(a)** P3HT LIPSS under air conditions, **(b)** PCDTBT LIPSS under air conditions, **(c)** PCDTBT LIPSS under vacuum conditions. DC voltage applied=-10 V.

Non-irradiated P3HT and PCDTBT films show homogeneous mapping of the C-AFM current as previously reported[36,38] whereas irradiated films, in all the cases, present conductivity segregation in which conducting stripes are located at the valleys of LIPSS and non-conducting lines are in the ridges. This is also reported for P3HT[36] and PCDTBT[38] thin films irradiated under air conditions. In this work, PCDTBT irradiated under vacuum conditions yields a similar distribution (Figure 4.21.c). The electric current in this sample (Figure 4.21.c) is more homogeneous than in the sample irradiated at air conditions (Figure 4.21.b), showing larger and more connected conducting domains than in Figure 4.21.b, and wider than in P3HT (Figure 4.21.a). This could be related to the lowest impact on the chain orientations of irradiation in vacuum showed in Figure 4.20. As it was previously discussed, both irradiated PCDTBT samples are heated over the glass transition temperature and this could promote disorder in the π-π stacking compared to the non-irradiated film[46]. If the non-irradiated film is preferentially "face-on" arranged, this would be favorable to the electric current through the π-π stacking direction between adjacent chains (see section 1.4.1), along the vertical direction of the sample, which is the current measured in C-AFM. The thin film irradiated under vacuum conditions is less affected (Figure 4.21.c), maintaining more chains in the "face-on" orientation and showing more homogeneous conducting paths.

4.3 Complex surface periodic nanostructures obtained by sequential nanosecond pulsed laser irradiation

In section 1.5.1, it was highlighted the efforts that are currently done to produce complex functional surfaces inspired by nature[47]. In the previous sections of this chapter, linear structures have been developed by using a single irradiation step with a linearly polarized laser. In this section, complex structures are fabricated by tuning the laser irradiation conditions. We report a library of ordered nanostructures in a polymer surface fabricated by sequential laser irradiation. In particular, we fabricate structures on two functional polymers: P3HT (see section 1.4.1) and P(VDF-TrFE) (see section 1.4.5). By using a combination of pulses at different wavelengths and several polarizations, it is possible to obtain different geometries of nanostructures in large areas.

Samples were prepared by spin-coating. Conditions for preparation of solutions of P3HT in $CHCl_3$ and P(VDF-TrFE) were listed in Table 2.8. The spin-coating conditions were included in Table 2.10.

4.3.1 Irradiation procedure

Several experimental parameters have been used to determine the optimal conditions to obtain different patterns by laser irradiation. In particular, number of laser irradiation steps, number of pulses, polarization vectors, laser wavelengths and different polymer films (P3HT and P3HT/P(VDF-TrFE)) have been employed to produce different nanostructures. For example, by using two consecutive laser irradiations rotating the polarization vector 90º we obtain a square-like pattern. If we change the wavelength in the second irradiation step, we obtain a rectangle-like pattern. In this work, we fabricate a library of ordered nanostructures in a polymer surface by using a combination of pulses at different wavelengths and several polarizations. The polarization of the laser was changed by using a half-wave plate attached in the additional holder of the optical system presented in section 2.2.1 (Figure 2.7).

During a typical generation of gratings obtained by repeated nanosecond pulsed laser irradiation, the polarization direction of the laser is kept constant and the fluence and number of pulses is optimized for each material[48–50]. Since our aim is not to ablate the polymer, the fluence and number of pulses must be similar to the ones for which optimum LIPSS were obtained. Thus, we use for both sequential irradiations the laser fluence which gives rise to the formation of the optimum LIPSS (fluence=26 mJ·cm^{-2} for irradiations at λ=532 nm and fluence=13.4 mJ·cm^{-2} for irradiations at λ=266 nm) and the total number of pulses is the one that induces the formation of LIPSS upon single irradiation (around 3600 pulses)[36].

4.3.2 Characterization of P3HT array patterns by AFM, GISAXS and GIWAXS

Figure 4.22 features AFM images of P3HT nanostructures forming squares of around 500 nm size (Figure 4.22.a), of around 200 nm (Figure 4.22.b), and 500 nm x 200 nm rectangles (Figure 4.22.c). Table 4.5 presents the irradiation conditions for these samples. Besides the real space inspection of the order, possible by the AFM images, the degree of order in the nanostructures can be inferred from their FFT. It can be seen that FFT image from the sample irradiated at 532 nm at both directions (Figure 4.22.a) shows intensity maxima along vertical and horizontal directions. P3HT thin film irradiated at 266 nm at both directions (Figure 4.22.b) shows lower order of the LIPSS. Its FFT image depicts two intensity maxima in the horizontal direction and one intensity maximum in the vertical direction. On the other hand, the AFM image from P3HT irradiated with both wavelengths (Figure 4.22.c) shows a clear rectangular structure, corroborated by its FFT image that shows intensity maxima along the vertical direction more separated from the origin than the intensity maxima along the horizontal direction.

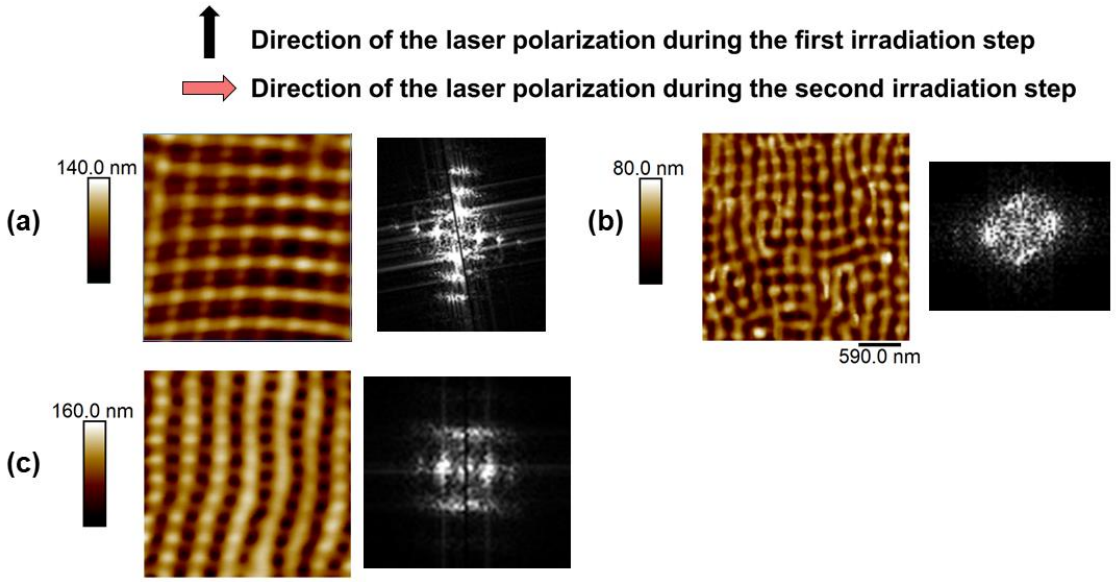

Figure 4.22 AFM topographical images taken in tapping mode of P3HT irradiated samples with **(a)** squares of ~500 nm, **(b)** squares of ~200 nm and **(c)** rectangles of ~500 nm x ~200 nm. Next to each AFM image, its corresponding FFT is presented.

Table 4.5 Conditions of sequential irradiations corresponding to samples presented in Figure 4.22.

Image	**1st irradiation**		**Polarization shift (º)**	**2nd irradiation**	
	λ (nm)	**Pulses**		**λ (nm)**	**Pulses**
(a)	532	3500	90	532	100
(b)	266	3300	90	266	300
(c)	532	3600	90	266	300

GISAXS patterns from samples irradiated with the irradiation conditions of Table 4.5 and their horizontal cuts are presented in Figure 4.23. The order detected by AFM (Figure 4.23) is present at the scale of millimeters as revealed by the appearance of diffraction maxima in the GISAXS patterns taken with the X-ray beam parallel to both irradiation directions. In the GISAXS cuts it is observed that, in the case of squares of ~500 nm (Figure 4.23.a), the array is more ordered along the direction of first irradiation, as revealed by the larger amount of diffraction maxima. Sample with squares of ~200 nm (Figure 4.23.b) shows only one clear diffraction maximum in both directions. The low order in P3HT LIPSS at λ=266 nm is clearly seen by AFM (Figure 4.23.b), and it was already reported[51]. The sample with rectangles shows good order in both directions (Figure 4.23.c).

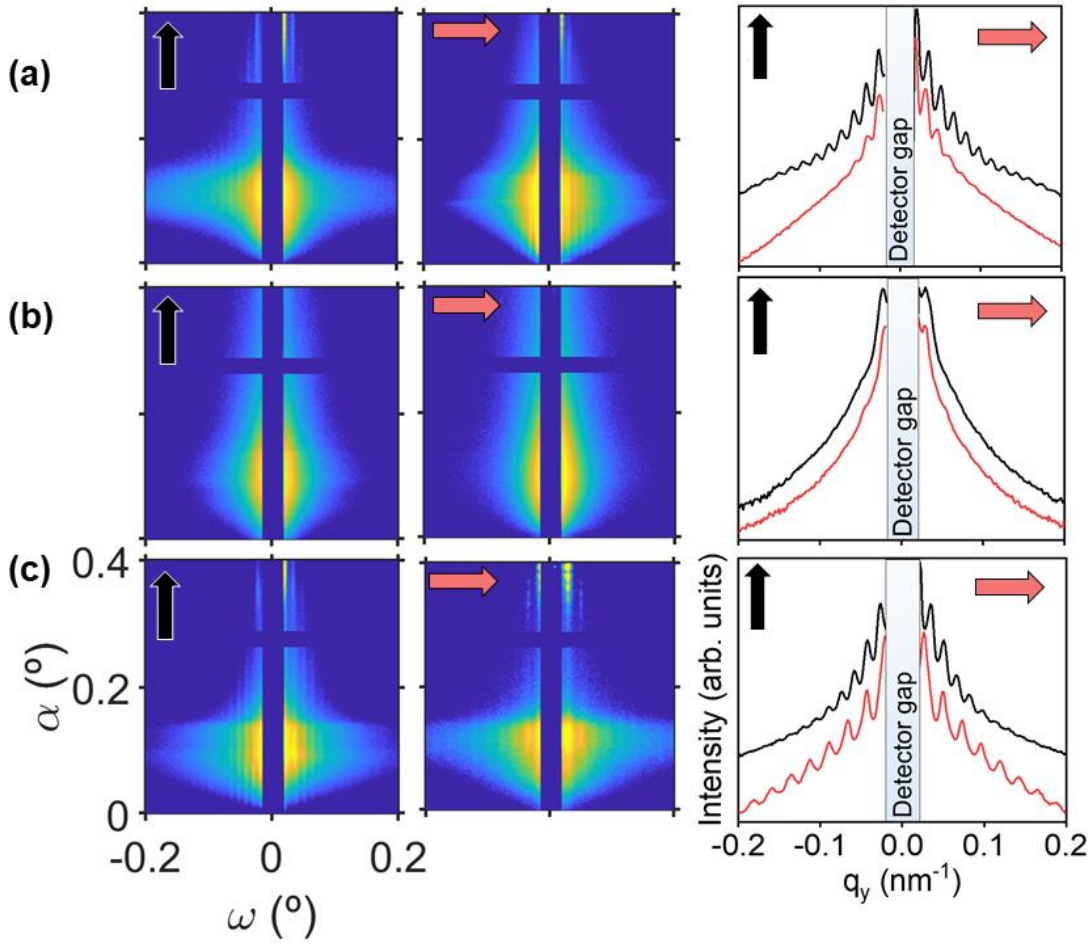

Figure 4.23 GISAXS patterns from P3HT irradiated samples with **(a)** squares of ~500 nm, **(b)** squares of ~200 nm and **(c)** rectangles of ~500 nm x ~200 nm. **Left column**: GISAXS patterns taken with the X-ray beam parallel to the first irradiation direction. **Center column**: GISAXS patterns taken with the X-ray beam parallel to the second irradiation direction. **Right column**: horizontal cuts from their corresponding GISAXS patterns in the same row, left column (black curves) and center column (red curves). Black arrows indicate the direction of the first irradiation step and red arrows the direction of the second irradiation step. GISAXS patterns taken at incident angle α=0.4º. Intensity in logarithmic scale.

Other structures were obtained by using different irradiation conditions. Figure 4.24 shows AFM images of patterns produced by fixing the wavelength (λ=532 nm) and polarization shift (90º) and varying the number of pulses, in a way that the total number of pulses is the optimal number to fabricate conventional P3HT LIPSS (3600 pulses). Irradiation conditions for samples in Figure 4.24 are included in Table 4.6.

It can be seen in Figure 4.24.a that with equal number of pulses in both irradiation steps, is the second polarization direction which determines the main direction of LIPSS. Even with less number of pulses during the second irradiation step (Figure 4.24.c-d), LIPSS are clearly better formed in the direction of the second polarization vector. By irradiating with 3300 pulses in the

vertical direction followed by 300 pulses in the horizontal direction, LIPSS have good order in both directions (Figure 4.24.d) as can be seen in the FFT image that show intensity maxima along both orthogonal directions.

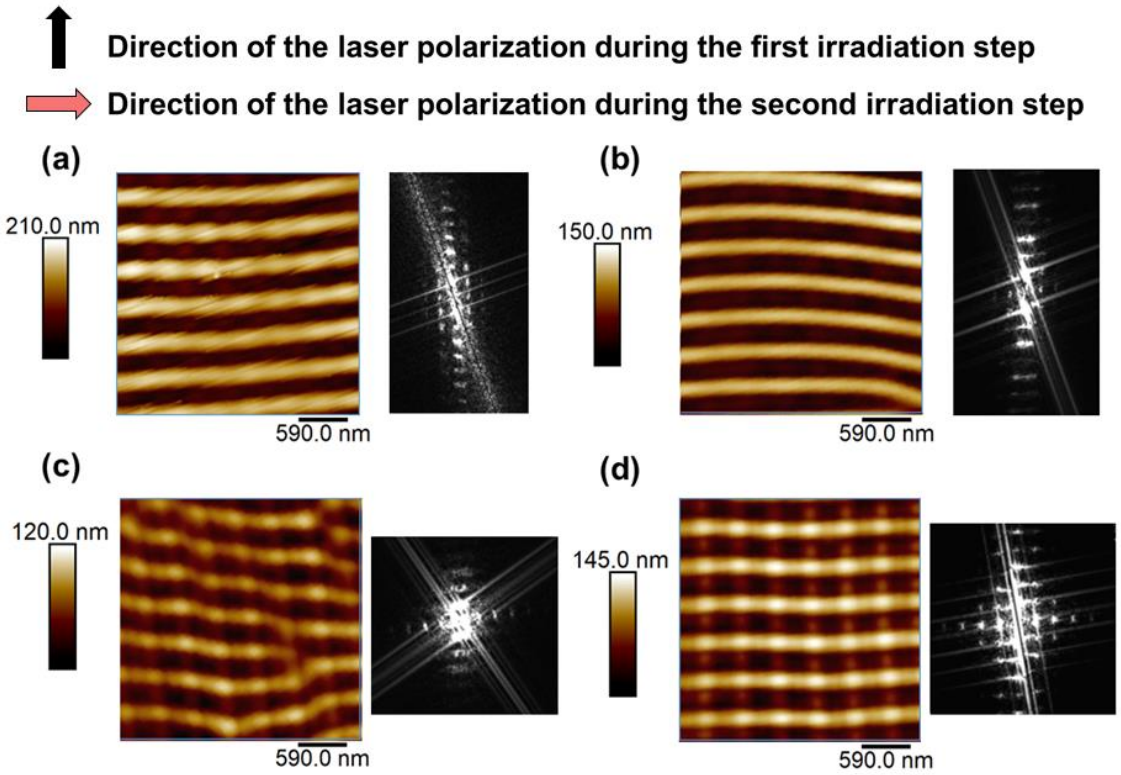

Figure 4.24 AFM images of combined LIPSS formed by sequential irradiation in P3HT at λ=532 nm by varying the number of pulses of each irradiation, with the corresponding FFT of every AFM image.

Table 4.6 Conditions of sequential irradiations corresponding to samples presented in Figure 4.24.

Image	1st irradiation		Polarization shift (º)	2nd irradiation	
	λ (nm)	Pulses		λ (nm)	Pulses
(a)	532	1800	90	532	1800
(b)	532	2400	90	532	1200
(c)	532	3000	90	532	600
(d)	532	3300	90	532	300

Moreover, more complex structures are fabricated by varying polarization shifts, number of pulses and adding more irradiation steps. Figure 4.25 shows AFM images of these patterns. Irradiation conditions are displayed in Table 4.7.

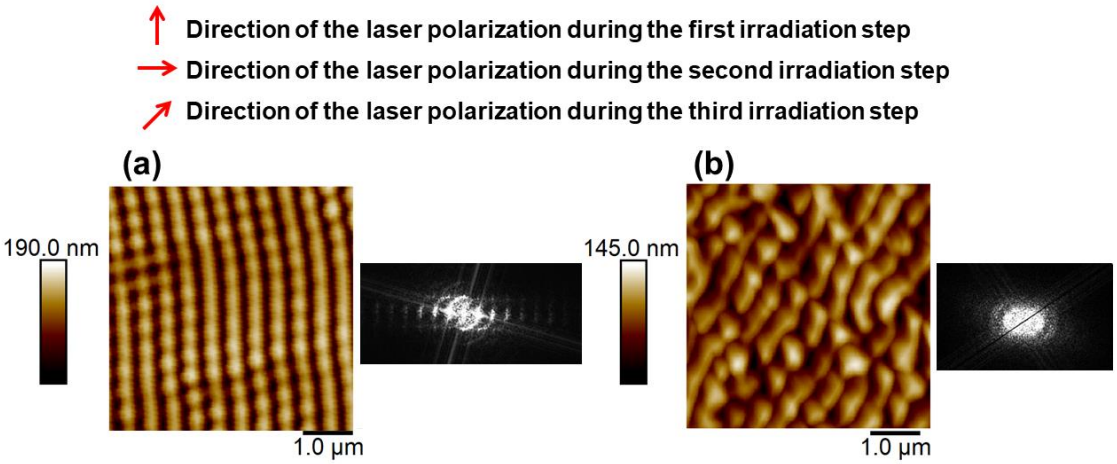

Figure 4.25 AFM images of combined LIPSS formed by sequential irradiation in P3HT at λ=532 nm by varying the polarization vector of the laser; together with the corresponding FFT image of every AFM image.

Table 4.7 Conditions of sequential irradiations corresponding to samples presented in Figure 4.25.

Image	**1st irradiation**		**Polarization shift (º)**	**2nd irradiation**		**Polarization shift (º)**	**3rd irradiation**	
	λ (nm)	**Pulses**		**λ (nm)**	**Pulses**		**λ (nm)**	**Pulses**
(a)	532	3600	90	532	100	45	532	100
(b)	532	3600	90	532	1800	45	532	1800

Figure 4.25.a shows the AFM image of a P3HT thin film irradiated first with 3600 pulses followed by 100 pulses polarized in the orthogonal direction and 100 pulses polarized 45º with respect to the initial polarization. It can be seen that LIPSS are formed preferentially in the original polarization direction with lower order at 45º, as revealed by several intensity maxima in FFT along the horizontal direction and one maximum along the direction of the polarization used in the third irradiation step. On the other hand, Figure 4.25.b shows an AFM image of the sample irradiated with the same polarization shifts but with 3600 pulses initially followed by 1800 pulses and then other 1800 pulses. The total number of pulses exceeds the optimum value so LIPSS hardly preserved a preferential orientation and the corresponding FFT indicates loss of order compared with Figure 4.25.a. This shows that the polarization used during the last irradiation step

will be determinant to the final order of the sample using a number of pulses about an order of magnitude lower than the number of pulses used during the first irradiation step.

GIWAXS measurements were carried out to see changes in their inner structure, in particular whether the crystallinity degree and orientation is affected. Samples with squares of ~500 nm, ~200 nm and rectangles of ~500 nm x ~200 nm were selected. GIWAXS patterns are presented in Figure 4.26.

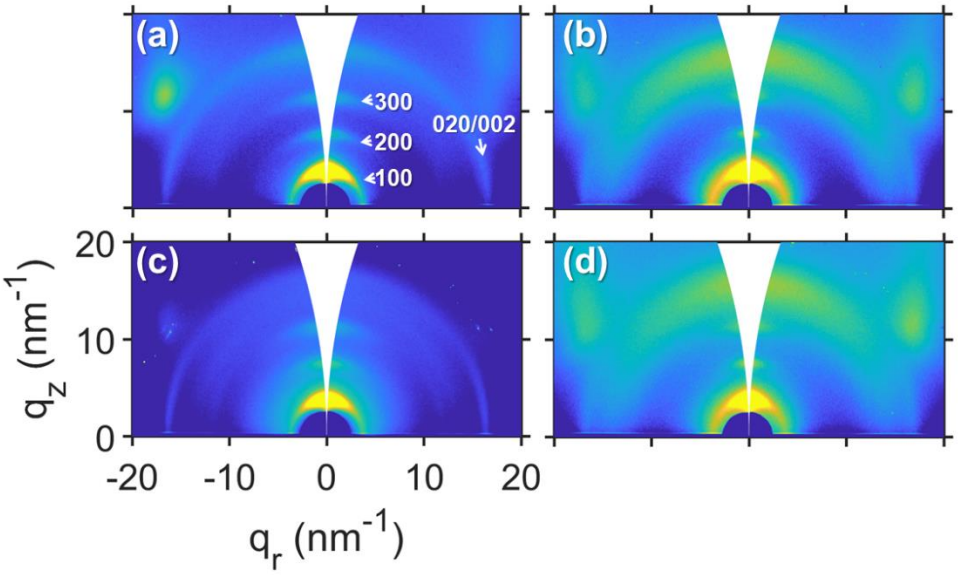

Figure 4.26 GIWAXS patterns of **(a)** P3HT thin film –non-irradiated-, and irradiated: (**b)** squares ~500 nm, **(c)** squares ~200 nm, **(d)** rectangles. Main reflections of crystalline P3HT labelled in **(a)**. Intensity of GIWAXS patterns in logarithmic scale.

GIWAXS patterns from Figure 4.26 show typical P3HT diffraction pattern with preferential "edge-on" orientation, with {h00} reflections oriented along the q_z axis (see section 1.4.1). The (020/002) reflection and the halo from the amorphous domains are located around q=17 nm^{-1}. It can be seen that GIWAXS patterns from irradiated samples (Figure 4.26.b-d) present a broad amorphous halo, compared with the pattern from non-irradiated P3HT (Figure 4.26.a).

Azimuthal integrations from GIWAXS patterns were done and represented in Figure 4.27. It can be observed that the amorphous halo of P3HT increases in the irradiated samples in comparison to the non-irradiated one. Therefore, laser irradiation implies a reduction of the crystallinity degree, as previously reported, as a consequence of rapid heating and cooling processes involved during LIPSS formation[36]. Interestingly enough, the amorphous halo is more prominent in the profiles from samples which have been irradiated at 266 nm in at least one of the irradiation steps: the sample with squares ~200 nm (Figure 4.27, blue curve) and the sample with rectangles (Figure 4.27, green curve).

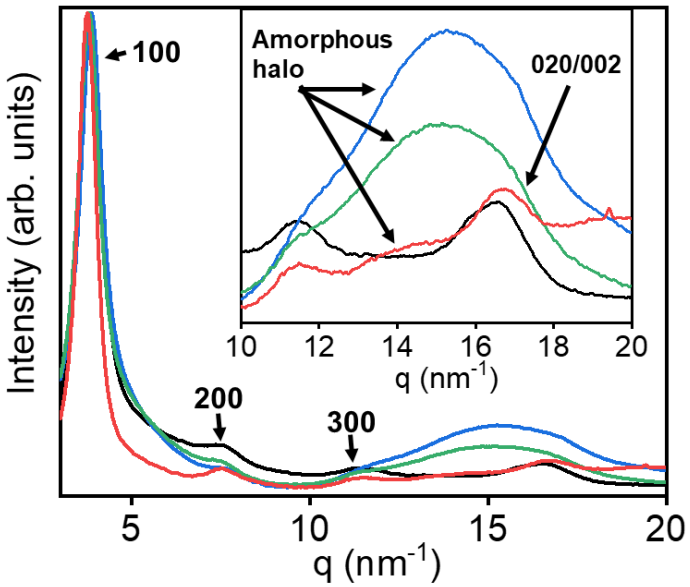

Figure 4.27 Azimuthal integrated intensity profiles of GIWAXS patterns displayed in Figure 4.26: non-irradiated thin film of P3HT (black curve), squares ~500 nm (red curve), squares ~200 nm (blue curve) and rectangles (green curve). GIWAXS of irradiated samples taken with X-ray beam parallel to first irradiation. Inset shows a magnification of the q-range region where the (020/002) reflection and amorphous halo of P3HT appear.

4.3.3 Patterning of large areas

The process of obtaining large patterned areas consists of mounting the sample in a translation stage. In this way, areas of several centimeters can be patterned within a few minutes by scanning the sample with the laser beam. For this purpose, the scanning speed, and consequently the spatial overlap of successive pulses, was chosen to ensure the delivery of optimal amount of pulses for LIPSS formation, previously determined by usual single spot irradiation. Nanostructuring in large areas conferred iridescence to the polymer surface. Figure 4.28 shows a 1 cm x 1 cm piece of P3HT structured with 532 nm squares on a silicon wafer. Pictures are taken by illuminating with white light at different incident angles so changes in the structural color can be observed.

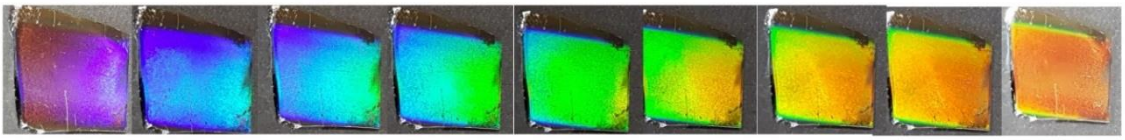

Figure 4.28 Optical images, obtained under different angle of white light illumination, of 1 cm x 1 cm nanostructured samples obtained by using the sequential nanosecond pulsed laser irradiation.

4.3.4 Characterization of P3HT/P(VDF-TrFE) array pattern. Functionality of the pattern

A square pattern was obtained by sequential irradiation at 532 nm (3500 pulses plus 100 pulses after a 90º polarization shift) in a functional polymer bilayer P3HT (bottom, thickness≈130 nm) / P(VDF-TrFE) (up, thickness≈20 nm). The multilayered sample was prepared using the same conditions as those used for the study of ferroelectricity on bilayers in section 3.1. It has been proven in the past that this configuration is suitable in order to obtain nanostructures by laser irradiation on ferroelectric polymers, besides the fact that they are non-absorbers at the used laser wavelength[52]. Figure 4.29 shows the morphology of the structured bilayer and its piezoelectric nature as revealed by Piezoresponse Force Microscopy (PFM) (see section 2.3.1.1.3).

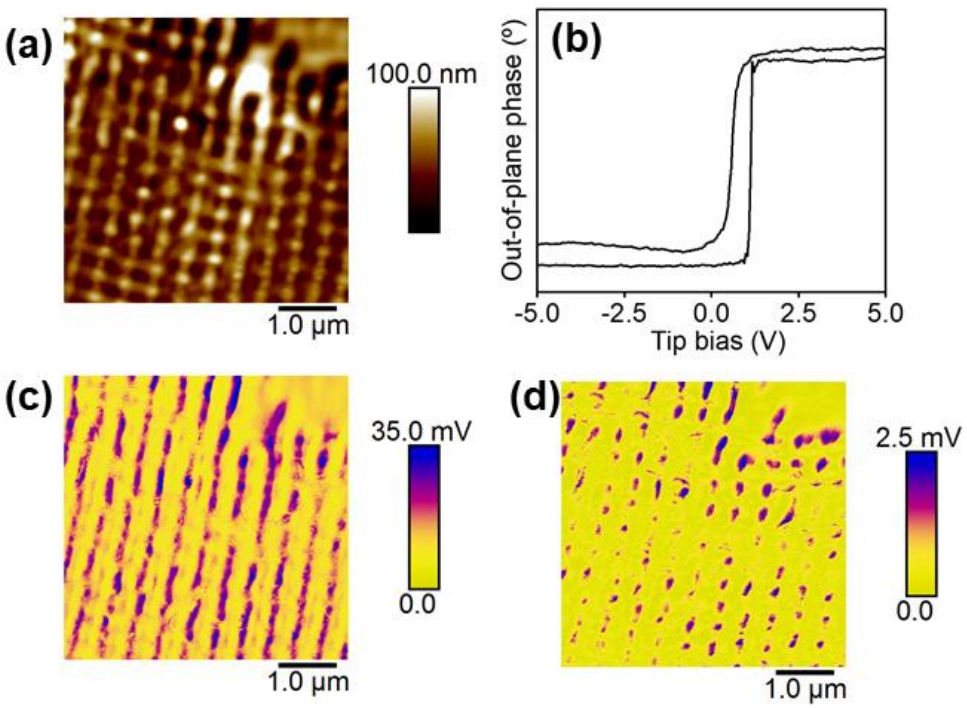

Figure 4.29 AFM height **(a)** and PFM results **(b-d)** of a patterned functional polymer surface exhibiting ferroelectricity: **(b)** Hysteresis of the out-of-plane PFM phase as a function of a DC bias applied to the conducting AFM tip. **(c)** Out-of-plane amplitude mapping of the patterned surface. **(d)** In-plane amplitude mapping of the patterned surface.

These results demonstrate that by the technique described in this section it is possible to obtain an ordered square array of ferroelectric dots, as can be seen in Figure 4.29.d, in which isolated dots present in-plane piezoelectric amplitude. The preserved ferroelectricity in the nanostructured surface, already proved on the original unstructured polymer surface (see section 3.1.2, Figure 3.2), is demonstrated by the existence of hysteresis in the out-of-plane phase signal obtained by

PFM (Figure 4.29.b), although GIWAXS results show an almost completely disappearance of the P(VDF-TrFE) Bragg peak when irradiated (Figure 4.30).

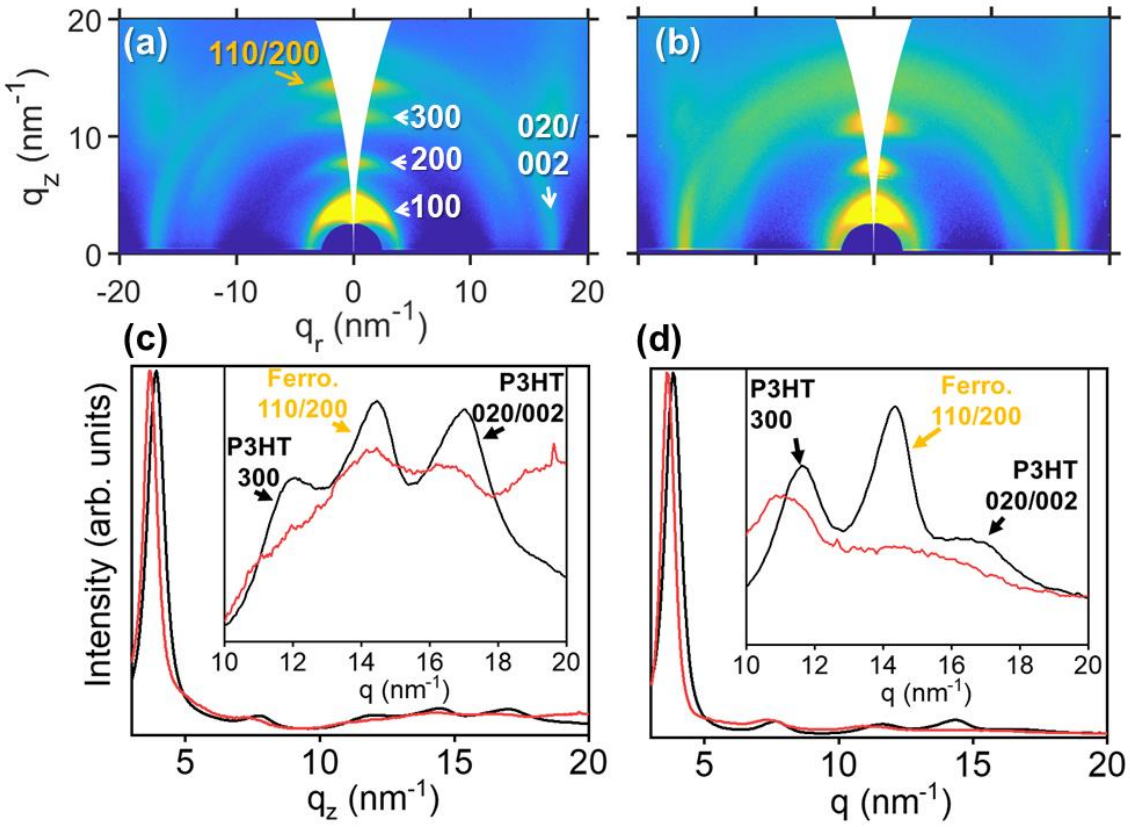

Figure 4.30 GIWAXS patterns of **(a)** bilayer of P3HT and P(VDF-TrFE) –non-irradiated- and **(b)** bilayer irradiated with two orthogonal polarizations at 532 nm (3500 + 100 pulses). In the right half of **(a)**, reflections from P3HT are labelled, and in the left half the P(VDF-TrFE) reflection is labelled. **(c)** Integration along the q_z axis of non-irradiated bilayer (black curve) and irradiated bilayer (red curve). **(d)** Integration along the whole azimuthal range of non-irradiated bilayer (black curve) and irradiated bilayer (red curve). Insets in **(c)** and **(d)** are magnifications of the q-range where reflection from P(VDF-TrFE) appears. Reflections from P3HT and P(VDF-TrFE) (ferro.) are labelled in black and orange respectively. Intensity of GIWAXS patterns in logarithmic scale.

Figure 4.30.a shows the reflections associated with the (110/200) planes of ferroelectric phase of P(VDF-TrFE) highly oriented in the q_z axis, whereas the GIWAXS pattern from the irradiated bilayer does not show this orientation (Figure 4.30.b). In Figure 4.30.c, it can be seen that the (110/200) reflections from P(VDF-TrFE) along the q_z axis are clearly detected in the profile from non-irradiated bilayer (black curve) and they are slightly detected in the profile from irradiated bilayer (red curve). Looking at Figure 4.30.d, the peak from P(VDF-TrFE) is highly reduced between the profile from non-irradiated (black curve) and the irradiated bilayer (red curve). Therefore, there is a clear loss of crystallinity in P(VDF-TrFE) when it is irradiated, as well as in irradiated P3HT (Figure 4.27). However, since PFM results (Figure 4.29) shows piezoelectric

behavior, it is supposed that the irradiated P(VDF-TrFE) in the bilayer keeps some degree of crystallinity. Radial integration in the q-range of the (110/200) reflections of P(VDF-TrFE) (Figure 4.31) reveals indeed a complete disorientation of a crystalline order that was originally highly oriented in the out-of-plane axis, corresponding with the azimuthal angle χ=90º, as can be seen in Figure 4.30.a.

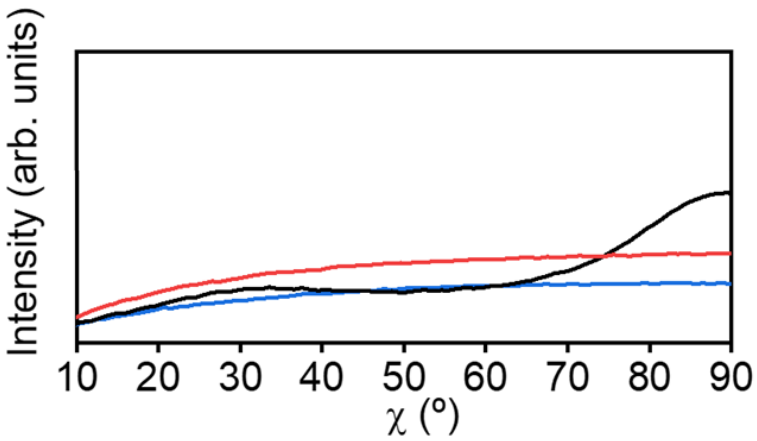

Figure 4.31 Radial integration of GIWAXS patterns displayed in Figure 4.30 in the q-range to delimit the (110/200) reflections of P(VDF-TrFE). Non-irradiated P3HT/P(VDF-TrFE) bilayer (black curve), irradiated sample with two orthogonal polarizations at 532 nm (3500 + 100 pulses) (red curve) and silicon-background (blue curve). χ=90º represents the q_z axis and χ=0º represents the q_r axis.

Therefore, the crystallinity of irradiated P(VDF-TrFE) is not completely removed but it loses the original preferential orientation that it presents in the non-irradiated bilayer.

4.4 Functional surface nanostructures induced by laser on fullerene thin films

Micrometric patterning of fullerene materials as C_{60} and $PC_{61}BM$ by light has been previously reported[53–55]. At nanometer scale, the ordering of fullerene molecules typically implies bottom-up strategies involving either a template surface[56,57] or a template nanoadditive[58]. In this section, we introduce a novel one-step top-down laser-induced method based on LIPSS capable of nanostructuring fullerene materials. We demonstrate the possibility of producing nanostructured functional materials on spin-coated $PC_{71}BM$ films.

Thin films of $PC_{71}BM$ were prepared by spin-coating. Conditions for preparation of solutions were displayed in Table 2.8. Spin-coating conditions were compiled in Table 2.10.

4.4.1 Laser irradiation: effect of different fluences and wavelengths studied by optical microscope and AFM

Irradiations were performed at air conditions, at normal incidence. The laser was linearly polarized. A wavelength of λ=532 nm was used by selecting the second harmonic of the Nd:YAG laser at a repetition rate of 10 Hz. This wavelength was selected for the experiment since $PC_{71}BM$ absorbs efficiently with an absorption coefficient $\alpha_{532}\approx 8\cdot 10^4$ cm^{-1}. Another wavelength of λ=266 nm (4th harmonic of Nd:YAG) was used, at which absorption coefficient of $PC_{71}BM$ is higher[59] than at 532 nm ($\alpha_{266}\approx 3.4\cdot 10^5$ cm^{-1}). The spot of the laser in the sample was defined by using an iris of 1.2 mm in diameter, attached to the additional holder of the optical system (section 2.2.1, Figure 2.7). These irradiation conditions for λ=532 nm were chosen on the basis of previous experiments about LIPSS formation in P3HT/$PC_{71}BM$ blends[36,60]. As long as the material absorbs more efficiently at λ=266 nm, the fluences chosen for this wavelength were lower. All the fluences used are presented in Table 4.8. In every sample, 3600 pulses were used.

Table 4.8 Fluences chosen for irradiating $PC_{71}BM$ thin films.

Spot diameter= 1.2 mm. Pulses= 3600						
Fluence (mJ · cm^{-2}) λ=532 nm						
13.6	15.4	17.2	19.0	20.8	22.6	24.4
Fluence (mJ · cm^{-2}) λ=266 nm						
7.2	9.0	10.8	12.6	14.4		

The shape of the spot in the sample was captured with an optical microscope (Figure 4.32 and 4.33). Either irradiating with λ=532 nm (Figure 4.32) or with λ=266 nm (Figure 4.33), the spots present homogeneous regions and brighter regions that have received more energy because the spatial distribution of energy in the spot is not perfectly homogeneous. Therefore, in some zones of the spot, the ablation threshold of the material is achieved before than in others. However, within a range of fluences above the LIPSS formation threshold and below the ablation threshold, the spot shows a nearly homogeneous aspect as in samples irradiated at λ=532 nm with fluence=15.4-17.2 mJ·cm^{-2}. In the case of samples irradiated at λ=266 nm, the evolution of the spot is similar with two marked differences. An intense ring due to diffraction from the iris is present in every sample. In addition, the gap of fluences between LIPSS formation and ablation of material (12.6 mJ·cm^{-2}) is much narrower than upon irradiations at λ=532 nm. This is caused by the higher absorption coefficient of $PC_{71}BM$ at λ=266 nm than at λ=532 nm.

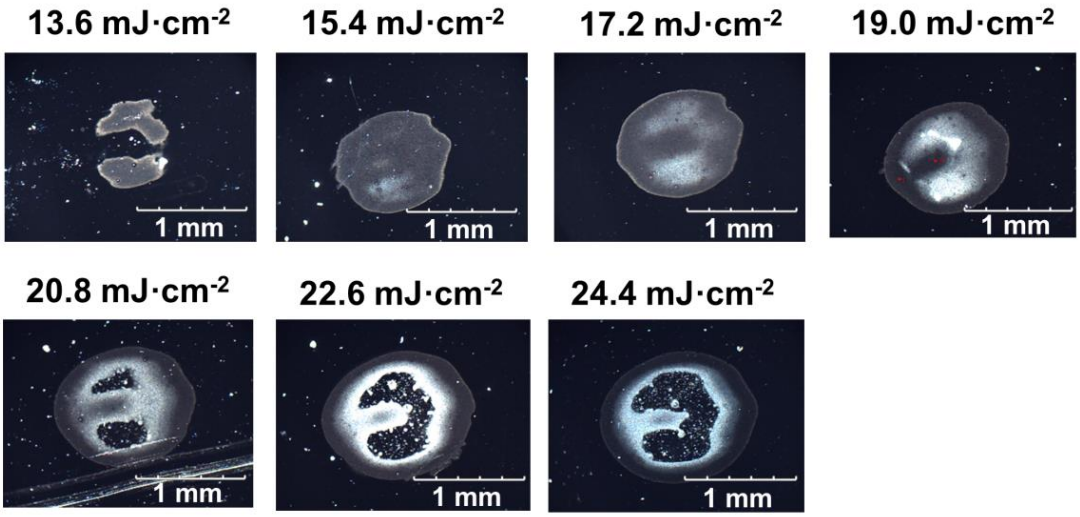

Figure 4.32 Optical micrographs of the laser spots of $PC_{71}BM$ thin films irradiated with different fluences at λ=532 nm.

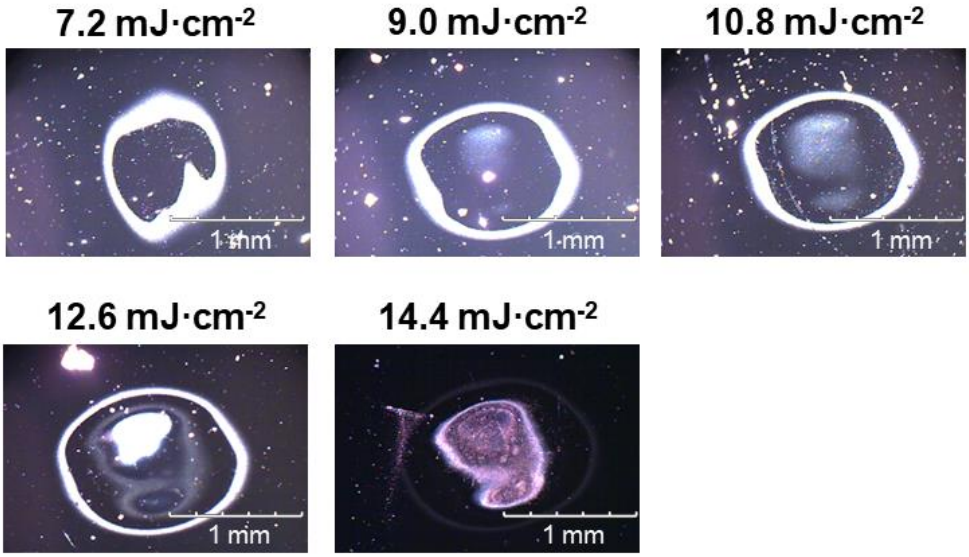

Figure 4.33 Optical micrographs of the laser spots of $PC_{71}BM$ thin films irradiated with different fluences at λ=266 nm.

AFM images in tapping mode were taken at the same zone of the spot for all the samples irradiated at λ=532 nm (Figure 4.34). These images show an initial grating-like pattern with low depth at 13.6 mJ·cm^{-2} followed by an increase in depth and order of the LIPSS between 15.4-19 mJ·cm^{-2} and a droplet-like structure with loss of order at 20.8-24.4 mJ·cm^{-2}. The period and depth of the LIPSS were measured from AFM images in Figure 4.34 and represented in Figure 4.35.

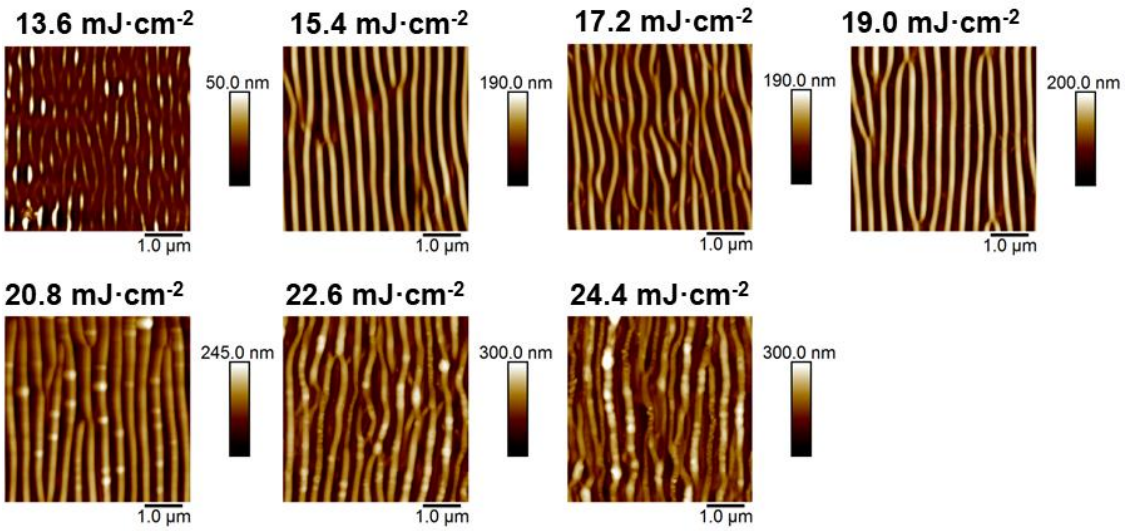

Figure 4.34 AFM tapping images of LIPSS in $PC_{71}BM$ irradiated with λ=532 nm.

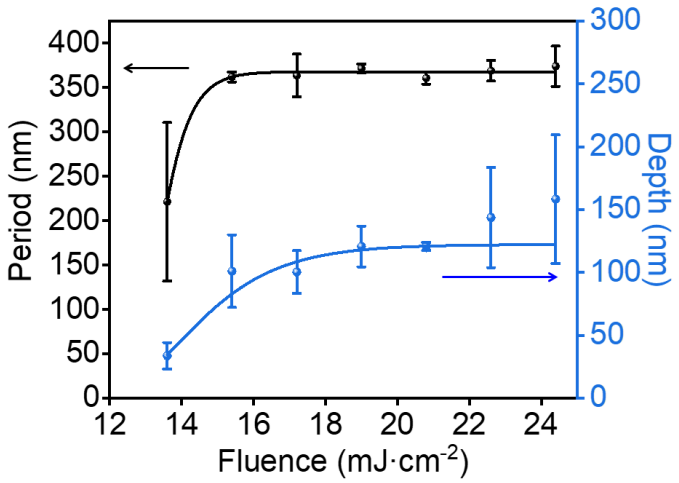

Figure 4.35 Period and depth of LIPSS in $PC_{71}BM$ irradiated at λ=532 nm as a function of fluences. Curves are added as visual guides.

Average of depth and period of LIPSS formed by irradiation at λ=532 nm (Figure 4.35) shows the increase until reaching a plateau in both values (~365 nm in period and ~125 nm in depth).

In the case of LIPSS formed by irradiation at λ=266 nm, the situation is similar. However, there are fewer samples to compare since, as it was said before, the range of fluences that form gratings without material degradation is lower when irradiating at this wavelength due to the higher absorption coefficient of $PC_{71}BM$ at λ=266 nm. Figure 4.36 shows the AFM images taken at the same zone of the spot for the samples irradiated at λ=266 nm.

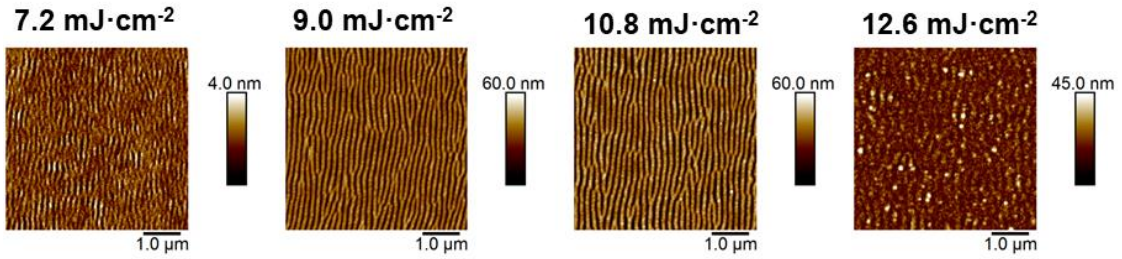

Figure 4.36 AFM tapping images of LIPSS in $PC_{71}BM$ irradiated with λ=266 nm.

It can be seen in Figure 4.36 that for the lowest fluence (7.2 mJ·cm^{-2}), the LIPSS are barely formed. For the next two fluences (9-10.8 mJ·cm^{-2}), LIPSS are deeper and better formed. The sample irradiated at 12.6 mJ·cm^{-2} shows degradation of the LIPSS. The period and depth of the LIPSS were measured and represented in Figure 4.37. Data from sample irradiated at 12.6 mJ·cm^{-2} was not included.

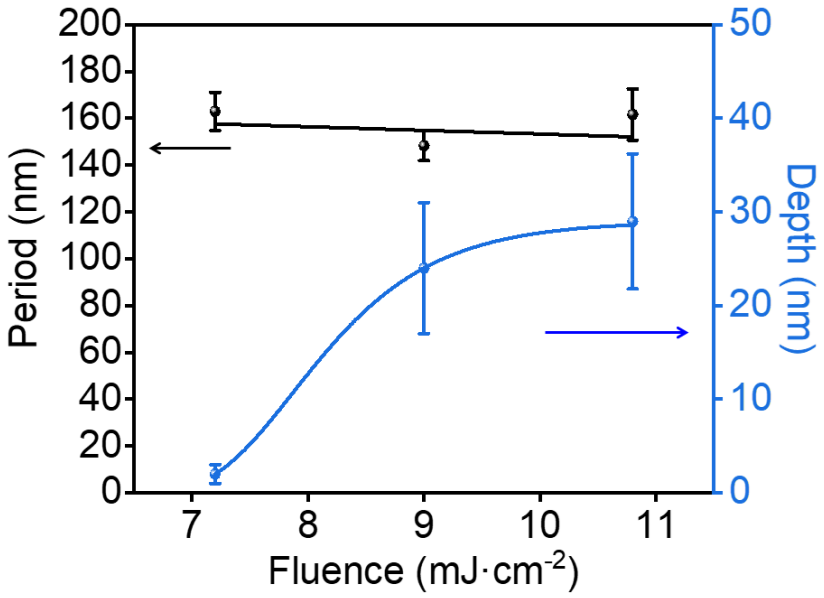

Figure 4.37 Period and depth of LIPSS in $PC_{71}BM$ irradiated at λ=266 nm as a function of fluences. Curves are added as visual guides.

The depth of LIPSS formed by irradiating at λ=266nm presents an initial value below 5 nm for the sample irradiated with fluence=7.2 mJ·cm^{-2}. For the next two fluences (9-10.8 mJ·cm^{-2}) the depth is around 20-30 nm. The period maintains a similar value around 160 nm for all the fluences.

The periods of the gratings are a function of the laser wavelength, the angle of incidence and the refractive index of the material (see section 2.2.1, Equation 2.1). The depth of the LIPSS is a direct consequence of the absorption coefficient of the material at a particular wavelength. Since the absorption coefficient of $PC_{71}BM$ is higher at λ=266 nm ($3.4 \cdot 10^5$ cm^{-1}) than at λ=532 nm

(~$8 \cdot 10^4$ cm^{-1})[59], the penetration depth of the laser will be lower at λ=266 nm. For this reason, it is reasonable that LIPSS formation would be more superficial with λ=266 nm and the nanostructures would have lower depth. Figure 4.38 shows this effect, comparing the sections profiles of LIPSS formed by irradiation at λ=532 nm and λ=266 nm.

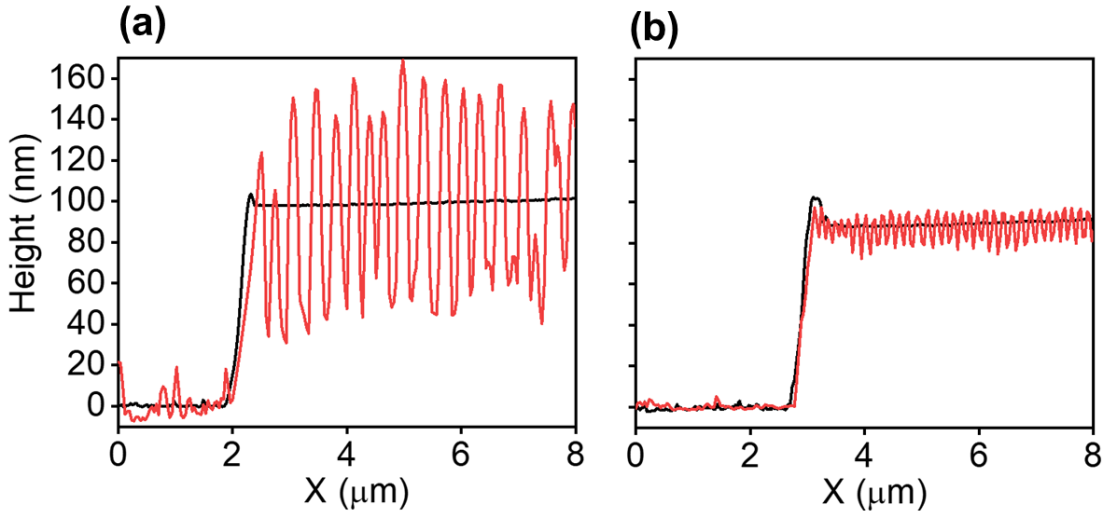

Figure 4.38 Sections of LIPSS obtained by irradiating $PC_{71}BM$ **(a)** at λ=532 nm with fluence=17.2 mJ·cm^{-2}, and **(b)** at λ=266 nm with fluence=9 mJ·cm^{-2} (red curves) and initial spin-coated $PC_{71}BM$ film (black curves). Profiles were obtained by making a scratch with a razor blade on the irradiated spot of the sample and taking an AFM image on the cut profile. The left flat zone of the profiles corresponds to the part which has been removed by the razor blade.

The superposition of the height profiles of both the initial spin-coated films and those of the irradiated ones suggests that LIPSS formation in both cases proceeds on the $PC_{71}BM$ surface by a redistribution of the material into hills and valleys.

4.4.2 Post-irradiation washing treatment: morphology of the residue

LIPSS formed by laser irradiation of $PC_{71}BM$ films present the characteristics of a photoinduced and resist-free imprinting (PRI). The non-irradiated areas can be removed by a solution development procedure while irradiated ones partially remain on the silicon substrate. The solution development procedure is a repetition of the same initial spin-coating process carried out to prepare the films but using the pure solvent (C_6H_5Cl). All fluences for both wavelengths were "washed" with the solvent. Optical micrographs were taken at the residue left on the laser spot (Figure 4.39). The sample irradiated at λ=532 nm with the lowest fluence (13.6 mJ·cm^{-2}) did not leave a visible residue.

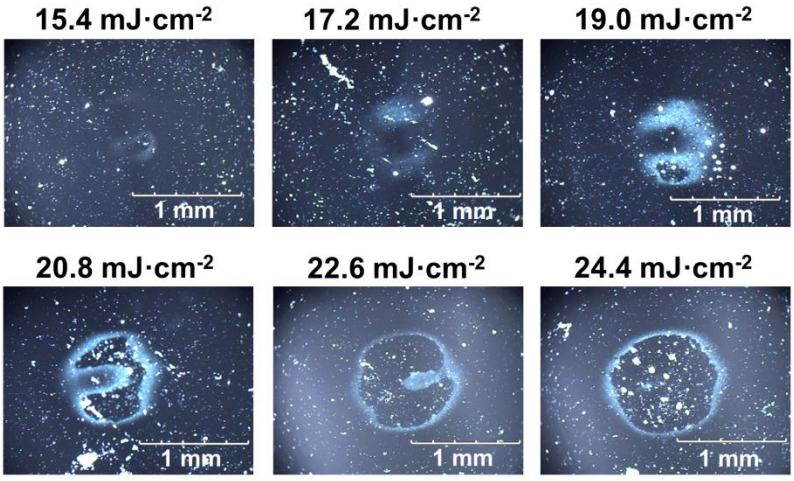

Figure 4.39 Optical micrographs of the laser spots of $PC_{71}BM$ thin films irradiated with different fluences at λ=532 nm after solution development.

Optical microscopy images suggest that, apparently after development, only the central part of the irradiated area remains. Additional information about the developed irradiated area can be obtained by further AFM inspection (Figure 4.40).

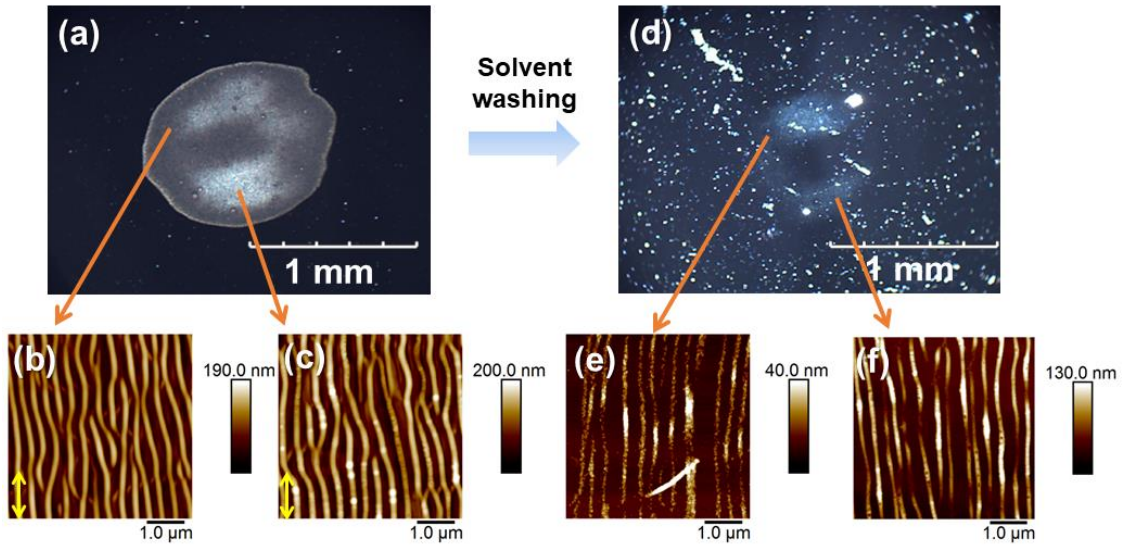

Figure 4.40 (a) Optical micrograph of the laser fingerprint on a spin-coated $PC_{71}BM$ film after irradiation at λ=532 nm with 3600 pulses and fluence=17.2 mJ·cm^{-2}. **(b** and **c)** AFM topographic images in the indicated positions. The yellow double arrow indicates the laser polarization. **(d)** Optical micrograph of the residue remaining after solvent washing. **(e** and **f)** AFM topographic images in the indicated positions.

Figure 4.40.a-c shows the optical microscopy and AFM images of the irradiated zone from the sample irradiated at λ=532 nm and fluence=17.2 mJ·cm^{-2}. Figure 4.40.d-f shows the analog optical microscopy and AFM images of the $PC_{71}BM$ sample irradiated at λ=532 nm after solvent

washing. Interestingly enough LIPSS appear in all zones even in outer part of the spot, where no optical contrast is detected (Figure 4.40.d). However, a different morphology is observed especially in the outer region. Here the LIPSS are characterized by thinner hills of ≈5-10 nm forming nanowires with a granular texture (Figure 4.40.e). Height profiles were extracted from Figure 4.40.e-f and presented in Figure 4.41.

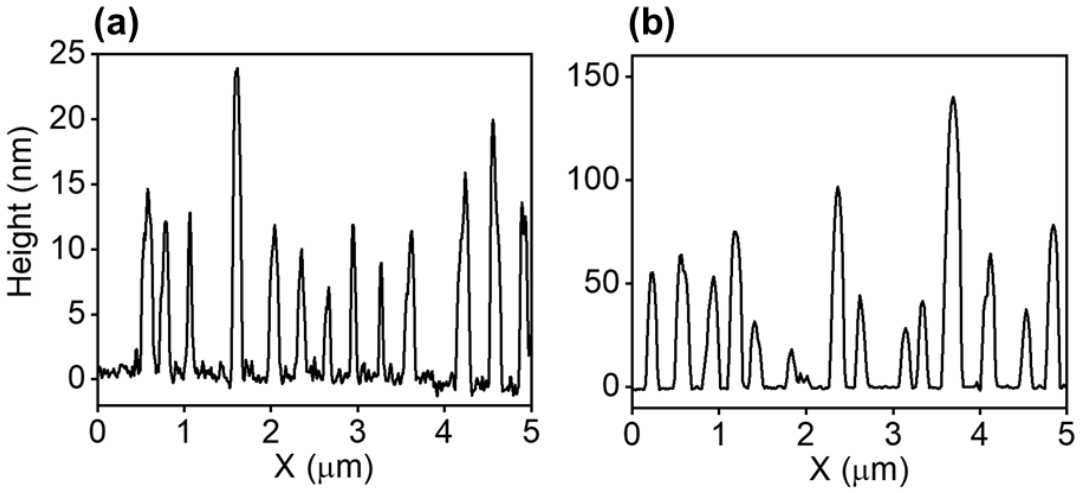

Figure 4.41 (a,b) 5-μm horizontal profiles of AFM topographic images 4.41 **(e,f)**, respectively.

It can be seen in Figure 4.41 that in both cases (different zones of the residue), the washed LIPSS emerge from flat level. In Figure 4.38.a, original LIPSS after irradiation at λ=532 nm consist of both hills and valleys roughly centered on the surface of the initial spin-coated $PC_{71}BM$ film. On the contrary, in the washed LIPSS residue (Figure 4.41) the hills seem to protrude from the silicon substrate level indicating that the solvent was capable of removing a significant superficial layer of the film though leaving a remnant LIPSS profile. In addition, these results also reveal that the non-irradiated material can be effectively removed by a solvent in the present conditions.

The solution development was applied on samples irradiated at λ=266 nm the same way as on samples irradiated at λ=532 nm. Optical microscope images were taken on the irradiated spot after solution development (Figure 4.42). In this case, the solution development also left in the sample a visible residue. Further inspection by AFM shows quite a different behavior after solution development between samples irradiated at both wavelengths. In the central part of the spot, LIPSS preserve their original form and height though there is a general decrease of thickness of the thin film where the LIPSS are. This effect is seen in Figure 4.43.

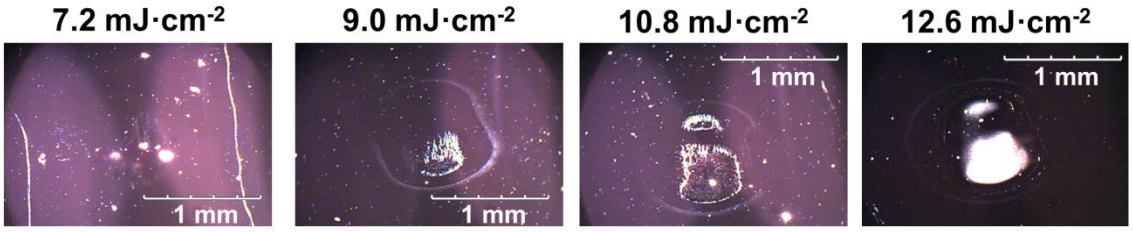

Figure 4.42 Optical micrographs of the laser spots of $PC_{71}BM$ thin films irradiated with different fluences at λ=266 nm after solution development.

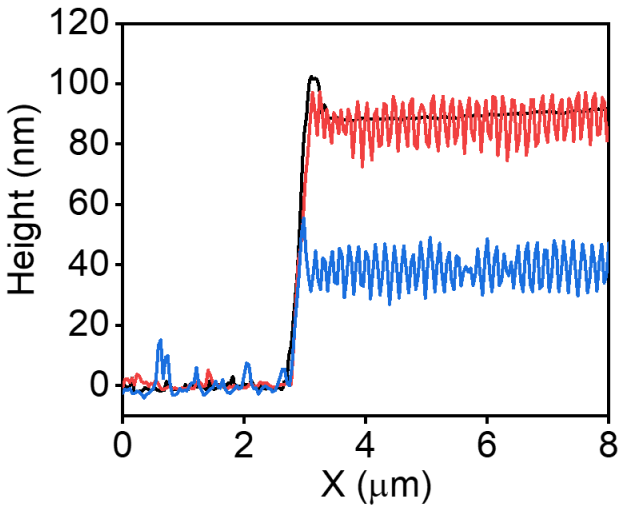

Figure 4.43 Sections of $PC_{71}BM$ thin film non-irradiated (black curve), and irradiated at λ=266nm, fluence=9 mJ·cm^{-2}, before (red curve) and after (blue curve) solution development. Profiles were obtained by making a scratch with a razor blade on the irradiated spot of the sample and on the residue left after solution development, and taking an AFM image on the cut profile. The left flat zone of the profiles corresponds to the part which has been removed by the razor blade.

This result suggests a different chemical change on $PC_{71}BM$ induced by using different wavelengths.

4.4.3 Chemical and structural characterization of resist-free LIPSS by Raman spectroscopy and GIWAXS

It has been proven for both low-solubility fullerene C_{60} and $PC_{61}BM$ that during exposure to light, chemically connected fullerene structure appears[55]. In these cases, Raman spectroscopy has been shown to be a powerful method in order to investigate intramolecular bond formation (see section 2.3.4). Figure 4.44 shows the Raman spectra of $PC_{71}BM$ spin-coated films before and after irradiation with λ=532 nm, and after solution development.

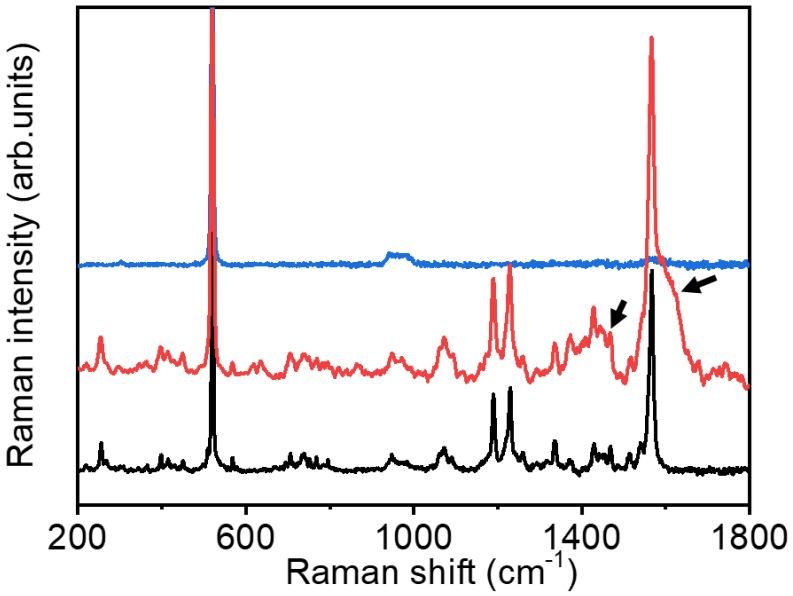

Figure 4.44 Raman spectra taken at λ=532 nm of $PC_{71}BM$ spin-coated film (black data), $PC_{71}BM$ after irradiation with λ=532 nm, fluence=17.2 mJ·cm^{-2} (red data), and subsequently washed with chlorobenzene (blue data). Spectra have been baseline corrected and shifted vertically for comparison reasons. The arrows indicate the two new broad bands that appear after irradiation.

The spectrum of the reference non-irradiated $PC_{71}BM$ spin-coated film (Fig. 4.44, black data) presents the characteristic bands associated to C_{70}[61,62] and $PC_{71}BM$[63]. In particular the ones at ≈1565 cm^{-1} and 1467 cm^{-1} which are assigned to the anti-symmetry and symmetry C=C stretch mode, respectively[63]. For the $PC_{71}BM$ film after irradiation (Figure 4.44, red data), the Raman spectrum presents two additional broad bands, indicated by arrows, centered around ≈1400 cm^{-1} and ≈1600 cm^{-1}. The appearance of the two mentioned broad bands suggests the onset of a graphitization process upon laser irradiation since the observed bands can be associated to the characteristic D (1350 cm^{-1}) and G (1584 cm^{-1}) bands of graphene oxide[24–26]. It is known that fullerenes are not stable at high temperature. As a matter of fact, the synthesis of graphene films obtained by thermal treatment of fullerenes in the presence of a metal substrate has been reported in the literature[25,64]. Dimers of C_{70}, i.e. C_{140}, have been obtained[61] by high pressure and high temperature treatment of C_{70}. In this case, the characteristic Raman bands associated to the coupled translational and rotational motions of the two C_{70} molecules appear at low frequency, namely at 89, 118 and 129 cm^{-1}. In our case, the presence of such bands is not detectable. Similarly to C_{60}, for C_{70} cycloaddition across parallel double bonds is also possible[65]. However it has been reported that for C_{70}, although insoluble films upon irradiation are obtained, no significant changes in the vibrational spectra are detected[65]. This was explained considering that vibronic properties of C_{70} and its dimer, i.e. C_{140}, are very similar[61]. The Raman spectrum of the washed

sample (Figure 4.44, blue data), essentially shows the bands associated to the silicon substrate corroborating that a substantial amount of material was removed during solution development.

Figure 4.45 shows the Raman spectra of $PC_{71}BM$ spin-coated films before and after irradiation with λ=266 nm, and after solution development.

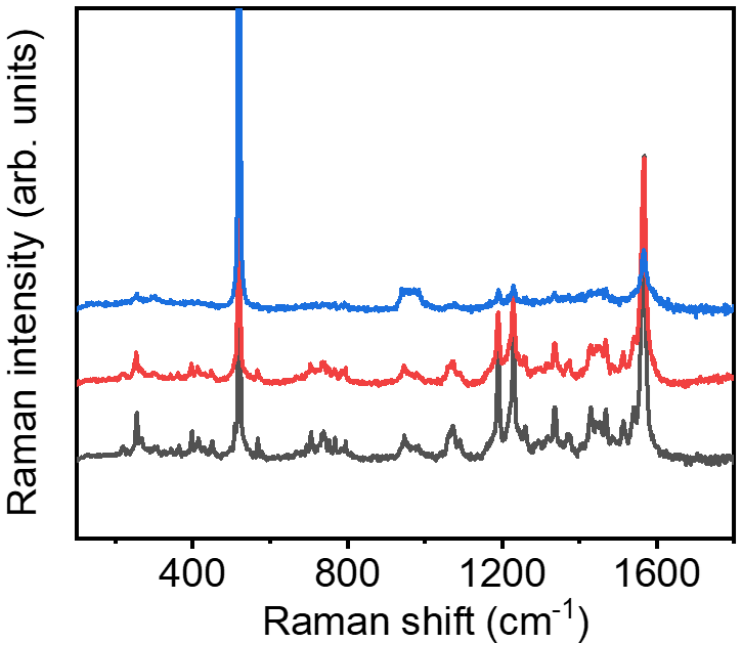

Figure 4.45 Raman spectra at λ=532 nm of $PC_{71}BM$ spin-coated film (black data), $PC_{71}BM$ after irradiation with λ=266 nm, fluence=9 $mJ \cdot cm^{-2}$ (red data), and subsequently washed with chlorobenzene (blue data). Spectra have been baseline corrected and shifted vertically for comparison reasons.

For the $PC_{71}BM$ spin-coated films after irradiation with λ=266 nm, the situation is qualitatively similar (Figure 4.45, red data) although the presence of the new bands associated with graphene oxide are not as apparent as for the sample irradiated at λ=532 nm (Figure 4.44, red data). Noteworthy, the Raman spectrum after irradiation at λ=266 nm and subsequent washing (Figure 4.45, red and blue data) exhibits the characteristic bands of the original $PC_{71}BM$ sample corroborating that a substantial amount of material remains over the silicon substrate after development as previously illustrated in Figure 4.43. On the basis of the Raman spectroscopy, data are in agreement with previous reports[61,65], in which dimers is the most likely structure to be formed. Similarly as for $PC_{61}BM$[55], it is expected that the side group hinders the formation of higher molecular weight oligomers. Accordingly, it seems plausible that the PRI effect is caused by a chemical modification of the $PC_{71}BM$ upon laser irradiation rendering to a fraction of dimers and graphene oxide.

In order to gain further information, GIWAXS experiments were performed on these samples. Figure 4.46 shows a series of GIWAXS patterns for the $PC_{71}BM$ spin-coated sample and for the irradiated ones at λ=532 nm for different fluences as labelled.

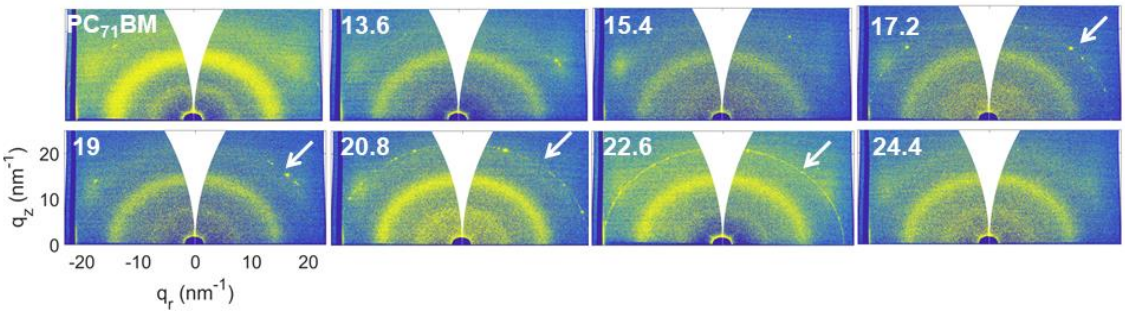

Figure 4.46 GIWAXS patterns for the $PC_{71}BM$ spin-coated sample and for the irradiated ones at λ=532 nm for different fluences, in mJ·cm^{-2}, as labelled. The arrows indicate the appearance of a sharp peak for fluences in the range between 17.2 mJ·cm^{-2} and 22.6 mJ·cm^{-2}. Intensity in logarithmic scale.

GIWAXS patterns for spin-coated $PC_{71}BM$ show a broad maximum around q=15 nm^{-1} (Figure 4.46). Along a range of fluences, patterns from irradiated samples at λ=532 nm display a sharp peak, marked with arrows. GIWAXS patterns were azimuthally integrated and the resulting intensity profiles are presented in Figure 4.47.

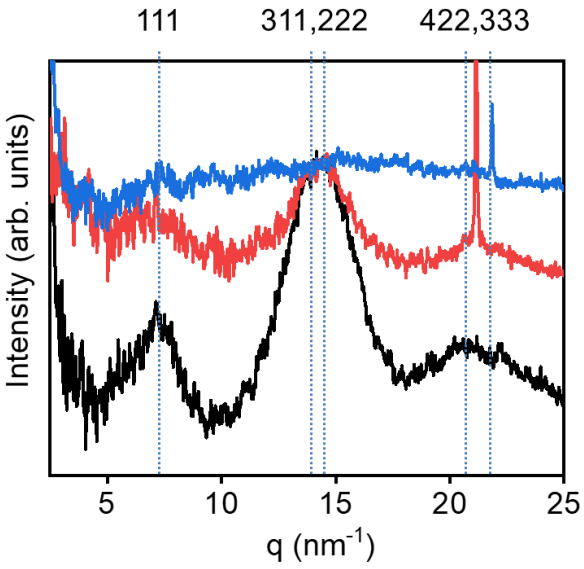

Figure 4.47 Normalized intensity profiles extracted from the integration of the GIWAXS patterns for: $PC_{71}BM$ spin-coated film (black curve), $PC_{71}BM$ irradiated at λ=532 nm, fluence=17.2 mJ·cm^{-2} (red curve) and subsequently washed with chlorobenzene (blue curve). Curves have been vertically displaced for the sake of clarity.

The intensity profile of non-irradiated spin-coated $PC_{71}BM$ thin film (Figure 4.47, black data) exhibits three main broad maxima appearing at q-values of 7.27 nm^{-1}, 14.23 nm^{-1} and 21.19 nm^{-1}

which agree with previously reported data[42] for $PC_{71}BM$ and correspond to the reflections associated to the (111), (311/222,) and (422/333) planes, of the fcc (face-centered cubic) crystalline structure[66] of C_{70}[66]. The broadness of the diffraction maxima suggests that $PC_{71}BM$ spin-coated films exhibit low crystallinity in agreement with previous reports[67,68]. Figure 4.47 (red data) shows the diffraction pattern of the $PC_{71}BM$ spin-coated film after irradiation with λ=532 nm. The pattern presents essentially the same features of the non-irradiated samples although a sharp peak appears in the region of the (422/333) reflections. This fact has been visualized by arrows in Figure 4.46 where one detects the appearance of a sharp peak for fluences in the range between 17.2 $mJ \cdot cm^{-2}$ and 22.6 $mJ \cdot cm^{-2}$. In a first approach we can assign this peak with the formation of a genuine crystalline phase upon irradiating starting around fluences of 17.2 $mJ \cdot cm^{-2}$, reaching a maximum around 22.6 mJ·cm-^{2} and disappearing at high fluence values (24.4 $mJ \cdot cm^{-2}$). The appearance of a sharper maxima decorated with discrete spots is characteristic of the formation of larger crystals as previously described for thermal treated $PC_{61}BM$ and $PC_{71}BM$ spin-coated films[67,68].

As it was described in detail in section 2.2.1 and mentioned several times along this chapter, upon irradiation with nanosecond laser pulses the sample is heated. The temperature increment can be estimated as a function of time and different depths from the film surface by solving the one-dimensional heat conduction equation, the same procedure performed for LIPSS in PEDOT:PSS (see section 4.1.4, Equation 4.4). The values of the magnitudes used for the calculation of the temperature profiles have been taken from the literature and are presented in Table 4.9.

Table 4.9 Physical parameters of $PC_{71}BM$: specific heat (c), density (ρ) and thermal conductivity (κ).

c ($J \cdot kg^{-1} \cdot K^{-1}$) [69]	**ρ ($kg \cdot m^{-3}$)** [70]	**κ ($W \cdot m^{-1} \cdot K^{-1}$)** [69]
820	1630	0.07

As with PEDOT:PSS LIPSS, the temperature dependence of the material physical parameters and the possible changes in the thermal properties during the process were not taken into account in the calculation. Figure 4.48 shows the temperature reached at the surface of $PC_{71}BM$ after irradiation with a single pulse at λ=532 nm and at fluence=17 $mJ \cdot cm^{-2}$. Temperature reaches a value of around 123ºC which is close to the glass transition temperature (T_g) reported for $PC_{61}BM$[67,71].

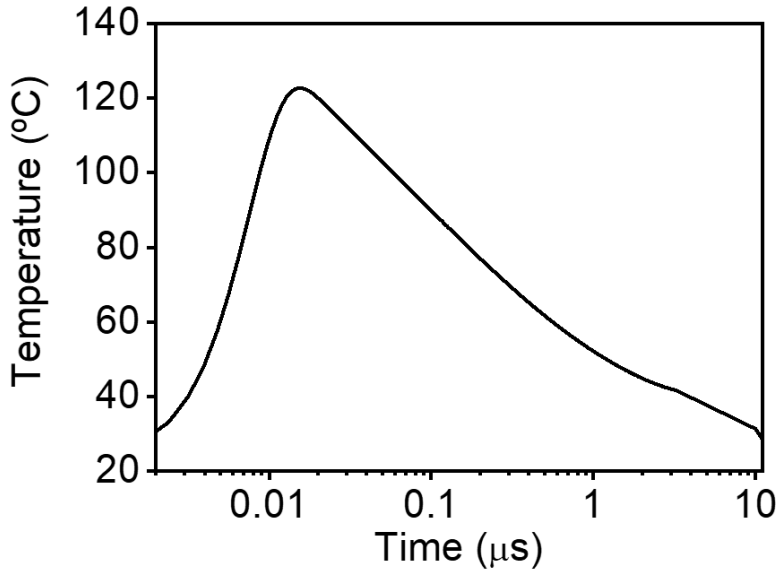

Figure 4.48 Time dependence of the temperature reached at the surface of $PC_{71}BM$ after irradiation with a single pulse at λ=532 nm and at a fluence=17 $mJ \cdot cm^{-2}$.

It is known that increasing the temperature of a glass above its T_g but below its melting temperature induces a metastable supercooled state that may give rise to the formation of a crystalline state by a process frequently referred to as cold crystallization[72,73]. It is also important to mention that the optical penetration depth, i.e. the inverse of the absorption coefficient (α^{-1}) is around 100 nm at λ=532 nm and thus, all the material is affected and heated by the laser irradiation. Then heat is subsequently dissipated mostly through the silicon substrate[11]. Thus, it is plausible that during laser irradiation the sample suffers a heat treatment leading to the development of a crystalline phase. Previous GIWAXS experiments performed in thermal annealed $PC_{61}BM$ spin-coated films have shown that the silicon substrate acts as a heterogeneous nucleation surface for crystallization[67]. This finding suggests that in our case the crystalline phase may appear close to the fullerene silicon interface.

In order to corroborate this hypothesis, chlorobenzene washed samples were subjected to GIWAXS experiments. Figure 4.49 compares the GIWAXS patterns of the irradiated $PC_{71}BM$ spin-coated films with those of the chlorobenzene washed samples. Although the overall scattered intensity decreases significantly after washing, the presence of the sharp ring although weak is still detected both in the GIWAXS patterns and on the intensity profiles (Figure 4.47, blue data). This finding indicates that in our case the crystalline phase appears as a buried phase close to the fullerene-substrate silicon interface.

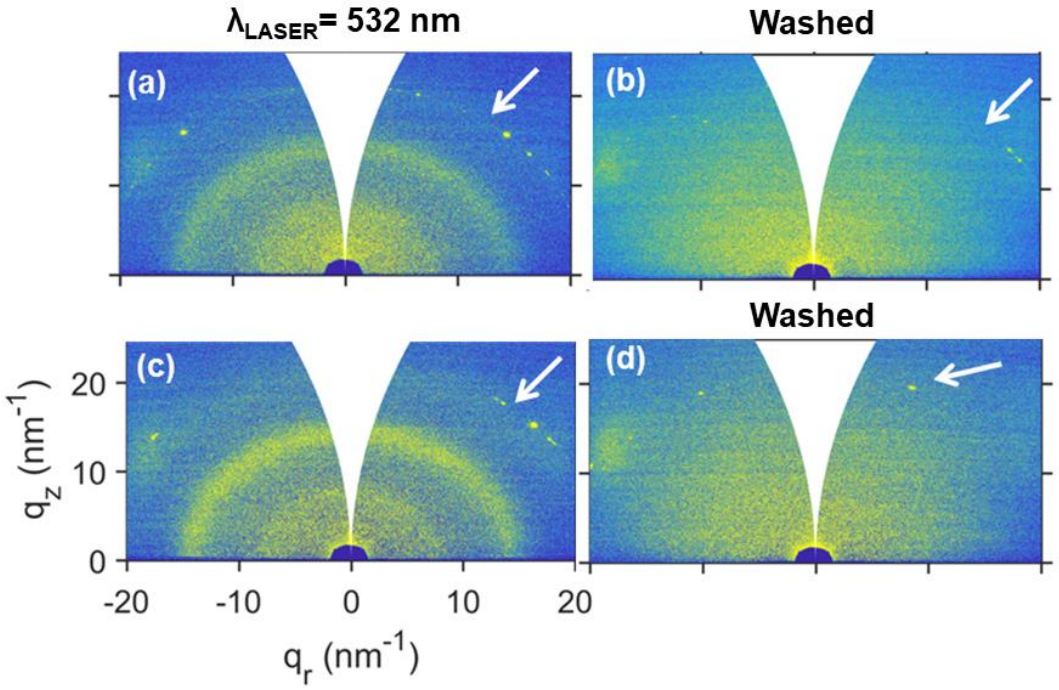

Figure 4.49 GIWAXS patterns for the $PC_{71}BM$ spin-coated sample irradiated at λ=532 nm for fluences **(a)** 17.2 mJ·cm^{-2} and **(c)** 19.0 mJ·cm^{-2} and those of their corresponding washed counterparts **(b)** and **(d)** respectively. Intensity in logarithmic scale.

There is another aspect in relation to the GIWAXS patterns that needs to be discussed. By comparing the data of the $PC_{71}BM$ spin-coated film (Figure 4.47, black data), with those of the irradiated one (Figure 4.47, red data), it can be seen that the irradiated sample exhibits a clear broadening of the peak around 15 nm^{-1}. On the basis of both Raman spectroscopy and GIWAXS experiments, our results suggest that irradiated $PC_{71}BM$ films suffer a fast heating/cooling process that reduces the overall crystallinity of the LIPSS while provoking the presence of a phase of larger crystals close to the fullerene-substrate silicon interface, that resist the solution development with C_6H_5Cl. A similar situation is observed for samples irradiated at λ=266 nm, as illustrated in Figure 4.50, where the appearance of discrete spots is much scarce as with samples irradiated at λ=532 nm. Following the previous explanation, the spots could be related with a buried crystalline phase close to the substrate. As long as $PC_{71}BM$ absorbs more at λ=266 nm, the nanostructuring effect is much more superficial (Figure 4.38). Its optical penetration length (α^{-1}) is around 30 nm. Therefore, the nucleation and development of a buried phase is limited by the surface of $PC_{71}BM$, reducing the thermal effects at the substrate interface.

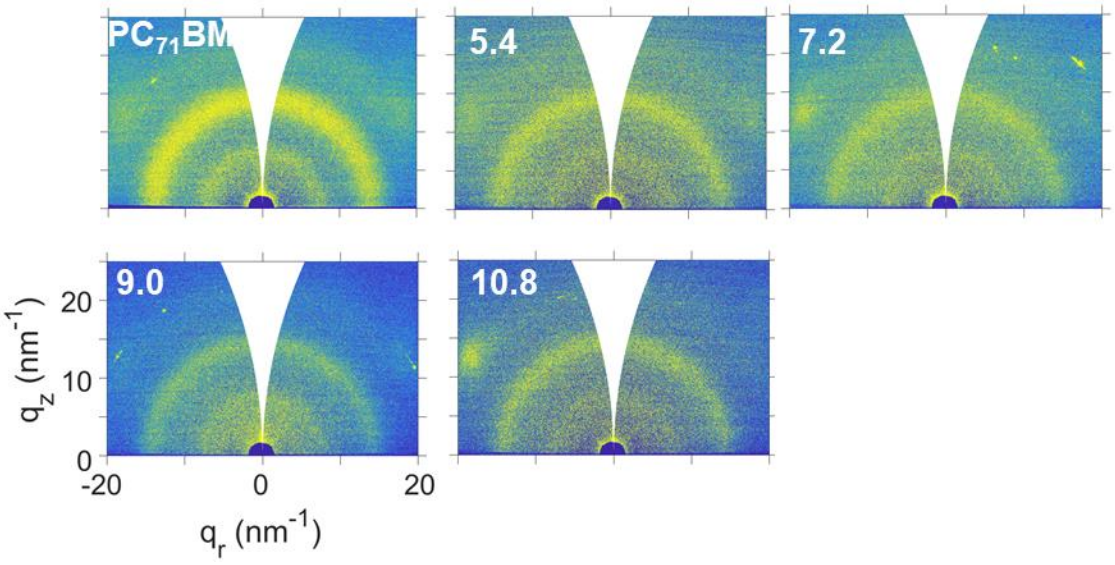

Figure 4.50 GIWAXS patterns of the $PC_{71}BM$ spin-coated sample and the irradiated ones at λ=266 nm for different fluences, in $mJ \cdot cm^{-2}$, as labelled. Intensity in logarithmic scale.

4.4.4 Functionality of resist-free LIPSS on $PC_{71}BM$ spin-coated films

In order to verify the functionality of the prepared fullerene LIPSS in terms of electrical conduction, we have accomplished C-AFM measurements in $PC_{71}BM$ spin-coated films, and in the irradiated and washed samples. Figure 4.51.a shows the topographical image of a thin film of $PC_{71}BM$ taken in contact mode. Its corresponding C-AFM image, taken applying a DC voltage of 10 V shows a homogeneous electrically conductivity in the whole area (Figure 4.51.b).

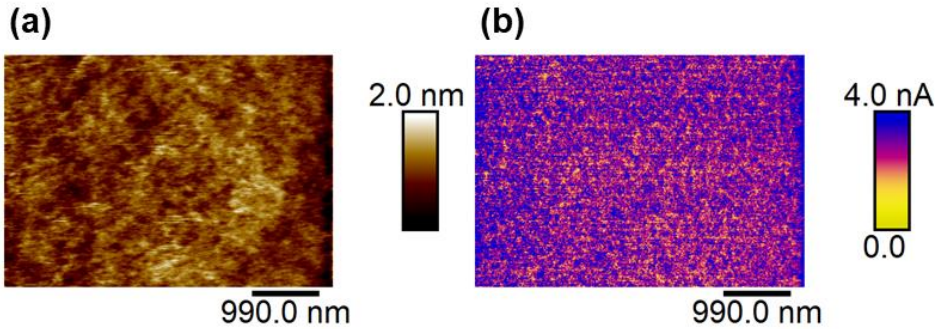

Figure 4.51 (a) AFM contact mode topographic images of original $PC_{71}BM$ spin-coated films and **(b)** its corresponding C-AFM images. DC voltage applied=+10V.

Figure 4.52 shows the electrical response of $PC_{71}BM$ LIPSS obtained irradiating with iris at λ=532 nm with fluence=17.2 $mJ \cdot cm^{-1}$ and the subsequent washed sample with chlorobenzene.

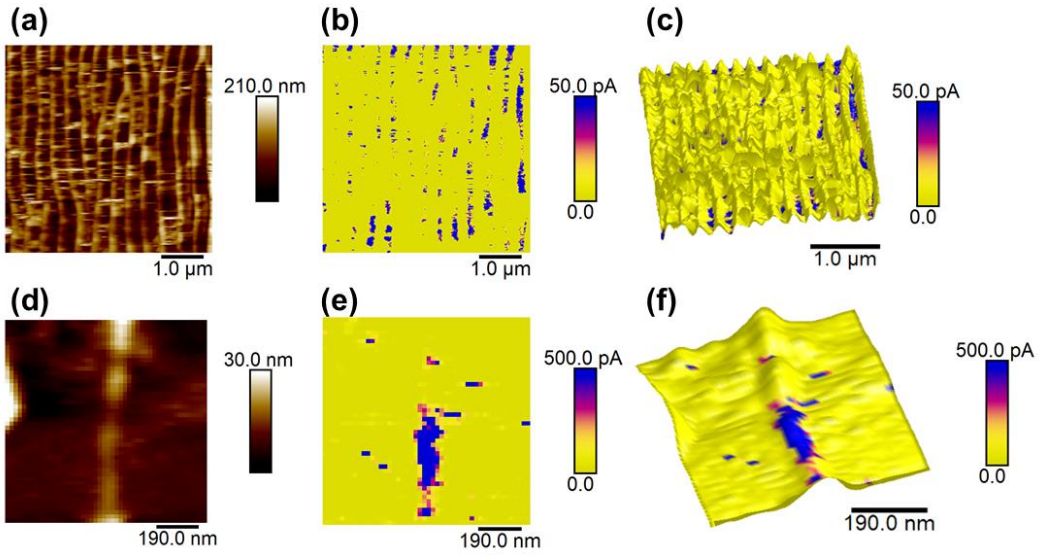

Figure 4.52 (a) AFM contact mode topographic image and **(b)** C-AFM image (DC voltage applied=10V) of a spin-coated $PC_{71}BM$ film irradiated at λ=532 nm for a fluence=17.2 mJ·cm^{-2}. **(c)** Docking of the topography and current images. **(d)** Topographic image of typical nanowire remaining after solvent washing and **(e)** corresponding C-AFM image (DC voltage applied=+10V.). **(f)** Docking of the topography **(d)** and current **(e)** images.

It is worth mentioning that since for C-AFM working in contact mode is a requirement, then the topographic image (Figure 4.52.a) exhibits lower resolution than the corresponding ones obtained in tapping mode (Figure 4.34). Additionally, in soft surfaces the cantilever tip provokes a dragging effect responsible for the horizontal lines observed in Figure 4.52.a. The irradiated $PC_{71}BM$ spin-coated sample (Figure 4.52.b) exhibits a series of conducting stripes alternating with non-conducting ones. A direct comparison with its topographic counterpart can be done by docking both topography and current images as illustrated in Figure 4.52.c. There one sees that the conducting regions of the irradiated sample correspond to the valleys of the LIPSS while the non-conducting regions are associated to the hills. P3HT and PCDTBT LIPSS also shows this effect (see section 4.2 of this Thesis), and LIPSS of PEDOT:PSS behave also in a similar way (see section 4.1 of this Thesis). It is proposed that the common component for this decrease of conductivity at the LIPSS hills of these systems is the lower crystallinity induced by laser irradiation.

There is another aspect in relation to the C-AFM experiments that needs to be discussed. As shown before, laser irradiation provokes the appearance of a sharp maximum in the GIWAXS patterns (Figure 4.47) that can be assigned to the formation of a buried crystalline phase close to the silicon substrate that can be related to the granular motives observed by AFM (Figure 4.40.e) for the washed $PC_{71}BM$ samples previously irradiated. Figure 4.52.e shows the C-AFM image of one of the nanowires remaining on the silicon substrate after washing the $PC_{71}BM$ samples

previously irradiated in comparison with its topographic image (Figure 4.52.d). A direct comparison with its topographic counterpart can be done by docking both topography and current images as illustrated in Figure 4.52.f. There one sees that the conducting region of the washed irradiated sample corresponds to the thinner part of the nanowire while the non-conducting regions are associated to the thicker part. In addition, some conducting dots appear suggesting that granular texture observed in the irradiated samples after washing (Figure 4.40.e) contains $PC_{71}BM$ crystallites with enhanced conductivity.

Moreover, the C-AFM image is consistent with the above formulated hypothesis proposing that irradiated $PC_{71}BM$ films: i) suffer a fast heating/cooling process tending to reduce the overall crystallinity of the LIPSS and therefore decreasing the electrical conductivity of the hills and leaving a remnant conducting film underneath the hills and ii) during laser irradiation the sample suffers a heat treatment leading to the development of a buried phase close to the substrate formed by larger crystals with enhanced electrical conductivity.

In the case of $PC_{71}BM$ irradiated samples at λ=266 nm, it was seen that they do not present any electrical response (Figure 4.53).

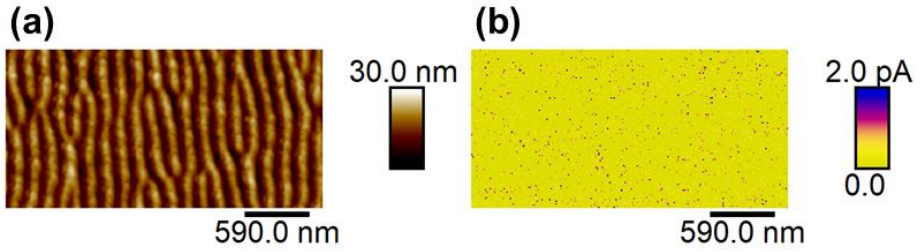

Figure 4.53 (a) AFM topographic image in contact mode and **(b)** corresponding C-AFM image of a spin-coated $PC_{71}BM$ thin film irradiated at λ=266 nm with fluence=9 $mJ \cdot cm^{-2}$. DC voltage applied=+10V.

It was described in section 4.4.1 that the effect of the laser irradiation at λ=266 nm is much more superficial than at λ=532 nm, due to a higher absorption coefficient of $PC_{71}BM$ at λ=266 nm. It is likely that irradiations at λ=266 nm would reduce the crystallinity of the surface of $PC_{71}BM$ enough to depict an insulating upper layer on the film that block the electrical current through the sample. In addition, irradiated samples at λ=266 nm show a high resistance to chlorobenzene (Figure 4.43), higher than irradiated samples at λ=532 nm (Figure 4.41). This supports a higher chemical change in $PC_{71}BM$ upon irradiation at λ=266 nm than at λ=532 nm. However, these chemical modifications are likely not detected by Raman spectroscopy (Figure 4.45) since this technique scans a depth of around 1 micron, i.e. the whole film thickness (≈80-100 nm), thus if the modifications occur along a depth of a few nanometers from the surface, the contribution of

this layer to the Raman signal is much weaker than the contribution from the rest of the underlying film.

4.4.5 Laser photoinduced and resist-free imprinting LIPSS on $PC_{71}BM$ spin-coated films over large areas

Larger irradiated areas can be obtained by eliminating the iris. In this case the spot of the laser illuminates a circular area of about 5 mm in diameter. As an example, Figure 4.54.a-b shows the AFM topography image in contact mode and the C-AFM current image respectively of a $PC_{71}BM$ thin film irradiated without iris at λ=532 nm and fluence=17.1 mJ·cm^{-1}.

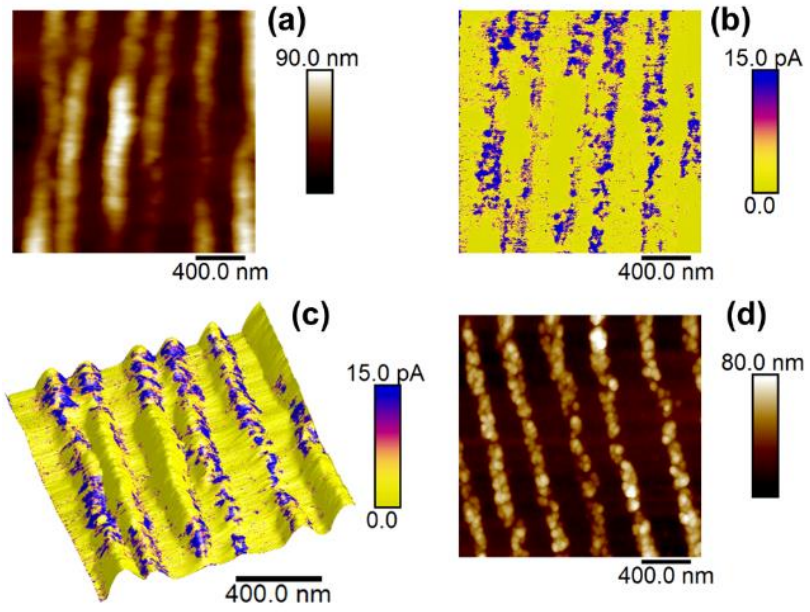

Figure 4.54 (a) AFM contact mode topographic image and **(b)** C-AFM image of a residue obtained after solvent development of $PC_{71}BM$ spin-coated sample irradiated without iris (using full laser beam area) at λ=532 nm for a fluence=17.1 mJ·cm^{-2}. **(c)** Docking of the topography and current images. **(d)** AFM tapping mode topographic image of the same sample. DC voltage applied=+10V

As emphasized by Figure 4.54.c, the more conducting regions, that in the C-AFM image appear as darker spots (Figure 4.54.b) are now located in the LIPSS hills of the samples. $PC_{71}BM$ crystallites can be better observed through the higher resolution AFM tapping mode topography image showed in Figure 4.54.d. Moreover, by depositing the sample over an automatic mobile X-Y displacement table it is possible to continuously illuminate macroscopic areas.

4.5 Conclusions

In this chapter, different polymeric materials and a fullerene derivative in the form of thin films have been nanostructured by irradiation with a nanosecond pulsed laser. It has been shown that formation of periodic superficial nanostructures depends on many variables being the absorption of the material at the wavelength of the laser crucial for the development of nanogratings or other geometries. Laser irradiation affects the material at several levels, from the nanograting structure until the inner structure of the material, being able to modify chain orientation and to generate new crystalline phases. These modifications have been analyzed in order to get insights about the possible applications of these functional nanostructured surfaces on organic electronics devices. Conclusions for each system are the following:

- As described in the first section, LIPSS on PEDOT:PSS thin films were successfully obtained and reported for the first time. Conditions were chosen based on the low absorption coefficient of PEDOT:PSS in the visible range and previous optimum irradiation conditions for another thiophene-based conjugated polymer (P3HT). The substrate seems to have a strong impact on the formation of LIPSS; we found that ITO-coated glass leads to deeper LIPSS than silicon substrate. On the other hand, silicon substrate seems to be crucial to induce a crystalline phase on the upper PEDOT:PSS layer, as revealed by GIWAXS. This crystalline phase seems to be absent in the samples deposited on ITO. Raman spectroscopy results do not show chemical damage and suggest that the heat treatment caused by laser induces a transition from benzoid to quinoid structure of PEDOT chains. C-AFM results of PEDOT:PSS LIPSS on ITO show a partial segregation of the conducting domains to the valleys of the gratings.

- The second section presents angle-dependent TEY-NEXAFS experiments over thin films of P3HT and PCDTBT that reveal preferential orientation of the polymer chains in the film surface, “edge-on” and “face-on” respectively. After laser irradiation of the films, the chains partially lose the preferential orientation. These results give us new insights about the impact of the laser treatment at the molecular level. PCDTBT LIPSS formed under vacuum atmosphere keep more “face-on” orientation that in the LIPSS grown under air conditions, suggesting a lower impact of laser irradiation at the molecular level. C-AFM results, on the other side, show images of electric current with conducting trenches and non-conducting ridges, similar in every sample. This result was described in P3HT as a reduction of crystallinity. However, in largely amorphous PCDTBT, the loss of “face-on” orientation could also be responsible for the segregation of electric current. LIPSS of PCDTBT in vacuum show more homogeneous electrical current

mapping than LIPSS formed in air because in vacuum PCDTBT maintains certain "face-on" orientation while it is vanished when LIPSS are formed in air.

- In the third section, we have reported the simple fabrication of a library of ordered nanostructures by repeated (sequential) irradiation steps using a nanosecond pulsed laser operating in the UV and visible region. We obtained nanoscale controlled patterns by varying irradiation parameters. We use this experimental approach to nanostructure a ferroelectric polymer so that an ordered square array of ferroelectric dots is obtained.

- In the fourth section, we have proven that it is possible to prepare LIPSS and photoinduced resist-free imprinting on $PC_{71}BM$ laser by illumination of spin-coated films with nanosecond pulsed laser. LIPSS prepared with a wavelength of 532 nm selectively preserve the electrical conductivity on the LIPSS valleys. The heterogeneous conducting pattern consisting in conducting valleys and less conducting hills observed in the LIPSS prepared under these conditions has been interpreted, on the basis of GIWAXS experiments, as due to a reduction in the crystallinity of the hills provoked by the fast heating/cooling process induced by every laser pulse. $PC_{71}BM$ LIPSS exhibit a resist free character and can be developed by spin-coating a solvent leaving the laser illuminated zone as an undissolved residue. On the basis of the experiments, it is proposed that irradiated $PC_{71}BM$ films suffer, on one hand, a fast heating/cooling process tending to reduce the overall crystallinity of the LIPSS and therefore decreasing the electrical conductivity of the hills and leaving a remnant conducting film underneath the hills. During laser irradiation the sample suffers a heat treatment induced by the substrate leading to the development of a buried phase close to the substrate formed by larger crystals with enhanced electrical conductivity. Further solvent treatment reveals the buried phase which remains in the form of partially electrically conducting nanowires. On the other hand, this is not achieved with samples irradiated at λ=266 nm. At this wavelength, the effect of the laser is much more superficial than at λ=532 nm. It is shown that samples irradiated at λ=266 nm have strong resistance to solution development, keeping the original LIPSS shape over a thin film with reduced thickness, thus indicating chemical changes upon irradiation. In addition, LIPSS of $PC_{71}BM$ obtained by irradiation at λ=266 nm does not show any electrical response.

4.6 References

(1) Guo, L. J. Nanoimprint Lithography: Methods and Material Requirements. *Adv. Mater.* **2007**, *19* (4), 495–513. https://doi.org/10.1002/adma.200600882.

(2) Tang, Z.; Tress, W.; Inganäs, O. Light Trapping in Thin Film Organic Solar Cells. *Mater. Today* **2014**, *17* (8), 389–396. https://doi.org/10.1016/j.mattod.2014.05.008.

(3) Bi, Y.-G.; Feng, J.; Ji, J.-H.; Yi, F.-S.; Li, Y.-F.; Liu, Y.-F.; Zhang, X.-L.; Sun, H.-B. Nanostructures Induced Light Harvesting Enhancement in Organic Photovoltaics. *Nanophotonics* **2017**, *7* (2). https://doi.org/10.1515/nanoph-2017-0060.

(4) Radivo, A.; Sovernigo, E.; Caputo, M.; Zilio, S. D.; Endale, T.; Pozzato, A.; Goldoni, A.; Tormen, M. Patterning PEDOT:PSS and Tailoring Its Electronic Properties by Water-Vapour-Assisted Nanoimprint Lithography. *RSC Adv.* **2014**, *4* (64), 34014–34025. https://doi.org/10.1039/C4RA04807E.

(5) Zhao, W.; Yalcin, B.; Cakmak, M. Dynamic Assembly of Electrically Conductive PEDOT:PSS Nanofibers in Electrospinning Process Studied by High Speed Video. *Synth. Met.* **2015**, *203*, 107–116. https://doi.org/10.1016/j.synthmet.2015.02.018.

(6) Lasagni, A. F.; Hendricks, J. L.; Shaw, C. M.; Yuan, D.; Martin, D. C.; Das, S. Direct Laser Interference Patterning of Poly(3,4-Ethylene Dioxythiophene)-Poly(Styrene Sulfonate) (PEDOT-PSS) Thin Films. *Appl. Surf. Sci.* **2009**, *255* (22), 9186–9192. https://doi.org/10.1016/j.apsusc.2009.06.130.

(7) Schaefer, M.; Holtkamp, J.; Gillner, A. Ablation of PEDOT/PSS with Excimer Lasers for Micro Structuring of Organic Electronic Devices. *Synth. Met.* **2011**, *161* (11–12), 1051–1057. https://doi.org/10.1016/j.synthmet.2011.03.014.

(8) Tseng, S. F.; Hsiao, W. T.; Huang, K. C.; Chiang, D. Electrode Patterning on PEDOT:PSS Thin Films by Pulsed Ultraviolet Laser for Touch Panel Screens. *Appl. Phys. A Mater. Sci. Process.* **2013**, *112* (1), 41–47. https://doi.org/10.1007/s00339-012-7172-3.

(9) Xia, Y.; Ouyang, J. Significant Conductivity Enhancement of Conductive Poly(3,4-Ethylenedioxythiophene): Poly(Styrenesulfonate) Films through a Treatment with Organic Carboxylic Acids and Inorganic Acids. *ACS Appl. Mater. Interfaces* **2010**, *2* (2), 474–483. https://doi.org/10.1021/am900708x.

(10) Dusastre, V.; KIM, Y.; COOK, S.; TULADHAR, S. M.; CHOULIS, S. A.; NELSON, J.; DURRANT, J. R.; BRADLEY, D. D. C.; GILES, M.; MCCULLOCH, I.; et al. A Strong Regioregularity Effect in Self-Organizing Conjugated Polymer Films and High-Efficiency Polythiophene: Fullerene Solar Cells. In *Materials for Sustainable Energy*; World Scientific, 2012; pp 63–69. https://doi.org/10.1142/9789814317665_0009.

(11) Cui, J.; Nogales, A.; Ezquerra, T. A.; Rebollar, E. Influence of Substrate and Film Thickness on Polymer LIPSS Formation. *Appl. Surf. Sci.* **2017**, *394*, 125–131. https://doi.org/10.1016/j.apsusc.2016.10.045.

(12) Khusayfan, N. M.; El-Nahass, M. M. Study of Structure and Electro-Optical Characteristics of Indium Tin Oxide Thin Films. *Adv. Condens. Matter Phys.* **2013**, *2013*, 1–8. https://doi.org/10.1155/2013/408182.

(13) Yagi, T.; Tamano, K.; Sato, Y.; Taketoshi, N.; Baba, T.; Shigesato, Y. Analysis on Thermal Properties of Tin Doped Indium Oxide Films by Picosecond Thermoreflectance Measurement. *J. Vac. Sci. Technol. A Vacuum, Surfaces, Film.* **2005**, *23* (4), 1180–1186. https://doi.org/10.1116/1.1872014.

(14) Ashida, T.; Miyamura, A.; Oka, N.; Sato, Y.; Yagi, T.; Taketoshi, N.; Baba, T.; Shigesato, Y. Thermal Transport Properties of Polycrystalline Tin-Doped Indium Oxide Films. *J. Appl. Phys.* **2009**, *105* (7), 2–5. https://doi.org/10.1063/1.3093684.

(15) Green M.A. Self-Consistent Optical Parameters of Intrinsic Silicon at 300 K Including Temperature Coefficients. *Sol. Energy Mater. Sol. Cells.* **2008**, *92* (11), 1305–1310. https://doi.org/10.1016/j.solmat.2008.06.009.

(16) https://www.crystran.co.uk/optical-materials/silicon-si.

(17) Vogel, A.; Venugopalan, V. Mechanisms of Pulsed Laser Ablation of Biological Tissues. *Chem. Rev.* **2003**, *103* (2), 577–644. https://doi.org/10.1021/cr010379n.

(18) Rebollar, E.; Pérez, S.; Hernández, J. J.; Martín-Fabiani, I.; Rueda, D. R.; Ezquerra, T. A.; Castillejo, M. Assessment and Formation Mechanism of Laser-Induced Periodic Surface Structures on Polymer Spin-Coated Films in Real and Reciprocal Space. *Langmuir* **2011**, *27* (9), 5596–5606. https://doi.org/10.1021/la200451c.

(19) Palumbiny, C. M.; Liu, F.; Russell, T. P.; Hexemer, A.; Wang, C.; Müller-Buschbaum, P. The Crystallization of PEDOT:PSS Polymeric Electrodes Probed in Situ during Printing. *Adv. Mater.* **2015**, *27* (22), 3391–3397. https://doi.org/10.1002/adma.201500315.

(20) Aasmundtveit, K. E.; Samuelsen, E. J.; Pettersson, L. A. A.; Inganäs, O.; Johansson, T.; Feidenhans'l, R. Structure of Thin Films of Poly(3,4-Ethylenedioxythiophene). *Synth. Met.* **1999**, *101* (1), 561–564. https://doi.org/10.1016/S0379-6779(98)00315-4.

(21) Cho, B.; Park, K. S.; Baek, J.; Oh, H. S.; Koo Lee, Y. E.; Sung, M. M. Single-Crystal Poly(3,4-Ethylenedioxythiophene) Nanowires with Ultrahigh Conductivity. *Nano Lett.* **2014**, *14* (6), 3321–3327. https://doi.org/10.1021/nl500748y.

(22) Wang, Y.; Zhu, C.; Pfattner, R.; Yan, H.; Jin, L.; Chen, S.; Molina-Lopez, F.; Lissel, F.; Liu, J.; Rabiah, N. I.; et al. A Highly Stretchable, Transparent, and Conductive Polymer. *Sci. Adv.* **2017**, *3* (3), e1602076. https://doi.org/10.1126/sciadv.1602076.

(23) Xu, B.; Gopalan, S. A.; Gopalan, A. I.; Muthuchamy, N.; Lee, K. P.; Lee, J. S.; Jiang, Y.; Lee, S. W.; Kim, S. W.; Kim, J. S.; et al. Corrigendum: Functional Solid Additive Modified PEDOT:PSS as an Anode Buffer Layer for Enhanced Photovoltaic Performance and Stability in Polymer Solar Cells. *Sci. Rep.* **2017**, *7*, 46779. https://doi.org/10.1038/srep46779.

(24) Kudin, K. N.; Ozbas, B.; Schniepp, H. C.; Prud'homme, R. K.; Aksay, I. A.; Car, R. Raman Spectra of Graphite Oxide and Functionalized Graphene Sheets. *Nano Lett.* **2008**, *8* (1), 36–41. https://doi.org/10.1021/nl071822y.

(25) Tiwari, R. N.; Ishihara, M.; Tiwari, J. N.; Yoshimura, M. Synthesis of Graphene Film from Fullerene Rods. *Chem. Commun.* **2012**, *48* (24), 3003. https://doi.org/10.1039/c2cc17512f.

(26) Ezquerra, T. A.; Rosłaniec, Z.; Špitalský, Z.; Mosnáček, J.; Paszkiewicz, S.; Soccio, M.; Szymczyk, A. Electrical Conductivity of Poly(Ethylene Terephthalate)/Expanded Graphite Nanocomposites Prepared by in Situ Polymerization . *J. Polym. Sci. Part B Polym. Phys.* **2012**, *50* (23), 1645–1652. https://doi.org/10.1002/polb.23176.

(27) Ouyang, J.; Xu, Q.; Chu, C. W.; Yang, Y.; Li, G.; Shinar, J. On the Mechanism of Conductivity Enhancement in Poly(3,4- Ethylenedioxythiophene):Poly(Styrene Sulfonate) Film through Solvent Treatment. *Polymer (Guildf).* **2004**, *45* (25), 8443–8450. https://doi.org/10.1016/j.polymer.2004.10.001.

(28) Funda, S.; Ohki, T.; Liu, Q.; Hossain, J.; Ishimaru, Y.; Ueno, K.; Shirai, H. Correlation between the Fine Structure of Spin-Coated PEDOT:PSS and the Photovoltaic Performance of Organic/Crystalline-Silicon Heterojunction Solar Cells. *J. Appl. Phys.* **2016**, *120* (3). https://doi.org/10.1063/1.4958845.

(29) Zhou, J.; Anjum, D. H.; Chen, L.; Xu, X.; Ventura, I. A.; Jiang, L.; Lubineau, G. The Temperature-Dependent Microstructure of PEDOT/PSS Films: Insights from Morphological{,} Mechanical and Electrical Analyses. *J. Mater. Chem. C* **2014**, *2* (46), 9903–9910. https://doi.org/10.1039/C4TC01593B.

(30) Csete, M.; Bor, Z. Laser-Induced Periodic Surface Structure Formation on Polyethylene-Terephthalate. *Appl. Surf. Sci.* **1998**, *133* (1–2), 5–16. https://doi.org/10.1016/S0169-4332(98)00192-5.

(31) Liu, J.; Wang, X.; Li, D.; Coates, N. E.; Segalman, R. A.; Cahill, D. G. Thermal Conductivity and Elastic Constants of PEDOT:PSS with High Electrical Conductivity. *Macromolecules* **2015**, *48* (3), 585–591. https://doi.org/10.1021/ma502099t.

(32) https://www.chemicalbook.com/ChemicalProductProperty_EN_CB3165285.htm.

(33) Gasiorowski, J.; Menon, R.; Hingerl, K.; Dachev, M.; Sariciftci, N. S. Surface Morphology, Optical Properties and Conductivity Changes of Poly(3,4-Ethylenedioxythiophene):Poly(Styrenesulfonate) by Using Additives. *Thin Solid Films* **2013**, *536*, 211–215. https://doi.org/10.1016/j.tsf.2013.03.124.

(34) Lang, U.; Naujoks, N.; Dual, J. Mechanical Characterization of PEDOT:PSS Thin Films. *Synth. Met.* **2009**, *159* (5–6), 473–479. https://doi.org/10.1016/j.synthmet.2008.11.005.

(35) Vitoratos, E.; Sakkopoulos, S.; Dalas, E.; Paliatsas, N.; Karageorgopoulos, D.; Petraki, F.; Kennou, S.; Choulis, S. A. Thermal Degradation Mechanisms of PEDOT:PSS. *Org. Electron. physics, Mater. Appl.* **2009**, *10* (1), 61–66. https://doi.org/10.1016/j.orgel.2008.10.008.

(36) Rodríguez-Rodríguez, Á.; Rebollar, E.; Soccio, M.; Ezquerra, T. A.; Rueda, D. R.; Garcia-Ramos, J. V.; Castillejo, M.; Garcia-Gutierrez, M. C. Laser-Induced Periodic Surface Structures on Conjugated Polymers: Poly(3-Hexylthiophene). *Macromolecules* **2015**, *48* (12), 4024–4031. https://doi.org/10.1021/acs.macromol.5b00804.

(37) Gutiérrez-Fernández, E.; Rodríguez-Rodríguez, Á.; García-Gutiérrez, M.-C.; Nogales, A.; Ezquerra, T. A.; Rebollar, E. Functional Nanostructured Surfaces Induced by Laser on Fullerene Thin Films. *Appl. Surf. Sci.* **2019**, *476*. https://doi.org/10.1016/j.apsusc.2019.01.141.

(38) Rodríguez-Rodríguez, Á.; Rebollar, E.; Ezquerra, T. A.; Castillejo, M.; Garcia-Ramos, J. V.; García-Gutiérrez, M. C. Patterning Conjugated Polymers by Laser: Synergy of Nanostructure Formation in the All-Polymer Heterojunction P3HT/PCDTBT. *Langmuir* **2018**, *34* (1), 115–125. https://doi.org/10.1021/acs.langmuir.7b03761.

(39) Nahid, M. M.; Gann, E.; Thomsen, L.; McNeill, C. R. NEXAFS Spectroscopy of Conjugated Polymers. *Eur. Polym. J.* **2016**, *81*, 532–554. https://doi.org/10.1016/j.eurpolymj.2016.01.017.

(40) Dhez, O.; Ade, H.; Urquhart, S. G. Calibrated NEXAFS Spectra of Some Common Polymers. *J. Electron Spectros. Relat. Phenomena* **2003**, *128* (1), 85–96. https://doi.org/10.1016/S0368-2048(02)00237-2.

(41) Rodríguez-Rodríguez, Á.; Soccio, M.; Martínez-Tong, D. E.; Ezquerra, T. A.; Watts, B.; García-Gutiérrez, M. C. Competition between Phase Separation and Structure Confinement in P3HT/PCDTBT Heterojunctions: Influence on Nanoscale Charge Transport. *Polymer (Guildf).* **2015**, *77*, 70–78. https://doi.org/10.1016/j.polymer.2015.09.012.

(42) Staniec, P. A.; Parnell, A. J.; Dunbar, A. D. F.; Yi, H.; Pearson, A. J.; Wang, T.; Hopkinson, P. E.; Kinane, C.; Dalgliesh, R. M.; Donald, A. M.; et al. The Nanoscale Morphology of a PCDTBT:PCBM Photovoltaic Blend. *Adv. Energy Mater.* **2011**, *1* (4), 499–504. https://doi.org/10.1002/aenm.201100144.

(43) Beiley, Z. M.; Hoke, E. T.; Noriega, R.; Dacuña, J.; Burkhard, G. F.; Bartelt, J. A.; Salleo, A.; Toney, M. F.; McGehee, M. D. Morphology-Dependent Trap Formation in High Performance Polymer Bulk Heterojunction Solar Cells. *Adv. Energy Mater.* **2011**, *1* (5), 954–962. https://doi.org/10.1002/aenm.201100204.

(44) Glynn, T.; Sherlock, R.; Prendergast, Ú.; Kudzma, S.; O'Connell, C. TEM Investigation of Laser-Induced Periodic Surface Structures on Polymer Surfaces. *Phot. Process. Microelectron. Photonics VI* **2007**, *6458* (March 2007), 64581V. https://doi.org/10.1117/12.699999.

(45) Chae, S.; Yi, A.; Lee, H. H.; Choi, J.; Kim, H. J. Laser-Induced Orientation Transformation of a Conjugated Polymer Thin Film with Enhanced Vertical Charge Transport. *J. Mater. Chem. C* **2018**, *6* (35), 9374–9382. https://doi.org/10.1039/c8tc02393j.

(46) Wang, T.; Pearson, A. J.; Dunbar, A. D. F.; Staniec, P. A.; Watters, D. C.; Yi, H.; Ryan, A. J.; Jones, R. A. L.; Iraqi, A.; Lidzey, D. G. Correlating Structure with Function in Thermally Annealed PCDTBT:PC 70BM Photovoltaic Blends. *Adv. Funct. Mater.* **2012**, *22* (7), 1399–1408. https://doi.org/10.1002/adfm.201102510.

(47) Bar-Cohen, Y. *Biomimetics: Biologically Inspired Technologies*; CRC Press, 2005.

(48) Rebollar, E.; Castillejo, M.; Ezquerra, T. A. Laser Induced Periodic Surface Structures on Polymer Films: From Fundamentals to Applications. *Eur. Polym. J.* **2015**, *73*, 162–174. https://doi.org/10.1016/j.eurpolymj.2015.10.012.

(49) Neděla, O.; Slepička, P.; Sajdl, P.; Veselý, M.; Švorčík, V. Surface Analysis of Ripple Pattern on PS and PEN Induced with Ring-Shaped Mask Due to KrF Laser Treatment. *Surf. Interface Anal.* **2017**, *49* (1), 25–33. https://doi.org/10.1002/sia.6054.

(50) Csete, M.; Marti, O.; Bor, Z. Laser-Induced Periodic Surface Structures on Different Poly-Carbonate Films. *Appl. Phys. A Mater. Sci. Process.* **2001**, *73* (4), 521–526. https://doi.org/10.1007/s003390100973.

(51) Rodríguez-Rodríguez, Á.; Gutiérrez-Fernández, E.; García-Gutiérrez, M.-C.; Nogales, A.; Ezquerra, T. A.; Rebollar, E. Synergistic Effect of Fullerenes on the Laser-Induced Periodic Surface Structuring of Poly(3-Hexyl Thiophene). *Polymers (Basel).* **2019**, *11* (2), 190. https://doi.org/10.3390/polym11020190.

(52) Martínez-Tong, D. E.; Rodríguez-Rodríguez, Á.; Nogales, A.; García-Gutiérrez, M. C.; Pérez-Murano, F.; Llobet, J.; Ezquerra, T. A.; Rebollar, E. Laser Fabrication of Polymer Ferroelectric Nanostructures for Nonvolatile Organic Memory Devices. *ACS Appl. Mater. Interfaces* **2015**, *7* (35), 19611–19618. https://doi.org/10.1021/acsami.5b05213.

(53) Wang, J.; Larsen, C.; Wågberg, T.; Edman, L. Direct UV Patterning of Electronically Active Fullerene Films. *Adv. Funct. Mater.* **2011**, *21* (19), 3723–3728. https://doi.org/10.1002/adfm.201100568.

(54) Li, Z.; Wong, H. C.; Huang, Z.; Zhong, H.; Tan, C. H.; Tsoi, W. C.; Kim, J. S.; Durrant, J. R.; Cabral, J. T. Performance Enhancement of Fullerene-Based Solar Cells by Light Processing. *Nat. Commun.* **2013**, *4*, 1–7. https://doi.org/10.1038/ncomms3227.

(55) Dzwilewski, A.; Wågberg, T.; Edman, L. Photo-Induced and Resist-Free Imprint Patterning of Fullerene Materials for Use in Functional Electronics. *J. Am. Chem. Soc.* **2009**, *131* (11), 4006–4011. https://doi.org/10.1021/ja807964x.

(56) Sanchez, L.; Otero, R.; Gallego, J. M.; Miranda, R.; Martin, N. Ordering Fullerenes at the Nanometer Scale on Solid Surfaces. *ChemInform* **2009**, *40* (33), 2081–2091. https://doi.org/10.1002/chin.200933277.

(57) Diaconescu, B.; Yang, T.; Berber, S.; Jazdzyk, M.; Miller, G. P.; Tománek, D.; Pohl, K. Molecular Self-Assembly of Functionalized Fullerenes on a Metal Surface. *Phys. Rev. Lett.* **2009**, *102* (5), 4–7. https://doi.org/10.1103/PhysRevLett.102.056102.

(58) Meshot, E. R.; Patel, K. D.; Tawfick, S.; Juggernauth, K. A.; Bedewy, M.; Verploegen, E. A.; De Volder, M. F. L.; Hart, A. J. Photoconductive Hybrid Films via Directional SelfAssembly of C60 on Aligned Carbon Nanotubes. *Adv. Funct. Mater.* 2012, *22* (3), 577–584. https://doi.org/10.1002/adfm.201102393.

(59) Rodríguez-Rodríguez, Á.; Gutiérrez-Fernández, E.; García-Gutiérrez, M.-C.; Nogales, A.; Ezquerra, T. A.; Rebollar, E. Synergistic Effect of Fullerenes on the Laser-Induced Periodic Surface Structuring of Poly(3-Hexyl Thiophene). *Polymers (Basel).* **2019**, *11* (2). https://doi.org/10.3390/polym11020190.

(60) Cui, J.; Rodríguez-Rodríguez, Á.; Hernández, M.; García-Gutiérrez, M.-C.; Nogales, A.; Castillejo, M.; Moseguí González, D.; Müller-Buschbaum, P.; Ezquerra, T. A.; Rebollar, E. Laser-Induced Periodic Surface Structures on P3HT and on Its Photovoltaic Blend with PC $_{71}$ BM. *ACS Appl. Mater. Interfaces* **2016**, *8* (46), 31894–31901. https://doi.org/10.1021/acsami.6b09053.

(61) Lebedkin, S.; Hull, W. E.; Soldatov, A.; Renker, B.; Kappes, M. M. Structure and Properties of the Fullerene Dimer C 140 Produced by Pressure Treatment of C 70 . *J. Phys. Chem. B* **2002**, *104* (17), 4101–4110. https://doi.org/10.1021/jp994330l.

(62) Refson, K.; Parker, S. F. Assignment of the Internal Vibrational Modes of C70 by Inelastic Neutron Scattering Spectroscopy and Periodic-DFT. *ChemistryOpen* **2015**, *4* (5), 620–625. https://doi.org/10.1002/open.201500069.

(63) Tsoi, W. C.; Zhang, W.; Razzell Hollis, J.; Suh, M.; Heeney, M.; McCulloch, I.; Kim, J. S. In-Situ Monitoring of Molecular Vibrations of Two Organic Semiconductors in Photovoltaic Blends and Their Impact on Thin Film Morphology. *Appl. Phys. Lett.* **2013**, *102* (17). https://doi.org/10.1063/1.4803912.

(64) Lu, J.; Yeo, P. S. E.; Gan, C. K.; Wu, P.; Loh, K. P. Transforming C 60 Molecules into Graphene Quantum Dots. *Nat. Nanotechnol.* **2011**, *6* (4), 247–252. https://doi.org/10.1038/nnano.2011.30.

(65) Menon, M.; Rao, A. M.; Subbaswamy, K. R.; Eklund, P. C. Anisotropic Covalent Bonding and Photopolymerization of C70. *Phys. Rev. B* **1995**, *51* (2), 800–803. https://doi.org/10.1103/PhysRevB.51.800.

(66) Ohno, T.; Yatsuya, S. Growth of Fullerene Nanoparticles Prepared by the Gas-Evaporation Technique. *J. Mater. Sci.* **1998**, *33* (24), 5843–5847. https://doi.org/10.1023/A:1004422703786.

(67) Verploegen, E.; Mondal, R.; Bettinger, C. J.; Sok, S.; Toney, M. F.; Bao, Z. Effects of Thermal Annealing upon the Morphology of Polymer-Fullerene Blends. *Adv. Funct. Mater.* **2010**, *20* (20), 3519–3529. https://doi.org/10.1002/adfm.201000975.

(68) Hopkinson, P. E.; Staniec, P. A.; Pearson, A. J.; Dunbar, A. D. F.; Wang, T.; Ryan, A. J.; Jones, R. A. L.; Lidzey, D. G.; Donald, A. M. A Phase Diagram of the P3HT:PCBM Organic Photovoltaic System: Implications for Device Processing and Performance. *Macromolecules* **2011**, *44* (8), 2908–2917. https://doi.org/10.1021/ma102524a.

(69) Pöhls, J. H.; Johnson, M. B.; White, M. A. Origins of Ultralow Thermal Conductivity in Bulk [6,6]-Phenyl-C61-Butyric Acid Methyl Ester (PCBM). *Phys. Chem. Chem. Phys.* **2016**, *18* (2), 1185–1190. https://doi.org/10.1039/c5cp06575e.

(70) Heumueller, T.; Mateker, W. R.; Distler, A.; Fritze, U. F.; Cheacharoen, R.; Nguyen, W. H.; Biele, M.; Salvador, M.; von Delius, M.; Egelhaaf, H.-J.; et al. Morphological and Electrical Control of Fullerene Dimerization Determines Organic Photovoltaic Stability. *Energy Environ. Sci.* **2015**, *9* (1), 247–256. https://doi.org/10.1039/C5EE02912K.

(71) Zhao, J.; Swinnen, A.; Van Assche, G.; Manca, J.; Vanderzande, D.; Van Mele, B. Phase Diagram of P3HT/PCBM Blends and Its Implication for the Stability of Morphology. *J. Phys. Chem. B* **2009**, *113* (6), 1587–1591. https://doi.org/10.1021/jp804151a.

(72) Sanz, A.; Jiménez-Ruiz, M.; Nogales, A.; Martín y Marero, D.; Ezquerra, T. A. Hydrogen-Bond Network Breakage as a First Step to Isopropanol Crystallization. *Phys. Rev. Lett.* **2004**, *93* (1), 015503–1. https://doi.org/10.1103/PhysRevLett.93.015503.

(73) Sanz, A.; Nogales, A.; Ezquerra, T. A.; Lotti, N.; Munari, A.; Funari, S. S. Order and Segmental Mobility during Polymer Crystallization: Poly(Butylene Isophthalate). *Polymer (Guildf).* **2006**, *47* (4), 1281–1290. https://doi.org/10.1016/j.polymer.2005.12.047.

Chapter 5. On the fabrication of glycerol-assisted nanogratings of PEDOT:PSS by Nanoimprint Lithography

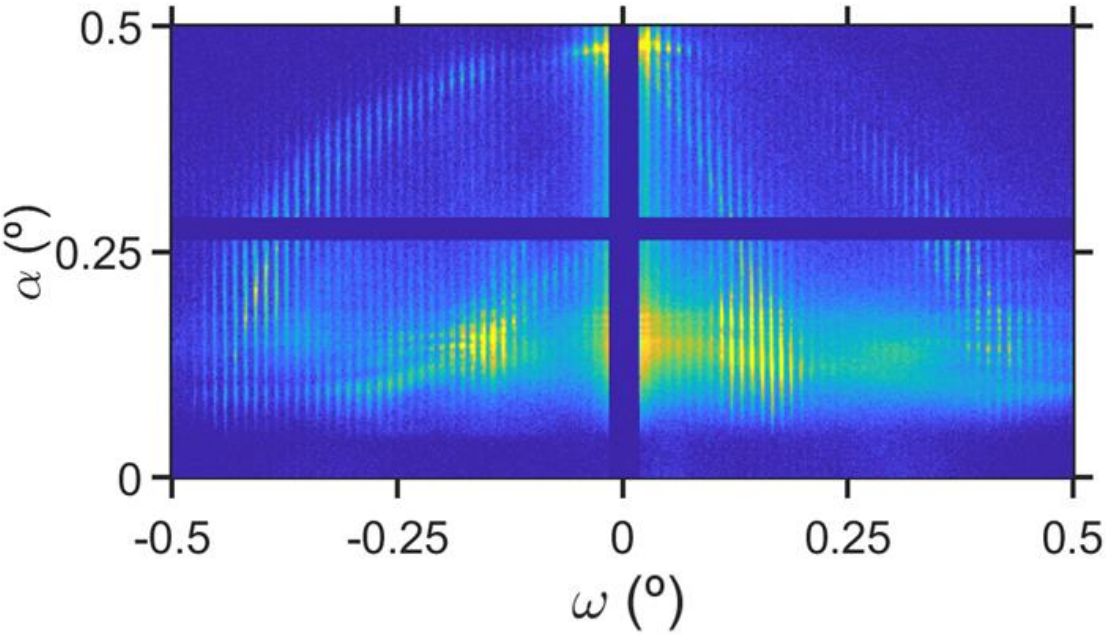

This chapter is devoted to the fabrication of nanostructured surfaces of PEDOT:PSS by nanoimprint lithography (NIL) (see section 2.2.2). Nanogratings of PEDOT:PSS fabricated by non-ablation laser irradiation are presented in this Thesis (see section 4.1). Regarding nanoimprint lithography[1], imprinted nanodots of PEDOT:PSS with enhanced light absorption have increased the solar cell performance[2]. Nanochannels of PEDOT:PSS have also been achieved using silicon stamps with a strong control of the ambient conditions[3–5]. In order to avoid this critical control of ambient parameters, glycerol has been used as a plasticizer agent[6–8] for the fabrication of micrometric size and low aspect ratio structures. In the case of organic solar cells, superficial nanostructures with high aspect ratios (high height, low width) are required in order to increase the superficial area of the PEDOT:PSS with the active layer and approach the exciton diffusion length[9]. In addition, as much as we know, low attention has been paid to the inner structure of the PEDOT:PSS once it is nanostructured.

In this chapter we present imprinted nanometric gratings of PEDOT:PSS with heights beyond 100 nanometers, using glycerol as plasticizer agent, and straightforward fabrication conditions in terms of pressure and temperature. In addition, the effect of glycerol concentration on the grating geometry and extent of order is studied by means of AFM and GISAXS, respectively. Furthermore, changes in the PEDOT:PSS structure, after the nanostructuring procedure, are observed by GIWAXS and Raman spectroscopy. Thin films of concentrated PEDOT:PSS with glycerol were prepared by spin-coating. Conditions for preparation of dispersions were detailed in Table 2.9. Spin-coating conditions were included in Table 2.10.

5.1 Thickness of samples: effect of glycerol

Thin films of PEDOT:PSS with glycerol for NIL were not subjected to thermal annealing in order to retain the glycerol plasticizer effect. This is in contrast to the samples studied in section 3.2. Therefore, films with higher quantities of glycerol are thicker (Figure 5.1, black data).

As it can be seen in Figure 5.1, the thickness of concentrated PEDOT:PSS thin films increases with the addition of glycerol, rising linearly with increasing glycerol concentration. The decrease of thickness with time (Figure 5.1, blue data) suggests complete glycerol removal. After several months, the thickness of these samples are around 200 nm, slightly higher than the thickness of a pristine concentrated PEDOT:PSS thin film (≈ 160 nm). The increased thickness of PEDOT:PSS thin films after glycerol removal was observed in section 3.2.2 of this Thesis.

When thin films of PEDOT:PSS with glycerol are prepared more than one week in advance, the nanoimprint process fails and the nanostructures are not obtained. We associated this effect to the loss of glycerol with time and the loss of its plasticizer effect, avoiding the flow of PEDOT:PSS and the filling of the cavities in the mold. Because of that, the series of PEDOT:PSS films

investigated and presented in the following sections were prepared 12 hours before the NIL procedure.

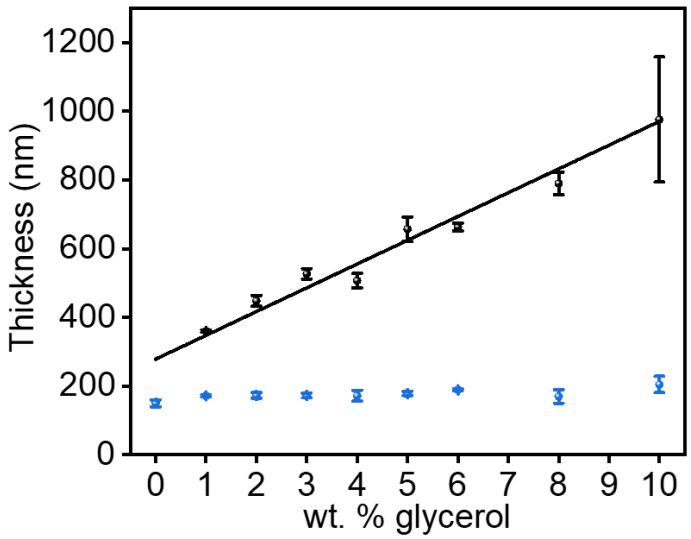

Figure 5.1 Thicknesses of concentrated PEDOT:PSS fresh (black data) and five months stored (blue data). The line is added for visual guide.

5.2 Nanoimprint Lithography conditions

Nanoimprint lithography experiments were performed in a clean room (see section 2.2.2), with a controlled ambient temperature of 20 ± 1 ºC and a relative humidity of 52 ± 2 %. As it was described in section 2.2.2, molds were made of polydimethylsiloxane (PDMS), replicating the geometry of a master mold of silicon. The final molds of PDMS present tetrahedral grating with cavities of around 200 nm deep and 500 nm of period. The profile of one of the molds, measured by SEM (see section 2.3.1.2) and AFM is presented in Figure 5.2.

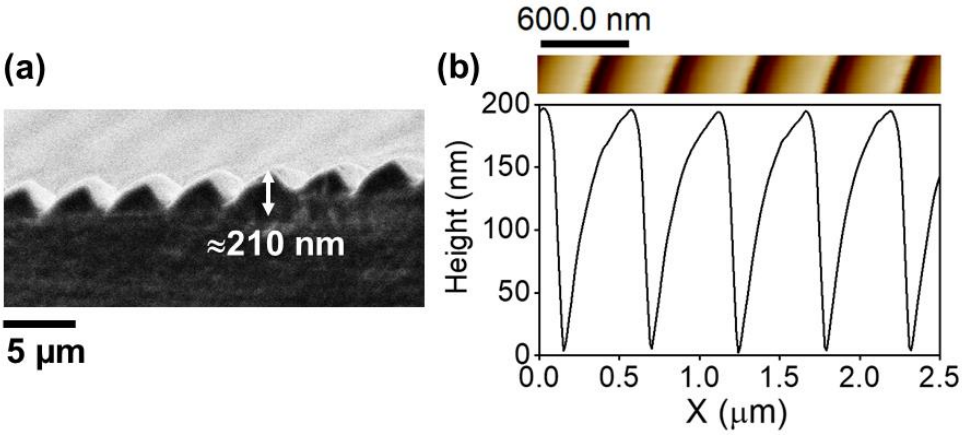

Figure 5.2 (a) SEM image of a transversal cut of a PDMS mold. **(b, up)** AFM topographical image of the PDMS mold, **(down)** height profile of the upper image.

Temperature conditions for nanoimprinting were selected close to reported values[4]. However, the selected pressure was an order of magnitude lower than the reported one, due to the presence of the plasticizer agent. Steps during NIL procedure are compiled in Table 5.1.

Table 5.1 Temperature, pressure and time conditions for NIL procedure.

NIL parameters		
Step	**Variable**	**Time (min)**
Heating	20 → 150 ºC	2
Moulding	Pressure = 8 bar	-
Holding	Temperature = 150 ºC	10
Cooling	Temperature = 70 ºC	3
Demoulding	Pressure = ambient	-

The success of the fabrication can be checked at first glance by eye since the sample with well-ordered nanostructures is iridescent. This is due to the dimensions of the gratins, with the pitch in the wavelength range of the visible region of the electromagnetic spectrum. The fabricated structure acts as a diffraction grating (Figure 5.3).

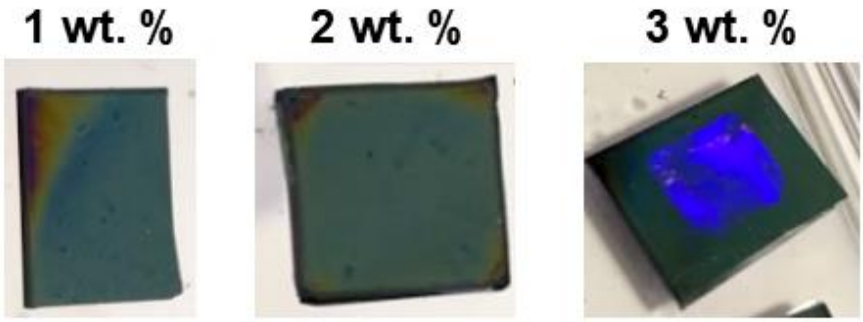

Figure 5.3 Photography of thin films of concentrated PEDOT:PSS with a weight concentration of glycerol (labelled) and nanoimprinted with the same stamp and conditions.

As can be seen in Figure 5.3, samples with glycerol concentrations of 1 and 2 wt. % imprinted with the same stamp and through the same procedure from Table 5.1 did not generate nanostructures. Glycerol concentrations from 3 to 10 wt. % did generated grating nanostructures.

5.3 Sample morphology as revealed by AFM and SEM

Morphology of the grating nanostructures was investigated by AFM and SEM. In this case, AFM and SEM are complementary visualization techniques since AFM can give precise information about the height and shape of a particular region of the grating whereas SEM scans larger areas.

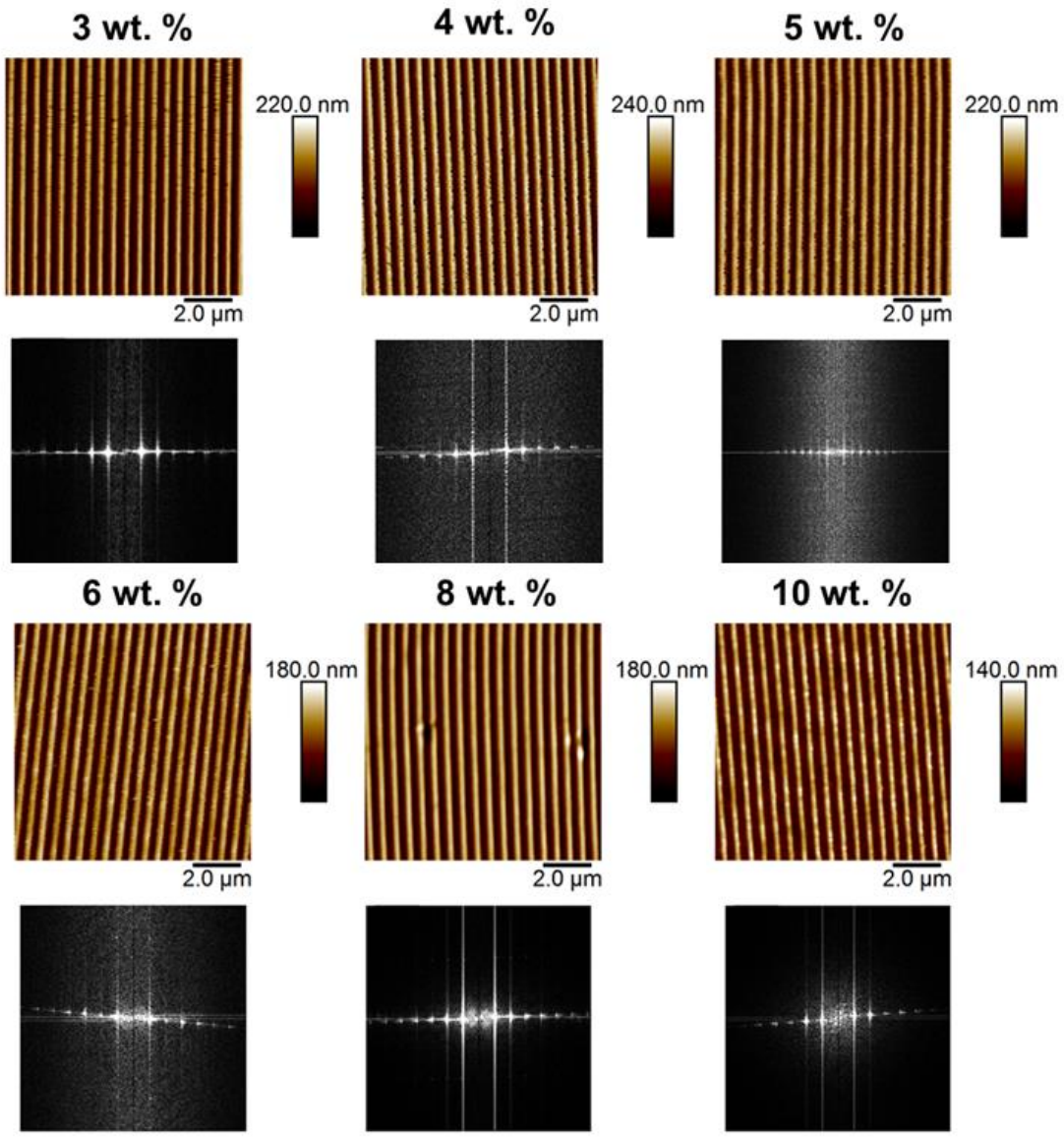

Figure 5.4 Topography AFM images in tapping mode of nanostructured thin films of concentrated PEDOT:PSS with different glycerol concentration (labelled). Below every AFM image its corresponding FFT is presented.

It can be seen in Figure 5.4 that PEDOT:PSS thin films with concentrations of glycerol from 3 to 10 wt. % present similar nanograting structures. FFT images below each AFM image show several intensity maxima associated with high spatial order. Looking at the height scale of the AFM images, the height of the gratings seems to decrease at higher glycerol concentrations.

Further geometrical analysis of the gratings is presented along this section. On the other hand, SEM images (Figure 5.5) of selected samples show good quality in areas of hundreds of square microns.

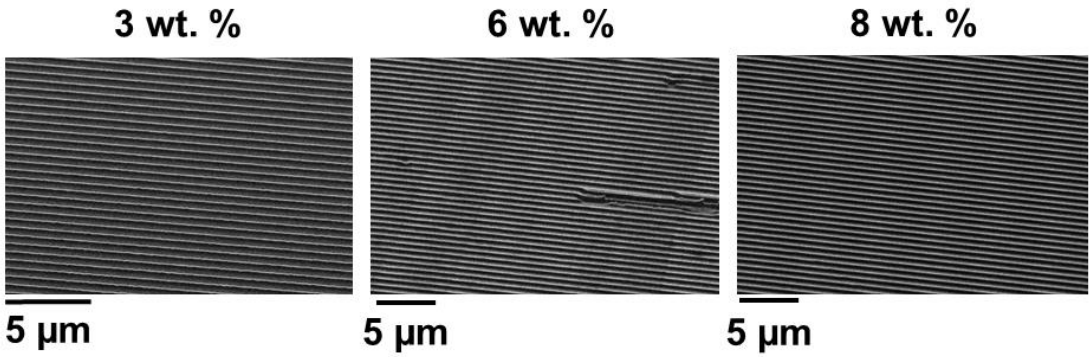

Figure 5.5 SEM images of nanostructured thin films of concentrated PEDOT:PSS with different glycerol concentration (labelled).

The height profiles of the gratings, taken as horizontal sections from AFM images of Figure 5.4 are shown in Figure 5.6.

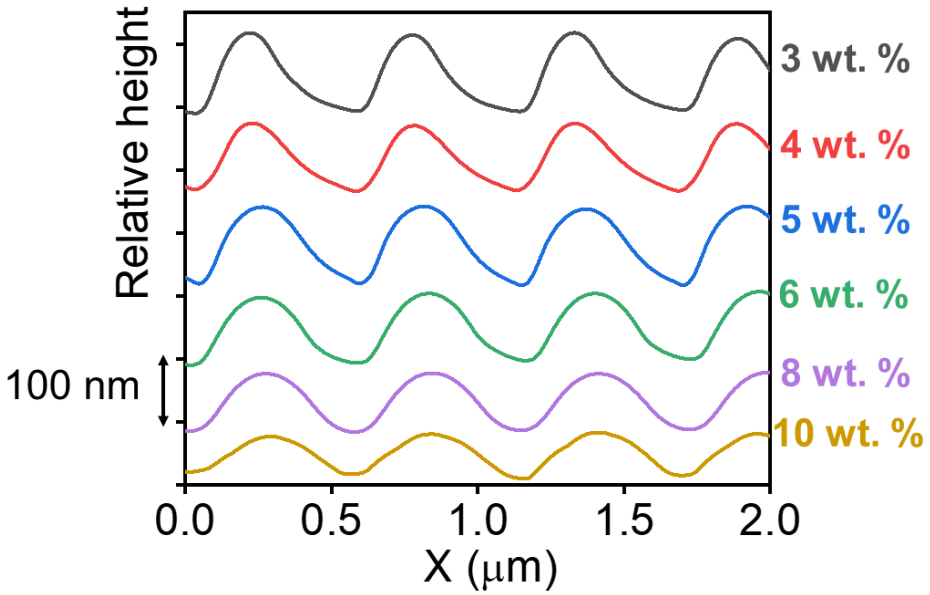

Figure 5.6 Height profiles of nanostructured thin films of concentrated PEDOT:PSS with a certain weight relation of glycerol (labelled). The profiles are vertically shifted for better visualization.

Several geometrical features can be extracted from Figure 5.6. It can be seen that the PEDOT:PSS nanostructures present the negative of the shape of the mold (Figure 5.2), with a tetrahedral shape and a slight asymmetry that is more accused in the nanostructured samples with 3-4 wt. % of glycerol. The height of the gratings decreases with increasing glycerol concentration whereas the

width of the gratings increases with higher glycerol concentrations. The height of the gratings was measured as the average value of the distance between valleys and ridges. The width was measured as the average full width at half maximum of the gratings. Then, the aspect ratio was calculated as the relation between the height and the width. Height, width and aspect ratio are presented in Figure 5.7 as a function of glycerol concentration.

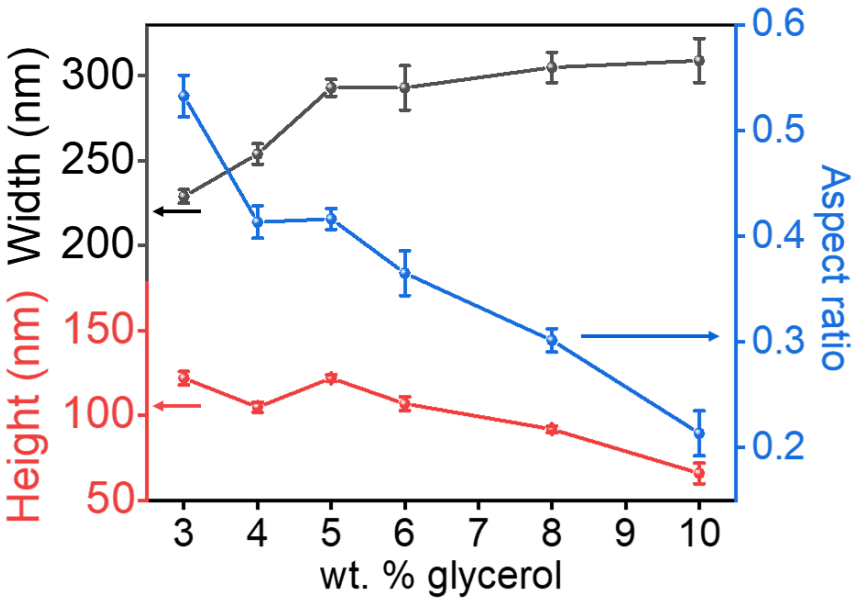

Figure 5.7 Geometrical features of the nanostructured gratings of PEDOT:PSS as a function of glycerol concentration: width (black), height (red) and the aspect ratio –height/width- (blue).

As can be seen in Figure 5.7, the highest aspect ratio (≈ 0.55) is achieved by nanostructuring the PEDOT:PSS film with 3 wt. % of glycerol. Higher concentrations of glycerol render nanostructures with lower height and higher width. This can be explained as a more efficient filling of the cavities in the mold when the pressure is applied. As it was shown in Figure 5.3, thin films with 1-2 wt. % of glycerol did not generate nanostructures. In the NIL procedure, before the pressure is applied, films are heated until 150ºC (see Table 5.1). We suggest that films with initially 1-2 wt. % of glycerol lose part of the glycerol by evaporation during heating so that the material cannot flow into the mold when the pressure is applied. For 3-4 wt. % of glycerol, when the pressure is applied, there is still enough glycerol in the PEDOT:PSS film to flow into the cavities but not enough to fill them efficiently, inducing high and narrow structures. During the pressurization, the glycerol is removed and the material in the cavities keeps the shape of nanogratings with height around 120 nm and width around 210 nm. In the case of higher concentrations of glycerol, the material is fluid enough that it can fill the cavities more efficiently generating wider structures. Meanwhile the pressure is being applied, and the glycerol is being

evaporated from the film, the PEDOT:PSS in the cavities may redistribute towards the underlying film of PEDOT:PSS due to chemical affinity, lowering the height of the gratings.

Therefore, with these nanostructuring conditions, 3 wt. % of glycerol seems to be the optimum concentration for the generation of nanogratings of PEDOT:PSS with the highest possible aspect ratio.

5.4 Order of PEDOT:PSS nanostructured samples as revealed by GISAXS

GISAXS experiments were performed to obtain a quantitative estimation of the order and quality of gratings. It was seen that in the range of microns (Figure 5.4), all the samples present gratings with good order. However, high concentrations of glycerol clearly affect the geometrical features of the samples (Figure 5.7). GISAXS allows getting insights about the impact of glycerol on the gratings order in areas of square millimeters. GISAXS patterns from nanostructured PEDOT:PSS samples were taken using an incident angle α_i=0.4º and they are shown in Figure 5.8.

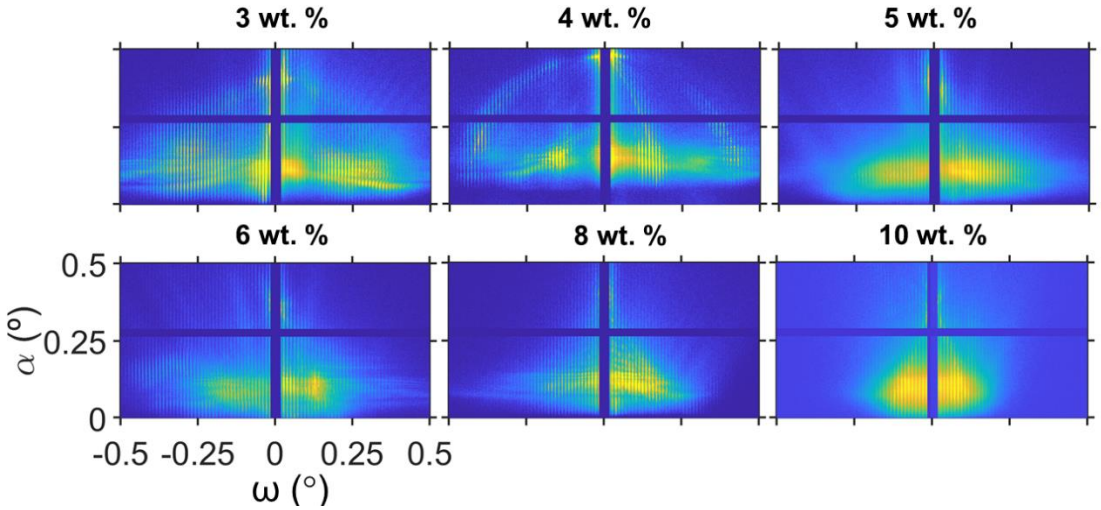

Figure 5.8 GISAXS patterns of nanostructured PEDOT:PSS thin films with different glycerol concentrations (labelled). Incident angle=0.4º. The intensity of GISAXS pattern is in logarithmic scale.

GISAXS patterns present numerous vertical rods, characteristic of a highly regular lattice whose planes are perpendicular to the substrate[10,11]. The spacing between rods is determined by the period of the array. It can be seen that the scattered intensity is concentrated at α≈0.1-0.15°, which is close to the critical angle of the silicon. This intense scattering is known as Yoneda peak[12]. Several features can be extracted from GISAXS patterns. The large number of diffraction peaks shows that nanostructured samples of PEDOT:PSS are highly regular arrays. Patterns from samples with concentrations of 3 and 4 wt. % show arcs whose radius coincide with the incident

angle (0.4º). These arcs appear when the X-ray beam is well aligned along the grating direction and are the result of the intersection between the Ewald sphere (see section 2.3.5.2) and the grating truncated rods determined by the period of the structure[13]. The formation of this arc is highly dependent on the length of the nanostructures[14] and hence on the good quality of the gratings. The well-defined arc for the sample with 4 wt. % of glycerol evidences long gratings free of defects in large regions of the sample[14]. All the GISAXS patterns present intense globules at both sides of the vertical origin, at $\omega \approx \pm 0.2º$, followed by lower intensity zones. These kind of intensity cancelations are due to the convolution between the interference function and the form factor, that modulates the intensity function[10]. Another feature in Figure 5.8 is the slight asymmetric intensity respect to the vertical axis exhibited in the patterns. Asymmetric GISAXS intensity patterns have been reported to appear when analyzing faceted germanium quantum dots[15] and thin films with tilted columns of titanium dioxide (TiO_2) respect to the normal vector of the substrate[16], due to the asymmetry of the scattering objects with respect to the plane of the sample. Therefore, our nanostructured samples yield asymmetric patterns (Figure 5.8) due to the inherent asymmetric shape of the nanoimprinted gratings (Figure 5.6). Another contribution to the asymmetry of the GISAXS patterns could be the presence of regions in the film that are not perfectly parallel to the substrate, slightly detached from the substrate during demolding of the PDMS mold.

In order to clarify the tendency of the long-range order in the nanostructured samples as a function of glycerol concentrations, horizontal cuts were made from GISAXS patterns of Figure 5.8 at $\alpha = 0.1º$ and transformed to q_y using Equation 2.12. Cuts are presented in Figure 5.9.

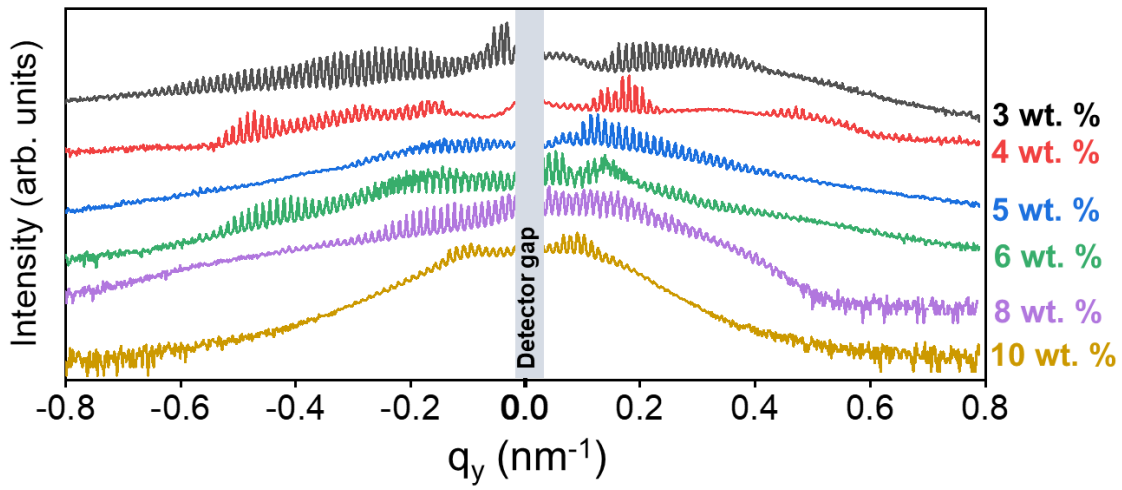

Figure 5.9 Horizontal cuts at $\alpha = 0.1º$ from GISAXS patterns of Figure 5.8. The intensity profiles have been shifted vertically for clarity.

A diffraction pattern can present two types of intensity maxima; those with a sharper shape are associated with the structure factor (interference function) whereas form factor yields rounded

maxima[14]. The correlation between the paracrystalline disorder parameter *g* and the number of peaks related to the structure factor has been reported[17]. The number of intensity maxima from every intensity profile in Figure 5.9 associated with the structure factor were counted and presented as a function of the glycerol concentration in Figure 5.10.

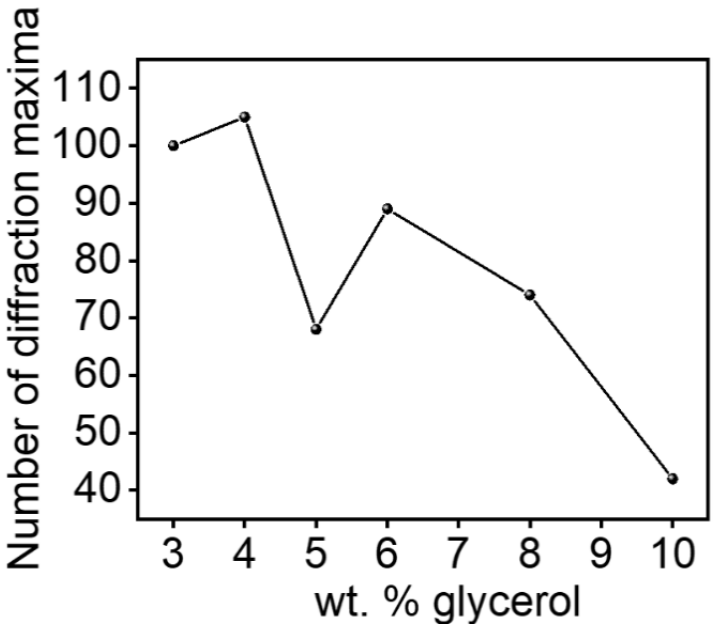

Figure 5.10 Number of intensity maxima associated with the structure factor from GISAXS cuts in Figure 5.9 as a function of glycerol concentration.

The number of diffraction maxima is maximized in the sample with 4 wt. %, which is the sample that generates an arc in the GISAXS pattern (Figure 5.8). A higher number of diffraction maxima is correlated with a lower paracrystalline value[17], thus with an order improvement. The intensity profile presenting more diffraction maxima corresponds to the pattern with an arc related with longer gratings free of defects; this fact supports that the sample with 4 wt. % of glycerol presents the best ordered nanogratings, whereas nanostructured samples with the highest concentrations of glycerol have more morphological defects along the direction of the gratings.

5.5 Inner structure of nanoimprinted PEDOT:PSS as revealed by GIWAXS and Raman spectroscopy

Raman spectroscopy (see section 2.3.4) experiments were performed to elucidate chemical and conformational changes between nanostructured and non-nanostructured PEDOT:PSS thin films. Figure 5.11 shows the comparison between Raman spectra from a spin-coated PEDOT:PSS thin film, a PEDOT:PSS thin film with 10 wt. % of glycerol and a nanostructured sample with 3 wt. % of glycerol.

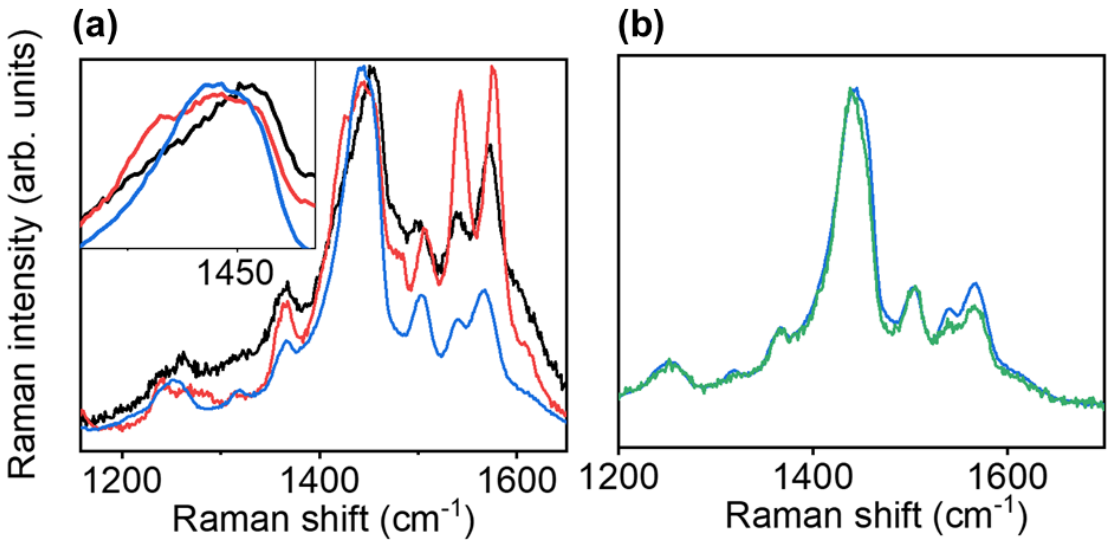

Figure 5.11 (a) Raman spectra from a thin film of PEDOT:PSS (black curve), a thin film of PEDOT:PSS thin film with 10 wt. % of glycerol (red curve) and a nanostructured PEDOT:PSS with 3 wt. % of glycerol over the nanostructured area (blue curve). The inset is a magnification of the most intense band around 1450 cm^{-1}. **(b)** Raman spectra from a nanostructured PEDOT:PSS thin film with 3 wt. % of glycerol over the nanostructured area (blue curve) and over a non-nanostructured area (green curve).

Raman spectra (Figure 5.11.a) present several bands associated with molecular modes from PEDOT. The bands around 1250 cm^{-1} and 1365 cm^{-1} are identified with C_α-C_α' inter-ring stretching vibration and C_β-C_β' stretching vibration respectively of the PEDOT thiophene ring[18]. The most intense band is around 1450 cm^{-1} and it is associated with the symmetric stretching of C_α=C_β. The rest of the bands between 1510 cm^{-1} and 1570 cm^{-1} are identified as asymmetric stretching modes of C_α=C_β[18].

In Raman spectra from spin-coated pristine PEDOT:PSS thin film (Figure 5.11.a, black curve), the most intense band is centered at 1453 cm^{-1}. It can be seen in the inset of Figure 5.11.a that this peak is shifted to 1443 cm^{-1} in the Raman spectrum from the nanostructured sample (blue curve) and also in the Raman spectrum from spin-coated thin film of PEDOT:PSS with glycerol (red curve). In addition, the peak in Raman spectrum from the nanostructured sample is narrower. Furthermore, it can be seen in Figure 5.11.b that Raman spectra from a nanostructured zone of PEDOT:PSS and a non-nanostructured zone of the same sample yield a quite similar spectra. It can be inferred that the heat treatment during NIL procedure induces the narrowing of the band at 1443 cm^{-1}.

This shift and narrowing of the C_α=C_β symmetric stretching mode peak is associated with a transition from the benzoid structure of PEDOT:PSS to the quinoid structure[19]. Ouyang et al. reported this effect when PEDOT:PSS was mixed with ethylene glycol[19]; the additive would induce a conformational change from coil-like to extended chains, in which the quinoid structure

would be preferential. In section 3.2.1 of this Thesis, this conformational change is reported based on SAXS analysis when PEDOT:PSS dispersion is mixed with glycerol. Therefore, it can be inferred that the transition from benzoid to quinoid structure of PEDOT are likely to be induced by glycerol and then this effect is enhanced by the thermal treatment applied during the NIL process.

The Raman spectrum from PEDOT:PSS with glycerol (Figure 5.11.a, red curve) presents a strong enhancement of the bands at 1540 and 1570 cm^{-1}. This enhancement could be a signature of glycerol interacting with PEDOT and enhancing these Raman modes associated with asymmetric stretching modes. After the nanostructuring process, this effect is not observed (Figure 5.11.a, blue curve). We have used also Raman spectroscopy in order to probe the presence of glycerol in the samples (Figure 5.12). The appearance of a band at 470 cm^{-1}, close to a reported band from glycerol[20], associated with CCO rocking mode, in the Raman spectrum from the fresh spin-coated film of PEDOT:PSS with 10 wt. % of glycerol proves the presence of glycerol in the sample. On the other hand, this band is absent in the spectrum from spin-coated pristine PEDOT:PSS thin film and in the spectrum from nanostructured sample. This supports the idea that all the glycerol contained in the film is removed during thermal treatment, both in the nanostructured zone and outside of it.

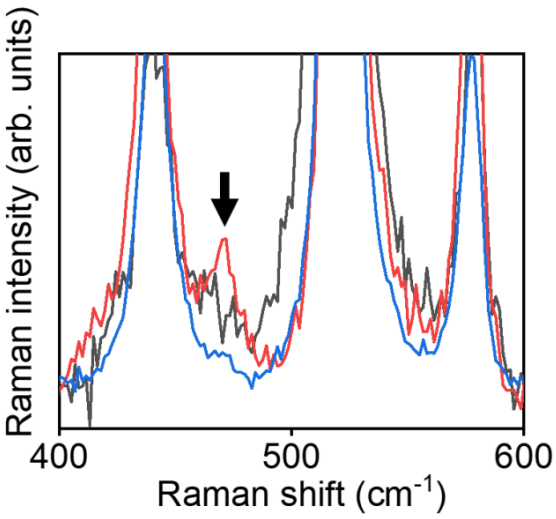

Figure 5.12 Raman spectra from thin film of PEDOT:PSS (black curve), of PEDOT:PSS thin film with 10 wt. % of glycerol (red curve) and from nanostructured PEDOT:PSS with 3 wt. % of glycerol over the nanostructured area (blue curve). The downward arrow points to the Raman band associated with glycerol.

Furthermore, the whole set of nanostructured samples with different glycerol concentrations present almost identical Raman spectra.

GIWAXS measurements were carried out in order to study the impact of nanostructuring on the inner structure of PEDOT:PSS. First of all, patterns of samples with and without glycerol are presented to see the initial impact of the plasticizer agent on PEDOT:PSS (Figure 5.13).

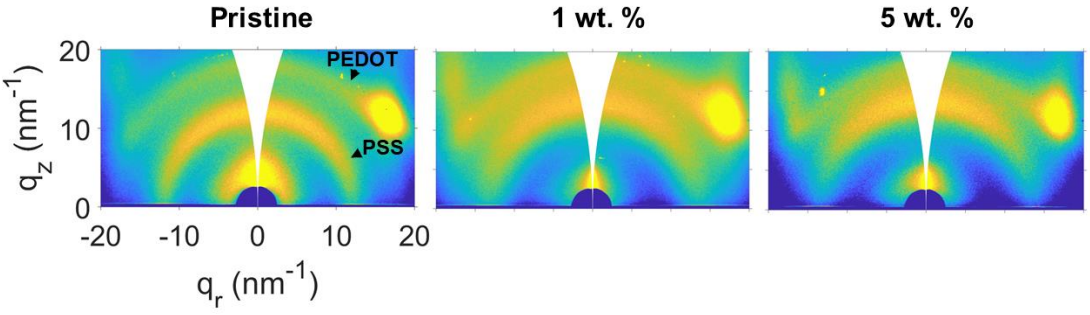

Figure 5.13 GIWAXS patterns from a PEDOT:PSS thin film **(left)** and from PEDOT:PSS thin films with different glycerol concentrations as labelled (**center** and **right**). Reflections from PEDOT and PSS are labelled in the **left** pattern. High intense dots around the same q as PEDOT reflection come from scattering from silicon substrate. Intensity in logarithmic scale.

The diffraction pattern from PEDOT:PSS shows two main reflections from PSS and PEDOT[21,22]. When glycerol is added, some differences are observed in the patterns (Figure 5.13, center and right). In order to clarify these differences, the patterns have been azimuthally integrated (Figure 5.14).

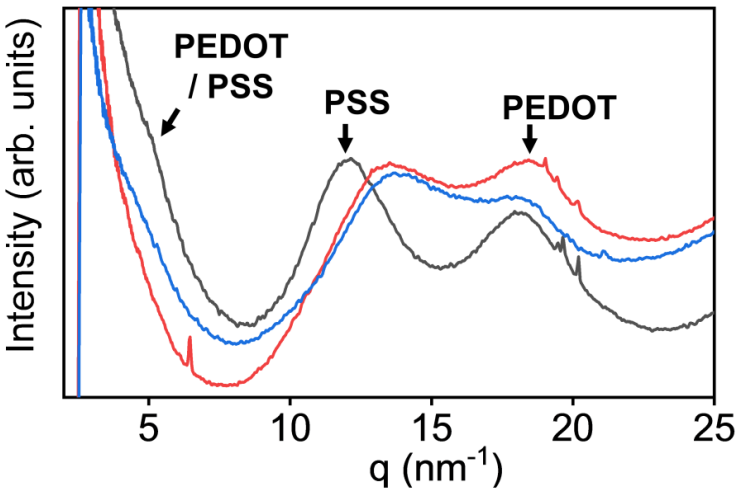

Figure 5.14 Azimuthal integrations of GIWAXS patterns from a PEDOT:PSS thin film (black curve) and from PEDOT:PSS thin films with 1 wt. % of glycerol (red curve) and with 5 wt. % of glycerol (blue curve). Reflections associated with PEDOT and/or PSS are labelled.

The intensity profiles were obtained from the azimuthal integration of GIWAXS patterns of Figure 5.13 over a sector centered at q_z in order to avoid the scattered intensity from the silicon.

The intensity profile from pristine PEDOT:PSS film (Figure 5.14, black curve) presents two known reflections at q=12 nm^{-1} (d=0.52 nm) and q=18.1 nm^{-1} (d=0.35 nm), which are related to the PSS amorphous halo[23,24] -although other works refer to the π-π stacking of PSS[21,22,25]- and from the π-π stacking of PEDOT[21,22,24,25], respectively. The shoulder around q=5 nm^{-1} may be composed of several reflections from the (100) lamellar stacking of PEDOT (q=4.5 nm^{-1}, d=1.37 nm) and PSS interdigitation packing (q= 4.6 nm-1, d= 1.37 nm)[21,25], although it is blurred with the scattering from the direct beam and cannot be identified independently. In section 3.3 of this Thesis, GIWAXS pattern from PEDOT:PSS deposited on ITO showed the same issue.

The glycerol has a clear effect on the structure of PSS, whose associated peak at q=12 nm^{-1} (d=0.52 nm) suffers a shift to higher q (q≈13.5 nm^{-1}, d=0.47 nm) in the thin film with 1 wt. % of glycerol and to q≈13.9 nm^{-1} (d=0.45 nm) in the film with 5 wt. %. The peak from PEDOT at q=18.1 nm^{-1} (d=0.35 nm) also suffers a slight shift to higher q, (q≈18.5 nm^{-1}, d=0.34 nm). Both shifts are indicative of lower distances between molecular planes. This result would be in line with previous Raman results that suggest more extended chains in the case of PEDOT, associated with the quinoid structure. The transition from benzoid to quinoid structure has been reported to be accompanied by a reduction in the π-π stacking distance of PEDOT[26]. In fact, in section 3.2.1, it was shown that the screening effect of glycerol between PEDOT and PSS induces extended chains either in PEDOT and PSS, thus promoting a better compact structure with smaller π-π stacking distances. Palumbiny et al[22] reported shorter π-π stacking distances of PEDOT and PSS when PEDOT:PSS was deposited in presence of ethylene glycol. Glycerol seems to induce similar effects as ethylene glycol. The intensity of the shoulder around q=5 nm^{-1} (d=1.26 nm) is reduced in the profiles from PEDOT:PSS with glycerol compared with the profile from pristine PEDOT:PSS.

GIWAXS patterns from nanostructured samples are presented in Figure 5.15. Several reflections have appeared in GIWAXS patterns after NIL procedure compared to the pattern from pristine PEDOT:PSS and from PEDOT:PSS with glycerol (Figure 5.13). Patterns from Figure 5.15 have been azimuthally integrated in a region centered at q_z in order to avoid the scattered intensity from silicon, and they are presented in Figure 5.16. The intensity profiles of nanostructured samples present both peaks from PEDOT and PSS π-π stacking around q=12 nm^{-1} and q=18 nm^{-1} respectively. However, all the nanostructured samples present shifted peaks towards higher values of q in comparison to the peaks in the profile from the pristine spin-coated PEDOT:PSS thin film (Figure 5.16). The intensity profiles from nanostructured samples present the peak associated to π-π stacking of PSS at q=12.5-12.8 nm^{-1} (d=0.503-0.491 nm) and the one associated to π-π stacking of PEDOT at q=18.3-18.6 nm^{-1} (d=0.343-0.338 nm). Therefore, the reduction of the

interplanar distance of both PSS and PEDOT π-π stackings already induced by glycerol (Figure 5.14) is still present in nanostructured samples.

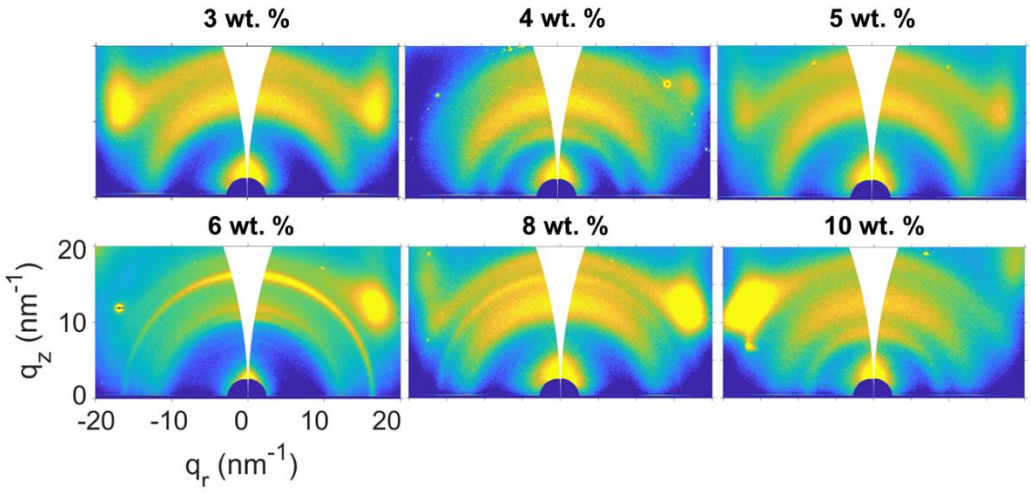

Figure 5.15 GIWAXS patterns from concentrated PEDOT:PSS thin films, with different glycerol concentrations as labelled, after NIL procedure. GIWAXS were taken with the beam parallel to the grating directions. High intensity dots at the sides of patterns come from scattering from silicon substrate. Intensity in logarithmic scale.

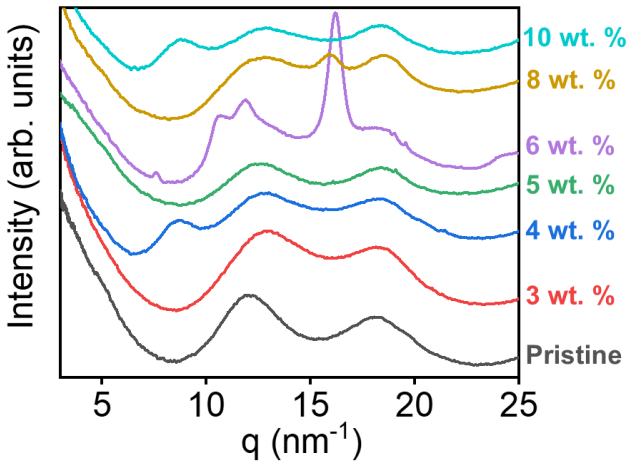

Figure 5.16 Azimuthal integration of GIWAXS patterns from a PEDOT:PSS thin film (black curve) and from nanostructured PEDOT:PSS thin films with different concentrations of glycerol as labelled.

In addition, new reflections appear in the patterns of samples with 4, 6, 8 and 10 wt. % of glycerol. The reflection located at q=8.9 nm^{-1} (d=0.706 nm) which is present in the profile from nanostructured samples with 4 and 10 wt. % of glycerol has been previously detected and attributed to PEDOT, but no crystalline index has been reported[27]. This reflection has been associated with a more conducting state of PEDOT:PSS that appears when it is mixed with an ionic liquid, that in presence of PEDOT:PSS is suggested to lower the electrostatic barrier

between PEDOT and PSS, producing a phase segregation and generating larger PEDOT-rich (conducting) domains with increased conductivity. This reported effect is also accompanied by a decrease in the d-spacing associated to the PEDOT π-π stacking[27]. Interestingly, other narrow reflections are detected in the profile from the sample with 6 wt. % of glycerol at q=7.6, 10.5, 11.9 and 16.2 nm^{-1} (d=0.827, 0.598, 0.528 and 0.388 nm respectively). The intensity profile from the nanostructured sample with 8 wt. % of glycerol presents another reflection at q=15.95 nm^{-1} (d=0.394 nm). The reflections at q=7.6 nm^{-1}, q=11.9 nm^{-1} and q=15.95-16.2 nm^{-1} match with the reflections from a reported crystallization of PSS mixed with the same ionic liquid mentioned that induce a new reflection at q=8.9 nm^{-1} associated with PEDOT[27]. The appearance of new reflections in the GIWAXS patterns from nanostructured PEDOT:PSS samples and the reduced π-π stacking distances of both PEDOT and PSS suggest that the nanostructuring process is promoting the ordering and crystallization of PEDOT and PSS.

The fact that the new reflections do not appear in all the patterns from the nanostructured samples may be related with an anisotropy effect detected during the GIWAXS measurements. It was seen that the appearance of these new reflections (Figure 5.15), that are absent in the pattern from the non-nanostructured sample (Figure 5.13), depends highly on the angle between the X-ray beam and the gratings direction, as it is shown in Figure 5.17.

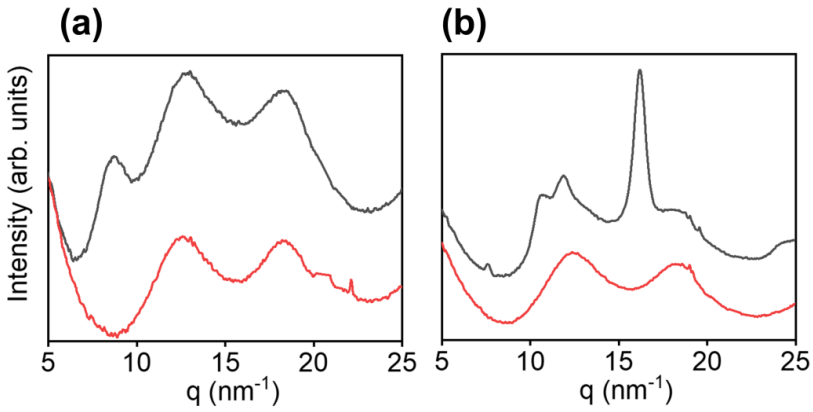

Figure 5.17 Azimuthal integrations of GIWAXS patterns from **(a)** nanostructured PEDOT:PSS thin film with 4 wt. % of glycerol and **(b)** nanostructured sample with 6 wt. % of glycerol. Black curves correspond to GIWAXS taken with the beam parallel to nanogratings direction. Red curves correspond to GIWAXS taken with the nanogratings direction rotated 40º from the beam direction.

Regarding the nanostructured sample with 4 wt. % of glycerol (Figure 5.17.a), the reflection at q=8.9 nm^{-1} (d=0.71 nm) is detected when the beam is nearly parallel to the gratings direction but is absent when the sample is rotated 40º. A similar trend is found for the new reflections observed in the pattern from the nanostructured sample with 6 wt. % of glycerol (Figure 5.17.b). These reflections that appear after the nanostructuring process are detected when the X-ray beam is

parallel to the gratings direction, and is missed when the sample is rotated around the normal to the substrate plane. This clearly points out a particular crystallographic orientation induced during the nanostructuring procedure.

In order to elucidate the chain orientation within the nanostructured samples, reflections from PEDOT and PSS π-π stacking were radially integrated as it is schematized in Figure 5.18.a and Figure 5.18.b respectively. The in-plane (IP) intensity component of a reflection is defined by the radial integration of the reflection from the azimuthal angle χ=0º (the equator of the GIWAXS pattern) to χ=45º and the out-of-plane (OOP) intensity component is defined by the radial integration of the reflection from χ=45º to χ=90º (the meridian of the GIWAXS pattern). However, in the case of the reflection from PEDOT π-π stacking (Figure 5.18.a), these integration limits would include the scattered intensity from the silicon. Therefore, the IP intensity component has been radially integrated between χ=0º and χ=20º and the OOP intensity component between χ=70º and χ=90º. The ratio between the IP and OOP intensity components was calculated for both reflections from PEDOT and PSS π-π stacking and represented in Figure 5.18.c and Figure 5.18.d respectively.

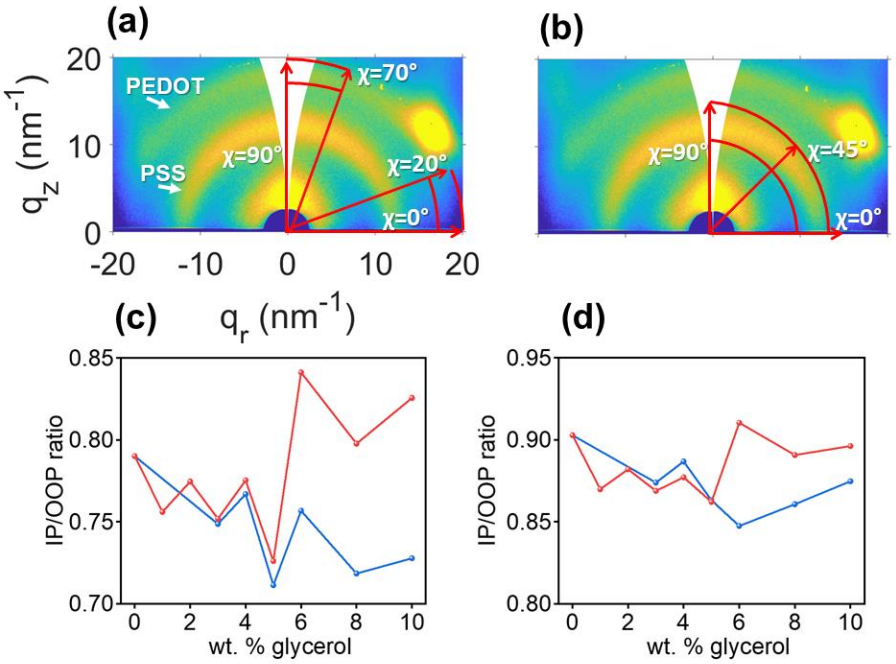

Figure 5.18 (a-b) GIWAXS pattern from a spin-coated pristine PEDOT:PSS thin film with labels that determine the integration limits of the radial integration for the reflection of PEDOT π-π stacking **(a)** and PSS π-π stacking **(b). (c-d)** Ratio between IP and OOP intensity components of **(c)** PEDOT π-π stacking reflection, and **(d)** PSS π-π stacking reflection. Red data correspond to non-nanostructured PEDOT:PSS thin films with glycerol and blue data correspond to nanostructured samples. Intensity of GIWAXS patterns in logarithmic scale.

It can be seen that, initially (Figure 5.18.c), pristine PEDOT:PSS thin film has a PEDOT π-π stacking reflection mainly oriented in the OOP direction, which means a preferential "face-on" orientation (see section 1.4.1). Increasing concentrations of glycerol (Figure 5.18.c, red data) enhance this molecular orientation until a critical concentration of 5 wt. %. Above this concentration, the preferential orientation is partially lost compared to the original value. However, nanostructured samples (Figure 5.18.c, blue data) follows the tendency of enhanced "face-on" structure also at the highest glycerol concentrations. The effect of promoting a PEDOT "face-on" orientation by adding glycerol has been previously observed[28].

The π-π stacking reflection of PSS was also integrated (Figure 5.18.d) using the cake integration shown in Figure 5.18.b. In this case, the effect seems to be the same but less pronounced than in the case of the PEDOT reflection (see that Figure 5.18.c and Figure 5.18.d are plotted using the same Y relative scale). Initially, there is also a preferential "face-on" orientation of PSS π-π stacking, and it is promoted with increasing glycerol concentrations (Figure 5.18.d, red data) until 6 wt. %, where the original value is approximately recovered. Nanostructured samples (Figure 5.18.d, blue data) follow this tendency until 6 wt. % where the IP/OOP ratio starts to increase. Thus the relative "face-on" orientation decreases, but it is still higher than the non-structured samples. Therefore, these last results suggest a promoting tendency of glycerol to induce "face-on" orientations of both PEDOT and PSS π-π stacking. The nanostructuring enhances this effect also on both PEDOT and PSS π-π stacking.

5.6 Conclusions

In this chapter, fabrication and characterization of nanogratings of PEDOT:PSS by nanoimprint lithography has been accomplished. NIL procedure employs a pressure and temperature conditions that affect the structure of the material. In addition, some requirements have been taken into account in order to fabricate nanostructures in PEDOT:PSS through this procedure. The conclusions for this chapter are the following:

- The effect of glycerol concentration on the formation of nanogratings, on the geometrical features and on the order of nanogratings have been elucidated. It was found that thin films of concentrated PEDOT:PSS with glycerol were not nanostructured if the relative weight of glycerol (aqueous PEDOT:PSS / glycerol) was below 3 wt. %. The sample with 3 wt. % of glycerol presents the highest gratings and the highest aspect ratio. The decrease of height and increase of width of gratings with further increasing glycerol concentrations was associated to a more effective filling of the cavities of the mold at the highest glycerol concentrations. The highest order of the nanogratings and the lowest density of defects is obtained for the sample with 4 wt. % of glycerol. Raman analysis shows spectral changes

related to enhancement of planarization in PEDOT molecules associated to its quinoid structure, although this seems to be an effect caused by the addition of glycerol and enhanced by the thermal treatment applied during the NIL procedure. On the other side, clear changes have been found on the inner structure of PEDOT:PSS after nanostructuring. Interplanar distances of both PEDOT and PSS π-π stacking are reduced, indicating a stronger coupling of the molecules. Nanostructured samples with 4 and 10 wt. % of glycerol present a reflection at q=8.9 nm^{-1} (d=0.71 nm) associated with a more-conducting phase of PEDOT:PSS. Other extra reflections present in samples with high concentration of glycerol resemble a reported crystallization of PSS through addition of an ionic liquid. Therefore, the nanostructuring process seems to be inducing an enhancement of the PEDOT and PSS crystallization. Detected anisotropy in GIWAXS measurements indicates a strong chain orientation within the gratings. The addition of glycerol promotes a "face-on" orientation of PEDOT and PSS molecules. NIL enhances this orientation also in both PEDOT and PSS chains.

5.7 References

(1) Chou, S. Y. Nanoimprint Lithography. *Nanofabrication Handb.* **2012**, *4129* (1996), 187–206. https://doi.org/10.1201/b11626.

(2) Choi, J. H.; Choi, H. J.; Shin, J. H.; Kim, H. P.; Jang, J.; Lee, H. Enhancement of Organic Solar Cell Efficiency by Patterning the PEDOT:PSS Hole Transport Layer Using Nanoimprint Lithography. *Org. Electron. physics, Mater. Appl.* **2013**, *14* (12), 3180–3185. https://doi.org/10.1016/j.orgel.2013.09.020.

(3) Yang, Y.; Lee, K.; Mielczarek, K.; Hu, W.; Zakhidov, A. Nanoimprint of Dehydrated PEDOT:PSS for Organic Photovoltaics. *Nanotechnology* **2011**, *22* (48), 485301. https://doi.org/10.1088/0957-4484/22/48/485301.

(4) Radivo, A.; Sovernigo, E.; Caputo, M.; Zilio, S. D.; Endale, T.; Pozzato, A.; Goldoni, A.; Tormen, M. Patterning PEDOT:PSS and Tailoring Its Electronic Properties by Water-Vapour-Assisted Nanoimprint Lithography. *RSC Adv.* **2014**, *4* (64), 34014–34025. https://doi.org/10.1039/C4RA04807E.

(5) Hlaing, H.; Lu, X.; Nam, C. Y.; Ocko, B. M. Water-Vapor-Assisted Nanoimprinting of PEDOT:PSS Thin Films. *Small* **2012**, *8* (22), 3443–3447. https://doi.org/10.1002/smll.201201267.

(6) Meier, R.; Birkenstock, C.; Palumbiny, C. M.; Müller-Buschbaum, P. Efficiency-Improved Organic Solar Cells Based on Plasticizer Assisted Soft Embossed PEDOT:PSS Layers. *Phys. Chem. Chem. Phys.* **2012**, *14* (43), 15088–15098. https://doi.org/10.1039/c2cp42918g.

(7) Li, D.; Guo, L. J. Micron-Scale Organic Thin Film Transistors with Conducting Polymer Electrodes Patterned by Polymer Inking and Stamping. *Appl. Phys. Lett.* **2006**, *88* (6), 2004–2007. https://doi.org/10.1063/1.2168669.

(8) Tan, L.; Kong, Y. P.; Pang, S. W.; Yee, A. F. Imprinting of Polymer at Low Temperature and Pressure. *J. Vac. Sci. Technol. B Microelectron. Nanom. Struct.* **2004**, *22* (5), 2486. https://doi.org/10.1116/1.1800353.

(9) Yang, Y.; Mielczarek, K.; Aryal, M.; Zakhidov, A. A.; Hu, W. Nanoimprinted Polymer Solar Cell. *Mater. Sci.* **2012**, *6* (4), 2877–2892. https://doi.org/10.1021/nn3001388.

(10) Ezquerra, T. A.; Garcia-Gutierrez, M. C.; Nogales, A.; Gomez, M. *Applications of Synchrotron Light to Scattering and Diffraction in Materials and Life Sciences*; Springer, 2009; Vol. 776.

(11) Metzger, T. H.; Haj-Yahya, K.; Peisl, J.; Wendel, M.; Lorenz, H.; Kotthaus, J. P.; Cargill, G. S. Nanometer Surface Gratings on Si(100) Characterized by x-Ray Scattering under Grazing Incidence and Atomic Force Microscopy. *J. Appl. Phys.* **1997**, *81* (3), 1212–1216. https://doi.org/10.1063/1.363864.

(12) Yoneda, Y. Anomalous Surface Reflection of X Rays. *Phys. Rev.* **1963**, *131* (5), 2010–2013. https://doi.org/10.1103/PhysRev.131.2010.

(13) Yan, M.; Gibaud, A. On the Intersection of Grating Truncation Rods with the Ewald Sphere Studied by Grazing-Incidence Small-Angle X-Ray Scattering. *J. Appl. Crystallogr.* **2007**, *40* (6), 1050–1055. https://doi.org/10.1107/s0021889807044482.

(14) Rueda, D. R.; Martín-Fabiani, I.; Soccio, M.; Alayo, N.; Pérez-Murano, F.; Rebollar, E.; García-Gutiérrez, M. C.; Castillejo, M.; Ezquerra, T. A. Grazing-Incidence Small-Angle X-Ray Scattering of Soft and Hard Nanofabricated Gratings. *J. Appl. Crystallogr.* **2012**, *45* (5), 1038–1045. https://doi.org/10.1107/s0021889812030415.

(15) Renaud, G.; Lazzari, R.; Leroy, F. Probing Surface and Interface Morphology with Grazing Incidence Small Angle X-Ray Scattering. *Surf. Sci. Rep.* **2009**, *64* (8), 255–380. https://doi.org/10.1016/j.surfrep.2009.07.002.

(16) González-García, L.; Barranco, A.; Páez, A. M.; González-Elipe, A. R.; García-Gutiérrez, M. C.; Hernández, J. J.; Rueda, D. R.; Ezquerra, T. A.; Babonneau, D. Structure of Glancing Incidence Deposited TiO 2 Thin Films as Revealed by Grazing Incidence Small-Angle x-Ray Scattering. *ChemPhysChem* **2010**, *11* (10), 2205–2208. https://doi.org/10.1002/cphc.201000136.

(17) Rebollar, E.; Rueda, D. R.; Martín-Fabiani, I.; Rodríguez-Rodríguez, Á.; García-Gutiérrez, M.-C.; Portale, G.; Castillejo, M.; Ezquerra, T. A. In Situ Monitoring of Laser-Induced Periodic Surface Structures Formation on Polymer Films by Grazing Incidence Small-Angle X-Ray Scattering. *Langmuir* **2015**, *31* (13), 3973–3981. https://doi.org/10.1021/acs.langmuir.5b00285.

(18) Xu, B.; Gopalan, S. A.; Gopalan, A. I.; Muthuchamy, N.; Lee, K. P.; Lee, J. S.; Jiang, Y.; Lee, S. W.; Kim, S. W.; Kim, J. S.; et al. Corrigendum: Functional Solid Additive Modified PEDOT:PSS as an Anode Buffer Layer for Enhanced Photovoltaic Performance and Stability in Polymer Solar Cells. *Sci. Rep.* **2017**, *7*, 46779. https://doi.org/10.1038/srep46779.

(19) Ouyang, J.; Xu, Q.; Chu, C. W.; Yang, Y.; Li, G.; Shinar, J. On the Mechanism of Conductivity Enhancement in Poly(3,4- Ethylenedioxythiophene):Poly(Styrene Sulfonate) Film through Solvent Treatment. *Polymer (Guildf).* **2004**, *45* (25), 8443–8450. https://doi.org/10.1016/j.polymer.2004.10.001.

(20) Mendelovici, E.; Frost, R. L.; Kloprogge, T. Cryogenic Raman Spectroscopy of Glycerol. *J. Raman Spectrosc.* **2000**, *31* (12), 1121–1126. https://doi.org/10.1002/1097-4555(200012)31:12<1121::AID-JRS654>3.0.CO;2-G.

(21) Massonnet, N.; Carella, A.; de Geyer, A.; Faure-Vincent, J.; Simonato, J.-P. Metallic Behaviour of Acid Doped Highly Conductive Polymers. *Chem. Sci.* **2015**, *6* (1), 412–417. https://doi.org/10.1039/C4SC02463J.

(22) Palumbiny, C. M.; Liu, F.; Russell, T. P.; Hexemer, A.; Wang, C.; Müller-Buschbaum, P. The Crystallization of PEDOT:PSS Polymeric Electrodes Probed in Situ during Printing. *Adv. Mater.* **2015**, *27* (22), 3391–3397. https://doi.org/10.1002/adma.201500315.

(23) Kim, S. M.; Kim, C. H.; Kim, Y.; Kim, N.; Lee, W. J.; Lee, E. H.; Kim, D.; Park, S.; Lee, K.; Rivnay, J.; et al. Influence of PEDOT:PSS Crystallinity and Composition on Electrochemical Transistor Performance and Long-Term Stability. *Nat. Commun.* **2018**, *9* (1), 3858. https://doi.org/10.1038/s41467-018-06084-6.

(24) Wei, Q.; Mukaida, M.; Naitoh, Y.; Ishida, T. Morphological Change and Mobility Enhancement in PEDOT:PSS by Adding Co-Solvents. *Adv. Mater.* **2013**, *25* (20), 2831–2836. https://doi.org/10.1002/adma.201205158.

(25) Kim, N.; Lee, B. H.; Choi, D.; Kim, G.; Kim, H.; Kim, J. R.; Lee, J.; Kahng, Y. H.; Lee, K. Role of Interchain Coupling in the Metallic State of Conducting Polymers. *Phys. Rev. Lett.* **2012**, *109* (10), 1–5. https://doi.org/10.1103/PhysRevLett.109.106405.

(26) Zhou, J.; Li, E. Q.; Li, R.; Xu, X.; Ventura, I. A.; Moussawi, A.; Anjum, D. H.; Hedhili, M. N.; Smilgies, D.-M.; Lubineau, G.; et al. Semi-Metallic, Strong and Stretchable Wet-Spun Conjugated Polymer Microfibers. *J. Mater. Chem. C* **2015**, *3* (11), 2528–2538. https://doi.org/10.1039/C4TC02354D.

(27) Wang, Y.; Zhu, C.; Pfattner, R.; Yan, H.; Jin, L.; Chen, S.; Molina-Lopez, F.; Lissel, F.; Liu, J.; Rabiah, N. I.; et al. A Highly Stretchable, Transparent, and Conductive Polymer. *Sci. Adv.* **2017**, *3* (3), e1602076. https://doi.org/10.1126/sciadv.1602076.

(28) Palumbiny, C. M.; Heller, C.; Schaffer, C. J.; Körstgens, V.; Santoro, G.; Roth, S. V.; Müller-Buschbaum, P. Molecular Reorientation and Structural Changes in Cosolvent-Treated Highly Conductive PEDOT:PSS Electrodes for Flexible Indium Tin Oxide-Free Organic Electronics. *J. Phys. Chem. C* **2014**, *118* (25), 13598–13606. https://doi.org/10.1021/jp501540y.

Chapter 6. Nanoparticles of functional semiconducting and ferroelectric polymers

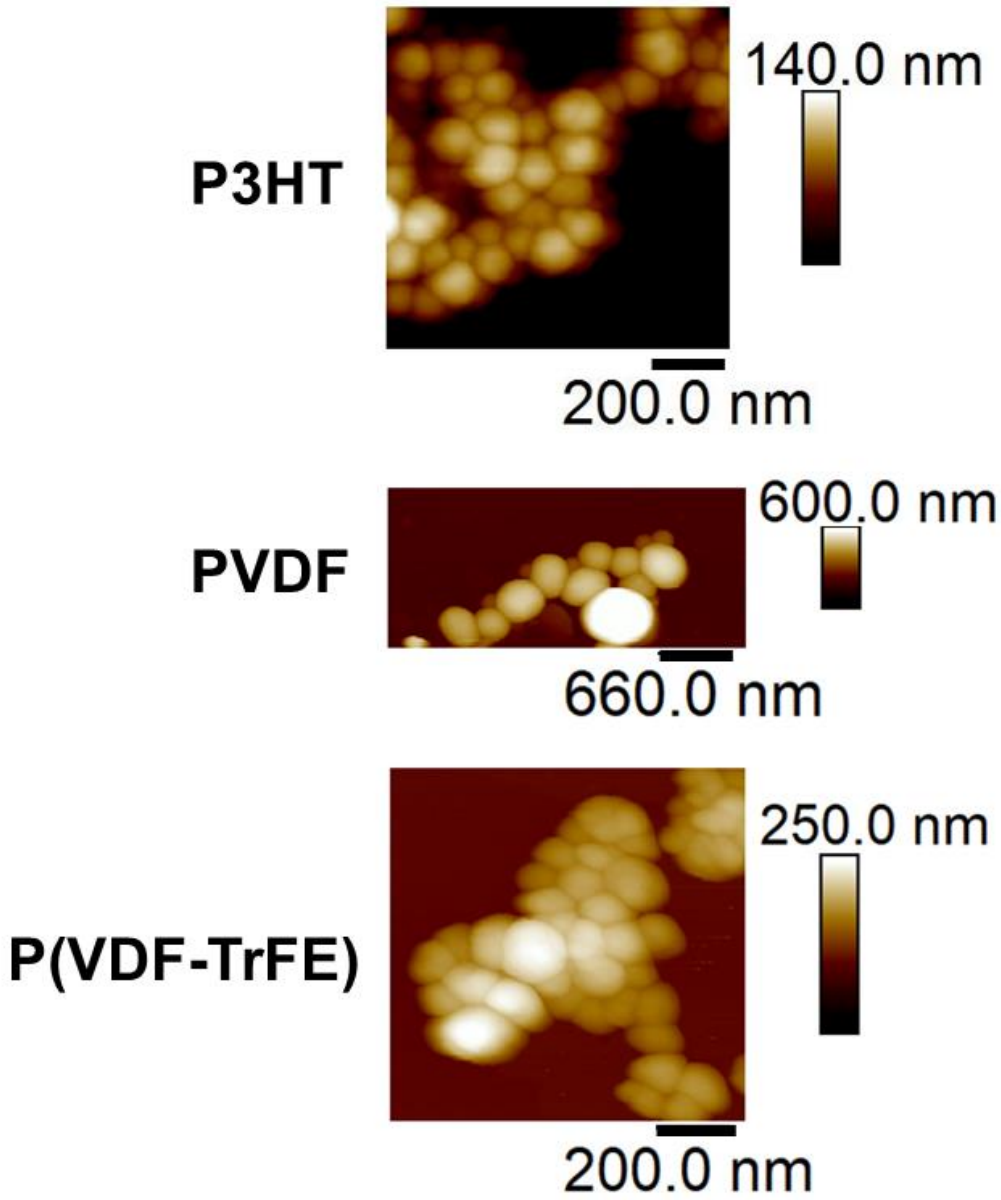

This chapter deals with nanoparticulated polymeric systems. The geometry of nanoparticles imposes restrictions to the three dimensions, and therefore, this approach could lead to changes in their properties when compared to those of the bulk. This chapter is separated in three sections, one for each polymer under study:

- P3HT nanoparticles: the main section is dedicated to the semiconducting polymer P3HT. Optical and structural features of nanoparticles fabricated by two methods are compared.

- PVDF nanoparticles: in this section, the inner structure of PVDF nanoparticles prepared by dialysis is analyzed.

- P(VDF-TrFE) nanoparticles: the last section is centered on this copolymer and the ferroelectric characterization by PFM of PEDOT:PSS/P(VDF-TrFE)-nanoparticles composite system.

6.1 P3HT Nanoparticles: Optical and structural properties

In section 1.5.1, the interest of semiconducting polymeric nanoparticles was introduced. P3HT is the touchstone among conjugated polymers for organic solar cell applications (see section 1.4.1). In this sense, nanoparticles are an interesting way of controlling the size of the electronic donor domains.

In this section, P3HT nanoparticles are prepared by two different approaches, one of them using a surfactant. Structural differences between nanoparticles prepared by both methods are elucidated by optical experiments. These differences are explained considering the results obtained by calorimetry experiments and X-ray scattering measurements as a function of temperature, where the influence of surfactant on the P3HT nanoparticles is detected. Nanoparticles were prepared either by the miniemulsion procedure described in section 2.2.3.2, that employs SDS as surfactant, or by flash procedure described in section 2.2.3.3. The experimental conditions for the P3HT solutions needed for the preparation of nanoparticles were those indicated in Table 2.8.

6.1.1 AFM characterization: size and shape

P3HT nanoparticles prepared by miniemulsion and flash precipitation were deposited over silicon chips by drop-casting or spin-coating and they were visualized using AFM to analyze their sizes and shapes. Figure 6.1 shows AFM topographical images in tapping mode.

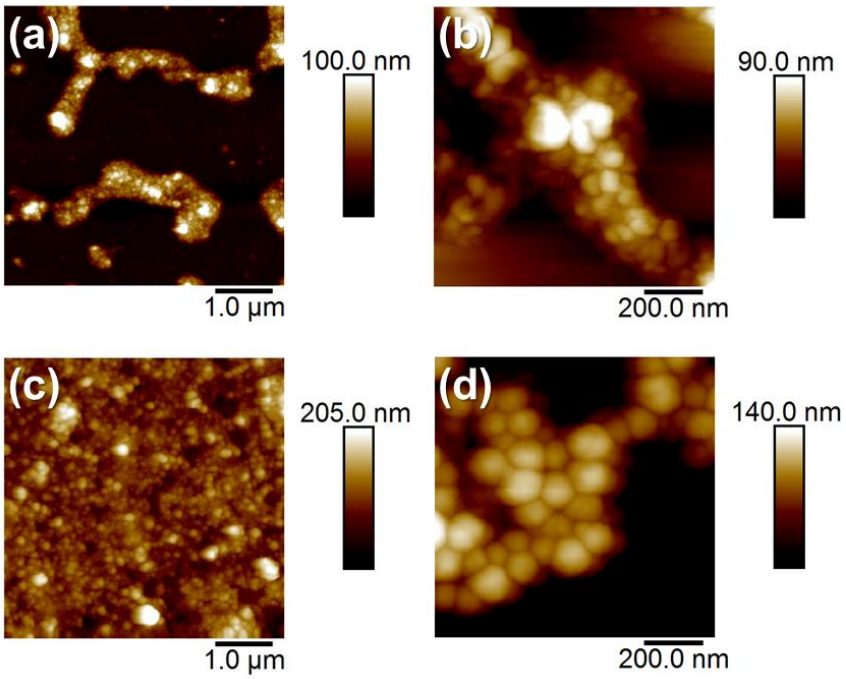

Figure 6.1 AFM topography images of **(a), (b)** P3HT nanoparticles obtained by miniemulsion technique and deposited by spin-coating, and **(c)** P3HT nanoparticles obtained by flash technique and deposited by drop-casting, and **(d)** spin-coating.

In every image, the diameters of 50 particles were measured. The mean and the standard deviation of these values are shown in Table 6.1. Histograms for measured diameters of P3HT nanoparticles prepared by both methods are presented in Figure 6.2.

Table 6.1 Size values of P3HT nanoparticles.

Technique	Mean diameter (nm)	Standard deviation (nm)
Flash	89	33
Miniemulsion	72	19

From Figure 6.2, it can be seen that nanoparticles from miniemulsion precipitation are smaller with a narrower size distribution than those from flash approach. It must be considered that, in

the miniemulsion approach, besides the polymer solution concentration, the concentration of the surfactant in water highly influences the nanoparticles size. As a general rule, higher SDS concentration in water allows coating larger polymer-water interfaces leading to formation of smaller particles[1,2]. When deposited by spin-coating, miniemulsion nanoparticles (Figure 6.1.a-b) are highly aggregated and present a randomly close packed (RCP) array, as previously reported in P3HT nanoparticulated films[3]. It can be seen that the miniemulsion nanoparticles do not present a complete spherical shape, with some sharp, straight sides or even an almost rectangular shape. Flash nanoparticles (Figure 6.1.d) are not totally spherical either. This feature has been associated with the presence of semicrystalline P3HT domains within the nanoparticles[3]. The semicrystalline nature of nanoparticles is later confirmed by X-ray scattering experiments.

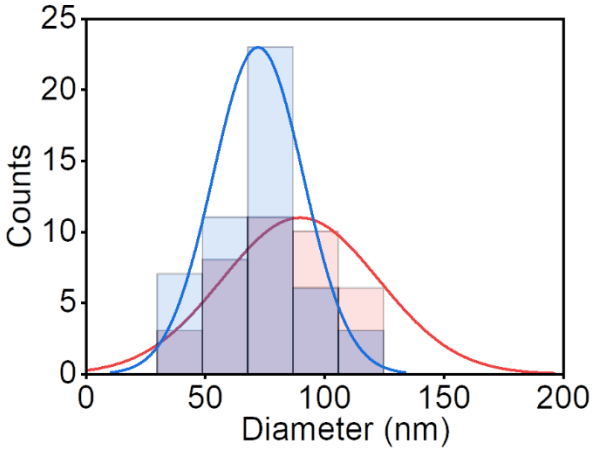

Figure 6.2 Histograms for the measured diameters of P3HT nanoparticles prepared by miniemulsion (blue bars) and flash (red bars). Histograms adjusted with normal distributions. Total counts= 50 for each distribution.

6.1.2 Optical properties of P3HT nanoparticles: UV-VIS absorption and emission

In order to obtain absorption and emission spectra, the colloids were diluted in water until the original concentration of polymer in water was reduced around ten times (Figure 6.3). UV-VIS absorption spectra were collected in the range of λ from 300 nm to 800 nm and later normalized taking the maximum of each spectrum as 1 and the minimum as 0. Figure 6.4 shows the absorption spectra of P3HT nanoparticles prepared by flash precipitation and by miniemulsion, together with the absorption spectra of thin films and solutions prepared with their respective solvents ($CHCl_3$ in the case of miniemulsion and THF for flash precipitation).

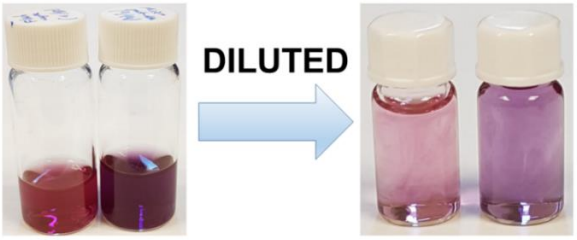

Figure 6.3 Colloids of P3HT nanoparticles obtained by flash precipitation (left vial in both images) and by miniemulsion (right vial in both images).

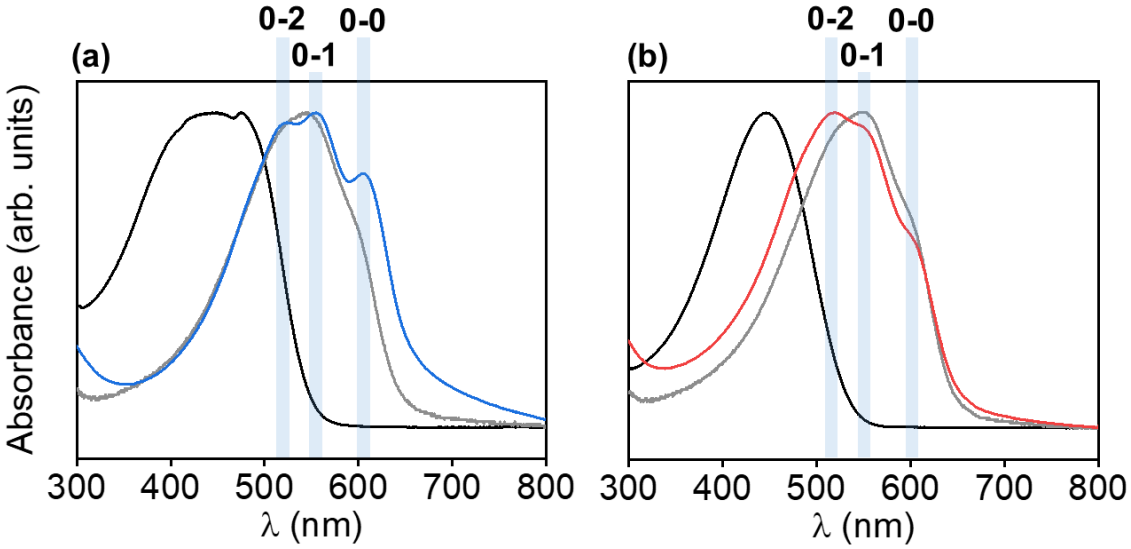

Figure 6.4 (a) UV-VIS absorption spectra of P3HT solved in chloroform (black curve), thin film of P3HT spin-coated from a chloroform solution (3 $g \cdot L^{-1}$) (gray curve) and P3HT nanoparticles prepared by miniemulsion (blue curve). **(b)** UV-VIS absorption spectra of P3HT solved in THF (black curve), thin film of P3HT spin-coated from a THF solution (3 $g \cdot L^{-1}$) (gray curve) and P3HT nanoparticles prepared by flash (red curve). Vibronic peaks are labelled.

In both cases (Figure 6.4.a-b), the spectra from solutions (black curves) present an almost bell-shaped curve, with an absorption peak around 450 nm that is associated with the π-π* transition in disordered P3HT chains[6,7]. The spectrum from the $CHCl_3$ solution is broader than the one from THF solution, although both peaks are centered on the same wavelength. Spectra from thin films and nanoparticles exhibit an absorbance that is redshifted (i.e. shifted towards higher wavelengths) with respect to the solutions spectra. Thin films and nanoparticles spectra present three absorption peaks associated with electronic transitions to different vibronic states labelled as 0-0 at λ=605 nm, 0-1 at λ=555 nm and 0-2 at λ=518nm[4] (see section 1.1.1). However, thin films and nanoparticles spectra exhibit several differences regarding the relative intensities between peaks.

The redshift of the thin film and nanoparticles spectra, compared with that of the solution, is a known effect when conjugated polymers are aggregated and adopt more extended conformations, enhancing their conjugation lengths[5]. Spectra from both thin films (Figure 6.4, gray curves) deposited from P3HT solved in $CHCl_3$ and THF are almost identical and their maximum is at the 0-1 peak. For miniemulsion nanoparticles, the main difference between their absorbance (Figure 6.4.a, blue curve) and the one from the thin film (Figure 6.4.a, gray curve) is the enhanced 0-0 peak intensity. This effect has been related to stronger intrachain coupling[8,9]. In the case of flash nanoparticles (Figure 6.4.b, red curve), their spectrum is blueshifted, i.e. shifted toward lower wavelengths, compared with the spectrum from the corresponding thin film (Figure 6.4.b, gray curve) and the maximum is at the 0-2 peak. This could be related with a higher amount of amorphous regions within the nanoparticles.

Figure 6.5 shows the absorption and emission spectra from both type of P3HT nanoparticles. The emission spectra were taken using an excitation wavelength of λ=555 nm. This wavelength is located at the 0-1 vibronic peak of the absorption spectrum of P3HT. Emission spectra were normalized by the same protocol as absorption spectra.

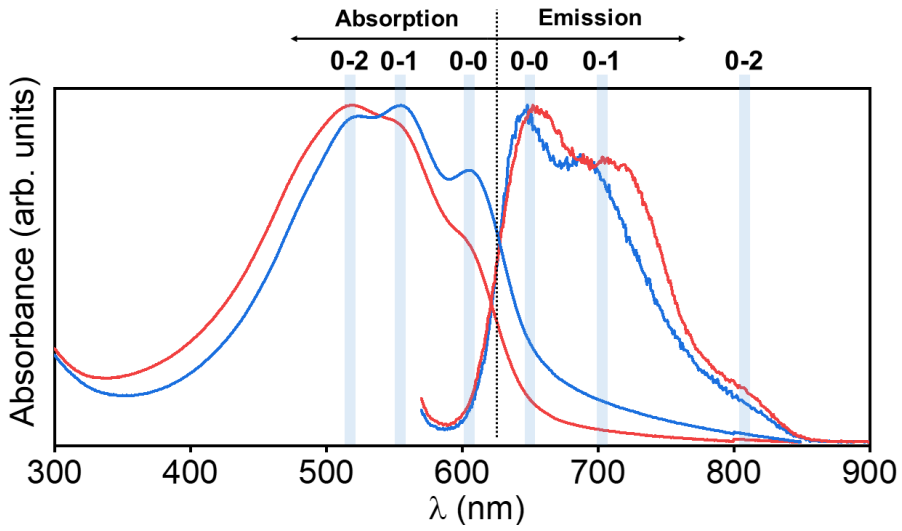

Figure 6.5 UV-VIS absorption and emission spectra of P3HT nanoparticles prepared by miniemulsion (blue curves) and prepared by flash (red curves). Vibronic peaks are labelled.

The emission spectra present three peaks located at λ≈650 nm (0-0), at λ≈700 nm (0-1) and at λ≈800 nm (0-2)[9]. The intensity ratio between 0-0 and 0-1 peaks are different between miniemulsion and flash absorption spectra. The relation between intensities of 0-0 and 0-1 emission peaks are similar, though the peaks from flash emission spectrum are broader and redshifted in comparison to the peaks from miniemulsion emission spectrum.

The relations between the intensities of the peaks are closely related with the arrangement of the molecules in conjugated polymeric systems (see section 1.1.1). The 0-0 and 0-1 absorption intensity ratio for miniemulsion nanoparticles ($I_{0\text{-}0}/I_{0\text{-}1}$=0.81) is higher than in the case of flash nanoparticles ($I_{0\text{-}0}/I_{0\text{-}1}$=0.63). Enhanced 0-0/0-1 absorption peak ratios are characteristic of enhanced intra-molecular interactions[9]. A similar result was reported previously, for both P3HT and P3HT:$PC_{61}BM$ nanoparticles[10]. In addition, the absorption spectrum for the miniemulsion nanoparticles shows narrowing from the low-wavelength side. This region is generally attributed to the absorption of disordered molecules in an amorphous state since molecular absorption of P3HT in diluted solutions is observed just around λ~450 nm (Figure 6.4, black curves). This blueshift in the absorption spectrum from flash nanoparticles relative to the one from miniemulsion nanoparticles resembles the difference reported between P3HT and graft polymer poly(3-but(ethylene oxide)thiophene)[11], and the absorption difference reported between regiorandom P3HT and regioregular P3HT[12]; this effect has been attributed to torsionally disordered chain segments.

As it was described in section 1.1.1, the optical features of P3HT can be described in terms of J-aggregates and H-aggregates[9]. Enhanced J-aggregate behavior in P3HT has been related directly with larger conjugation lengths[10]. Higher contributions from low-energy transitions in conjugated polymers are characteristic of stronger intrachain interactions and longer conjugation lengths. Therefore, these results suggest longer conjugation lengths within P3HT nanoparticles prepared by miniemulsion compared with P3HT within flash nanoparticles. Emission spectra of flash and miniemulsion nanoparticles (Figure 6.5) at room temperature show similar 0-0 to 0-1 intensity ratios. However, the peak positions are different. The emission from flash nanoparticles is redshifted with respect to the one of miniemulsion particles. This has also been reported as a feature from H-aggregates[13].

The emission spectra were taken at three temperatures: 0ºC, 25ºC and 50ºC. It has been reported that J- and H-aggregate scenarios exhibit different temperature evolution[9]. Figure 6.6 show the temperature evolution of the emission spectra from both types of P3HT nanoparticles, excited at λ=555 nm. For both types of nanoparticles, as temperature increases, the spectrum gradually shifts towards lower wavelengths. In the case of flash nanoparticles (Figure 6.6.b), the shift is accompanied by a decrease of the intensity of the 0-1 peak. Spano et al. has interpreted this blueshift with increasing temperature as an indicative of H-aggregate behavior[9,14]. Bearing this in mind, our absorption and emission results suggest a more marked H-aggregate behavior in P3HT in flash nanoparticles than in miniemulsion ones.

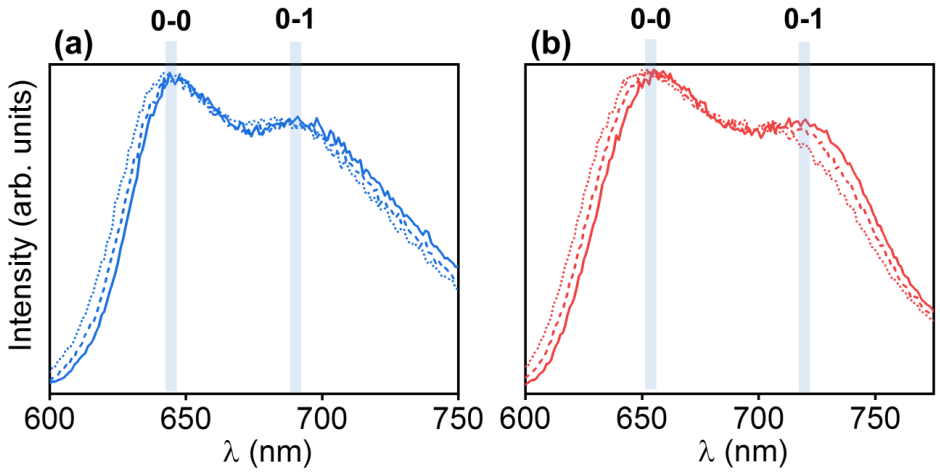

Figure 6.6 Emission spectra of P3HT nanoparticles prepared by **(a)** miniemulsion and **(b**) flash. In both figures, solid lines correspond to temperature T=0ºC, dashed lines to T=25ºC, and dotted lines to T=50ºC. Vibronic peaks are labelled. Excitation wavelength=555 nm.

6.1.3 Inner structure of P3HT nanoparticles: X-ray scattering at room temperature

The crystalline structure of bulk P3HT and P3HT nanoparticles were characterized by WAXS and SAXS using synchrotron radiation. Figure 6.7.a-c shows the diffraction pattern of P3HT in bulk and in the form of nanoparticles, prepared either by miniemulsion or by flash precipitation. Also in Figure 6.7.d, the diffraction from the surfactant SDS is shown.

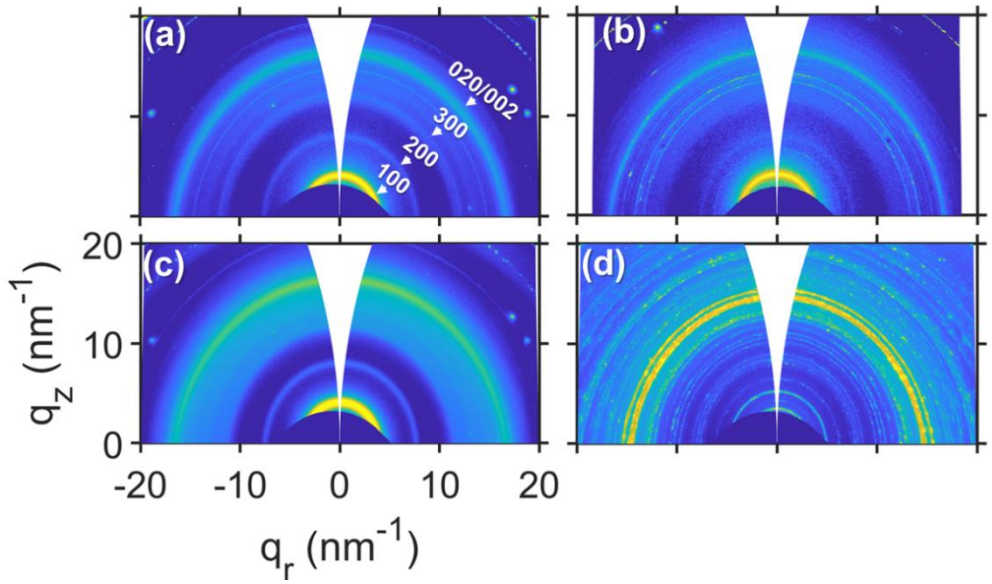

Figure 6.7 WAXS patterns at room temperature of P3HT bulk **(a)**, P3HT nanoparticles prepared by miniemulsion **(b)** and by flash **(c),** and SDS **(d)**. Intensity in WAXS patterns is in logarithmic scale. Main reflections from P3HT are labelled in **(a)**.

All the diffraction patterns obtained from the P3HT systems (Figure 6.7.a-c) show the reflections corresponding to the (100) plane of the P3HT unit cell (q=3.8 nm^{-1}), higher orders of the same family of planes, and the (020/002) reflection (q~17 nm^{-1})[15]. P3HT unit cell (h00) reflections are associated with the lamellar stacking (with spacing d=1.65 nm). The (020) reflection is due to chain stacking along the π molecular orbitals, and (002) reflection derived from the periodicity along the conjugated main chain (see Figure 1.8 in section 1.4.1). In the case of miniemulsion nanoparticles, the diffraction pattern (Figure 6.7.b) shows several narrow rings between q=10 nm^{-1} and q=15 nm^{-1} that, in a first approach can be attributed to residual crystalline SDS, since similar narrow rings are present in the SDS diffraction pattern (Figure 6.7.d).

Azimuthal integrations were made on the diffraction patterns from Figure 6.7. The intensity profiles as a function of the modulus of the scattering vector **q** are presented in Figure 6.8 together with the intensity profiles integrated from SAXS patterns.

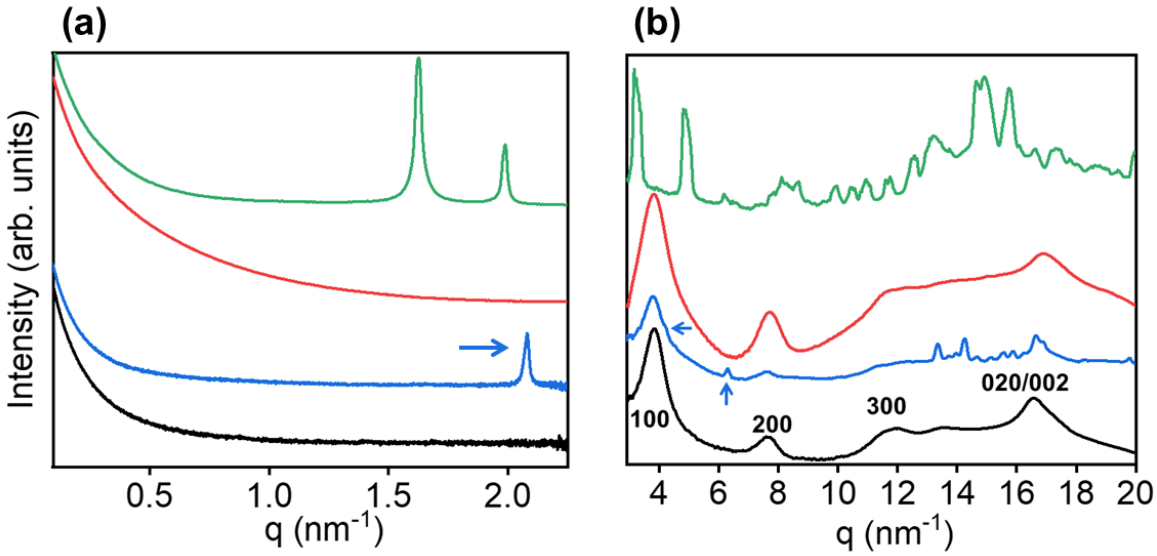

Figure 6.8 Logarithmic intensity profiles at room temperature from **(a)** SAXS patterns and **(b)** WAXS patterns of P3HT in bulk state (black curves), P3HT nanoparticles obtained by miniemulsion (blue curves), by flash (red curves) and SDS (green curves). Plots are vertically shifted for better visualization. Main crystalline peaks from P3HT are labelled in black. Blue arrows highlight the peaks and features present in the diffractogram from miniemulsion P3HT nanoparticles but not in the diffractograms from other P3HT systems.

Black curves from Figure 6.8.a-b represent the intensity profiles from SAXS and WAXS patterns of bulk P3HT. Labels indicate the indexes of the Bragg reflections from the crystalline phase of P3HT. Flash nanoparticles yield similar intensity profiles (red curves) as bulk P3HT. Profiles from miniemulsion nanoparticles (blue curves) present the same Bragg peaks from P3HT and additional features already seen in the 2D WAXS patterns (Figure 6.7.b): a shoulder embedded

in the P3HT (100) reflection at q=4.2 nm^{-1} (leftward arrow), a little sharp peak at q=6.3 nm^{-1} (upward arrow) and a group of peaks between q=13 nm^{-1} and q=18 nm^{-1}. The SAXS profile of the same sample (Figure 6.8.a, blue curve) reveals a sharp peak at q=2.08 nm^{-1} (rightward arrow). SAXS and WAXS profiles from neat SDS present many Bragg peaks, indicative of highly ordered structures.

In general, the X-ray scattering results (Figure 6.7 and Figure 6.8) reveal the semicrystalline nature of P3HT nanoparticles, with equal q-position of the reflections as in the bulk state and thus the same crystallographic distances. This suggests that confinement does not affect the P3HT crystalline cell within nanoparticles. Millstone et al reported the same conclusion with P3HT nanoparticles prepared by flash[16]. In fact, the WAXS profile from flash nanoparticles (Figure 6.8.b, red curve) is quite similar to that of the bulk (black curve). The profiles of these two systems present prominent (100), (200) and (300) peaks in comparison with those shown in the intensity profile from miniemulsion nanoparticles (Figure 6.8.b, blue curve). This is an indication of weaker long-range order of P3HT within nanoparticles prepared by miniemulsion. The shoulder and peak at q=4.2 nm^{-1} and q=6.3 nm^{-1} respectively in the WAXS profile of the miniemulsion nanoparticles (Figure 6.8.b, blue curve) could be higher orders of the peak at q=2.08 nm^{-1} observed in its corresponding SAXS profile (Figure 6.8.a, blue curve). This reflection corresponds to a distance d=3.02 nm, which is close to the reported distance between crystalline lamellas in the hemihydrated state of SDS (d=3.08 nm)[17], i.e. a crystalline lattice that contains one water molecule per two SDS molecules. The group of peaks between q=13 nm^{-1} and q=18 nm^{-1} in Figure 6.8.b (blue curve) are likely to be reflections associated with crystalline distances around d=0.35-0.5 nm within SDS crystals[18]. Therefore, it is clear that in the analyzed system of nanoparticles prepared by miniemulsion, there are SDS molecules which have endured the dialysis procedure, and arrange in a periodical way giving rise to additional Bragg peaks.

In the SAXS intensity profile from neat SDS (Figure 6.8.a, green curve), there are two Bragg peaks located at q=1.63 nm^{-1} and q=1.99 nm^{-1}. The peak at q=1.63 nm^{-1} (d=3.86 nm) agrees with the reported reflection associated with the lamellar ordering of anhydrous SDS crystal[19], i.e. SDS crystallized without water. The peak at q=1.99 nm^{-1} (d=3.16 nm) does not agree exactly, to our knowledge, with any other reported phase. As it was mentioned in the previous paragraph, SDS can present different crystalline phases depending on the level of hydration. SDS crystals present fully extended molecules arranged in a lamellar configuration. Each lamella is formed by adjacent, parallel SDS chains, so the lamellas present a polar face with all the sulphate heads of SDS, and another non-polar face with all the dodecyl hydrocarbon chains (Figure 6.9).

The anhydrous crystalline phase has their SDS molecules almost perpendicular to the lamella plane[20]. The inclusion of water molecules in the phase tends to increase the tilt angle of the

hydrocarbon chains. This effect is shown in Figure 6.9, comparing the unit cells of the anhydrous phase and the monohydrated phase of SDS. The more tilted the molecules in the lamella, the smaller is the lamella thickness. The longest side of the lattice unit cell in anhydrous and hydrated SDS is determined by the stacking of two or more SDS molecules in the direction of the hydrocarbon chain[20]. As the level of hydration increases, it is reported that the tilt angle is higher and the interplanar distance between lamellas is reduced[20], thus the reflection associated with this ordering is shifted to higher q. Therefore, it is possible that the peak at q=1.99 nm^{-1} is associated with a partial hydrated phase of SDS.

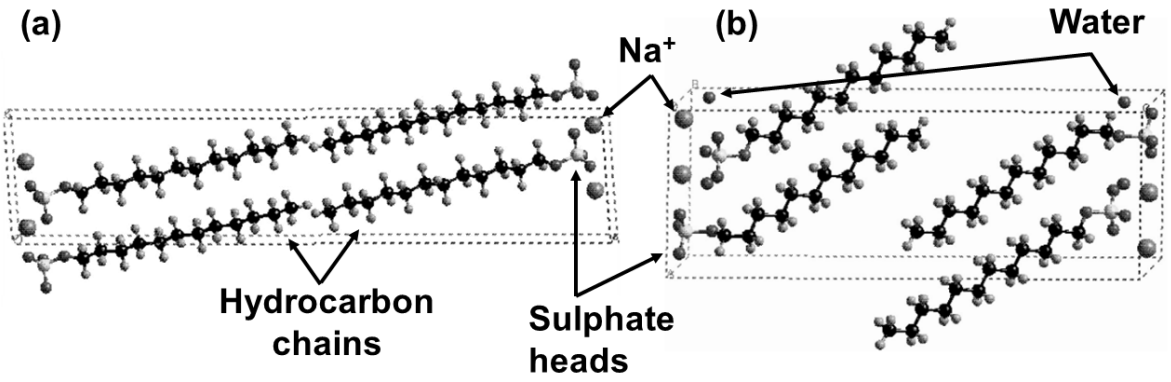

Figure 6.9 Scheme of the unit cell of **(a)** the anhydrous phase of SDS and **(b)** the monohydrated phase of SDS. The components of the unit cell are labelled, indicating the presence of water in the monohydrated phase **(b)**, and the two ends of the SDS molecule: the hydrocarbon (apolar) chain and the sulphate head (polar) which is negatively charged and compensated with the sodium ion (Na^+). Figure adapted from reference[19].

In order to evaluate whether the presence of these extra reflections in the X-ray patterns from the miniemulsion nanoparticles is due to an excess of free SDS or, on the contrary, is inherent to the P3HT nanoparticles, a new batch of them was prepared with an extra step of time extended dialysis (five days). GIWAXS measurements were performed to evaluate this effect and also to visualize the orientations of the reflections from P3HT within nanoparticles when deposited on the film. Figure 6.10.a-b shows the GIWAXS patterns before and after the dialysis step, respectively.

The GIWAXS pattern from the non-dialyzed sample (Figure 6.10.a) presents several narrow rings associated with SDS crystallization. Figure 6.10.b shows the GIWAXS from the dialyzed sample, when the SDS has been presumably removed. In order to compare with the other P3HT systems, GIWAXS patterns have also been measured on spin-coated P3HT thin film (Figure 6.10.c) and on drop-casted P3HT nanoparticles prepared by flash (Figure 6.10.d).

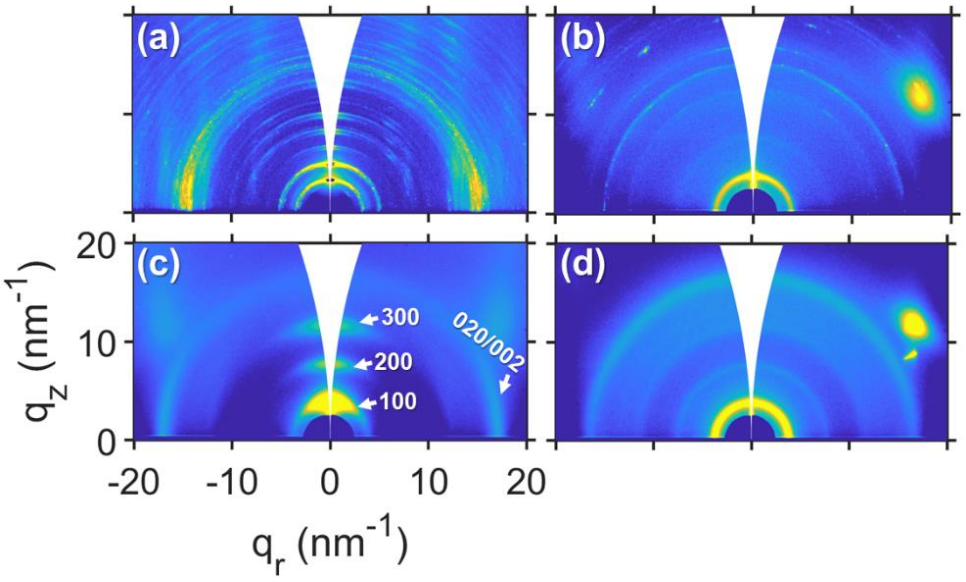

Figure 6.10 GIWAXS patterns of films of P3HT nanoparticles prepared by miniemulsion **(a)** before and **(b)** after the dialysis step. **(c)** P3HT thin film deposited by spin-coating from chloroform solution. **(d)** P3HT nanoparticles prepared by flash. Main reflections from P3HT are labelled in **(c)**. Intensity in GIWAXS patterns is in logarithmic scale.

The closest rings to the beam stop in Figure 6.10.a are likely to correspond to higher orders of a reflection placed at q=1.66 nm^{-1} (d=3.79 nm), not seen in this pattern, which is close to the distance between lamellas of the anhydrous SDS crystal[20]. In Figure 6.10.b, the pattern from the dialyzed miniemulsion nanoparticles does not exhibit such a large amount of rings as the non-dialyzed sample but only two rings around q=15 nm^{-1} remain. The P3HT reflections observed in the GIWAXS patterns from the P3HT thin film (Figure 6.10.c, as labelled) and from the flash nanoparticles (Figure 6.10.d) are also observed in the dialyzed miniemulsion nanoparticles pattern. The presence of the extra rings in the dialyzed miniemulsion nanoparticles pattern suggests that, even after a five days-long dialysis procedure, some SDS is still present in the nanoparticles. This SDS does not exhibit long range order (d≈3.79 nm) (Figure 6.10.a), but it has short-range order (d≈0.4 nm) (Figure 6.10.b) detectable by GIWAXS. These reflections located around q≈14 nm^{-1} have been observed also by other authors[21], although the location of them with respect to the nanoparticles was not discussed. Presumably, this SDS is coating the P3HT nanoparticles produced during the miniemulsion procedure[21].

GIWAXS patterns of nanoparticles film can also give us information about the orientation of the crystals within the nanoparticles. The GIWAXS pattern from P3HT nanoparticles, prepared either by miniemulsion (Figure 6.10.b) or by flash (Figure 6.10.d) does not show preferential orientation. On the contrary, in the GIWAXS pattern from the P3HT thin film (Figure 6.10.c), {h00} reflections present a strong orientation of the intensity along the q_z axis, typical from "edge-

on" orientation described in section 1.4.1. Therefore, P3HT nanoparticles prepared by both methods are structurally isotropic.

6.1.4 Thermal behavior of nanoparticles: differential scanning calorimetry and X-ray scattering as a function of temperature

In order to see the thermal transitions of P3HT and SDS systems, DSC measurements (see section 2.3.2) on bulk P3HT, P3HT nanoparticles systems and neat SDS were performed (Figure 6.11).

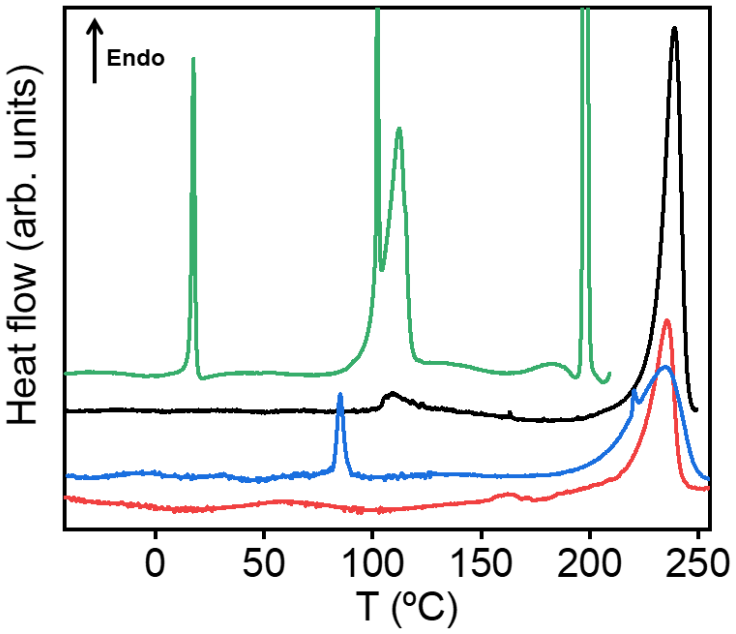

Figure 6.11 DSC heating ramps of P3HT bulk (black curve), P3HT nanoparticles prepared by miniemulsion (blue curve), and by flash (red curve), and SDS (green curve). Rate=10°C·min^{-1}.

Figure 6.11 (black curve) represents the DSC heating curve of P3HT in bulk state. The glass transition is not visible in this diagram. There is a transition between 100ºC and 130ºC, already reported before[22,23], and associated to a loss of order in the side chains[23]. Complete melting of the crystals occurs at higher temperatures and it is revealed in the DSC with an endothermic peak at 239ºC. The red curve in Figure 6.11 is the calorimetric response from P3HT nanoparticles prepared by flash during heating. The features of this curve are quite similar to the ones corresponding to the bulk, with its peak associated with melting at 236ºC. For miniemulsion nanoparticles, the DSC trace is richer. The maximum of the melting endothermic peak is placed at 235ºC and it extends up to 253ºC, around 10ºC above the end of melting of flash nanoparticles. Around 80ºC a sharp endothermic peak appears that does not correspond with any endothermic peak from neat SDS heating ramp, though its width suggests an SDS transition (Figure 6.11, green curve). Therefore, this peak could be an indicator of a mixed phase between P3HT and SDS. The

DSC curve of SDS (Figure 6.11, green curve) reveals several narrow endothermic peaks that could correspond to melting or transition between different crystalline phases[24]. The transition at 19ºC could be related with a polymorphic transformation from other hydrated states[24]. The endothermic peak at 110ºC may be associated with the melting of the alkyl non-polar tails[24] and the narrow intense peak at 190ºC with the total melting of the material. Soon after the melting point of the SDS, it starts to degrade[25].

WAXS measurements as a function of temperature were carried out to compare with calorimetry and thus obtaining a global picture of thermal behavior of P3HT nanoparticles. Samples were heated from room temperature up to 300ºC. Every temperature pattern was integrated in the whole azimuthal range to get an intensity profile as a function of q (Figure 6.12). Figure 6.12 shows the intensity maps as a function of q (nm^{-1}) and T (ºC) for the three P3HT systems. At room temperature, the characteristic (100), (200), (300) and (020/002) reflections (labelled at the top of the figure) are observed in every map. The reflections evolve as the temperature increases in terms of intensity and q-position. In the case of the (100) reflection, its intensity increases with temperature and its position shifts to lower q until it starts to fade around 220ºC, which corresponds to the melting process. This occurs in the three P3HT systems (Figure 6.12.a-c). The evolution with temperature of the (020/002) in the three P3HT systems consist of an initial displacement towards higher q and then a shift to lower q, simultaneously with an intensity decrease until melting.

To see quantitative differences between the three P3HT systems regarding the evolution of (100) and (020/002) peaks, the q-positions and intensities of peak maxima have been represented in Figure 6.13. The q-position of the (100) peak shows a similar evolution in the three systems: a gradual reduction of q_{100} from $q \approx 3.8\ nm^{-1}$ to $q \approx 3.48\ nm^{-1}$, which corresponds to an increase of the interplanar distance from $d \approx 1.65$ nm to $d \approx 1.8$ nm[26,27]. The evolution of $q_{020/002}$ is also similar in the three systems: its value increases up to a given value of q (that is a minimum π-π packing distance) around T=100ºC, and then decreases. This behavior has already been observed for P3HT[28]. However, $q_{020/002}$ for the miniemulsion nanoparticles is slightly higher than for flash nanoparticles and bulk P3HT. This implies a shorter π-π stacking correlation distance. Interestingly, the difference in π-π stacking distance has been associated with a dominant H or J-aggregation[28], in which J-aggregation yields shorter π-π stacking distances than in H-aggregation. In line with the optical results presented in section 6.1.2, we can conclude a higher presence of J-aggregates in the miniemulsion nanoparticles.

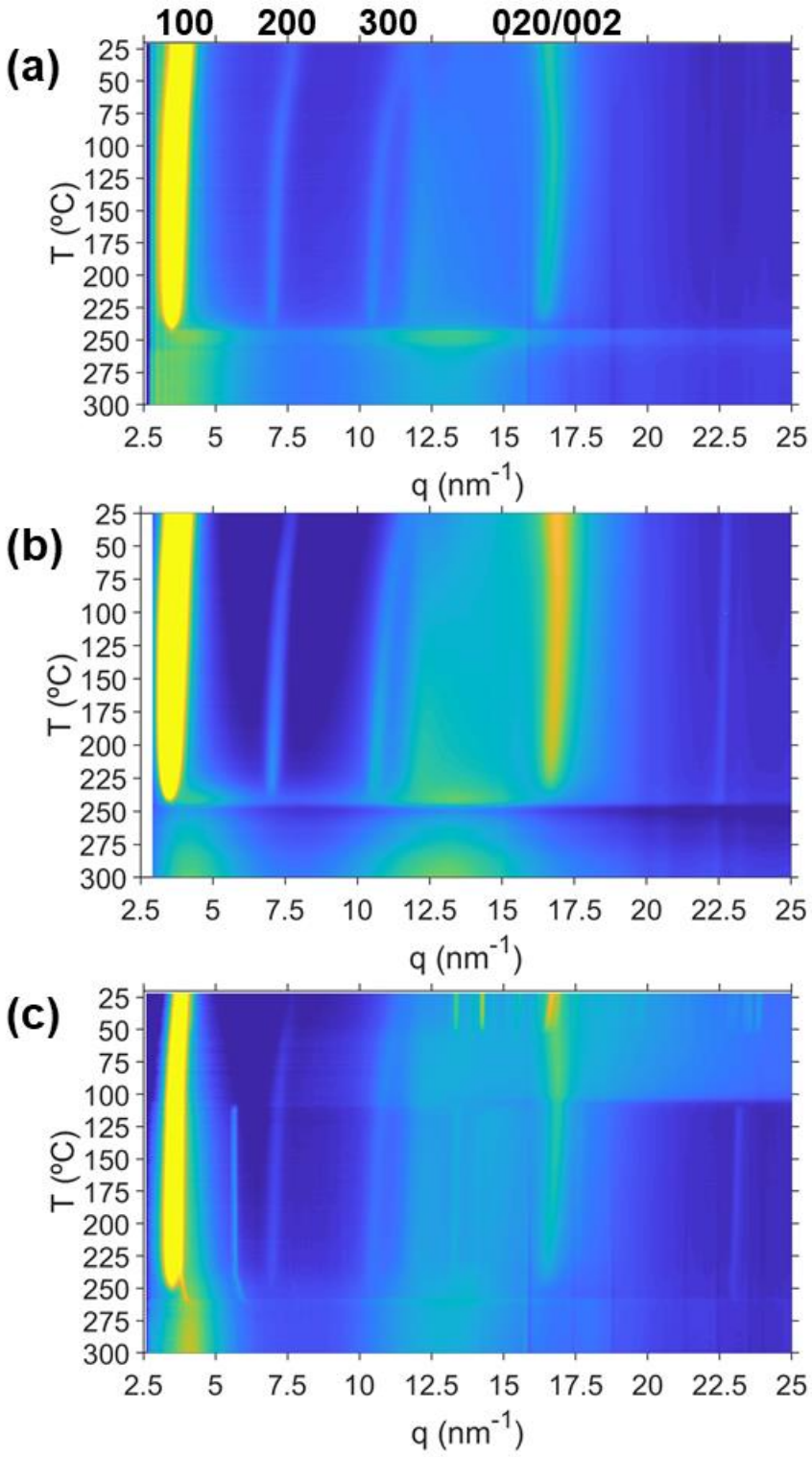

Figure 6.12 Two-dimensional map of the temperature-dependent WAXS data for **(a)** P3HT bulk and P3HT nanoparticles prepared by **(b)** flash, and **(c)** miniemulsion. In every sample, heating ramps were taken from 25°C to 300°C at 20°C per minute rate. Intensities are in logarithmic scale.

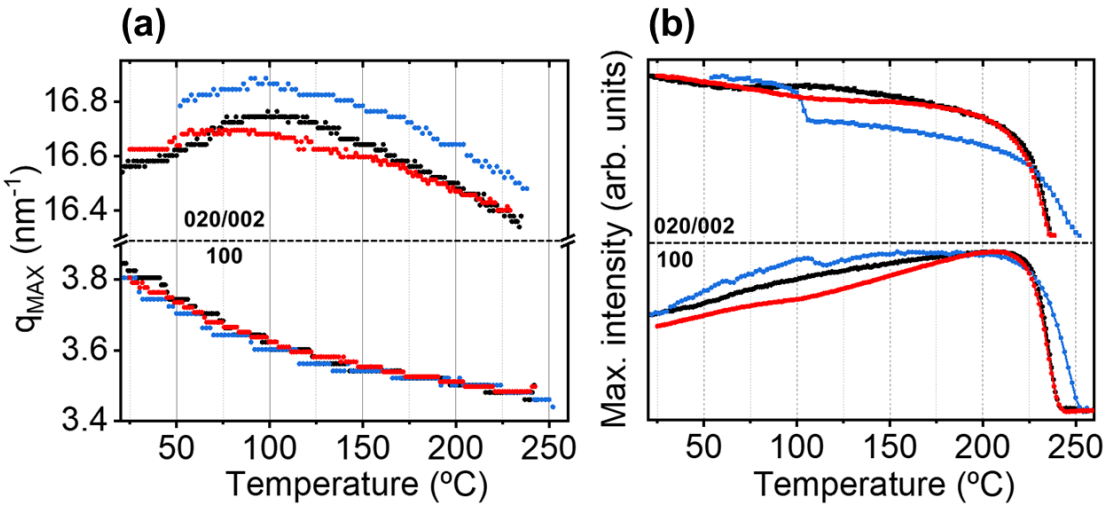

Figure 6.13 (a) q-position of the maximum of intensity of the (020/002) peak **(top)** and (100) peak **(bottom)** as a function of temperature. **(b)** Intensity of the maximum of the (020/002) peak **(top)** and (100) peak (**bottom)** as a function of temperature. In every case, black data correspond to P3HT bulk, blue data to P3HT nanoparticles prepared by miniemulsion and red data to P3HT nanoparticles prepared by flash. Intensities of (100) and (020/002) peaks have been normalized setting the lowest value to 0 and the highest value to 1.

We will now consider the features observed in the dependence of the (100) reflection intensity with temperature. For P3HT bulk (Figure 6.13.b black data), the intensity of (100) reflection (q=3.8 nm^{-1}) increases as the temperature rises. It reaches a maximum at T=200ºC and starts to decrease at T=210ºC. This point could be seen as the onset of the melting process, which ends at T=243ºC. On the other hand, the intensity of the (020/002) reflection for P3HT bulk remains almost constant up to T=110ºC, where it starts decreasing, until melting at T=237ºC. Therefore, there is an offset of 6ºC between the loss of π-π stacking order, observed by the disappearance of the (020/002) peak, and the loss of lamellar order, related with (100) peak.

For flash nanoparticles, the temperature evolution for X-ray diffraction (Figure 6.12.b and Figure 6.13, red data) is quantitatively similar to that of bulk P3HT. The intensity decrease of (100) peak starts at T=213ºC and ends at T=245ºC. The intensity of (020/002) peak starts decreasing and cancel at the same temperatures as in P3HT bulk system. Therefore, for flash nanoparticles, there is a difference of 8ºC between the vanishing of both peaks.

The analysis for miniemulsion nanoparticles (Figure 6.12.c and Figure 6.13, blue data) presents additional diffraction features and a rather different evolution. Both (100) and (020/002) peaks present a sudden drop in intensity around 110ºC. At higher temperatures, the intensity of (100) peak starts decreasing at T=204ºC and this peak almost vanishes around at T=252ºC, almost 10ºC above the vanishing temperature of the (100) reflection for the flash nanoparticles. This result is

consistent with the DSC experiments (Figure 6.11), in which an offset of around 10ºC was found between the melting peak of the miniemulsion particles and the one of the flash nanoparticles. On the other hand, the (020/002) peak vanishes at T=252ºC, 15ºC over the one corresponding to P3HT bulk and flash nanoparticles.

Additionally, other specific features appear in the diffractograms of P3HT miniemulsion particles as temperature increases (Figure 6.12.c). The shoulder that appears in the (100) P3HT peak region (q=4.2 nm^{-1}), the peak at q=6.3 nm^{-1} and the group of sharp peaks that appears in the q region between 13 nm^{-1} and 18 nm^{-1} vanish at 54ºC. Between 54ºC and 110ºC, the diffractogram is very similar to that of bulk P3HT. However, above 110ºC, new sharp peaks appear at q=3.7 nm^{-1} and q=5.6 nm^{-1}, close to P3HT (100) reflection. They correspond to the second and third order, respectively, of a reflection at q=1.85 nm^{-1} (d=3.4 nm), visible with SAXS. The second and third order at q=3.7 nm^{-1} and q=5.6 nm^{-1} respectively are still present in the diffractogram above 250ºC.

The presence of these Bragg peaks at 250ºC in the diffractogram from P3HT miniemulsion nanoparticles (Figure 6.12.c), above the melting temperature of SDS located in its heating ramp (Figure 6.11) and absent in the diffractogram from flash nanoparticles (Figure 6.12.b), suggests the existence of a mixed crystalline phase between P3HT and SDS, that could be related with the optical and structural differences identified between flash and miniemulsion nanoparticles. To compare the behavior of the possible P3HT/SDS phase, with that of SDS crystals, the evolution of the diffractograms of SDS with temperature was studied (Figure 6.14).

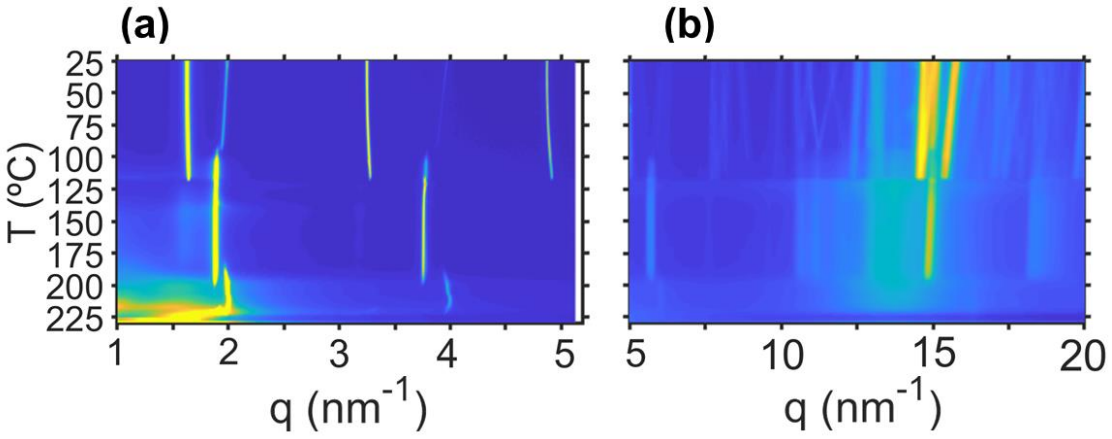

Figure 6.14 Two-dimensional map of the temperature-dependent **(a)** SAXS and **(b)** WAXS data for neat SDS. Intensities are in logarithmic scale.

Figure 6.14 shows the temperature evolution of SDS SAXS and WAXS intensities. The SAXS profile from SDS (Figure 6.14.a) at room temperature reveals several peaks at q=1.63 nm^{-1}, 1.99 nm^{-1}, 3.25 nm^{-1}, 3.97 nm^{-1} and 4.88 nm^{-1}. The peaks at q=1.63 nm^{-1}, 3.25 nm^{-1} and 4.88 nm^{-1} correspond to the first, second and third order of the reflection associated to the lamella ordering

in the anhydrous SDS system[20]. The peaks at q=1.99 nm^{-1} and 3.97 nm^{-1} are the first and second order of a reflection that has not been identified. However, as it was mentioned on section 6.1.3, it is possible that they could be related with a partially hydrated crystalline phase of the SDS, with different q-position of the reflection due to tilted SDS chains induced by the inclusion of water molecules in the crystal lattice[20], that result in a reduction of interplanar distances between lamellas. The SAXS results point to a coexistence of two different crystalline phases in SDS at room temperature. As the temperature increases, the peaks corresponding to the unreported phase (q=1.99 nm^{-1} and 3.97 nm^{-1}) shift toward lower q until they disappear at 94ºC. At the same temperature, a peak is formed at q=1.88 nm^{-1} with its second order at q=3.76 nm^{-1}. This suggests that the crystalline phase associated with the peaks detected at room temperature at q=1.99 nm^{-1} and 3.97 nm^{-1} suffers a phase transformation around 95ºC, and it is likely to be the responsible for the endothermic narrow peak that starts at 90ºC and peaks at 100ºC in the DSC heating ramp from neat SDS (Figure 6.11, green curve). As the temperature increases above 110ºC, the SAXS peaks associated with the anhydrous phase (q=1.63 nm^{-1}, 3.25 nm^{-1} and 4.88 nm^{-1}) disappear. The peaks at q=1.88 nm^{-1} and q=3.76 nm^{-1} that appeared at 95ºC remain until they disappear at 200ºC. Around 180ºC, another peak appears at q=2 nm^{-1}, with its second order at q=4 nm^{-1}. These peaks disappear at 220ºC.

WAXS intensity at room temperature (Figure 6.14.b) presents many Bragg peaks associated with order within SDS lamellas, between adjacent molecules in the same lamellar plane[18], either in the anhydrous system or the hemihydrated system identified in SAXS (Figure 6.14.a). At 110ºC, many of these Bragg peaks disappear, in parallel with the vanishing of the SAXS peaks associated with the anhydrous phase (q=1.63 nm^{-1}, 3.25 nm^{-1} and 4.88 nm^{-1}). At 200ºC, the rest of Bragg peaks in WAXS disappear, in parallel with the vanishing of SAXS peaks at q=1.88 nm^{-1} and 3.76 nm^{-1}.

The calorimetry results (Figure 6.11) pointed to the melting of the SDS hydrocarbon chains at 110ºC. We suggest that above 110ºC, SDS molecules with molten hydrocarbon chains form a crystalline structure with reduced interplanar distance between lamellas (q=1.88 nm^{-1}, d=3.34 nm) compared with the anhydrous system at room temperature (q=1.63 nm^{-1}, d=3.86 nm). Between 110ºC and 200ºC, this crystalline structure also has short order, as revealed by the presence of Bragg peaks in WAXS. At 200ºC, it melts and another Bragg peak of SAXS is present until 220ºC, but without short order since WAXS diffractograms do not show any Bragg peak.

Hereafter, the evolution with temperature of neat SDS can be compared with the one of P3HT miniemulsion nanoparticles. The evolution of SAXS profiles with temperature of P3HT nanoparticles prepared by miniemulsion is presented in Figure 6.15.

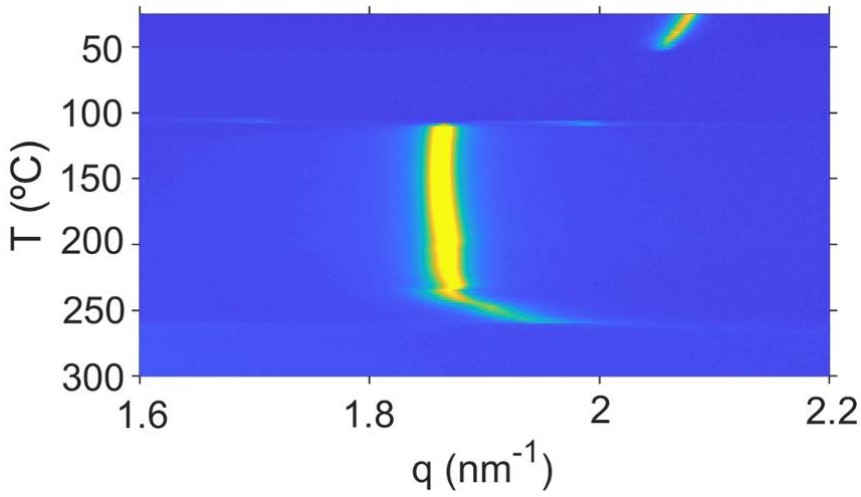

Figure 6.15 Two-dimensional map of the temperature-dependent SAXS intensity for P3HT nanoparticles prepared by miniemulsion. Intensity is in logarithmic scale.

At room temperature, there is a Bragg peak at q=2.08 nm^{-1} (d=3.02 nm) that was identified during description of Figure 6.8 as close to the hemihydrated phase of SDS (d=3.08 nm)[17]. This peak shifts to lower q as the temperature increases until it disappears around 55ºC. In the temperature range from 55ºC to 110ºC the SAXS intensity does not exhibit any feature. As temperature increases above 110ºC, a new peak appears. The q position of this new peak is nearly the same as in the neat SDS system (Figure 6.14.a) at this temperature (q=1.88 nm^{-1}). In addition, two other peaks appear at q=1.7 nm^{-1} and q=1.98 nm^{-1} but they are only visible in a narrow window of temperature around 106ºC. The evolution with temperature of the peak at q=1.88 nm^{-1} is quite different for P3HT miniemulsion nanoparticles and for neat SDS (Figure 6.14.a). While in the neat SDS this peak disappears at 200ºC (and another peak formed at q=2 nm^{-1} around 180ºC disappears at 220ºC), in miniemulsion P3HT nanoparticles (Figure 6.15), the peak is present beyond 250ºC. This behavior reinforces the idea of a P3HT-SDS blended system probably located in the nanoparticle surface.

Scherrer analysis of (100) reflections was made to compare the crystal mean size between P3HT bulk and the different nanoparticles as a function of temperature. In the Scherrer equation[29] (Equation 6.1) τ is the value for the crystal mean size, *K* is a dimensionless shape factor close to unity (≈0.9), θ is the scattering angle, λ is the used wavelength and β is the full width at half maximum of the Bragg peak in degrees.

$$\tau = \frac{K\lambda}{\beta \cos\theta} \qquad (\mathbf{6.1})$$

In every temperature step, the (100) peak is fitted using a Lorentzian function to obtain the full width at half maximum in q (nm^{-1}) of the peak. Bulk P3HT and P3HT nanoparticles prepared by miniemulsion and flash were analyzed in this way and the τ values are represented in Figure 6.16.

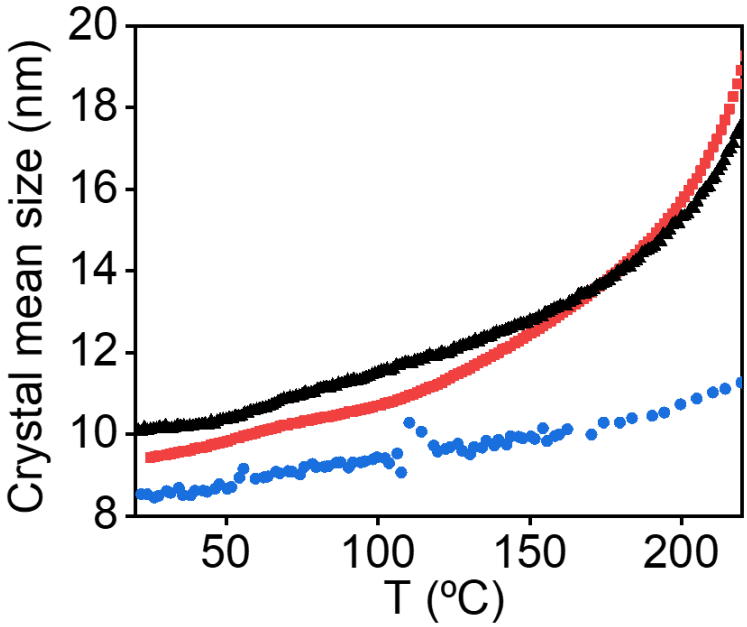

Figure 6.16 Crystal mean size –calculated from Scherrer equation with K=0.9- of P3HT in bulk (black triangles) and both nanoparticle systems (miniemulsion: blue dots, flash: red squares) as a function of increasing temperature.

Initially, the mean size of the P3HT crystals within miniemulsion nanoparticles (blue data) is lower than in bulk (black data) and flash nanoparticles systems (red data). This is consistent with the observation from Figure 6.8.b, in which the diffractogram at room temperature of miniemulsion nanoparticles shows much more reduced (200) and (300) peaks compared with the ones from bulk and flash nanoparticles diffractograms, indicating a poorer crystalline order. As the temperature rises, the crystal mean size increases in the three systems. When the temperature is over 100-120ºC, P3HT crystal size in bulk and in flash increases exponentially, whereas the growth of crystals within miniemulsion nanoparticles seems to be restricted, and the size increases linearly.

A recent work has discussed the interactions between P3HT and insulating additives, in that case with polyethylene oxide (PEO)[11]. They showed that a strong affinity between the side chains of P3HT and the insulating PEO reduces the steric interaction between P3HT side chains and conjugated backbone that normally induce torsional disorder. In our work, we propose the existence of a blended crystalline phase between P3HT and SDS. Following an analog explanation, P3HT side chains blended with SDS would reduce the steric hindrance on conjugated

backbones, thus enhancing the planarity of the chains within nanoparticles prepared by miniemulsion as it was demonstrated with the optical results (section 6.1.2). However, the presence of SDS chains in the direction of side chains of P3HT could be restraining the growth of P3HT crystals in this direction, which corresponds to the (100) plane. This explains the lower intensities of (100), (200) and (300) peaks in the diffractogram from miniemulsion nanoparticles taken at room temperature (Figure 6.8.b, blue curve) compared with the diffractograms from P3HT bulk and flash nanoparticles (Figure 6.8.b, black and red curves respectively), and also explains the slower growth of the crystals of P3HT within miniemulsion nanoparticles in the (100) direction as the temperature rises, compared with the growth of P3HT in bulk and within flash nanoparticles, that yield a similar crystal growth with temperature (Figure 6.16).

In addition, it is reported that the conjugation length of P3HT nanoparticles prepared by miniemulsion can be enhanced by using conjugated surfactants[30] instead of SDS. Therefore, we propose that the influence of the surfactant on the planarization of P3HT molecules is induced through the interaction between the lateral chains of P3HT and the hydrocarbon tails of SDS.

With all the previous results, the model proposed is the following: the P3HT colloid obtained by miniemulsion process contains a mixed P3HT:SDS phase in the surface of the nanoparticles connected via interaction between non-polar side chains of P3HT and hydrocarbon tails of SDS. This interaction plays a role in the planarization of the P3HT chains, discussed above based on the absorption and emission experiments. This is the initial state of the miniemulsion system. As the temperature rises, bulk P3HT and miniemulsion and flash nanoparticles enhances its crystalline length at the same rate until around 110ºC. From this point, the P3HT crystals within miniemulsion nanoparticles grow at the same rate as before whereas crystals in bulk and flash nanoparticles grow exponentially. This limited crystal growth on miniemulsion nanoparticles could be effect of the presence of a crystalline blended phase between P3HT and SDS, which may be the origin of the reflection at $q=1.88\ nm^{-1}$ detected in SAXS (Figure 6.15) that is still present beyond 250ºC.

6.2 Ferroelectric phase in free-surfactant PVDF nanoparticles prepared by dialysis

Recently, large research efforts are directed to include PVDF in organic electronics technologies, since PVDF can exhibit a large piezoelectric and ferroelectric response, due to the net dipole of polymer chains. However, PVDF can crystallize on different phases and not all these phases are polar, and thus ferroelectric. Looking at miniaturization of ferroelectric devices, nanoparticles of

PVDF have been prepared by dialysis procedure and their morphology, inner structure and thermal behavior have been characterized.

Nanoparticles of PVDF were prepared by dialysis procedure as described in section 2.2.3.1. The experimental conditions for the preparation of PVDF solutions employed to produced nanoparticles were included in Table 2.8.

6.2.1 AFM characterization of PVDF nanoparticles

The size and the height of PVDF nanoparticles were characterized by AFM on samples deposited by drop-casting on silicon (Figure 6.17). As can be seen, the morphology of the obtained nanoparticles is nearly spherical, with mean diameter around 230 nm and standard deviation of 125 nm, as determined by measuring the size of 70 nanoparticles observed by AFM. The histogram of the PVDF nanoparticles diameter is shown in Figure 6.18.

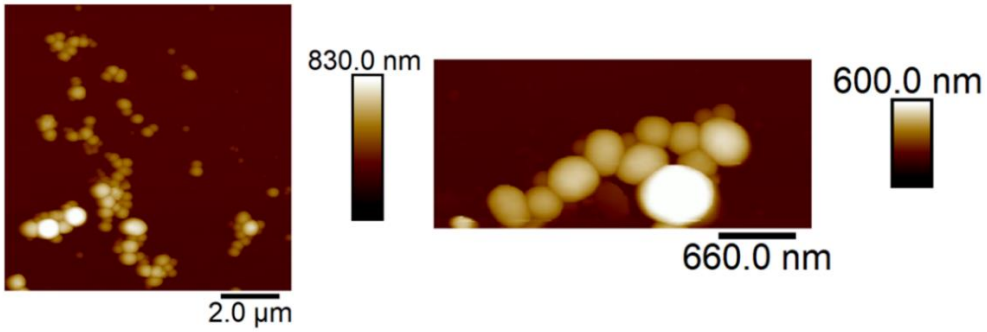

Figure 6.17 Topographical images taken by AFM of PVDF nanoparticles prepared by dialysis.

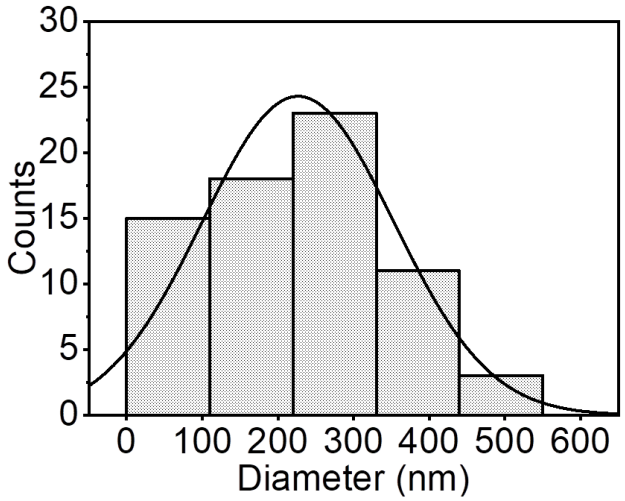

Figure 6.18 Histogram for the measured diameters of PVDF nanoparticles prepared by dialysis. Histogram adjusted with a normal distribution. Total counts= 70.

6.2.2 Inner structure and thermal properties of PVDF nanoparticles

GIWAXS experiments were performed on a PVDF film casted from DMA solution at 100ºC and on PVDF nanoparticles drop-casted from an aqueous dispersion (Figure 6.19).

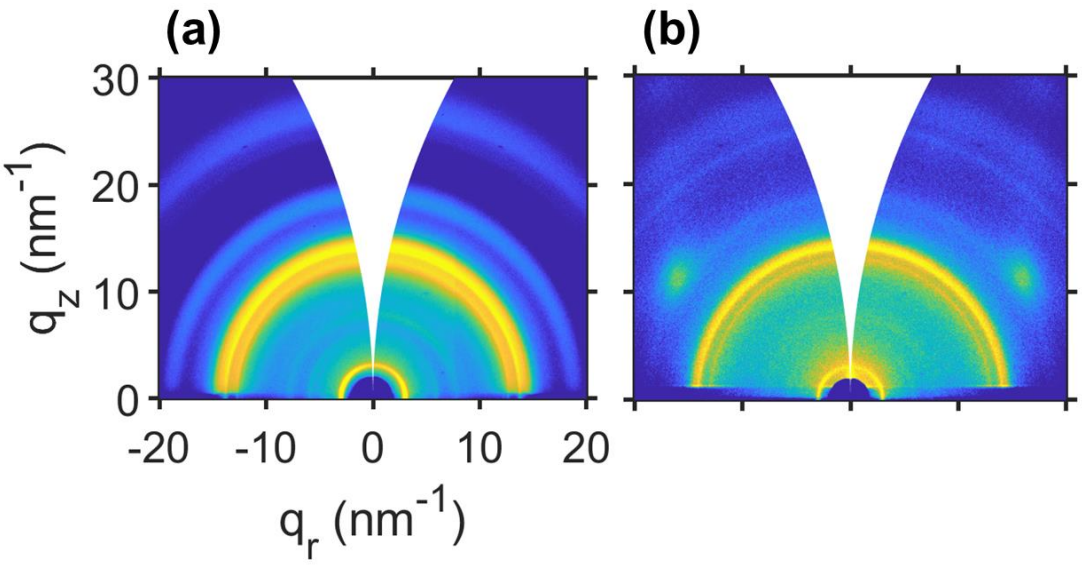

Figure 6.19 GIWAXS patterns taken at room temperature of **(a)** PVDF film, and **(b)** PVDF nanoparticles. Intensities of GIWAXS patterns are in logarithmic scale. The reflection around q=3 nm^{-1} is due to scattering from the Kapton window of the heating stage.

GIWAXS patterns from PVDF film (Figure 6.19.a) and from PVDF nanoparticles (Figure 6.19.b) present similar isotropic reflections around q≈15 nm^{-1}, q≈19 nm^{-1} and q≈28 nm^{-1}.

To identify subtle differences among the patterns from the two systems, azimuthal integrations of the patterns were made and they are presented in Figure 6.20. The diffractograms of both the film and the nanoparticles (Figure 6.20, black and red curve, respectively) share similar features with intense peaks between q=12 nm^{-1} and q=15 nm^{-1}, a broad peak at q≈19 nm^{-1} and a broad peak around q=28 nm^{-1}. However, there are also some subtle differences like a weak peak at q≈25 nm^{-1} only appreciated in the diffractogram from the nanoparticles (Figure 6.20, red curve). Labels were added to indicate the possible crystalline origin of the peaks that will be unraveled[31–34]. The main reflections observed in the diffractograms from the film sample and the nanoparticles correspond predominantly to α, γ or both phases[35]. Samples with almost pure content in α phase present two peaks between q=12 nm^{-1} and q=13 nm^{-1} associated with (100) and (020) reflections respectively[32]. The (020) reflection of γ phase is also located in this region (q=13.1 nm^{-1})[32]. The maximum of intensity in both diffractograms occurs around q≈14.1 nm^{-1}, which is near the α (110) reflection (q=14.17 nm^{-1})[31]. However, as it was indicated in the inset of

Figure 6.20, additionally this peak may have contributions from several reflections at higher q, like the (110/101) reflections of γ phase[31] at q=14.39 nm^{-1} or the (110/200) reflection from β phase[31] at q=14.6 nm^{-1}. The broad peak at q≈19 nm^{-1} is commonly found in PVDF samples with high α content, as it is associated with (021) reflection of this phase[31], however the (022) reflection from γ phase is located at q≈18.9 nm^{-1} [33]. The weak peak at q≈25 nm^{-1}, observed only in the nanoparticles diffractogram, is identified either as the (200) reflection of α phase[31] or (020) reflection from β phase[31,34].

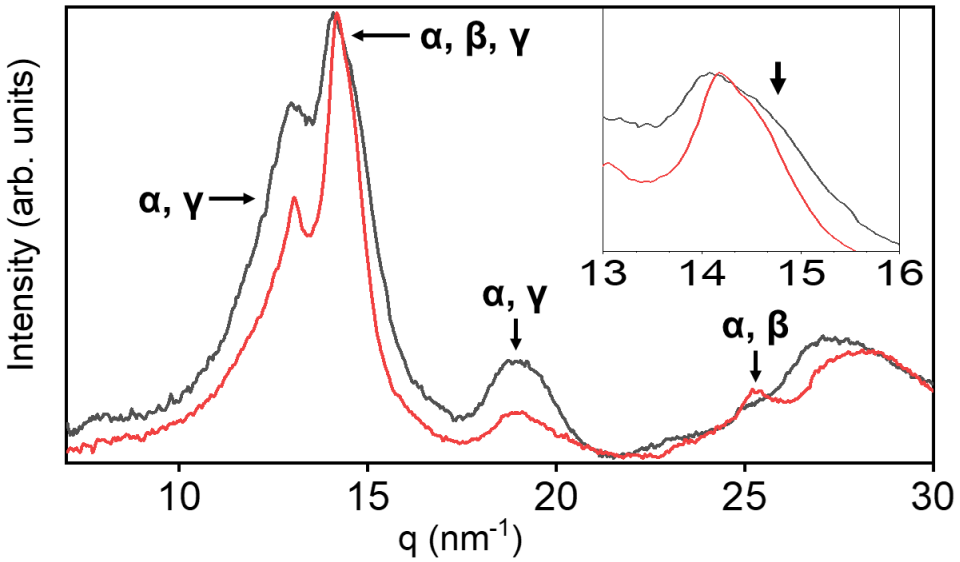

Figure 6.20 Intensity profiles from GIWAXS patterns of Figure 6.20: PVDF drop-casted (black curve) and PVDF nanoparticles (red curve). Both diffractograms are normalized by setting the intensity maximum of this q-range as 1 and the minimum as 0. The inset is a magnification of the zone of the most intense peak. The labels indicate the possible crystalline phases that would have a reflection in that particular position.

It is reasonable to think that the obtained diffractograms could include convoluted peaks from different crystalline phases that are hard to identify independently. As it was described in section 1.4.5, the most common crystalline phases found in PVDF are apolar α phase and polar β and γ phases[32]. The shape of the most intense peak indicates that is composed of more than one reflection (see inset of Figure 6.20) from different phases. In fact, the width of the most intense peak around q=14.6 nm^{-1} (marked with an arrow in the inset of Figure 6.20) could indicate the presence of the (110/200) reflection from β phase[31] at q=14.6 nm^{-1} in both diffractograms.

GIWAXS measurements as a function of temperature were performed to elucidate different behaviors from different crystalline phases from PVDF. Samples were heated from room temperature up to 200ºC. Figure 6.21 shows the diffractogram evolution in temperature of a PVDF film drop-casted from a DMA solution.

From 25ºC to 150ºC, the intensity of the peaks in the GIWAXS profile of a solution-casted PVDF film (Figure 6.21) systematically decreases and they shift to lower q (higher interplanar distances). From 150ºC to higher temperatures, all the crystalline peaks disappear due to melting. Since 162ºC, only one broad halo from amorphous melt is detected.

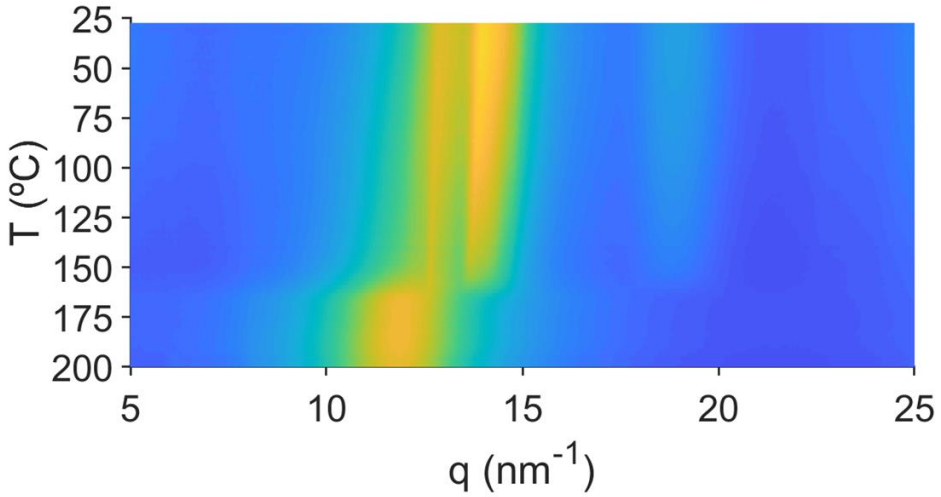

Figure 6.21 Two-dimensional map of the temperature-dependent GIWAXS of PVDF film drop-casted from solution. Intensities are in logarithmic scale.

However, the temperature evolution of PVDF nanoparticles diffractogram (Figure 6.22) is different from the one from drop-casted PVDF film (Figure 6.21).

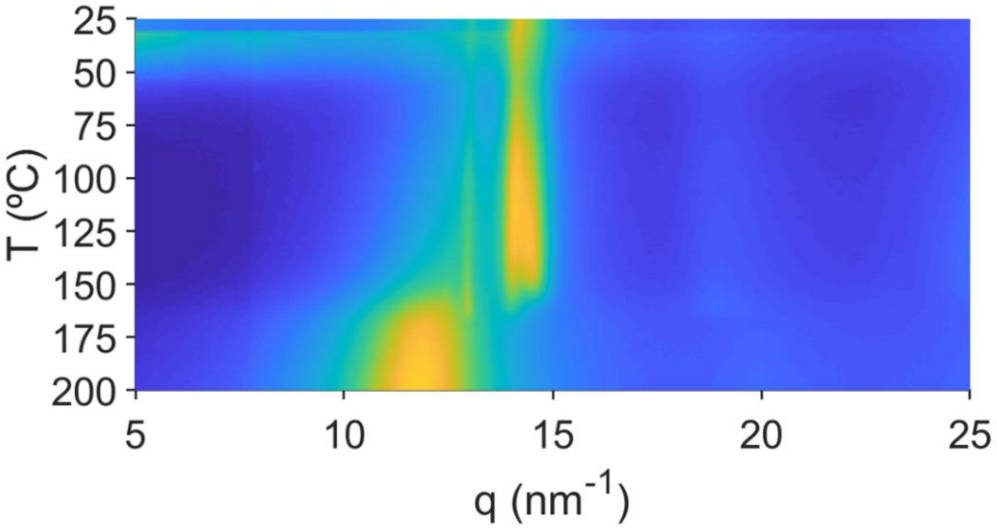

Figure 6.22 Two-dimensional map of the temperature-dependent WAXS of PVDF nanoparticles. Intensities are in logarithmic scale.

The GIWAXS profile of PVDF nanoparticles, from 30 to 100ºC is almost constant (Figure 6.22). However, around 130ºC, the most intense peak (q=14 nm^{-1}) splits into two separate peaks at

q=14.06 nm^{-1} and at q=14.43 nm^{-1}. At this temperature then, a total of three separated peaks are detected: at q=12.95 nm^{-1}, at q=14.06 nm^{-1} and q=14.43 nm^{-1}. The peak at q=12.95 nm^{-1} was located at room temperature at q=13.05 nm^{-1} and matches with the (020) reflection from α phase[31] and with the (020) reflection of γ phase[31]. The peak at q=14.06 nm^{-1} is detected at room temperature at q=14.17 nm^{-1} and matches with the (110) reflection from α phase[31] and with the (110)/(101) reflection of γ phase[31]. The peak at q=14.43 nm^{-1} was not resolved at room temperature and can be associated with the (110/200) reflection from β phase[31] but also with the previous mentioned (110)/(101) reflection of γ phase[31]. The evolution of these peaks with temperature is clearer in Figure 6.23.

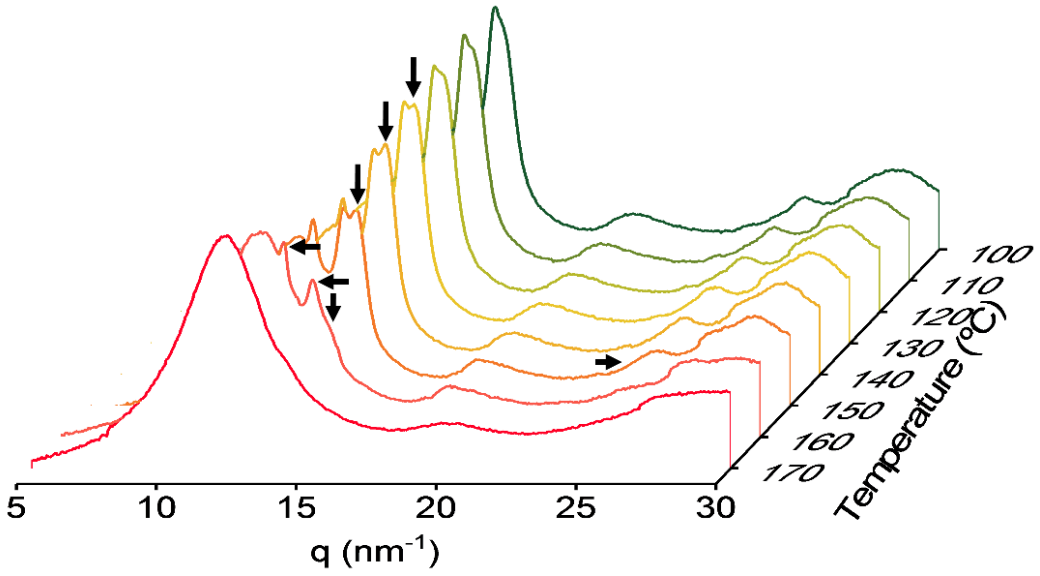

Figure 6.23 Temperature evolution of diffractograms of PVDF nanoparticles from T=100ºC until T=170ºC. Downward arrows highlight the split peak at q=14.43 nm^{-1}. Leftward arrows highlight the peaks at q=12.96 nm^{-1} and q=14 nm^{-1} at T=160ºC. Rightward arrow indicates the peak at q=25.2 nm^{-1}.

The mentioned features describing the intensity map on Figure 6.22 are observed easily in this figure: the splitting of the most intense peak (q=14 nm^{-1}) at 130ºC into two peaks at q=14.06 nm^{-1} and q=14.43 nm^{-1} (downward arrow), the vanishing at 160ºC (downward arrow) of the peak located at q=14.43 nm^{-1} and the disappearance also at 160ºC of the weak peak at q=25.2 nm^{-1} (rightward arrow), now unambiguously associated to the β phase. The simultaneous disappearance of both peaks allows to assign the peak located at q=14.43 nm^{-1} to the β phase[31] that is melt at T=160ºC, whereas the peaks that remain at this temperature (Figure 6.23, leftward arrows) correspond to other crystalline phase that melts later than 160ºC, specifically at T=168ºC.

The two peaks at q=12.95 nm^{-1} and q=14.06 nm^{-1} that were identified previously as α and/or γ phase, are present in the diffractogram from PVDF nanoparticles at T=165ºC whereas the diffractogram from PVDF film at 165ºC only shows the amorphous halo from the molten polymer

(Figure 6.24). The peaks marked with arrows indicate the presence of peaks at q=12.95 nm^{-1} and q=14.06 nm^{-1}, that at room temperature were localized at q=13.05 nm^{-1} and q=14.17 nm^{-1} respectively. It is reported that γ phase presents a higher melting temperature than α and β[32]. Therefore, this presence of these two peaks at high temperature in the nanoparticles diffractogram would indicate that they are reflections from the γ phase, specifically, the (020) reflection and the (110)/(101) reflections of γ phase, respectively[31]. Therefore, these results indicate the presence of the polar phases β and γ within PVDF nanoparticles.

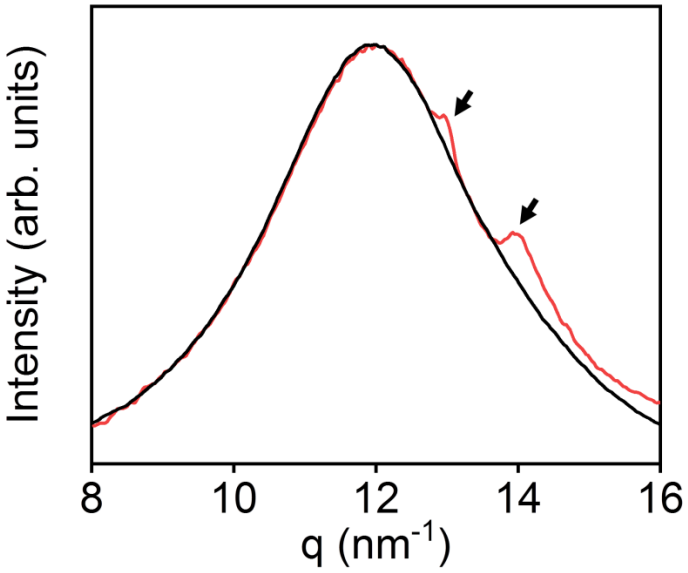

Figure 6.24 Intensity profiles from GIWAXS patterns taken at T=165 ºC of PVDF film (black curve) and PVDF nanoparticles (red curve). Both diffractograms are normalized by setting the maximum of this q-range as 1 and the minimum as 0. Arrows highlight the presence of peaks at q=12.96 nm^{-1} and q=14 nm^{-1} in the diffractogram from the nanoparticles.

The presence of polar phases (γ or β) in the nanoparticles sample can be explained in terms of interaction between PVDF chains and molecules of polar solvent used. PVDF was initially solved in DMA, which is a high polar solvent; the interaction between the NH_2 group in DMA molecules and the fluorine atoms in PVDF through hydrogen bonds has been reported to be precursor of the polar phases (β and γ) of the polymer[36,37]. This could be the origin of the polar phase in the nanoparticles, since PVDF is crystallized from a solution in polar solvent as the water molecules displaced the DMA molecules during dialysis procedure (see section 2.2.3.1).

DSC experiments were performed on PVDF film casted from solution and dried at 100ºC and on PVDF nanoparticles (Figure 6.25). Heating ramps of both PVDF systems show an endothermic peak around 160ºC, which is associated with the melting point of crystalline phases[38]. Subtle differences in DSC ramps are not enough to elucidate different crystalline phase because different crystalline sizes could yield higher melting temperature. However, it can be seen that both ramps

present multimodal shapes due to the presence of more than one crystalline phases. The melting point around 160ºC in both samples is coherent with the reported melting point of α and β phase[32], which in DSC are not distinguishable. The heating ramp from PVDF nanoparticles presents a shoulder at 170 ºC (marked with an arrow) not present in the heating ramp from PVDF film. This shoulder matches well with the evolution of nanoparticles diffractogram with temperature (Figure 6.24), where two Bragg peaks identified as reflections from γ phase disappear at 168ºC, whereas the diffractogram from PVDF film shows only an amorphous halo from 162ºC.

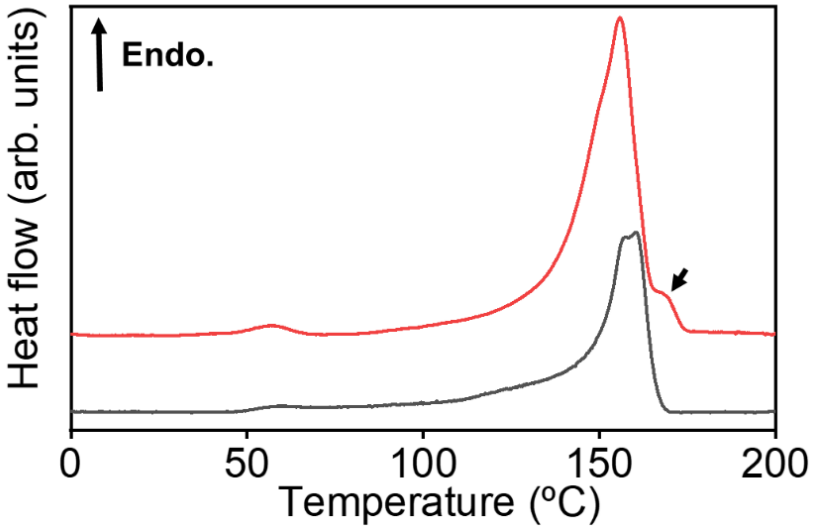

Figure 6.25 Differential Scanning Calorimetry (DSC) of PVDF film dried from DMA solution (black curve) and PVDF nanoparticles (red curve). Arrow highlights the shoulder present in the heating ramp from PVDF nanoparticles (red curve).

6.3 Fabrication of P(VDF-TrFE) nanoparticles with ferroelectric properties by flash precipitation

In section 1.4.5, random copolymer P(VDF-TrFE) was introduced as an interesting functional polymer as it presents spontaneous ferroelectric phase when it is deposited from solution. Therefore, the possibility of straightforward fabrication of thin films and other nanostructures with ferroelectric behavior has potential interest as functional material in several dielectric and ferroelectric devices as non-volatile memories[39,40] and piezoelectric sensors[41].

In this section, we fabricate nanoparticles of P(VDF-TrFE) by flash procedure (see section 2.2.3.3) and analyze its ferroelectric behavior by PFM. The P(VDF-TrFE) solutions employed to fabricate nanoparticles were prepared following the conditions included in Table 2.8.

6.3.1 AFM characterization of P(VDF-TrFE) nanoparticles

Nanoparticles of P(VDF-TrFE) were deposited by drop-casting over a silicon substrate and their size and shape were analyzed by AFM in tapping mode (Figure 6.26). It can be seen in Figure 6.26 that flash nanoparticles are not perfectly spherical with some irregular shapes. This could be associated with the semicrystalline nature of nanoparticles that will be confirmed by X-ray diffraction. The size distribution of nanoparticles measured by AFM is centered around 100 nm with a standard deviation around 30 nm. The histogram for the measured diameter of P(VDF-TrFE) nanoparticles is shown in Figure 6.27, and fitted using a lognormal distribution.

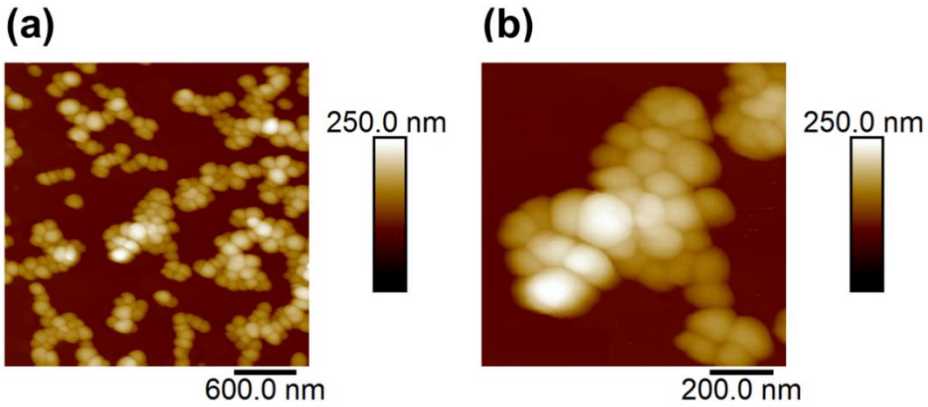

Figure 6.26 AFM topography images of P(VDF-TrFE) nanoparticles prepared by flash. **(b)** is a magnification of **(a)**.

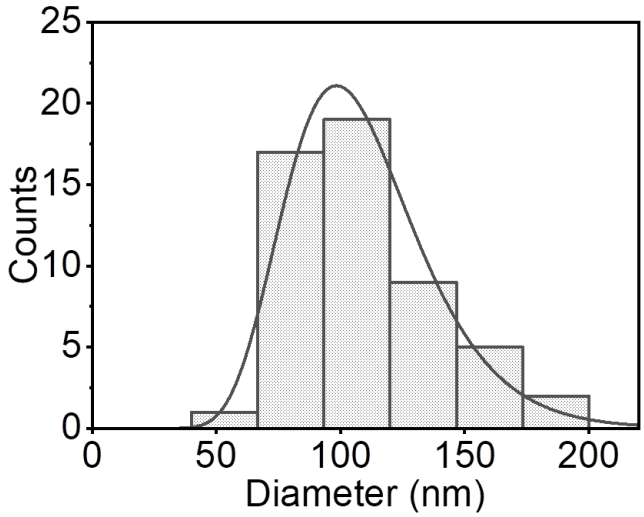

Figure 6.27 Histogram for the measured diameters of P(VDF-TrFE) nanoparticles prepared by flash. Histogram adjusted with a lognormal distribution. Total counts= 50.

6.3.2 Semicrystalline and ferroelectric characterization of P(VDF-TrFE) nanoparticles by means of GIWAXS and PFM

GIWAXS pattern of the P(VDF-TrFE) nanoparticles together with its corresponding integrated intensity profile are presented in Figure 6.28.

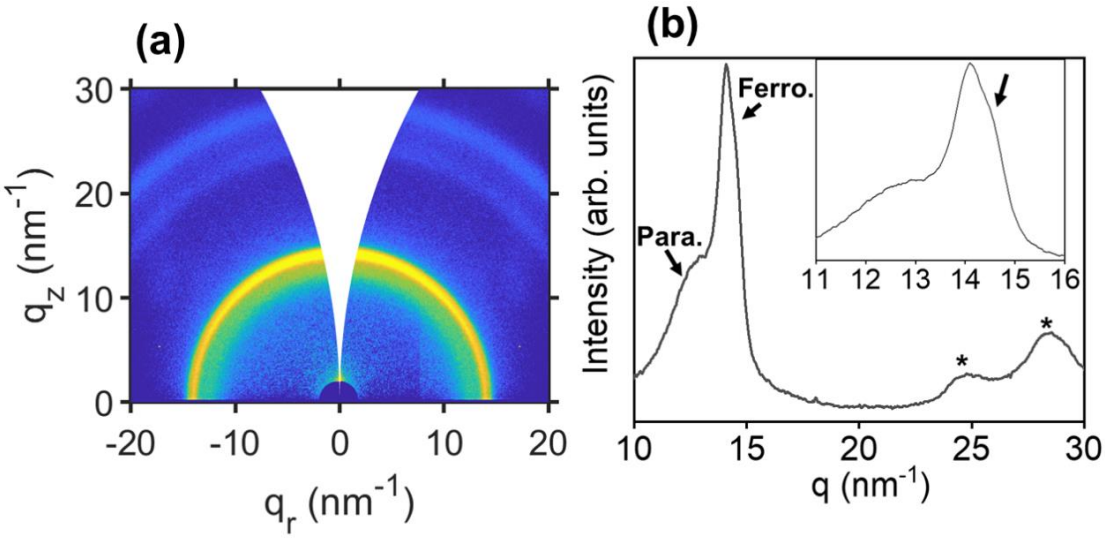

Figure 6.28 (a) GIWAXS pattern of P(VDF-TrFE) nanoparticles prepared by flash and deposited by drop-casting. **(b)** Diffractogram of P(VDF-TrFE) nanoparticles calculated by azimuthal integration of **(a)**. Most intense peaks associated with paraelectric and ferroelectric phase are labelled. Peaks marked with an * are associated to the ferroelectric phase. Inset in **(b)** is a magnification of the ferroelectric peak around q=14 nm^{-1}. The arrow in the inset indicates the presence of a shoulder in the peak associated with ferroelectric phase. Intensity in GIWAXS pattern is in logarithmic scale.

The semicrystalline nature of nanoparticles is revealed by the appearance of a narrow reflection at q≈14 nm^{-1} (Figure 6.28.a). This reflection shows a little orientation towards the out-of-plane direction (q_z) that could come from a certain degree of orientation of P(VDF-TrFE) nanoparticles induced by the substrate. By azimuthal integration of the GIWAXS pattern, the diffractogram is obtained (Figure 6.28.b). It shows four features associated with phases of P(VDF-TrFE): a broad peak centered at q=13.4 nm^{-1}, an intense Bragg peak at q=14.11 nm^{-1} and two peaks at q=24.7 nm^{-1} and at q=28.4 nm^{-1}, marked with *.

The broad peak at q=13.4 nm^{-1} matches with the superposition of (110/200) reflections from the paraelectric crystalline phase of P(VDF-TrFE), whereas the intense narrow peak at q=14.11 nm^{-1} contains the (110) and (200) reflections from the ferroelectric β phase[42]. This peak presents a bimodal shape (see inset in Figure 6.28.b), with the most intense peak at q=14.11 nm^{-1} and a shoulder at q=14.5 nm^{-1} (downward arrow in the inset of Figure 6.28.b). On the other hand, peaks

marked with * are also reported to be reflections due to the crystalline ferroelectric phase[42]. These results are in line with reported diffractograms from other P(VDF-TrFE) nanostructures[43,44].

To corroborate the ferroelectric nature, PFM measurements were performed on nanoparticles. When characterizing nanoparticles by contact methods, a classic problem is the sweeping effect of the probe. To avoid this issue, we fabricate a polymer-polymer composite where the polymer nanoparticles are embedded within a polymer matrix. We use PEDOT:PSS as matrix since it is an aqueous colloid (see section 1.4.4). The polymer-polymer composite was prepared by mixing the PEDOT:PSS dispersion with the P(VDF-TrFE) nanoparticles aqueous dispersion with a volume relation 1:1. The mixture was spin-coated onto a silicon substrate using the same conditions than for pristine PEDOT:PSS, included in Table 2.10. PFM images of the PEDOT:PSS/P(VDF-TrFE) nanoparticles sample are shown in Figure 6.29.

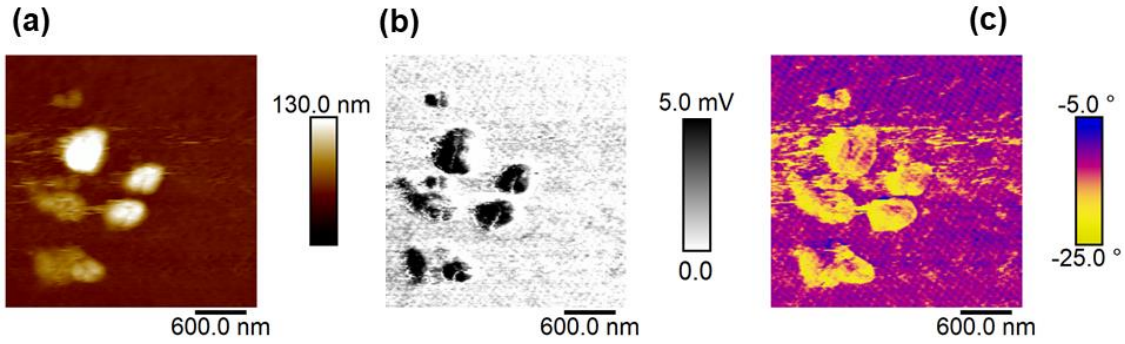

Figure 6.29 (a) Topography image in contact mode of PEDOT:PSS/(P(VDF-TrFE) nanoparticles, **(b)** piezoelectric amplitude in the out-of-plane direction, **(c)** piezoelectric phase in the out-of-plane direction.

The topography image (Figure 6.29.a) shows a continuous phase with some protuberances. Looking at Figure 6.29.b, the continuous phase does not show any piezoelectric amplitude, whereas the protuberances exhibit piezoelectric amplitude in the vertical direction demonstrating its ferroelectric nature. Therefore, the protuberances are likely to be aggregates of nanoparticles embedded in the continuous phase, that is formed by PEDOT:PSS without P(VDF-TrFE) remains. Changes in colors on the phase image (Figure 6.29.c) suggest that the nanoparticles present random orientations along the vertical direction. Loops of DC voltage were applied on the PEDOT:PSS domain (Figure 6.30.a) and on the embedded nanoparticle (Figure 6.30.b). It can be seen that the PEDOT:PSS conducting region does not show ferroelectric behavior whereas the embedded P(VDF-TrFE) nanoparticles can be measured and show a characteristic ferroelectric loop.

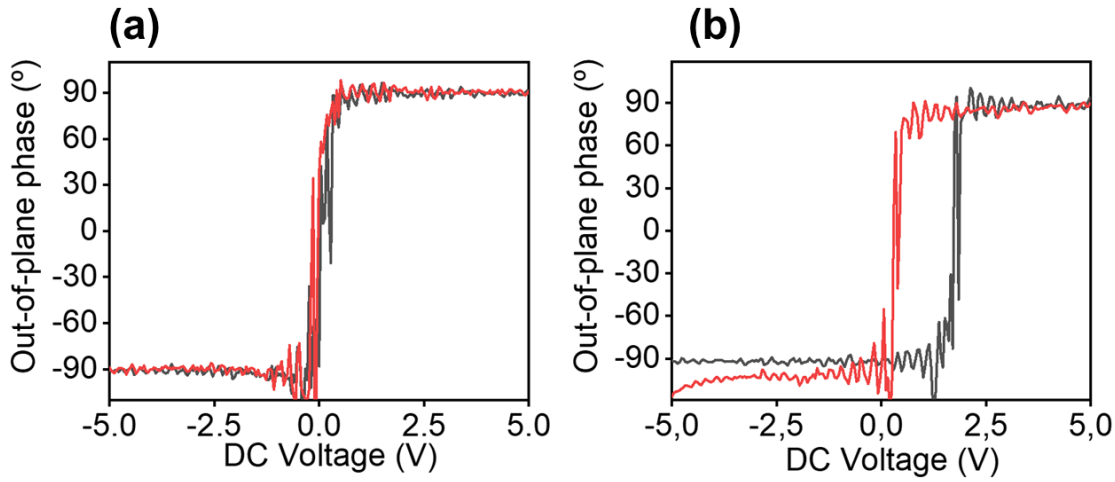

Figure 6.30 Piezoelectric phase in the out-of-plane direction measured applying a DC bias= -5V → 5V → -5V over **(a)** a flat zone associated with PEDOT:PSS film and over **(b)** one of the protuberances shown in Figure 6.29, associated with P(VDF-TrFE) nanoparticles embedded in the film.

6.4 Conclusions

In this chapter, nanoparticles of different functional polymers have been fabricated by several methods, based on solvent exchanging from the polymer solution in a good organic solvent to an aqueous colloid system formed by globules of ≈100 nm diameter. These polymers have been analyzed firstly by AFM and then by different characterization methods based on each respective functionality: conductivity or ferroelectricity. Conclusions for each system are the following:

- In the first section, P3HT nanoparticles have been prepared by two methods: miniemulsion and flash nanoprecipitation. The sizes are in the range of 50-100 nm and miniemulsion method produced smaller nanoparticles with the conditions used. Absorption and emission spectra indicate longer conjugation lengths for miniemulsion nanoparticles. X-ray and calorimetry experiments reveal synergy between P3HT and the surfactant used in miniemulsion (SDS) that indicates the existence of a blended phase of P3HT with SDS molecules probably located at the surface of nanoparticles. P3HT and SDS seem to interact through their respective apolar chains, and could be the responsible for the detected P3HT backbone planarization and the displacement of the melting point to higher temperatures in the case of nanoparticles prepared by miniemulsion. In addition, P3HT within miniemulsion nanoparticles exhibits a restriction on crystallite growth as the temperature rises compared with flash nanoparticles. This effect could be due to the proposed blended crystalline phase of P3HT with SDS.

- In the second section, nanoparticles of PVDF were prepared by dialysis procedure. X-ray diffraction experiments reveal the presence of polar phases β and γ within PVDF nanoparticles. It is suggested that the presence of polar phase within PVDF nanoparticles can be induced by the interaction between the polar solvent (DMA) and the fluorine atoms of PVDF.

- In the third section, P(VDF-TrFE) nanoparticles have been successfully prepared by flash method. These nanoparticles present a high content in ferroelectric phase, as demonstrated by X-ray diffraction. Piezoelectric effect has been proven by PFM in contact mode over nanoparticles previously embedded on a PEDOT:PSS thin film as a supporting matrix.

6.5 References

(1) Satapathi, S.; Gill, H. S.; Li, L.; Samuelson, L.; Kumar, J.; Mosurkal, R. Synthesis of Nanoparticles of P3HT and PCBM for Optimizing Morphology in Polymeric Solar Cells. *Appl. Surf. Sci.* **2014**, *323*, 13–18. https://doi.org/10.1016/j.apsusc.2014.07.175.

(2) Colberts, F. J. M.; Wienk, M. M.; Janssen, R. A. J. Aqueous Nanoparticle Polymer Solar Cells: Effects of Surfactant Concentration and Processing on Device Performance. *ACS Appl. Mater. Interfaces* **2017**, *9* (15), 13380–13389. https://doi.org/10.1021/acsami.7b00557.

(3) Holmes, N. P.; Marks, M.; Cave, J. M.; Feron, K.; Barr, M. G.; Fahy, A.; Sharma, A.; Pan, X.; Kilcoyne, D. A. L.; Zhou, X.; et al. Engineering Two-Phase and Three-Phase Microstructures from Water-Based Dispersions of Nanoparticles for Eco-Friendly Polymer Solar Cell Applications. *Chem. Mater.* **2018**, *30* (18), 6521–6531. https://doi.org/10.1021/acs.chemmater.8b03222.

(4) Keum, J. K.; Xiao, K.; Ivanov, I. N.; Hong, K.; Browning, J. F.; Smith, G. S.; Shao, M.; Littrell, K. C.; Rondinone, A. J.; Andrew Payzant, E.; et al. Solvent Quality-Induced Nucleation and Growth of Parallelepiped Nanorods in Dilute Poly(3-Hexylthiophene) (P3HT) Solution and the Impact on the Crystalline Morphology of Solution-Cast Thin Film. *CrystEngComm* **2013**, *15* (6), 1114–1124. https://doi.org/10.1039/c2ce26666k.

(5) Magnani, L.; Rumbles, G.; Samuel, I. D. W.; Murray, K.; Moratti, S. C.; Holmes, A. B.; Friend, R. H. Photoluminescence Studies of Chain Interactions in Electroluminescent Polymers. *Synth. Met.* **1997**, *84* (1–3), 899–900. https://doi.org/10.1016/s0379-6779(96)04202-6.

(6) Nagarjuna, G.; Baghgar, M.; Labastide, J. A.; Algaier, D. D.; Barnes, M. D.; Venkataraman, D. Tuning Aggregation of Poly(3-Hexylthiophene) within Nanoparticles. *ACS Nano* **2012**, *6* (12), 10750–10758. https://doi.org/10.1021/nn305207b.

(7) Rahimi, K.; Botiz, I.; Agumba, J. O.; Motamen, S.; Stingelin, N.; Reiter, G. Light Absorption of Poly(3-Hexylthiophene) Single Crystals. *RSC Adv.* **2014**, *4* (22), 11121–11123. https://doi.org/10.1039/c3ra47064d.

(8) Yamagata, H.; Spano, F. C. Interplay between Intrachain and Interchain Interactions in Semiconducting Polymer Assemblies: The HJ-Aggregate Model. *J. Chem. Phys.* **2012**, *136* (18), 184901. https://doi.org/10.1063/1.4705272.

(9) Spano, F. C.; Silva, C. H- and J-Aggregate Behavior in Polymeric Semiconductors. *Annu. Rev. Phys. Chem.* **2014**, *65* (1), 477–500. https://doi.org/10.1146/annurev-physchem-040513-103639.

(10) Schwarz, K. N.; Farley, S. B.; Smith, T. A.; Ghiggino, K. P. Charge Generation and Morphology in P3HT : PCBM Nanoparticles Prepared by Mini-Emulsion and Reprecipitation Methods. *Nanoscale* **2015**, *7* (47), 19899–19904. https://doi.org/10.1039/C5NR06244F.

(11) Dyson, M. J.; Lariou, E.; Martin, J.; Li, R.; Erothu, H.; Wantz, G.; Topham, P. D.; Dautel, O. J.; Hayes, S. C.; Stavrinou, P. N.; et al. Managing Local Order in Conjugated Polymer Blends via Polarity Contrast. *Chem. Mater.* **2019**. https://doi.org/10.1021/acs.chemmater.8b05259.

(12) Korovyanko, O. J.; Österbacka, R.; Jiang, X. M.; Vardeny, Z. V.; Janssen, R. A. J. Photoexcitation Dynamics in Regioregular and Regiorandom Polythiophene Films. *Phys. Rev. B* **2001**, *64* (23), 1–6. https://doi.org/10.1103/physrevb.64.235122.

(13) Santra, K.; Bobbitt, J. M.; Smith, E. A.; Bhattacharjee, U.; Petrich, J. W.; Chaudhary, S.; Elshobaki, M. Characterizing Electric Field Exposed P3HT Thin Films Using Polarized-Light Spectroscopies. *Macromol. Chem. Phys.* **2016**, *217* (16), 1801–1809. https://doi.org/10.1002/macp.201600113.

(14) Clark, J.; Silva, C.; Friend, R. H.; Spano, F. C. Role of Intermolecular Coupling in the Photophysics of Disordered Organic Semiconductors: Aggregate Emission in Regioregular Polythiophene. *Phys. Rev. Lett.* **2007**, *98* (20), 1–4. https://doi.org/10.1103/PhysRevLett.98.206406.

(15) Brinkmann, M.; Rannou, P. Molecular Weight Dependence of Chain Packing and Semicrystalline Structure in Oriented Films of Regioregular Poly(3-Hexylthiophene)Revealed by High-Resolution Transmission Electron Microscopy. *Macromolecules* **2009**, *42* (4), 1125–1130. https://doi.org/10.1021/ma8023415.

(16) Millstone, J. E.; Kavulak, D. F. J.; Woo, C. H.; Holcombe, T. W.; Westling, E. J.; Briseno, A. L.; Toney, M. F.; Fréchet, J. M. J. Synthesis, Properties, and Electronic Applications of Size-Controlled Poly(3-Hexylthiophene) Nanoparticles. *Langmuir* **2010**, *26* (16), 13056–13061. https://doi.org/10.1021/la1022938.

(17) Coiro, V. M.; Mazza, F.; Pochetti, G. Crystal Phases Obtained from Aqueous Solutions of Sodium Dodecyl Sulfate. The Structure of a Monoclinic Phase of Sodium Dodecyl Sulfate Hemihydrate. *Acta Crystallogr. Sect. C Cryst. Struct. Commun.* **1986**, *42* (8), 991–995. https://doi.org/10.1107/s0108270186093757.

(18) Summerton, E.; Hollamby, M. J.; Zimbitas, G.; Snow, T.; Smith, A. J.; Sommertune, J.; Bettiol, J.; Jones, C.; Britton, M. M.; Bakalis, S. The Impact of N,N-Dimethyldodecylamine N-Oxide (DDAO) Concentration on the Crystallisation of Sodium Dodecyl Sulfate (SDS) Systems and the Resulting Changes to Crystal Structure, Shape and the Kinetics of Crystal Growth. *J. Colloid Interface Sci.* **2018**, *527*, 260–266. https://doi.org/10.1016/j.jcis.2018.05.058.

(19) Smith, L. A.; Hammond, R. B.; Roberts, K. J.; Machin, D.; McLeod, G. Determination of the Crystal Structure of Anhydrous Sodium Dodecyl Sulphate Using a Combination of Synchrotron Radiation Powder Diffraction and Molecular Modelling Techniques. *J. Mol. Struct.* **2000**, *554* (2–3), 173–182. https://doi.org/10.1016/S0022-2860(00)00666-9.

(20) Smith, L. A.; Duncan, A.; Thomson, G. B.; Roberts, K. J.; Machin, D.; McLeod, G. Crystallisation of Sodium Dodecyl Sulphate from Aqueous Solution: Phase Identification, Crystal Morphology, Surface Chemistry and Kinetic Interface Roughening. *J. Cryst. Growth* **2004**, *263* (1–4), 480–490. https://doi.org/10.1016/j.jcrysgro.2003.11.025.

(21) Bag, M.; Gehan, T. S.; Algaier, D. D.; Liu, F.; Nagarjuna, G.; Lahti, P. M.; Russell, T. P.; Venkataraman, D. Efficient Charge Transport in Assemblies of Surfactant-Stabilized Semiconducting Nanoparticles. *Adv. Mater.* **2013**, *25* (44), 6411–6415. https://doi.org/10.1002/adma.201301302.

(22) Wu, Z.; Petzold, A.; Henze, T.; Thurn-Albrecht, T.; Lohwasser, R. H.; Sommer, M.; Thelakkat, M. Temperature and Molecular Weight Dependent Hierarchical Equilibrium Structures in Semiconducting Poly(3-Hexylthiophene). *Macromolecules* **2010**, *43* (10), 4646–4653. https://doi.org/10.1021/ma902566h.

(23) Martín, J.; Campoy-Quiles, M.; Nogales, A.; Garriga, M.; Alonso, M. I.; Goñi, A. R.; Martín-González, M. Poly(3-Hexylthiophene) Nanowires in Porous Alumina: Internal Structure under Confinement. *Soft Matter* **2014**, *10* (18), 3335. https://doi.org/10.1039/c3sm52378k.

(24) Kékicheff, P.; Grabielle-Madelmont, C.; Ollivon, M. Phase Diagram of Sodium Dodecyl Sulfate-Water System. 1. A Calorimetric Study. *J. Colloid Interface Sci.* **1989**, *131* (1), 112–132. https://doi.org/10.1016/0021-9797(89)90151-3.

(25) Wang, W.; Lu, H.; Liu, Y.; Leng, J. Sodium Dodecyl Sulfate/Epoxy Composite: Water-Induced Shape Memory Effect and Its Mechanism. *J. Mater. Chem. A* **2014**, *2* (15), 5441. https://doi.org/10.1039/c3ta15204a.

(26) Thurn-Albrecht, T.; Thomann, R.; Heinzel, T.; Hugger, S. Semicrystalline Morphology in Thin Films of Poly(3-Hexylthiophene). *Colloid Polym. Sci.* **2004**, *282* (8), 932–938. https://doi.org/10.1007/s00396-004-1100-9.

(27) Prosa, T. J.; Winokur, M. J.; Moulton, J.; Smith, P.; Heeger, A. J. X-Ray Structural Studies of Poly(3-Alkylthiophenes): An Example of an Inverse Comb. *Macromolecules* **1992**, *25* (17), 4364–4372. https://doi.org/10.1021/ma00043a019.

(28) Yuan, Y.; Shu, J.; Liu, P.; Zhang, Y.; Duan, Y.; Zhang, J. Study on π-π Interaction in H- and J-Aggregates of Poly(3-Hexylthiophene) Nanowires by Multiple Techniques. *J. Phys. Chem. B* **2015**, *119* (26), 8446–8456. https://doi.org/10.1021/acs.jpcb.5b02805.

(29) Cullity, B. D.; Stock, S. R. *Elements of X-Ray Diffraction*; Pearson Education, 2014.

(30) Tan, B.; Li, Y.; Palacios, M. F.; Therrien, J.; Sobkowicz, M. J. Effect of Surfactant Conjugation on Structure and Properties of Poly(3-Hexylthiophene) Colloids and Field Effect Transistors. *Colloids Surfaces A Physicochem. Eng. Asp.* **2016**, *488*, 7–14. https://doi.org/10.1016/j.colsurfa.2015.10.002.

(31) Cai, X. M.; Lei, T. P.; Sun, D. H.; Lin, L. W. A Critical Analysis of the Alpha, Beta and Gamma Phases in Poly(Vinylidene Fluoride) Using FTIR. *Rsc Adv.* **2017**, *7* (25), 15382–15389. https://doi.org/10.1039/c7ra01267e.

(32) Martins, P.; Lopes, A. C.; Lanceros-Mendez, S. Electroactive Phases of Poly(Vinylidene Fluoride): Determination, Processing and Applications. *Prog. Polym. Sci.* **2014**, *39* (4), 683–706. https://doi.org/10.1016/j.progpolymsci.2013.07.006.

(33) DM, E.; BJ, L. Phase Transformation to Beta-Poly(Vinylidenefluoride) by Milling. *J. Polym. Sci. Part B* **2003**, 91–97. https://doi.org/10.1002/polb.10613.

(34) Lei, T.; Cai, X.; Wang, X.; Yu, L.; Hu, X.; Zheng, G.; Lv, W.; Wang, L.; Wu, D.; Sun, D.; et al. Spectroscopic Evidence for a High Fraction of Ferroelectric Phase Induced in Electrospun Polyvinylidene Fluoride Fibers. *RSC Adv.* **2013**, *3* (47), 24952–24958. https://doi.org/10.1039/c3ra42622j.

(35) Gregorio, R. Determination of the α, β, and γ Crystalline Phases of Poly(Vinylidene Fluoride) Films Prepared at Different Conditions. *J. Appl. Polym. Sci.* **2006**, *100* (4), 3272–3279. https://doi.org/10.1002/app.23137.

(36) Salimi, A.; Yousefi, A. A. Conformational Changes and Phase Transformation Mechanisms in PVDF Solution-Cast Films. *J. Polym. Sci. Part B Polym. Phys.* **2004**, *42* (18), 3487–3495. https://doi.org/10.1002/polb.20223.

(37) Horibe, H.; Sasaki, Y.; Oshiro, H.; Hosokawa, Y.; Kono, A.; Takahashi, S.; Nishiyama, T. Quantification of the Solvent Evaporation Rate during the Production of Three PVDF Crystalline Structure Types by Solvent Casting. *Polym. J.* **2014**, *46* (2), 104–110. https://doi.org/10.1038/pj.2013.75.

(38) Merlini, C.; Barra, G. M. O.; Medeiros Araujo, T.; Pegoretti, A. Electrically Pressure Sensitive Poly(Vinylidene Fluoride)/Polypyrrole Electrospun Mats. *RSC Adv.* **2014**, *4* (30), 15749–15758. https://doi.org/10.1039/c4ra01058b.

(39) Kang, S. J.; Bae, I.; Shin, Y. J.; Park, Y. J.; Huh, J.; Park, S. M.; Kim, H. C.; Park, C. Nonvolatile Polymer Memory with Nanoconfinement of Ferroelectric Crystals. *Nano Lett.* **2011**, *11* (1), 138–144. https://doi.org/10.1021/nl103094e.

(40) Hu, Z.; Tian, M.; Nysten, B.; Jonas, A. M. Regular Arrays of Highly Ordered Ferroelectric Polymer Nanostructures for Non-Volatile Low-Voltage Memories. *Nat. Mater.* **2009**, *8* (1), 62–67. https://doi.org/10.1038/nmat2339.

(41) Hong, C. C.; Huang, S. Y.; Shieh, J.; Chen, S. H. Enhanced Piezoelectricity of Nanoimprinted Sub-20 Nm Poly(Vinylidene Fluoride-Trifluoroethylene) Copolymer Nanograss. *Macromolecules* **2012**, *45* (3), 1580–1586. https://doi.org/10.1021/ma202481t.

(42) Bellet-Amalric, E.; Legrand, J. F. Crystalline Structures and Phase Transition of the Ferroelectric P(VDF-TrFE) Copolymers, a Neutron Diffraction Study. *Eur. Phys. J. B* **1998**, *3* (2), 225–236. https://doi.org/10.1007/s100510050307.

(43) Martínez-Tong, D. E.; Soccio, M.; Sanz, A.; García, C.; Ezquerra, T. A.; Nogales, A. Ferroelectricity and Molecular Dynamics of Poly(Vinylidenefluoride-Trifluoroethylene) Nanoparticles. *Polymer (Guildf).* **2015**, *56*, 428–434. https://doi.org/10.1016/j.polymer.2014.11.040.

(44) García-Gutiérrez, M. C.; Linares, A.; Martín-Fabiani, I.; Hernández, J. J.; Soccio, M.; Rueda, D. R.; Ezquerra, T. A.; Reynolds, M. Understanding Crystallization Features of P(VDF-TrFE) Copolymers under Confinement to Optimize Ferroelectricity in Nanostructures. *Nanoscale* **2013**, *5* (13), 6006–6012. https://doi.org/10.1039/c3nr00516j.

Chapter 7. Conclusions

In this Thesis several soft, functional materials including polymers and one fullerene derivative have been used to fabricate nanostructured systems that could be used as active materials in organic electronic devices as organic solar cells (OSCs), organic field-effect transistors (OFETs), non-volatile organic memories and mechanical transductors. In particular, this Thesis is focused to study two functional properties, electrical conductivity and ferroelectricity, and the formation of nanostructures in three different geometries: thin films with thicknesses below 100 nm, surface nanogratings with periods around 250 and 500 nm, and nanoparticles with diameters from 50 to 600 nm.

The main conclusions of this Thesis are listed below:

- Semiconducting and ferroelectric thin films of P3HT/P(VDF-TrFE) were studied as synergetic bilayered systems of potential interest for the fabrication of OFETs and non-volatile organic memories. It was shown that the thickness of the semiconducting P3HT bottom layer has a strong impact on the polarization switching of the ferroelectric P(VDF-TrFE) upper layer through the crystallinity and orientation of P3HT chains confined in thin film geometry.

- The structural and morphological changes of dispersions of PEDOT:PSS with high boiling point additives can be explained as a two-step mechanism depending on the additive concentration. At low concentrations, a compaction of PEDOT:PSS grains and thinning of their shells is observed. In a second stage, at larger concentrations, the additive acts as an intermediate layer between PEDOT-core and PSS-shell producing a swelling of the grains and also a phase segregation induced by the screening effect of the additive between PEDOT and PSS segments. Additionally, an increase of film thickness and roughness with increasing additive concentration is observed for all the additives investigated.

- PEDOT:PSS thin films were fabricated using inkjet printing deposition, which is a method of interest for manufacturing industry due to the possibility of fabricating extended thin layers with tunable shapes. Large areas with a broad range of thicknesses of PEDOT:PSS on ITO were obtained with both homogeneous electrical and mechanical properties as determined by local probe methods, i.e. PeakForce QNM and C-AFM. These results provide support for the use of inkjet methods for the extensive area

processing of PEDOT:PSS in the form of thin films with adequate electrical conductivity and mechanical stability.

- Nanogratings have been fabricated on PEDOT:PSS since they are promising systems for buffer layers in OSCs. Laser Induced Periodic Surface Structures (LIPSS) have been formed on thin films of PEDOT:PSS by irradiation at 266 nm, since the material absorbs at this wavelength, and surface gratings parallel to the laser polarization vector, with a period of $\Lambda \approx$200-300 nm and height of around 10-50 nm were obtained. LIPSS were fabricated on PEDOT:PSS deposited both on silicon wafers and on indium-tin oxide (ITO) substrates, aiming at future applications of this nanostructured material on OSCs. ITO substrate shows to induce deeper and more ordered ripples in a wider range of number of pulses than silicon substrate while GIWAXS measurements show the appearance of a crystalline phase in nanostructured PEDOT:PSS deposited on silicon. Raman spectroscopy analysis does not show signs of chemical modification after laser irradiation although a transition from benzoid to quinoid structure in PEDOT molecules is observed. C-AFM measurements of LIPSS on ITO show conducting nanogratings with a partial segregation of the conducting domains to the valleys of the ripples.

- LIPSS have also been fabricated on the conjugated polymers P3HT and PCDTBT and the modification of chain orientations on the material surface was investigated by TEY-NEXAFS. It was observed that after laser irradiation of the films, the chains lose the initial preferential orientation, although the modification of chain orientation by laser irradiation can be reduced by irradiating under vacuum conditions. The ambient conditions during irradiation have also impact on the LIPSS formation and on their electrical properties. TEY-NEXAFS has been shown to be a useful technique to study the chain modifications induced by laser irradiation since it is a surface sensitive technique. Therefore, this technique provides a valuable complementary information to that of GIWAXS technique for the investigation of nanostructured material surfaces.

- Changing the polarization of the laser is an effective and straightforward method to create complex patterns on functional material surfaces. Generation of complex surfaces has been investigated on P3HT surfaces by sequential irradiation changing the number of pulses and the angle of polarization of the laser, showing that the last irradiation step modifies the geometry of already formed nanostructures within a shorter irradiation time, i.e. lower number of pulses, in comparison to the first irradiation step. The control of this procedure could be used on bilayered P3HT/P(VDF-TrFE) systems to fabricate an array of ferroelectric dots that can be of interest on non-volatile memory devices.

- LIPSS have been formed on the fullerene derivative $PC_{71}BM$ by irradiation at 532 nm and 266 nm. At both wavelengths, laser irradiation reduces the solubility of $PC_{71}BM$. After solution washing of the samples irradiated at λ=266nm, LIPSS are maintained whereas solution-developed samples irradiated at 532 nm maintain the grating structures with lower height and a granular texture that shows enhanced electrical current. This is explained considering that during laser irradiation the sample suffers a heat treatment leading to the development of a buried phase, close to the substrate, formed by larger crystals with enhanced electrical conductivity. Further solvent treatment reveals the buried phase which remains in the form of partially electrically conducting nanowires. Generation of conducting resist-free fullerene nanowires could be of interest on fabrication of organic electronic devices.

- Nanogratings of PEDOT:PSS were also fabricated by Nanoimprint Lithography (NIL). The addition of glycerol to the pristine material, as a plasticizer, was used for grating formation. The aspect ratio and the order of the gratings depend on the glycerol concentration, achieving the highest values of both aspect ratio and order at the lowest glycerol concentrations that was able to generate gratings. Raman spectroscopy shows an enhancement of the quinoid structure in PEDOT chains that is likely to be induced by the glycerol additive and also enhanced by the consequent thermal treatment during nanoimprinting. GIWAXS measurements reveal new reflections related to a reported high conductivity phase of PEDOT and other reflections that could be associated with crystallization of PSS.

- Nanoparticles of P3HT with diameters between 30-150 nm were prepared by surfactant-aided miniemulsion and flash techniques, showing quantitative structural differences between both methods. Optical results concluded that P3HT chains within nanoparticles prepared by miniemulsion have more extended conjugated chains than nanoparticles prepared by flash. This lower level of torsional disorder is suggested to be associated with the interaction of the surfactant (SDS) with the lateral chains of P3HT, which would reduce the steric hindrance between them, favoring longer conjugation lengths over the backbone. Nanoparticles prepared by flash, on the other side, show optical properties similar as bulk P3HT. As the temperature rises, inner structure of the nanoparticles prepared by both methods evolve quite differently; while flash nanoparticles show a similar behavior to that of the bulk, miniemulsion nanoparticles reveal properties that have been associated with a blended crystalline phase of P3HT and SDS. These result highlight the interaction between insulating additives and semiconducting polymers.

Nanoparticles of conjugated polymers are seen as potential candidates for electronic-donor components in OSCs, since nanoparticles allow a better control of the nanometric domains between donor and acceptor components in bulk heterojunction geometries.

- Nanoparticles of ferroelectric polymers have also been fabricated. In particular, nanoparticles of PVDF with diameters between 50-600 nm were prepared by dialysis approach and GIWAXS revealed the presence of the crystalline polar phases β and γ. It is suggested that the generation of polar phases is induced by the interaction through hydrogen bonds between the polar solvent of the initial PVDF solution and the fluorine atoms of PVDF chains. Additionally, nanoparticles of P(VDF-TrFE) with diameters between 50-200 nm were prepared by flash approach. These nanoparticles showed ferroelectric phase as revealed by GIWAXS and PFM characterization over nanoparticles embedded in a PEDOT:PSS matrix. Fabrication of nanoparticles of ferroelectric polymers with crystalline domains and ferroelectric behavior is a straightforward approach and these functional nanoparticles could be used in miniaturized ferroelectric devices as non-volatile memories or mechanical transductors.

List of scientific publications

(1) Gutiérrez-Fernández, E.; Rodríguez-Rodríguez, Á.; García-Gutiérrez, M.-C.; Nogales, A.; Ezquerra, T. A.; Rebollar, E. Functional Nanostructured Surfaces Induced by Laser on Fullerene Thin Films. *Appl. Surf. Sci.* **2019**, *476* (January), 668–675. https://doi.org/10.1016/j.apsusc.2019.01.141.

(2) Gutiérrez-Fernández, E.; Gabaldón-Saucedo, I. A.; García-Gutiérrez, M. C.; Varea, A.; Nogales, A.; Rebollar, E.; Vilà, A.; Ezquerra, T. A.; Cirera, A. Quantitative Assessment by Local Probe Methods of the Mechanical and Electrical Properties of Inkjet-Printed PEDOT:PSS Thin Films over Indium Tin Oxide Substrates. *Org. Electron. physics, Mater. Appl.* **2019**, *70*. https://doi.org/10.1016/j.orgel.2019.04.020.

(3) Rodríguez-Rodríguez, Á.; Gutiérrez-Fernández, E.; García-Gutiérrez, M.-C.; Nogales, A.; Ezquerra, T. A.; Rebollar, E. Synergistic Effect of Fullerenes on the Laser-Induced Periodic Surface Structuring of Poly(3-Hexyl Thiophene). *Polymers (Basel).* **2019**, *11* (2), 190. https://doi.org/10.3390/polym11020190.

(4) Hernández, J. J.; Puente-Orench, I.; Ezquerra, T. A.; Gutiérrez-Fernández, E.; García-Gutiérrez, M.-C. Confinement Effects in One-Dimensional Nanoarrays of Polymer Semiconductors and Their Photovoltaic Blends. *Polymer (Guildf).* **2019**, *163* (December 2018), 13–19. https://doi.org/10.1016/j.polymer.2018.12.036.

(5) Gutiérrez-Fernández, E.; Rebollar, E.; Cui. J.; Ezquerra, T.A.; Nogales, A. Morphology and ferroelectric properties of semiconducting/ferroelectric polymer bilayers. *Macromolecules*.

In revision

(6) Guidotti, G.; Soccio, M.; García-Gutiérrez, M.C.; Gutiérrez-Fernández, E.; Ezquerra, T.A.; Siracusa, V.; Munari, A.; Lotti, N. Evidence of a 2D-ordered structure in biobased poly(pentamethylene furanoate) responsible for its outstanding barrier and mechanical properties. *ACS Sustainable Chemistry & Engineering*.

In revision

(7) Nogales, A.; Gutiérrez-Fernández, García-Gutiérrez, M.C.; Ezquerra, T.A.; Rebollar, E.; Sics, I.; Malfois, M.; Gaidukovs, S.; Gecis, E.; Celms, K.; Bakradze . Structure Development in Polymers during Fused Filament Fabrication (FFF): An in-situ Small and Wide Angle X-ray Scattering Study using Synchrotron Radiation. *Macromolecules.*

Submitted

(8) Gutiérrez-Fernández, E.; Nogales, A.; Rebollar, E. Straightforward patterning of functional polymers by sequential nanosecond pulsed laser irradiation.

In preparation

(9) Gutiérrez-Fernández, E.; Gabaldón-Saucedo, I. A.; García-Gutiérrez, M. C.; Varea, A.; Nogales, A.; Rebollar, E.; Vilà, A.; Ezquerra, T. A.; Cirera, A. Laser nanostructuring on PEDOT:PSS and its influence on its electrical properties.

In preparation

(10) Gutiérrez-Fernández, E.; Ezquerra T.A.; García-Gutiérrez M.C.; Rebollar E.; Nogales A. Crystallinity and thermal behavior of poly(3-hexylthiophene) nanoparticles prepared by miniemulsion and flash approaches.

In preparation